Material Engineering for Monolithic Semiconductor Mode-Locked Lasers

Kulkova, Irina; Yvind, Kresten; Semenova, Elizaveta; Larsson, David

Publication date:
2014

Document Version
Peer reviewed version

Material Engineering for Monolithic Semiconductor Mode-Locked Lasers

by

Irina V. Kulkova

DISSERTATION

Submitted in partial fulfilment of the Requirements for the degree of
Doctor of Philosophy

Main supervisor: Kresten Yvind
Co-supervisor: Elizaveta S. Semenova
Co-supervisor: David Larsson

DTU Fotonik – Department of Photonics Engineering
Technical University of Denmark
2800 Kgs. Lyngby, Denmark

August 2014

This dissertation is dedicated to

Professor Dr. Aleksandr Nikolaevich Pihtin

who celebrated his 75th birthday this year

For the love of light…

Abstract

This thesis is devoted to the materials engineering for semiconductor monolithic passively mode-locked lasers (MLLs) as a compact energy-efficient source of ultrashort optical pulses. Up to the present day, the achievement of low-noise sub-picosecond pulse generation has remained a challenge. This work has considered the role of the combined ultrafast gain and absorption dynamics in MLLs as a main factor limiting laser performance. An independent optimization of MLL amplifier and saturable absorber active materials was performed. Two promising approaches were considered: quantum dot (QD) or single quantum well (QW) amplifier in tandem with a fast multi-QW electroabsorption modulator (EAM) based on the InP/AlGaInAs/InGaAsP platform for operation in the 1.55 μm telecommunications range.

A butt-joint MOVPE regrowth technique was established for monolithic integration showing high crystalline quality and low internal reflection compatible with the severe requirements of monolithic MLLs. Experimental characterization of static material parameters of the fabricated devices revealed QW-like gain behavior of a self-assembled InAs/InP QD material and low internal efficiency which limited its application in MLLs. Improved QW laser performance was demonstrated using the asymmetric barrier layer approach. The analysis of the gain characteristics showed that the high population inversion beneficial for noise reduction cannot be achieved for 10 GHz QW MLLs and would have required lowering the modal gain or utilizing an extended cavity design. The offset QW design was introduced. The performance of 10 GHz passively MLLs consisting of integrated QW gain section with MQW EAM was demonstrated to allow for 890 fs pulse generation with reduced timing jitter compared to non-integrated QW MLLs owing to the fast EAM recovery.

Danish Resumé

Denne afhandling omhandler halvleder materialeteknologi for selvkørende kortpulslasere, der er kompakte og energieffektive kilder til meget korte optiske pulser. Opnåelse af støjsvage sub-picosekund pulser er en udfordring. I dette arbejde er indflydelsen af den kombinerede ultrahurtige dynamik fra forstærker og absorber materialerne, som primær begrænsende faktor i pulsgenereringen, gransket. En uafhængig optimering af forstærker og absorber sektion er gjort og to lovende retninger undersøgt: Kvantepunkter (QD) eller en enkelt kvantebrønd (QW) som forstærkermateriale sammensat med en multikvantebrønds (MQW) elektroabsorptionsmodulator i InP/AlGaInAs/InGaAsP materialesystemet for anvendelse omkring telekommunikationsstandarden 1550 nm.

En stødsamling MOVPE gendyrkningsproces blev etableret til monolitisk integration af forskellige materialer med god krystalkvalitet og lav intern refleksion, hvilket er påkrævet ved brug i kortpulslasere. De statiske materialeparametre blev karakteriseret eksperimentelt og kvantebrøndslignende forstærkningsegenskaber blev fundet for selvorganiserede InAs/InP QDs med lav intern effektivitet, hvilket begrænsede deres anvendelse i kortpulslaserne. Forbedret kvantebrønds ydelse blev demonstreret ved brug af asymmetriske barrierer. Analyse af forstærkningskarakteristikken viste dog at høj populations inversion, hvilket er fordelagtigt for støjreduktion, ikke kan opnås for standard 10GHz QW lasere og nedsættelse af mode-forstærkningen eller en delvis passiv bølgeleder ville være nødvendig for forbedring med denne struktur. Et ikke-centreret design blev testet i denne forbindelse. Ydelsen af 10GHz selvkørende kortpulslasere med QW forstærker sektion og MQW absorber blev demonstreret med 890fs pulser og reduceret tidsjitter sammenlignet med ikke-integreret QW lasere, hvilket tilskrives et hurtigere absorber respons.

Acknowledgments

This work was performed at DTU Fotonik within the FLASH project financially supported by the Danish research council for technology and production.

First and foremost, I would like to express sincere gratitude to my main supervisor, Associate Professor Dr. Kresten Yvind, for offering me the opportunity to join his group and get involved in high-level experimental research activities. This thesis would not have been completed without his wise guidance and invaluable assistance throughout my whole Ph.D. study. Under his supervision, I have greatly profited from his knowledge and experience in physics of semiconductors and photonic devices, as well as semiconductor growth and technology, which has enhanced my interest in photonics and promoted my professional advancement.

I owe my deepest appreciation to my co-supervisor, Assistant Professor Dr. David Larsson, for his supervision in the early part of the project and for teaching me cleanroom processing with his tremendous patience, encouragement and great sense of humor. He also helped me to get started with experimental work in the laboratory and enlightened me about mode-locked lasers in general. I am very grateful to my second co-supervisor, Assistant Professor Dr. Elizaveta S. Semenova, who has been working on QDs growth within the project and for providing her expertise and valuable advice in MOVPE growth.

I would like to thank Dr. Shima Kadkhodazadeh from DTU CEN who performed all the STEM experiments and EDS analysis presented in this thesis. I also appreciate Nadezda Kuznetsova, Dr. Alexander Huck and Dr. Weiqi Xue for their assistance in μ-PL measurements; Matthew Haines for developing of the ICP-RIE process used for the device fabrication. My special appreciation is addressed to Dr. Thor Ansbæk and Dr. Luisa Ottaviano for kind aid in the cleanroom and practical advice and discussion on all kinds of fabrication issues. I also would like to convey thanks to the staff of the DTU Danchip for the daily technical support in the cleanroom and facility maintenance. In particular, Dr. Leif Johansen, Dr. Jesper Hanberg and Roy Cork are recognized for sharing their process knowledge and always being helpful with practical problems.

I am very thankful for my current and former colleagues from the Nanophotonics group I have not mentioned: Dr. O. Kopylov, Dr. M. Schubert, Dr. M. Pu, Dr. L. H. Frandsen., A. Lupi, M. Mitrovic, L. F. Frellsen, A. S. Jensen, Dr. Y. Ding for the friendly and pleasant working atmosphere of our workplace and for all the nice times we spent together outside of work. These acknowledgments would not be complete without noting my amazing officemates: Nadia, Krzysztof, Minhao, Andrey Novitsky, Louise and Miranda for daily dose of support and fun. I would like to mention my DTU colleagues Vika B., Clau G., Corinna D., Maksim Z., Olena M., Niels G., Radu M., Andrei V. L. and many others with whom I had the great pleasure to meet here, share fume hoods in the cleanroom or work in the labs.

Last and not least, I would like to thank my family, my dear friends Nadia and Sveta who became essential part of it for their endless patient, support, encouragement and understanding, and the people who were standing behind me and taking care of me. Спасибо, мама!

List of Publications

The following publications have been authored or coauthored during the course of the Ph.D. project:

Journal publications

1. N. Kuznetsova, I. V. Kulkova, E. S. Semenova, S. Kadhodazadeh, N. V. Kryzhanovskaya, A. E. Zhukov, and K. Yvind, "Crystallographic dependent in-situ CBr4 selective nano-area etching and local regrowth of InP/InGaAs by MOVPE," *J. Cryst. Growth*, 2014. (accepted for publication) 10.1016/j.jcrysgro.2014.07.051
2. V. Kulkova, S. Kadkhodazadeh, N. Kuznetsova, A. Huck, E. S. Semenova and K. Yvind, "High-quality MOVPE butt-joint integration of InP/AlGaInAs/InGaAsP-based all-active optical components", *J. Cryst. Growth*, vol. 402, pp. 243–248, 2014. doi: 10.1016/j.jcrysgro.2014.06.026
3. E. S. Semenova, I. V. Kulkova, S. Kadkhodazadeh, M. Schubert and K. Yvind, "Metal organic vapor-phase epitaxy of InAs/InGaAsP quantum dots for laser applications at 1.5 μm," *Applied Physics Letters*, vol. 99, no. 10, p. 101106, 2011. doi: 10.1063/1.3634029

Conference proceedings

4. I. V. Kulkova, N. Kuznetsova, E. S. Semenova and K. Yvind, "Butt-Joint Integration of Active Optical Components Based on InP/AlInGaAsP Alloys," in *2014 Compound Semiconductor Week and 26th International Conference on Indium Phosphide and Related Materials Compound Semiconductor Week (CSW/IPRM)*, Montpellier, France - May 11-15, 2014 (to be published in IEEE Proc.)
5. E. S. Semenova, I. V. Kulkova, S. Kadkhodazadeh, D. Barettin, O. Kopylov, A. Cagliani, K. Almdal, M. Willatzen and K. Yvind, "Epitaxial growth of Quantum Dots on InP for device applications operating in the 1.55 μm wavelength range," in *SPIE Photonics West 2014. 8996, Quantum Dots and Nanostructures: Synthesis, Characterization, and Modeling XI*, 899606, 2014. doi: 10.1117/12.2039567
6. I. V. Kulkova, D. Larsson, E. S. Semenova and K. Yvind, "Individual optimization of InAlGaAsP-InP sections for 1.55-μm passively mode-locked lasers," in *2012 23rd IEEE International Semiconductor Laser Conference (ISLC)*, pp. 133-134, 2012. doi: 10.1109/ISLC.2012.6348364
7. E. S. Semenova, I. V. Kulkova, S. Kadkhodazadeh, M. Schubert, R. E. Dunin-Borkowski and K. Yvind, "InAs/InGaAsP Quantum Dots Emitting at 1.5 μm for Applications in Lasers," in *2011 Compound Semiconductor Week and 23rd International Conference on Indium Phosphide and Related Materials Compound Semiconductor Week (CSW/IPRM)*, 2011.

Table of Contents

Chapter 1

Introduction

A continually-increasing number of Internet consumers all over the world and rapid boost in visual networking during the last years continuously raises demands on high-speed and energy-efficient optical transmission systems [1]. Figure 1.1 shows the Cisco® Visual Networking Index (VNI) Forecast predicting a three-fold increase in the global traffic usage over the next five years (2013-2018) [2]. This demand accelerates the development of new data network architectures, digital processing (coding) and signal multiplexing formats to exploit ultimately the available bandwidth of an optical fiber[1] or, alternatively, to utilize the capacity of multi-core fibers (see e.g. in [3]–[5]).

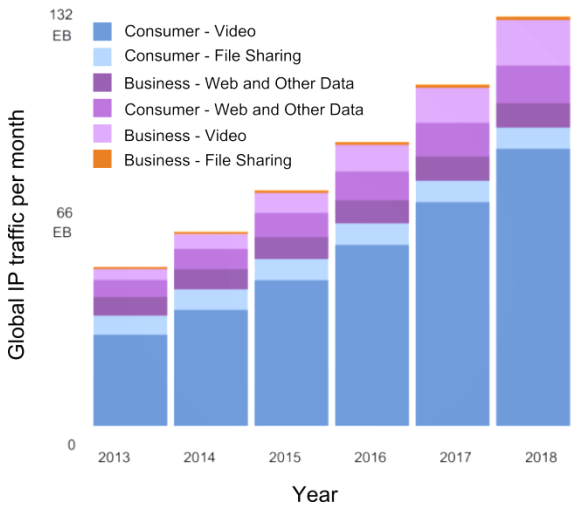

Figure 1.1: The Cisco® VNI forecast on the global Internet Protocol (IP) traffic growth for various network applications in 2013 - 2018 estimated in exabytes (EB) per month [2]. EB = Exabyte (10^9 GB).

To date, the modulation of a single data channel is limited by the electronics' capabilities to around 10 - 40 GHz, known as electronic speed bottleneck [6]. In order to increase transmission speed, optical channels can be combined into one data stream transmitted through the fiber by division of the signal in time, wavelength, polarization and quadrature. The most established platforms are based either on modulation of individual channels associated with particular wavelength bands in parallel (Wavelength Division Multiplexing (WDM)), or multiplexing of interleaved by a fixed time delay low bit rate signals into a high bit rate stream (Optical Time Division Multiplexing

[1] ~ 120 nm window in the 1.55 µm spectral range (C-band). However the bandwidth of a conventional Erbium Doped Fiber Amplifier (EDFA) is limited to ~ 30 nm (1.53 – 1.56 µm).

(OTDM)). Commonly system performance in terms of capacity, flexibility, complexity and cost is determined by state of modern technology in a component base. The following discussion will be led in the context of light sources as one of the main elements of any optical transmission system.

In WDM, state-of-the-art Vertical Cavity Surface-Emitting Laser (VCSEL) platform allows for direct modulation of a single channel up to ~ 30 GHz in the 850 nm wavelength band favorable for optical interconnects and, is expected, to deliver data rates above 50 Gbit/s (by means of on-off keying) in the future [7]–[9]. 25 Gbit/s rate was achieved in the 1.55 μm wavelength range of main interest for long haul transmission with ~ 10 GHz modulation speed [10]. VCSEL arrays can be used as a multi-wavelength source to increase a bit rate, however the problem of scalability can be expectable in the future [11]. The more advanced Orthogonal Frequency Division Multiplexing (OFDM) technique has a similar principle, but offers higher spectral efficiency when using the orthogonality property to demultiplex overlapped in frequency bands (subcarriers) without deterioration from interference [12]. Recently, 26 Tbit/s data transmission and processing was demonstrated using all-optical fast Fourier transform scheme [13].

In case of an OTDM system, as illustrated in Figure 1.2, the return-to-zero signal (desirable for long-haul networking) can be represented by a train of pulses emitted from a single source and modulated with base frequency (*B)* available for electrical data processing. The number of channels (*N)* and consequently, the highest achievable transmission speed (*N*B)* is determined by the pulse width, which has to be smaller than the interleaved time slot B^{-1}. The pulse shape, background noise and timing instability lead to detrimental crosstalk, and therefore increase the error detection probability or bit-error-rate (BER). Recently, OTDM symbol rate reached 1.28 Tbaud per polarization [14], which was employed to transmit 10.2 Tbit/s data streams over 29 km single fiber line using 16 Quadrature Amplitude Modulation [15].

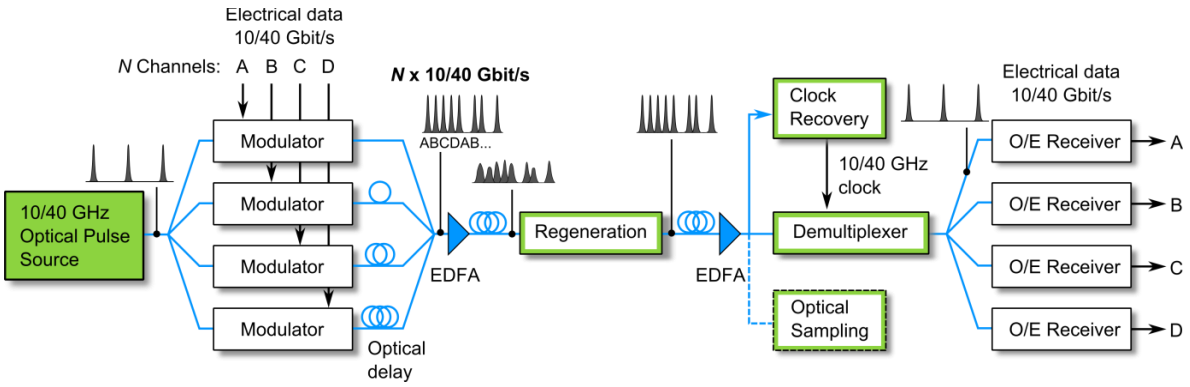

Figure 1.2: A schematic of an OTDM transmission system. Possible applications of a pulsed source are indicated using green box outlines.

A source of ultrashort optical pulses is an essential element of the ODTM transmitter, and moreover, can be utilized to perform data demultiplexing in the receiver prior detection. In order to synchronize a demultiplexing switch gate to the incoming signal, the base rate frequency has to be restored. This function is assigned to clock recovery which can be accomplished in different ways, e.g. using phase-locked loops [16] or in all-optical schemes [17]. Both approaches require pulse generation of high temporal stability. In addition, the pulse source can be used for re-amplification, reshaping and retiming (3R) of a noisy signal propagating through long dispersive and lossy optical fiber links [18].

Another promising application of ultrashort pulse sources is related to its wide optical spectrum consisting of equally-spaced phase-matched modes. These comb generators can be considered as a low-cost counterpart of VCSEL arrays in WDM and OFDM systems (e.g. [19]), and can be used in a hybrid WDM - OTDM platform [20], [21]. Furthermore, pulsed lasers are suitable for integrated data en/decoding schemes in the emerging Optical Code Division Multiple Access (OCDMA) technology [22], [23].

One of the most impressive results achieved so far using a single laser source (a 10 GHz solid-state MLL) is record 43 Tbit/s transmission at 1.55 μm over 67.4 km reported in [24]. The principle diagram of the experimental setup is shown in Figure 1.3. The system is utilized all five degrees-of-freedom of signal multiplexing mentioned above: wavelength (WDM), time (OTDM), polarization (Polarization-Division Multiplexing), quadrature (Quadrature Phase Shift Keying (QPSK)) and space (Space Division Multiplexing in a multicore fiber). The implementation of a MLL pulse source brings together the demanding broad optical spectrum, short pulse, polarization and phase control at once.

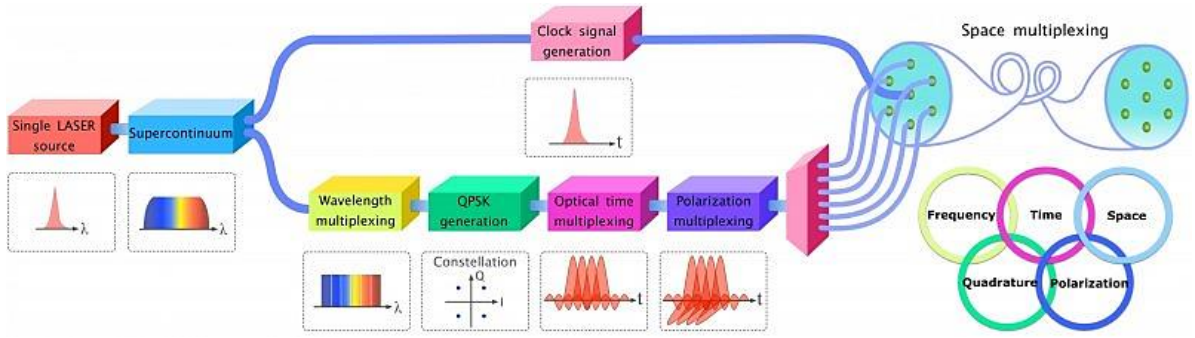

Figure 1.3: A principle diagram of the 43 Tbit/s transmission system using a single 10 GHz MLL based on combined space-, wavelength-, time-, polarization- and quadrature modulation [24]. Reprinted from [25].

Beside telecommunication applications, pulse laser sources are attracting considerable attention for time-resolved measurements e.g. optical sampling of an optical waveform [26]–[28], studying of nonlinear dynamic effects [26]–[28] and for the realization of analog-to-digital converters [29]. A maximum temporal resolution is limited by timing pulse fluctuation. The maximum timing jitter value is estimated to be around few tens fs [30]. Other prospective directions are energy-effective high-speed chip-to-chip optical interconnections [31], terahertz generation [32], optical coherence tomography and bio-imaging for medical diagnostics (see e.g. [33], [34]), and other.

1.1 Semiconductor Mode-Locked Lasers for OTDM Systems

In spite of the promising results, potential flexibility and cost-efficiency, commercial realization of OTDM has been restricted by a number of technological reasons, and in large measure, due to the feasibility of a compact transmitter pulse source. Semiconductor based lasers are an extremely attractive candidate as a highly-efficient, directly electrically-driven, compact, robust, compatible with electronic-photonic integrated circuits and cheap (by means of mass production) solution. Pulse generation can be obtained by a number of techniques, such as gain- or Q- switching, and in most cases referred to mode-locking.

The basic idea of mode-locking lies in introduction of coherence between the adjacent laser cavity modes (or "locking" them in phase) by modulating cavity losses or gain at the fundamental frequency

(the mode spacing). In this case, oscillating in phase modes experience constructive interference as shown in Figure 1.4, which results in a periodic pulse train generation at a frequency given by

$$f = \frac{v_g}{2L} = \frac{c}{2n_g L} \tag{1.1}$$

for a linear cavity of the length L, where v_g is the group velocity equal to the speed of light c divided by the group refractive index n_g. Using small-size monolithic Mode-Locked Laser (MLL) diodes, high pulse repetition rates up to hundreds GHz [35] can be obtain.

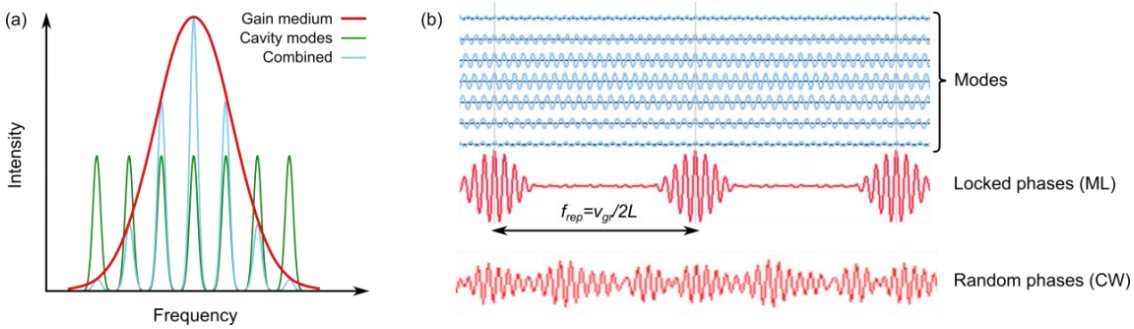

Figure 1.4: Illustration of light emission via multiple cavity modes amplified by a gain medium (a) in case of random phase between the modes (continuous-wave regime) and phase-matching (b).

The ultimately attained pulse duration is determined by the number of locked modes, which defines by the finite gain bandwidth of an active medium as shown in Figure 1.4 (a). The product of the spectral $\Delta\nu$ and temporal Δt width of the pulse of a certain shape is a constant value called the time-bandwidth product (TBP):

$$TBP = \Delta t \Delta\nu = \Delta t c \frac{\Delta\lambda}{\lambda^2}. \tag{1.2}$$

The TBP parameter is often applied to quantify the quality of the pulse, and commonly serves as a figure-of-merit for MLL. Depends on the temporal pulse shape commonly described by a Gaussian, a hyperbolic secans (*sech2*) or a Lorentzian function, the TBP product takes its minimum value for Fourier-transform-limited pulses of 0.441, 0.315 or 0.142, respectively. Considering the bandwidth of 30-50 nm available in semiconductors, the lower theoretical limit for a pulsewidth is predicted to be in order of 100 fs [36].

A basic two-section monolithic semiconductor MLL diode is presented in Figure 1.5. The laser cavity is formed by crystal facets and contains of electrically separated gain (can be referred to as semiconductor optical amplifier (SOA)) and saturable absorber (SA) sections. Typically, a single active material is used. A forward biased section provides light amplification, while absorption is generated by applying reverse bias.

Mode-locking can be realized by direct modulation applying a periodic (sinusoidal or δ-peak) electrical signal to the driven element, or in an indirect self-established free-running way with the assistance of an intensity dependent loss component, so called a saturable absorber (SA), embedded in the laser cavity [37]–[39]. The first schema is referred to active mode-locking and the second one is passive. Passive mode-locking allows for achieving significantly shorter pulses since pulse formation is based on ultrafast gain and loss dynamics, rather than on the relatively slow driven oscillator in

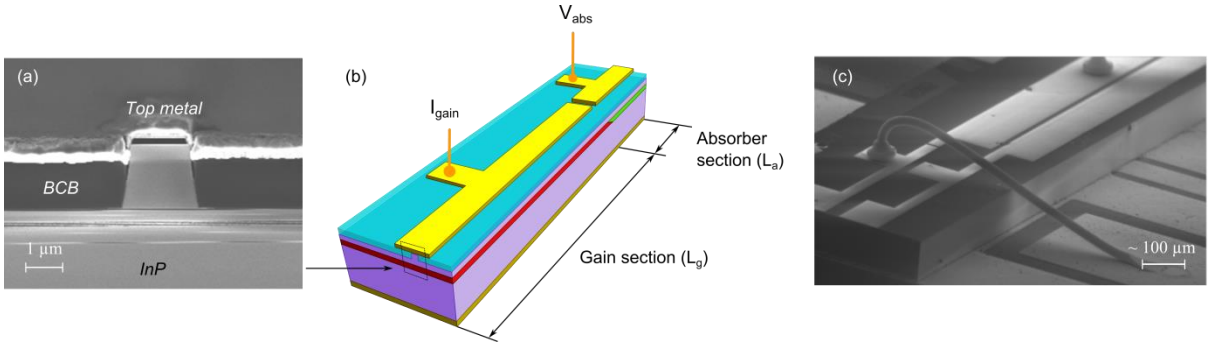

Figure 1.5: A schematic diagram of a two-section monolithic MLL diode (b); cross-sectional (a) and top-view (c) images of a processed device.

active mode-locking as will be discussed further in the following Chapter 2. The combination of active and passive techniques, namely hybrid mode-locking, makes passive MLLs more stable to timing jitter at a fixed frequency [40], controlled by external modulator. Moreover, it gives the possibility to synchronize the MLL output signal with the electronics, which is of great interest to data transmission and signal-processing systems along with the other benefits mentioned above.

Mode-locking from semiconductor lasers can be also achieved in a single-section configuration using Quantum Dot (QDs) or Quantum Dashes (QDashes) active media [41], [42]. Phase locking between the cavity modes in this case can be established as a result of nonlinear optical effects such as four-wave-mixing (FWM) enhanced in QD and QDashes amplifiers. Typically observed highly chirped output signal requires a proper dispersion compensation element (e.g. a single mode fiber) to achieve pulse generation. The need of external components limits the flexibility, however, potential applicability of an integrated Distributed Bragg reflector was recently demonstrated in [43].

The work presented in this thesis is concerned with the development of monolithic MLL diodes in particular for optical sampling and high-speed OTDM systems operating in the 1.55 µm range. A pulse repetition rate of interest is 9.953 GHz defined by the existing modulation standard (STM64), and 39.813 GHz expected to be utilized in the future. The emission wavelength can be designed using compound semiconductor materials and epitaxial crystal growth, while the repetition frequency corresponds to cavity length of a few millimeters (Eq. (1.1)) easily attainable in monolithic MLLs. Fine tuning can be performed e.g. by using thermal effect or carrier-density dependent refractive index change in additionally integrated passive section [44].

Minimum requirements imposed on pulse properties depicted in Figure 1.6 appropriate for OTDM transmission can be described as following:

- *Sub-picosecond pulse duration*

As stated above, the maximal number of multiplexed channels is limited by the pulse width. In order to avoid coherent superposition between the pulses, a Full Width at Half Maximum (FWHM) of a pulse should be at least half of the time slot for an ideal (transform limited) Gaussian or $sech^2$ pulse. In practice, a tolerable time slot is constrained to be 3 – 5 times longer than the pulse duration to obtain a low BER. To take concrete examples: for transmission at 160 Gbit/s (4 x 40 Gbit/s) a pulse width of 6.25 ps is needed, while 1280 Gbit/s (32 x 40 Gbit/s) lines require 0.78 ps pulses.

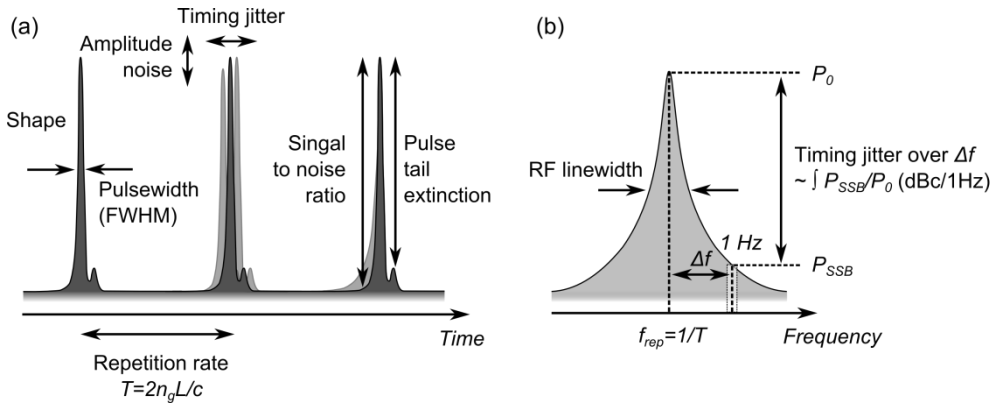

Figure 1.6: (a) Properties of a pulse train in time domain and (b) corresponding radio-frequency (RF) electrical spectrum (P_0 and P_{SSB} are the power at the carrier frequency and single-sideband (offset) frequency, respectively).

- *High pulse tail extinction ratio*

The appearance of trailing pulses and background component (pulse pedestal) leads to a high probability of signal detection error in the receiver due to interference with adjacent pulses. Therefore, a high pulse tail extinction ratio (PTER), which equals to the ratio between the peak pulse power and background level is needed. Consequently, a high average power is desirable. Simulation results for 40 Gb/s modulation base rate show the required PTER of 27 and 41 dB for transmission at 160 and 1280 Gbit/s speed, respectively, with 1 dB power penalty [45].

- *Low timing and amplitude noise*

The high temporal and amplitude stability of pulse sources both in the transceiver and the clock recovery circuit is critical to guarantee a low BER < 10^{-9}. The arrival time variation of 1/12 the switching window of the demultiplexer is desirable (for a pulse width of 1/5 the time slot) [46]. For example, transmission at 160 Gbit/s and 1280 Gbit/s requires the jitter less than 500 fs and 65 fs, respectively.

In-depth review of the application of semiconductor MLLs in in high-speed communication systems, characterization of MLL properties and its influence on OTDM performance is given in [47].

1.2 State-of-the-Art Monolithic Mode-Locked Lasers

Since the first demonstration of pulse generation from semiconductor lasers in 1978 [48], pulse width has been reduced from ~ 30 ps to a few picosecond using traditional Quantum Well (QW) gain medium (Figure 1.6) [49], which is much larger than the fundamental limit. Compared to diode-pumped fiber and solid-state MLLs, for example, used in high-speed OTDM transmission experiments in [24], semiconductor MLLs, especially passive ones [40], suffer from pulse instabilities and high noise, spectra chirp and pulse asymmetry, and exhibit moderate output power (typically ≤ 1 mW), which are attributed mainly to the gain saturation and ultrafast gain dynamics. Pulse noise can be reduced by incorporation of narrowing filters, such as distributed Bragg reflectors (DBR) [50], however it limits the minimum pulse width. The Fourier transform limited pulses were experimentally obtained using DBR filtering and dispersion compensation. However, in most experiments the pulse width does not get over the picosecond range for QW MLLs as shown in Figure 1.7 [24].

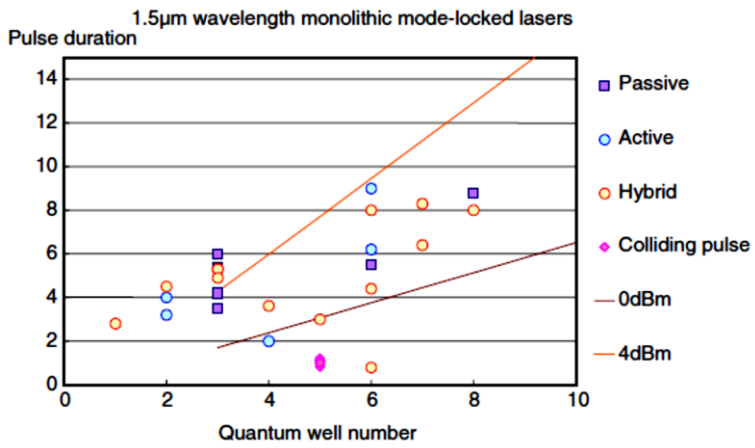

Figure 1.7: Optimum pulse width for QW monolithic mode-locked lasers operating at 1.5μm wavelength. Reprinted from [49].

Further development has been devoted to theoretical and experimental search of a proper laser active media and operation conditions utilizing better understanding of the role of ultrafast dynamics in MLLs (e.g. [51], [49], [52]). Commonly, studies show an increase of timing jitter with reducing pulse width. 2.8 ps pulse generation from 40 GHz QW hybrid MLLs with low timing jitter down to 73 fs (integrated over a 10 kHz - 320 MHz frequency range. For illustration see Figure 1.6 (b)) was demonstrated in [53]; 860 fs pulses with a low RF linewidth of 30 kHz from 20 GHz QW MLLs with was reported in [54]. Other approaches have involved the realization of intracavity dispersion compensation elements [55] or optimization of saturable absorber properties, e.g. using a monolithically integrated ultrafast Uni-Travelling Carrier photodiode [56]. However, unstable laser performance was demonstrated.

Significant improvements have been achieved in conjunction with advances in the fabrication of low dimension quantum structures over past years, namely QDs and elongated QDashes. Owing to the unique properties of QD material attributed to the modified (ideally δ-function-like) density of states, the reduced threshold current density and lower temperature sensitivity, low spontaneous emission noise, line width enhancement factor and unsaturated gain value compared to QW were predicted and experimentally proved [57]–[59]. Pulse width reduction down to 360 fs using flared waveguide configuration [60] was demonstrated in 1.1 - 1.3 μm range (GaAs-based QDs). A record low timing jitter of 124 fs (4 - 80 MHz) was shown for 10 GHz QD MLLs compared to 570 fs QW passively MLLs of similar configuration [61], [62]. The RF line width was reduced down to 1 kHz for QDs MLL.

The results for 1.55 μm QD/QDash-based MLLs have been rather moderate due the technological aspects of QD growth on InP and less conducive optical properties attributed to long-wavelength devices, which will be discussed in detail in the following. Thus, QD/QDash lasers typically exhibit much higher threshold current density in order of kA/cm^2 [63]. For comparison, the record-low threshold current density for 1.59 μm QDs reached 190 A/cm2 at room temperature [64] against ~ 20 A/cm^2 demonstrated for 1.3 μm QD [65]–[67]. Similar to QW MLLs, the pulse width is retained in the picosecond range while the noise and temperature performance has been improved [68]–[71].

The application of monolithic cavity semiconductor mode-locked lasers in high-speed OTDM systems for the realization of both data transmitter and receiver parts is highly attractive for commercial prospects. However, in order to fulfill the conditions on pulse quality and replace solid state MLLs lasers further research and development are required.

1.3 Objectives and Structure of this Thesis

The object of this work has been to extend performance of semiconductor monolithic MLLs toward low timing-jitter sub-picosecond pulse generation in the 1.55 µm range with 10 GHz pulse repetition rate for application in optical sampling and OTDM or hybrid data transmission systems. A key approach has been based on independent optimization of the active medium of the laser component, amplifier and absorber, to deliver ultimate device operation in combination. Both InP-based QW and QD materials were under investigation. As the main technology platform, butt-joint metalorganic vapour phase epitaxy (MOVPE) has been employed for monolithic integration.

This thesis is divided into four main parts excluding Introduction, Conclusion and two appendices. In the following ***Chapter 2***, a basic description of passive mode-locking and a pulse shaping mechanism in semiconductor lasers is given**.** A thorough consideration of dynamic properties in semiconductor, conditions for stable mode-locking and factors limiting the pulse width reduction beyond the one picosecond range are summarized. The main criteria for the design of gain and absorber active media are applied for evaluation of QD and QW materials. The advantages of QD or highly inverted single QW laser amplifiers for achieving short and low noise operation are outlined.

Chapter 3 moves the theoretical consideration toward the practical realization involving the optimization of active material and a separate confinement heterostructure (SCH) of the amplifier and the absorber independently. The InGaAsP/AlGaInAs/InP material system is considered for the band-gap engineering to achieve laser operation in the 1.55 µm wavelength range of interest. An asymmetric barrier layer single QW gain material with an asymmetric separate confinement heterostructure is shown to be compared favorably with a conventional (symmetric) InGaAsP-based QW amplifier using simplified modeling of static properties. Shallow MQWs embedded into cladding layers with a stepped energy bandgap profile are proposed for a fast saturable absorber. A brief overview of alternative materials and epitaxial structures is given along the discussion.

Chapter 4 deals with the technological aspects of the fabrication of the designed monolithically integrated MLLs. First, metalorganic vapour phase epitaxy (MOVPE) used for growth and integration is briefly introduced. Due to the high interest in utilization of QD potential for low-noise MLLs, the detailed description of challenges and achieved progress in growth of 1.55 µm emitting QDs are presented. The following discussion concerns issues related to MOVPE butt-joint regrowth employed for the integration of the laser section. The performed process development is supported by the investigation of crystalline and optical properties at the regrowth interface. In the end, an overview of the processing flow used for device fabrication is presented.

Chapter 5 is devoted to the experimental characterization of intrinsic properties of the fabricated material such as gain and absorption spectra, internal losses. Static lasing properties including temperature stability are evaluated using Fabry-Perot lasers. Special attention is placed upon the investigation of a butt-joint interface quality between the integrated sections (reflection, optical and carrier losses) as it has significant influence on MLL performance. Thereafter, measurement results are analyzed to estimate the operation range for 10 GHz passively MLL consisting of various integrated structures following the criteria outlined in Chapter 2. Finally, the performance of integrated MLLs based on QW gain section and MQW saturable absorber is demonstrated. The problems faced in achieving the desirable laser functionality for integrated QD and QW MLLs are discussed.

Chapter 2

Theory of Semiconductor Mode-Locked Lasers

This chapter covers the theory of passive mode-locking in semiconductors with an emphasis on ultrafast dynamics, which determine the pulse formation mechanism. The necessary conditions for stable mode-locking are provided. Since the project is aimed to achieve sub-picosecond pulse generation with sufficiently low noise component, the role of ultrafast gain dynamics responsible for the pulse broadening and instabilities are described. In the following, the main design criteria are presented and discussed for QD and QW semiconductor systems. The consideration leads to the conclusion of the need of independent optimization of the gain and absorber structures to achieve the desirable device performance. The QD active medium is shown to be the most promising candidate for a laser gain section, however, actual properties and hence performance can vary significantly depending on the parameters of a particular QD system. A highly inverted single QW is considered as a good alternative. A shallow multi-QW-based electro- absorption modulator is proposed to perform the function of a fast saturable absorber while giving flexibility in device geometry and operation conditions.

2.1 Passive Mode-Locking in Semiconductor Lasers

Generation of ultrashort pulses in mode-locked lasers is a phenomenon that can be described by a constructive interference between the cavity modes matched in phase with the assistance of gain or absorption modulation. The electric field of the output light composed of *N* modes, where the *n*-mode described by the amplitude A_n, angular frequency ω_n and phase φ_n, can be presented as a sum of the modes

$$E(t) = \sum_{N} A_n e^{i(\omega_n t + \varphi_n)}, \tag{2.1}$$

resulting in the total output intensity *I* nearly constant in time (continuous-wave (CW) regime):

$$I = < \mathrm{N} {A_n}^2 >_t . \tag{2.2}$$

When the optical modes circulating within the cavity experience amplitude modulation at a frequency equal to cavity mode spacing $\Delta\omega = 2\pi \frac{v_{gr}}{2L}$ or its harmonic (Eq. 1.1), the modulator impairs sidebands to each mode whose frequencies coincide with its neighboring modes. This process leads to

transferring energy from the central mode to the spectral wings and locking the modes in phase [72]. Then, if $\omega_{n\pm1} = \omega_n \pm \Delta\omega$ and $\Delta\varphi_n = const$, the electric field can be written as

$$E(t) = A_n e^{i(\omega_n t+\Delta\omega)} \sum_N e^{-in\Delta\omega t} = A_n e^{i(\omega_n t+\Delta\omega)} \frac{sin(\frac{N\Delta\omega t}{2})}{sin(\frac{\Delta\omega t}{2})}, \tag{2.3}$$

so that the intensity is a periodic function of time with a cycle frequency inversely proportional to the cavity roundtrip time:

$$I(t) = \mathrm{N}^2 {A_n}^2 \frac{sin^2(\frac{N\Delta\omega t}{2})}{sin^2(\frac{\Delta\omega t}{2})} = \mathrm{N}^2 {A_n}^2 | \, t = T_{rep} = \frac{2\pi}{\Delta\omega} \, . \tag{2.4}$$

In time domain, the process can be understood from Figure 2.1, which illustrates combined average gain and losses dynamics for the active (a) and passive (b) mode-locking case. Due to periodic modulation, the net gain is positive once per round trip allowing for propagation and amplification of the light pulses of a finite time duration. Sinusoidal amplitude modulation driven by an external oscillator in active mode-locking becomes less effective for pulse shaping with reducing pulsewidth. This results in longer achievable pulses compared to passive mode-locking with a steeper and narrower net gain opening as shown in Figure 2.1. Reducing the modulation depth in turn leads to a smaller number of the mode locked in phase. Therefore, the generation of ultrashort pulses is generally associated with the passive mode-locking technique.

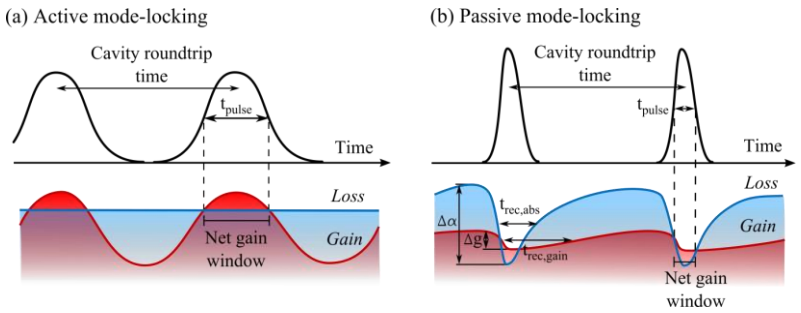

Figure 2.1: Schematic representation of the combined average gain and losses dynamics in case of (a) active and (b) passive mode-locking. The net gain and losses integrated over a round trip are shown as a function of time referenced to the pulse peak power [73].

The detailed theoretical treatment of the mode-locking process was described in the lumped element theory of Haus, in particular for the case of a slow saturable absorber of interest for semiconductor MLLs in [73], [74]. Further, the lumped-element and fully distributed time-domain theory or a travelling wave model were elaborated, which can be found in reviews [38], [51] and handbooks, e.g. [75]. Modeling of the mode-locking process is a powerful tool for understanding and predicting laser performance, however, was beyond the scope of this work, and thereby only qualitative description will be presented.

Passive mode-locking established in a self-running manner relies on nonlinear intensity-dependent light transmission provided by a saturable absorber incorporated into the laser cavity. In case of a semiconductor absorber, a large amount of carriers is generated during propagation of intense pulse,

and a significant filling of the active states can occur. This effect is known as spectral hole burning (SHB). As a result, further optical transitions turn out to be inhibited, and the absorption strength rapidly decreases. The bleached absorber transmits the light without significant changes. Subsequent carrier redistribution and thermalization recovers the absorption. That way, the net gain window is created. Likewise, a gain saturation behavior exhibits at high optical power associated with the depletion of the carriers available for stimulated emission and enhanced by instantaneous two-photon absorption (TPA) followed by gain recovery (schematic diagram of TPA can be found in Figure 2.5 (a)). The gain and absorption time evolution after transmission of a strong pulse is schematically illustrated in Figure 2.2. Typically, semiconductor passive MLLs operate at strong absorption saturation $\Delta\alpha$ and moderate gain saturation Δg as depicted in Figure 2.1 (b).

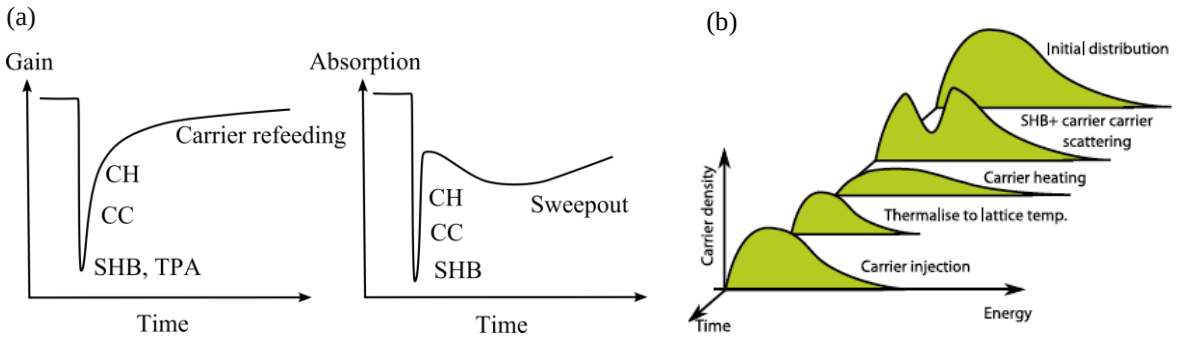

Figure 2.2: (a) Schematic illustrations of the gain and absorption saturation and recovery processes caused by pulse propagation associated with (b) ultrafast carrier density perturbation. CH – carrier heating, CC - carrier-carrier scattering.

The gain and absorption recovery times reflect the ultrafast carrier distribution response on the perturbations caused by the transmitted pulse. Figure 2.2 (b) shows the temporal evolution the carrier density for a bulk semiconductor amplifier. By definition, spectral hole "burning" means the modification of the system from a steady-state condition with Fermi-Dirac carrier distribution to the non-equilibrium. This unstable condition is rapidly solved by energy exchange between the carriers or carrier - phonon interaction. The fast carrier-carrier (CC) scattering recover the spectral "hole" in a time scale of 50-200 fs. However, the resulting carrier distribution is characterized by an elevated temperature with the lattice. Hot carriers are thermalized by phonon-carrier scattering which takes longer time up to 1 ps. Gain recovery is accomplished with the final carrier refeeding by carrier injection in a (0.1-1) ns timescale determined by the carrier transition time across the cladding layers and the external circuit characteristics. The absorption recovery due to spontaneous emission is about 1 ns, which is not sufficient for mode-locking. Hence, the fast absorption recovery (tens ps) is typically achieved by the carrier sweep out process via thermoionic emission under reverse biasing. The absorber recovery time $t_{rec,abs}$ in semiconductor MLLs can be longer than the pulse duration t_{pulse} [76]. In this respect, the pulse formation is referred to passive mode-locking with a slow saturable absorber mentioned above.

The pulse formation mechanism in passive MLLs starts when high intensity fluctuations or spontaneous emission spikes oscillating in the cavity can bleach the absorber and be partially transmitted, while the gain section continuously amplifies the light and makes the strongest spikes even more pronounced. This selection process takes several tens - hundreds round trips until the single pulse within the round trip can be supported. Further evolution of the pulse includes attenuation of the low intensity leading edge by the saturable absorber resulting in pulse shortening. The trailing part remains almost unchanged since $t_{rec,sat} > t_{pulse}$. This yields to asymmetric pulse shaping with steep

leading part and a slowly decay tail. At the same time, the absorber shifts the pulse spectrum towards the shorter wavelengths since an increase in the losses should be compensated by the gain. The amplifier continuously increases the pulse peak intensity and, when the energy of the pulse is enough to saturate the gain (typically tenths of pJ), the pulse narrowing performed by the absorber is compensated by broadening in the amplifier [77]. In practice, the effective pulse shaping breaks typically when the pulse duration reaches a value of around one picosecond. The main reason is an increased influence of intracavity dispersion arisen from the ultrafast nonlinear effects during gain suppression and recovery, which will discussed in detail in Section 2.3.

2.2 Mode-Locking Conditions

Saturation Energy

The given simplified description of the pulse build-in process requires the absorber being saturated at lower energies of the optical field than the gain [38]. High gain saturation energy is required to avoid strong gain damping and achieve high pulse intensities. The simulation provided in [78] suggests that Fourier-transform limited pulse generation requires the ratio between the saturation energies of the gain and SA sections $s = E_{sat,g}/E_{sat,\alpha}$ large than 6, where the saturation energy can by defined as

$$E_{sat} = \frac{h\nu A}{\Gamma \frac{dg}{dN}}, \tag{2.5}$$

where $h\nu$ is the photon energy, N is the carrier density, A is the optical mode cross-sectional area, Γ is the confinement factor and $a = \frac{dg}{dN}$ is the differential gain (or absorption). In QWs, the carrier – dependent material gain can be expressed using a logarithmic function as following

$$g = aN \ln \frac{N}{N_{tr}} \tag{2.6}$$

where N_{tr} is the transparency current density and aN represents the linear gain coefficient g_0 [79]. For QDs to describe gain saturation the dependence can be written as [80]

$$g_0(J) = g_{max}\left[1 - \exp(\frac{N_{tr} - N}{b})\right] + \alpha_i, \tag{2.7}$$

where g_{max} is the peak modal gain and b is a fitting parameter.

Due to the modified density of states (DOS) in low-dimensional quantum confined heterostructures illustrated in Figure 2.3 (a), the differential gain decreases faster with increasing carrier density for QDs and QWs (Figure 2.3 (b)), and thus, the ratio of saturation energies increases. Therefore, the condition $E_{sat,g} > E_{sat,\alpha}$ is met in semiconductors directly using a forward biased gain section and a reversed biased absorber. However, the fulfillment of this condition does not necessarily guarantee stable mode-locking.

A more stringent form of this condition was derived for passively MLLs in [81] by extending the net gain modulation phasor approach assuming sinusoidal light intensity modulation in the cavity

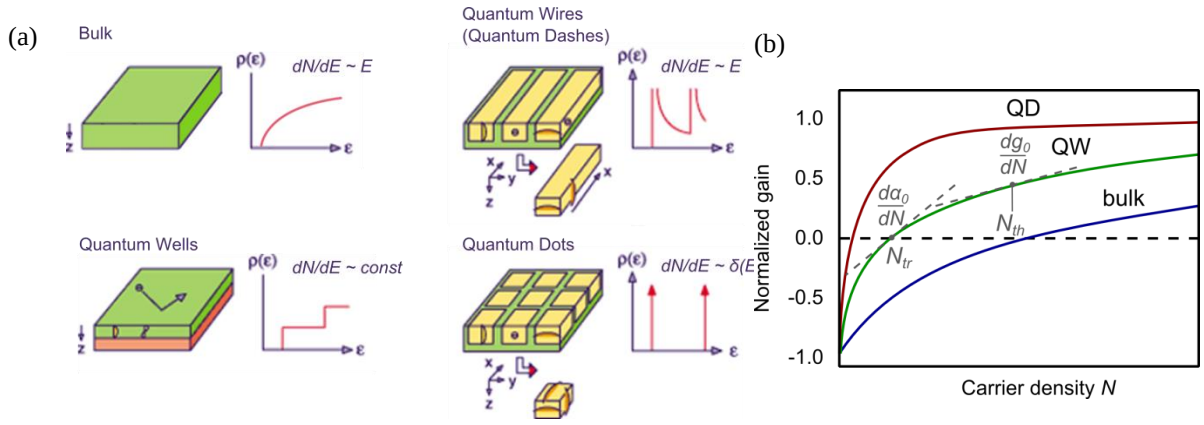

Figure 2.3: (a) Density of states as a function of energy in bulk and low dimensional quantum confined heterostructures. (b) Schematic illustration of the normalized gain versus carrier density for bulk, QW and QD material [60].

considering discrete gain and absorber sections. Analytical estimation of the stability range for a given laser geometry can be done using the next expression

$$\left(\frac{da_0}{dn}\right)^2 a_0 \frac{L_a}{L} - \left(\frac{dg_0}{dn}\right)^2 g_0 \frac{L_g}{L} > \frac{a_i}{2}\left(a_{mir} v_{gr} \frac{Wd}{\Gamma P} h\nu\right)^2, \tag{2.8}$$

where α_i is the internal loss coefficient, a_{mir} is the outcoupling (mirror) losses, $L = L_g + L_a$ is the total length equals to the sum of the lengths of the gain and absorption sections (see Figure 1.5), W is the width and d is the thickness of the active region, P is the peak optical power.

Taking into account that $\frac{da_0}{dn} \gg \frac{dg_0}{dn}$ and assuming a sufficiently high peak power, the Eq. (2.5) can be simplified to

$$\frac{a_0}{g_0}\frac{L_a}{L_g} > \left[\frac{\frac{dg_0}{dJ}}{\frac{da_0}{dJ}}\right]^2, \tag{2.9}$$

where $\frac{\mathrm{dg_0}}{\mathrm{dJ}}$ and $\frac{\mathrm{da_0}}{\mathrm{dJ}}$ are the differential gain and absorption with respect to the current density J, which is approximated through the carrier lifetime τ and the injection efficiency η_i as

$$\frac{dg_0}{dn} = \frac{qd}{\eta_i \tau}\frac{dg_0}{dJ}. \tag{2.10}$$

The $\frac{dg}{dJ}$ and $\frac{\mathrm{da}}{\mathrm{dJ}}$ values can be obtained directly from experimental measurements of the current dependent *net* modal gain spectra by fitting with the expression (2.6) for QWs and (2.7) for QDs. However, this simplified approximation requires the carrier lifetime be larger than the stimulated lifetime, which is not necessarily fulfilled for QWs due to enhanced carrier interaction.

At threshold, the *net* modal gain g_0 is in balance with the total optical losses presented by the sum of the mirror losses α_{mir} for the mirror reflectivities R_1 and R_2, and the *net* modal absorption a_0 in the absorber:

$$g_0 = a_0 + \alpha_{mir} = a_0 + \frac{1}{2L}\ln\left(\frac{1}{R_1 R_2}\right). \tag{2.11}$$

The given criteria (2.8) and (2.11) allow for predicting the range of the operation conditions (biasing, temperature) for a specified MLL laser cavity design (L_a/L_g) based on QDs in good agreement with the experimental data [82], [81]. Based on this approach, an improved pulse width and power using reconfigurable multi-section passive QD MLLs was demonstrated in [83].

For monolithic MLLs consisting of one type of an active medium, a low gain-to-absorber ratio L_a/L_g is shown to support higher power and shorter pulses [60]. For a short absorber section, pulse narrowing can be not sufficient. On the other hand, increased losses with an absorber section length result in higher noise. However, if the length of the absorber is short such as comparable to a pulse transit time, the reflected pulse passes the absorber at saturation, which promotes more symmetric and stable generation of pulses of shorter duration [49], [84]–[87]. This regime is known as colliding pulse mode-locking (CPM) which has been realized in ring cavity resonators, by insertion of the absorber in the middle of linear cavity MLLs or by applying high reflection coating to the rear facet in the two-section configuration (self-colliding mode-locking) [84], [88].

Recovery Time

Fast absorber recovery is necessary for maintaining stable pulse shaping by suppressing CW component. Moreover, slow absorption recovery assists the multi-pulse formation mechanism illustrated in Figure 2.4 (a). If the gain recovers faster than the absorber, the second (or multiple) net gain window can be opened, and then multiple trailing pulses are generated after the main pulse. This situation typically occur for pulses shorter than 1 ps, when a large amount of photo-generated carriers can rise Coulomb potential between the carriers leading to efficient screening of an external field. It reduces the unsaturable absorption and carrier mobility, which decelerates absorber recovery (see Figure 2.2 (a)).

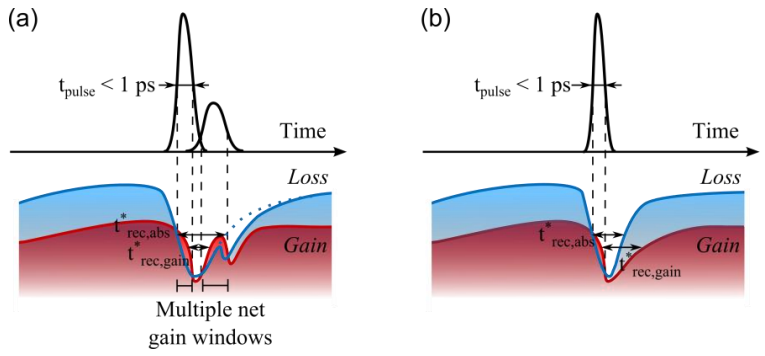

Figure 2.4: Sub-picosecond pulse generation: (a) in case of the fast gain recovery accompanied with secondary pulse formation and (b) in case of the slow gain recovery.

The recovery time can be shorten in a field-enhanced absorber by increasing reverse biasing [89], uni-traveling carrier (UTC) saturable absorber [56], or by introducing defects acting as recombination centers by proton bombardment [90]–[92] or ion implantation [93], [94]. Considering the simplest in

realization (by splitting a contact - see Figure 1.5 (b)) and reliable reverse biased absorber section, there are two main processes involved for the absorption recovery: thermionic emission and tunneling. It means that the recovery time depends on the carrier effective mass, presence of the confinement barriers, and applied electrical field [95]. Assuming the dominant thermionic escape process, the recovery time in QW EAM is exponential function of the reverse bias $\boldsymbol{V}$ estimated as following [96]:

$$\tau_{rec,\alpha} = \sqrt{\frac{2\pi m^* L_w^2}{k_B T}} \exp\left(\frac{E_b - L_w e(\boldsymbol{V} + V_{bi})/2d}{k_B T}\right), \tag{2.12}$$

where L_w is the QW width, E_b is the confinement potential, m^* is the effective mass, V_{bi} is the built-in potential, and d is the width of the depletion region. The recovery time reduction from hundreds of ps to few ps under reverse biasing ranged from 1 - 10 V was reported for band-gap engineered MQW EAM in [95], [96]. However, the recovery in the time scale of about 100 ps can be expected due to the detrimental screening effect, carrier pile-up at the edges of the confinement layers and carrier recapture. For comparison, the UTC approach allows for achieving complete absorption recovery within few ps since the relaxation governed solely by the fast electron sweep-out process [78].

2.3 Picosecond Barrier and Ultrafast Processes

As described above, stimulated emission and SHB are followed by dynamic carrier heating which results in gain compression

$$g = \frac{g_0}{1 + \frac{\tau_{rec,g} P}{E_{sat}}} = \frac{g_0}{1 + \frac{P}{P_{sat}}} \Big|_{if\ \tau_{rec,g} \ll \tau_{pulse}} \tag{2.13}$$

where P is the light power, E_{sat} and P_{sat} are the saturation energy and the saturation power of the gain medium, respectively. Considering sufficiently long pulses of few ps or more of relatively low pulse energy, the carrier redistribution corresponds to the total carrier density and the saturable absorber supports pulse narrowing [5], while if the pulse duration is on the timescale of ultrafast carrier processes, dynamic perturbations caused by SHB affect significantly on the pulse propagation (see below in Section 2.4.1). In addition to the heating processes, at high photon densities, free-carrier absorption (FCA) process (Figure 2.5 (b)) contributes to carrier heating and reduces the saturation energy accompanied by the TPA induced optical losses (Figure 2.5 (a)) pronounced for narrow-bandgap semiconductors such as InP alloys. In addition, the increased amount of hot carriers is attributed to Auger non-radiative recombination (Figure 2.5 (c)).

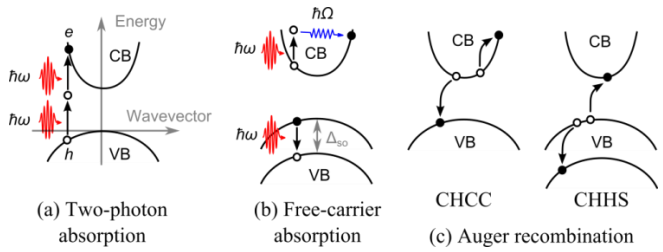

Figure 2.5: Schematic diagrams of (a) two-photon absorption, (b) free-carrier absorption and (c) the Auger recombination processes with the involvement of two electrons and one hole (CHCC) and one electron and two holes (CHHS or CHHL).

The nonlinear gain compression is a key mechanism responsible for the pulse broadening in semiconductor MLLs which restricts achieving of sub-ps pulse generation [97], [98]. Due to finite gain recovery time, the leading edge of the short pulse experiences higher amplification comparing the tail resulting in an asymmetric pulse shape. Furthermore, pulses of a large optical spectrum are affected largely by chromatic dispersion, which is enhanced for chirped pulses occurring due to the ultrafast carrier density change taking place in the gain and absorption under saturation.

Dispersion and Self-Phase Modulation

The fast variation in carrier density and gain suppression cause temporal change of the refractive index related through the Kramers - Kronig relation. This results in self-phase modulation (SPM) which consists in the time-dependent refractive index change inducing a temporally varying instantaneous frequency (frequency chirp):

$$\Delta\omega = -\frac{d\varphi}{dt} \sim \alpha \frac{\delta g}{\delta t}, \tag{2.14}$$

where α is the linewidth enhancement factor defined as [79]

$$\alpha = -\frac{4\pi}{\lambda}\frac{dn/dN}{dg/dN}. \tag{2.15}$$

Figure 2.6 illustrates the SPM process for gain and absorber saturation and the resulted changes in the optical spectrum (frequency chirp) in a semiconductor amplifier. A combination of the carrier depletion in the gain section and the carrier density rise in the absorber lead to asymmetric spectral broadening. Commonly, the leading edge of the pulse is up-chirped (shifted to a higher frequency) while the peak and trailing parts are rather down-chirped. This reduces the spectral efficiency (larger TBP product), causes pulse shape distortion and may results in pulse break-up [77], [99]. This is more critical for MLLs with a long gain section and strong gain saturation.

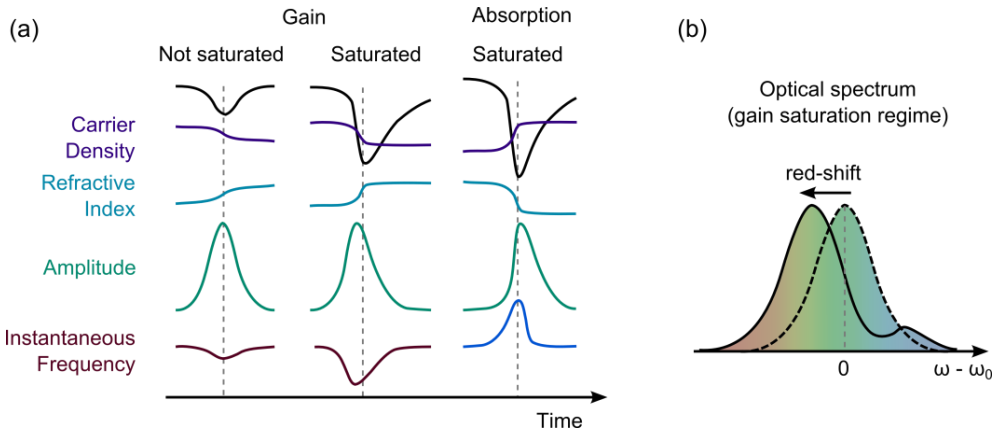

Figure 2.6: (a) Self-phase modulation in the gain and absorber section [84] and (b) induced by the gain saturation spectral red-shift [100].

Taking into account material dispersion, the resulted pulse can be narrowed or broadened with respect to the spectral dependence of the propagation constant given by the group delay dispersion (GDD) coefficient [85]:

$$\beta_2 = \frac{d}{d\omega}\left(\frac{1}{v_g}\right) = \frac{d^2\phi}{d\omega^2}. \tag{2.16}$$

If the net GDD is negative (anomalous dispersion), the soliton mode-locking regime can be achieved giving a pulse duration much less than the absorber recovery time [101].

The dispersion control can be realized using dispersion compensation elements, such as dispersion-shifted fibers (a normal dispersion fiber removes only the linear component), diffraction gratings, chirped fiber DBR and other [102]. Alternatively, the transition time through the dispersive media can be reduce by insertion of a passive waveguide within the cavity [83] or further improved by integration with a chirped DBR structure [103] (given that the gain and absorber can support the short pulses).

Amplitude and Timing Noise

As stated in the Introduction, the application of MLLs for long-range optical data transmission and optical sampling imposes strict requirements on the temporal position and amplitude fluctuations within a pulse train. This drift can be caused by a combination of external factors and technical noise and intrinsic physical processes arising when the pulse interacts with the laser medium. The technical noise impact, e.g. associated with changes in ambient conditions or noisy driving electronics, is significantly minimized in monolithic passively MLLs compared to external cavity devices, while the inherent processes give the major noise contribution. The detailed theoretical description of the noise in MLLs is addressed in [104]–[107].

The temporal shift within the pulse train is, firstly, the result of the spontaneous recombination and, secondly, fluctuation in carrier density, which causes refractive index change varying the cavity round-trip time. Gain and photon density variation have a direct impact on the amplitude noise [84]. Spontaneous emission into lasing modes adds instantaneous random phase change, and therefore induce timing phase error over the pulse and drift in pulse intensity [53]. At above-threshold conditions, the spontaneous emission rate is determined by the carrier density, which is clamped at its threshold value. The ratio between spontaneous $R_{sp}{}'$ and *net* stimulated emission R_{st} rates is proportional to the population inversion factor n_{sp}, as given by

$$\frac{R_{sp}{}'}{R_{st}} \propto n_{sp} = \frac{f_e f_h}{f_e + f_h - 1} = \frac{1}{1 - e^{(h\nu - \Delta E_F)/kT}} \tag{2.17}$$

where f_e and f_h are the Fermi occupation probability for electrons and holes, respectively, ΔE_F is the quasi-Fermi level separation. The spontaneous emission noise reduces with the required gain at threshold and at high population inversion, which can be achieved in QDs or a deep and narrow QW. Because the stimulated emission increases linearly with photon density, the pulses of high power are less affected by the spontaneous emission noise. The high pulse power can be supported by a medium with a high saturation energy, which can be achieved by reducing the confinement factor Γ or/and the modal area A according to Eq. (2.5). It is equally important to reduce gain compression and perturbation in carrier distribution over the pulse energy spectrum [53].

As noted above, timing jitter can be reduced when the repetition frequency is fixed by external modulation in hybrid mode-locking [108]. Other timing stabilization schemes based on the implementation of the opto-electrical and all-optical feedback can be found in [109]. Another approach is referred to overcoming of the intrinsic limitation and focused on a trade-off study and development of an optimal laser active medium, device configuration and operation conditions [60], [110].

General Recommendations on Passively MLLs

Taking all the aforesaid into consideration, the general criteria for the design of active media of monolithic MLLs can be outlined as following:

- *Saturation energy*

High gain saturation energy is required to achieve high pulse energies, reduce broadening effects and pulse chirp, and noise induced by ultrafast gain fluctuation. Low saturation energy in the absorber ensures self-start of the pulse formation and supports sufficient pulse narrowing.

- *Recovery time*

Fast absorber recovery is essential for achieving ultrashort optical pulses. It prevents the formation of secondary pulses when the ultrafast gain relaxation time (< 1 ps for QW) is larger than the absorber one. However, if the gain recovery is slow, the pulse width will depend largely on interplay between the saturation parameters rather than being defined by the absorber relaxation time (Figure 2.4 (b)).

- *Gain, losses and device geometry*

A short gain section with extended cavity or low amplification per roundtrip reduces SPM and noise [111]. A short absorber section is beneficial for the realization of the self-CPM effect to improve the stability; however, the absorption should be high enough to shape the pulse efficiently. Moreover, it is important to achieve low internal losses and hence a low threshold current density and a high population inversion favorable for reduced noise from spontaneous emission.

2.4 MLL Active Medium: Quantum Dots vs Quantum Wells

Ideal Quantum Dots

Quantum-dot-based semiconductor MLLs has been shown to maintain generation of the shortest pulses with the lowest noise figure and temperature stability compared to QW and bulk based devices [58], [60], [62], [112]. The advances are related to the superior material properties owing to the atomic-like energy level structure of QDs. For ideal QDs, it can be represented by a few discrete energy states coupled to a large carrier reservoir (see in Figure 2.7). The delta-function shaped DOS and low active volume results in low differential gain and potentially lower wavelength chirp comparing to bulk and QW material (Figure 2.3) [62], [61]. Furthermore, a high population inversion is easier achieved resulting in low threshold current density, spontaneous emission noise [113], [114] and optical losses. On the other hand, an extremely broad gain spectrum reaching a hundred nm can be achieved as a superposition of overlapped energy states of individual QDs slightly varied in size, shape and environment (inhomogeneously broadened QD envelope) [115], [116].

Low confinement factor and small modal gain attributed to QDs ensure that the pulse experience small changes during one round trip, thus, low pulse distortion compared to QWs is expected. Figure

2.7 illustrates the carrier distribution changes during the propagation of sub-ps pulse in QW (top row) and QD (bottom row) amplifier: at the initial state before the pulse amplification (left), during the pulse propagation associated with SCH and ultrafast carrier-carrier scattering (< 1 ps) (middle) and after the pulse passage (> 1 ps). Assuming that the energy levels are sufficiently uncoupled in a QD, the carrier populations localized on the different energy states do not interact with each other. This means that the carrier-carrier scattering process is suppressed, which inhibits ultrafast refilling of the active states in QDs during the pulse propagation. The carrier distribution is nearly unchanged compared to the QW, which minimizes pulse perturbation.

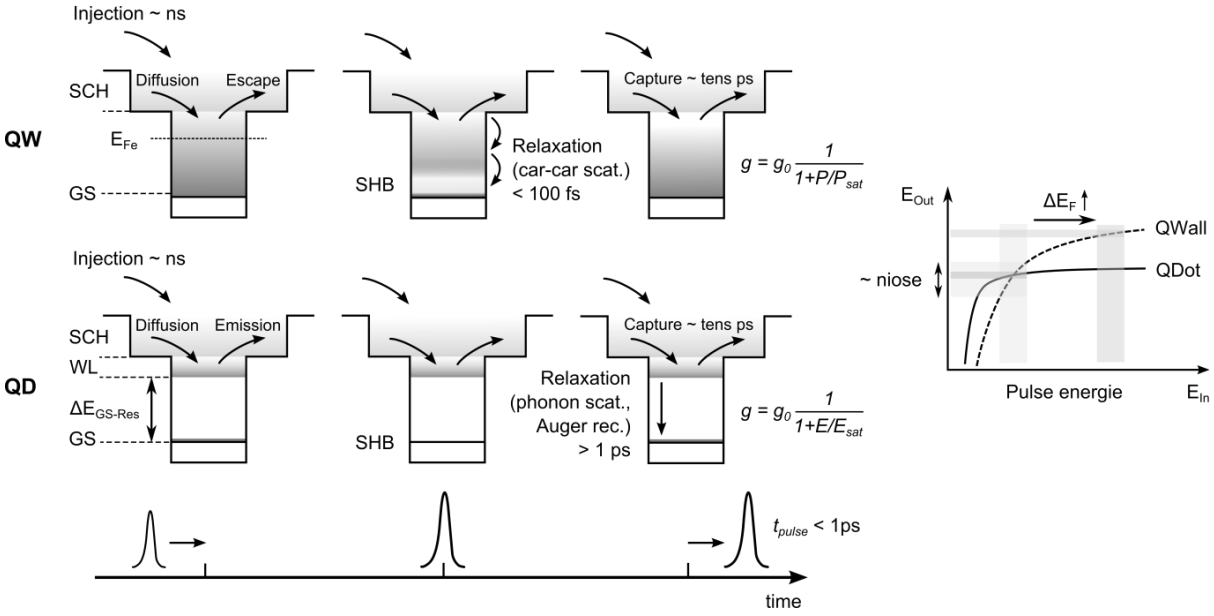

Figure 2.7: Schematic illustration of the evolution of the carrier redistribution in QW and QD material during propagation of the sub-ps pulse.

Carrier-phonon scattering and Auger recombination occurring in the ps range become the dominating mechanisms involved in the intradot carrier redistribution. These processes must comply with the requirements of momentum and energy conservation. As a result, relatively low efficiency of carrier phonon scattering impedes the population recovery of the active states. Figure 2.8 shows the dynamical change in occupation probability on the different levels calculated in [117]. Admitting the possibility of fast relaxation of the carriers from the excited states (ES) to the ground state (GS), the slow capture processes to the ES and a thin wetting layer (WL) from the reservoir can impede the recovery process. This phenomenon of the finite intradot carrier relaxation time in QDs is known as "the phonon bottleneck" [117]–[121].

The first consequence of the slow “ultrafast” QD gain recovery is the reduced SPM (more symmetric pulse shape) and noise affecting the short pulses < 1 ps. As illustrated in Figure 2.7, no significant carrier density fluctuation and gain change due to SCH during pulse propagation take place in QDs, while ultrafast carrier-carrier scattering occurs in QWs. Furthermore, the forthcoming pulses can be influenced by the memory effect due to incomplete refilling of the joint QW reservoir (occurs in the ns range, while the pulse period is ~ 100 and 25 ps for 10 and 40 GHz MLLs, respectively), which is not the case for QDs. Nevertheless, the low differential gain in QWs can reduce dynamic perturbation. It can be realized using fewer QWs (see e.g. calculation results in Figure 3.8) at high

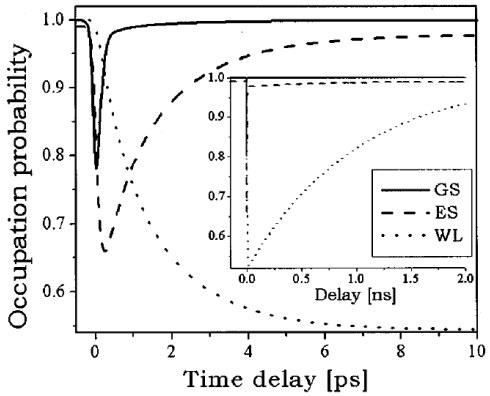

Figure 2.8: Changes in the occupation probability for the GS, ES and WL in the QD SOA after transmitting a 150 fs pulse calculated in [117].

population inversion ΔE_F as shown schematically on the plot in Figure 2.7 [62]. Another important effect advantageous for MLL stability is attributed to the slower "ultrafast" recovery time in QDs as it prevents multi-pulsation if the absorber recovers faster for long (> 1 ps) pulses.

"Real" Quantum Dots

QD material grown in a self-assembled way naturally exhibits a large size distribution (see Section 4.1.3 for details) and, therefore, a discrepancy in the quantized energy levels. This results in inhomogeneous broadening of the gain spectra. For the ultrashort pulses, the lasing modes in a wide spectral width can be supported by individual QDs. Ideally, only the phase have to be matched, while for QWs the amplitude is also susceptible to dynamical changes. However, as shown in Figure 2.9, this inhomogeneity in the QD ensemble can selectively depletes the states belonging to different QDs if the homogeneous broadening determines by the carrier lifetime is smaller than the pulse bandwidth, which gives a rise to CW background and "multiwavelength" pulsing when operation in tandem with a slow saturable absorber like QD-based [122]–[124].

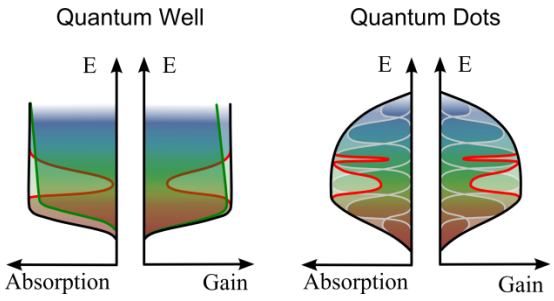

Figure 2.9: Schematics of gain and absorber dynamic changes in the carrier distribution during the pulse propagation in a QW and an inhomogenously broadened QD ensemble.

Another issue concerns the electronic structure and confinement of the carriers within QDs, which are inherent material properties of a particular QD system. QDs based on GaAs used for devices operating in the range from 1.1 to 1.3 μm typically have a shape close to pyramidal with a higher aspect ratio (QD height to base length) compared to large and flattened lens-shaped InP-based QDs emitting near 1.55 μm. The difference is due to the self-assembled mechanism of QDs discussed in Section 4.1.3. Accompanied by the less beneficial line-up in InP based QDs, this leads to weaker

carrier confinement for 1.55 μm QDs ("shallow" QDs), small energy separation between the levels (few tens meV), and strong coupling to the WL for large QDs. The DOS is further modified compared to the ideal 3D box toward quantum wire case in QDashes (see in Figure 2.3), which are often obtained using self-assembled growth (e.g. [125]).

Figure 2.10 shows the example of gain spectra calculated for deep and shallow QDs [126]. The small energy level spacing between GS and ES vanishes the dominant GS gain by contribution of a multiple ES state gain monotonously with increasing carrier density [127]. The affinity of the QD states to the WL results in enhanced thermal escape of the carrier from QDs, therefore, reduces quantum efficiency.

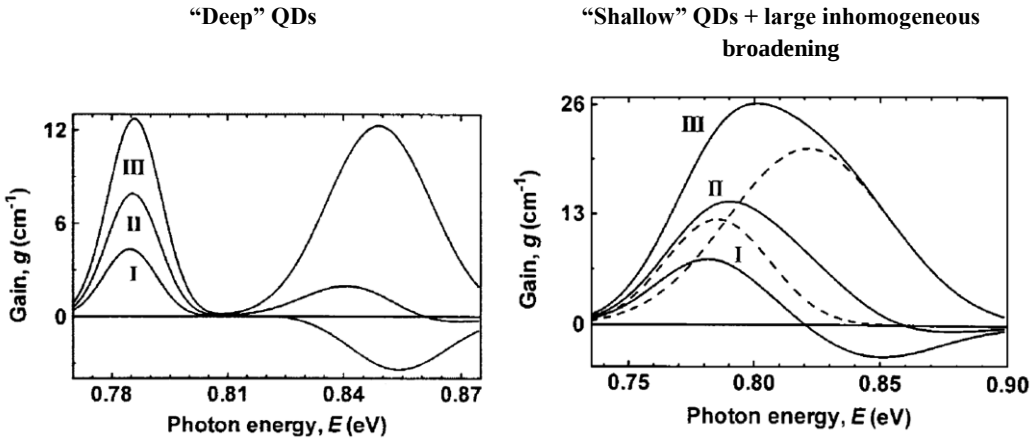

Figure 2.10: Theoretical gain spectra for "deep" ($\Delta E_{ES\text{-}GS}$=63 meV, $\Delta\varepsilon_{inhom1}$=7 meV, $\Delta\varepsilon_{inhom2}$=13 meV) and "shallow" ($\Delta E_{ES\text{-}GS}$=37 meV, $\Delta\varepsilon_{inhom1}$=21 meV, $\Delta\varepsilon_{inhom2}$=32 meV) QDs at different current densities: I < II < III. The dashed lines show the saturation spectra for GS and ES transitions. Reprinted from [128].

The shallow nature of InP-based QDs has drastic influence on the ultrafast intradot relaxation processes and gain dynamics as outlined in [129]. Figure 2.11 displays the calculated gain response of a shallow and deep QD for a GS state based on experimental data showing faster carrier relaxation in a sub-ps time scale for "shallow" dots against gain recovery times of 1-10ps for "deep" QDs (level separation of ~ 100 meV). This can be explained by enhanced Auger–assisted carrier capture [130], [117] and subsequent recovery through efficient interaction with the carrier reservoir. Nevertheless, the WL (reservoir) refilling time is limited by the injection on the order of 1 ns, and therefore WL

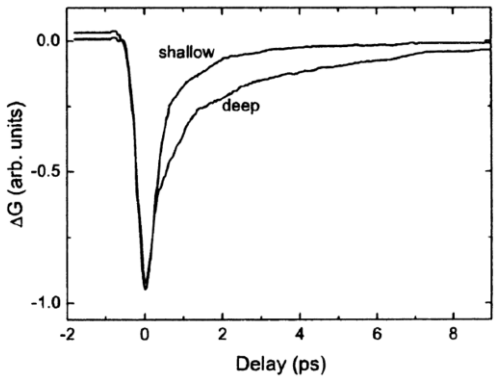

Figure 2.11. GS gain recovery for deep and shallow QDs calculated in [129].

depletion results in reduced saturation energy, may keep gain strongly damped between the pulses and progressively lowers the recovery time [117].

Since the QDs dynamical properties depend on its geometry and morphology, the fabrication issue is of high importance. The success has been achieved for InAs/GaAs QD operating in the O wavelength band [112], but the growth of InAs/InP QD needed for operation in the C and L telecommunication range remains a big challenge [131]. This explains the relatively poor results demonstrated for QD devices at the 1.55 μm range compared to theoretically predicted benefits as exemplified in the Introduction.

Quantum Well - based Amplifier

Conventional QW active material is a good alternative to QD considering the technological challenges in the growth of self-assembled QDs on the InP platform. The noise performance can be improved by reducing the differential gain and confinement factor, or put in other words, increasing the saturation energy [110]. This situation can be achieved by lowering the number of QWs. Specifically, a high population inversion of a narrow highly strained single QW was shown to improve the linewidth enhancement factor and minimizes pulse reshaping due to smaller carrier density fluctuation, dynamic losses and spontaneous emission, overall resulting in lower jitter [62], [49], [54]. More details on the design of QW amplifier is addressed in the following Chapter 3.

Saturable Absorber

The requirements to the absorber section including a low saturation energy and ultrafast recovery are contrary to those imposed on the amplifier. In case of QD absorber, the potential problem arises from the assumption that the saturation within the inhomogeneously broadened QD ensemble is not improved much at wider bandwidth. As depicted in Figure 2.9, this may lead to discrete spectral band absorption and pulse distortion. The weak absorption results in growth of CW background. Similar to a deep QW with high carrier confinement, the recovery process is slow due to obstructed extraction of photo-generated carriers (see Eq. (2.13)), although, was shown to be accelerated in the electric field by applying reverse bias, however, a long absorber section is required to achieve significant narrowing [60].

Using a stuck of shallow multi-QWs (MQWs) or bulk material allows for achieving lower saturated energies, while the ultrafast recovery is ensured by strongly interacting carrier states. Moreover, a MQW-based electroabsorption modulator (EAM) utilizing the quantum-confined Stark effect (QCSE) offers additional flexibility in a wide-range detuning of the absorption strength near the band edge by varying applied biasing. Therefore, the length of the absorber section can be chosen independently, e.g. for operation in the self-CPM mode. The non-linear unsaturated absorption near the spectral cut-off over the wide pulse bandwidth may cause detrimental spectral broadening, therefore, wider QWs can be used for a larger wavelength shift, in particular toward the excitonic absorption band [132]. Alternatively, a UTC saturable absorber [133],[78] is highly attractive solution due to the reduced recovery time. The stable pulse generation ~ 900 fs from the MLLs consisting of monolithically integrated MQW amplifier and UTC saturable absorber was reported in [134]. The main limitations in MLLs performance were associated with fabrication difficulties in monolithic integration giving a high internal reflectivity, limited bandgap tunability between the absorber and amplifier, and more importantly, not optimal amplifier medium, resulting in pulse instabilities. The closer attention to the influence of the internal reflection in monolithic MLLs will be paid in Chapter 4.2.

2.5 Summary

In this chapter, the theory of passive mode-locking in semiconductor lasers is described. It is shown that the gain saturation has the main influence on pulse broadening and increases the pulse jitter. Therefore, in order to obtain stable sub-picosecond pulse generation, the high gain saturation energy is required, while the fast saturable absorber ensures efficient pulse shaping and filtering. The consideration of the dynamic properties of semiconductor material leads to the conclusion that the trade-off between achieving short pulses and low noise cannot be solved without independent optimization of the gain and absorber sections.

The concept of this work is to utilize the combined dynamic of QDs or a highly inverted single QW as a gain medium favorable for stable pulse generation and MQW EAM as a fast and tunable saturable absorber. The benefits of QDs lie in a strong hole-burning of the uncoupled energy levels suppressing fast carrier density fluctuation, and hence SPM and noise. The damping of carrier scattering slows down the gain recovery and eliminate the multi-pulse formation. However, the reported results on QD devices at 1.55 μm suggest the strong influence of the QD structural and compositional non-uniformity on material properties, and therefore the success depends largely on the current technology. A more convenient for fabrication single QW amplifier allows for achieving a high saturation energy under high population inversion. This reduces the carrier heating effect on the ultrafast dynamic gain change, however in a minor manner compared to QDs. The use of a shallow MQW EAM offers the fast absorption and adds flexibility between the device geometry design and the choice of operation conditions. The realization of monolithic MLLs composed of different types of active media can be accomplished using the butt-joint regrowth technique described in Chapter 4. Special conditions imposed on the regrowth quality with respect to MLL performance will be covered in Chapter 5.

Chapter 3

Mode-Locked Lasers: Epitaxial Layer Design

This chapter describes the material choice and design of epitaxial structures of gain and absorption sections used for the realization of integrated MLLs with respect, to the fullest extent possible, to the criteria outlined in Chapter 2. A single narrow compressive-strained QW SOA with asymmetric barrier layers in the InP/AlInGaAs/InGaAsP material platform is considering for the amplifier. The principal purpose is to improve the quantum efficiency via minimization of carrier losses involving Auger recombination and carrier leakage compared to a conventional QW SOA, while possessing a large saturation energy and a high population inversion for stable pulse generation. The design of a QD SOA epitaxial structure is constrained by technological aspects, and therefore will be addressed in Section 4.2. Shallow MQWs are assigned for an active medium of a fast saturable absorber based on QCSE EAM. The design of separate confinement heterostructure (SCH) and cladding layers is of importance for optimal optical confinement, low-loss light guiding and carrier transport properties. These functions are designated to complex asymmetric waveguide structures. The mode matching between the gain and absorber sections being integrated into a single cavity is taken into account. An optimization of the doping profile is discussed concerning dopant diffusivity.

3.1 Material Selection

The realization of active devices for long-haul telecom applications is generally associated with the exploitation of the C spectral band (1.53 - 1.57 μm) due to the lowest fiber attenuation and, at the same time, the applicability of an EDFA for signal re-amplification [135]. Compound semiconductor materials allow for engineering desirable device performance by proper epitaxial structure design where its material properties can be varied with a high degrees of flexibility [136].

Figure 3.1 shows the material and technology map available or prospective for fiber data transmission in the present. InP and related materials are a common choice for the fabrication of photonic devices operating around 1.55 μm. The traditional InGaAsP/InP (PQ(λ)[2]) material system covers the wide energy range between 0.75 eV (1.65 μm) and 1.35 eV (0.91 μm). The mature epitaxial technology and profound processing knowledge make this materials dominant in commercial optoelectronics as well as a major platform for the realization of high functionality photonic integrated circuits [137].

[2] By convention, further in the text InGaAsP and AlGaInAs quaternary compounds lattice matched to InP will be referenced as PQ(λ) and AlQ(λ) whereas λ denotes an energy band gap in μm.

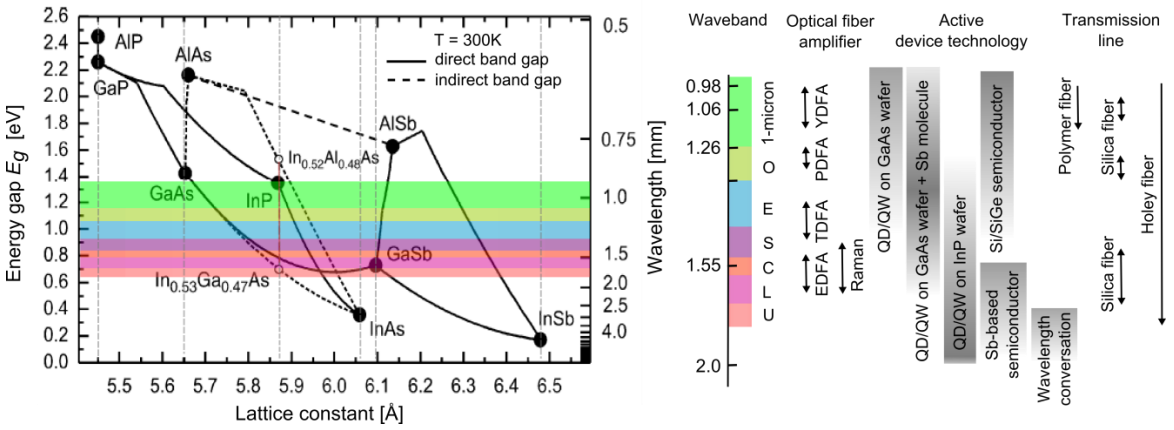

Figure 3.1: Energy bandgap as a function of lattice constant for various III-V semiconductors (left). The colored fields represent optical communication spectral bands shown with corresponding technology map (right) [138]. The abbreviations YDFA, PDFA, TDFA and EDFA denote the ytterbium-doped, praseodymium-doped, thulium-doped and erbium-doped fiber amplifier, respectively.

AlGaInAs/InP (AlQ(λ)[1]) alloys open greater possibility in the range up to 1.46 eV (0.86 μm) due to the favorable band discontinuity properties and the possibility to obtain a higher refractive index contrast [139]. The comprising diagram of the refractive index and band edges for AlQ and PQ compounds lattice matched to InP as a function of energy bandgap [140] are presented in Figure 3.2. An inherently high conduction-band offset ratio $\Delta E_c/\Delta E_g$ of ~ 0.7 in AlQ against 0.4 in PQ results in stronger carrier confinement in quantum heterostructures [141]. As a result, an increased differential gain and quantum efficiency, lower temperature sensitivity comparing to PQ/InP QW based lasers were theoretically predicted and successfully employed for multiple applications (see e.g. [142], [143]). Increased hole localization in QWs was shown to provide lower gain compression at high photon densities [144]. Among these benefits, lower carrier losses have been reported in [145] for 1.3 μm AlGaInAs/InP lasers. However, in case of long-wavelength 1.55 μm lasers, the achieved improvement has been rather moderate, which can be explained by the efficient Auger recombination process

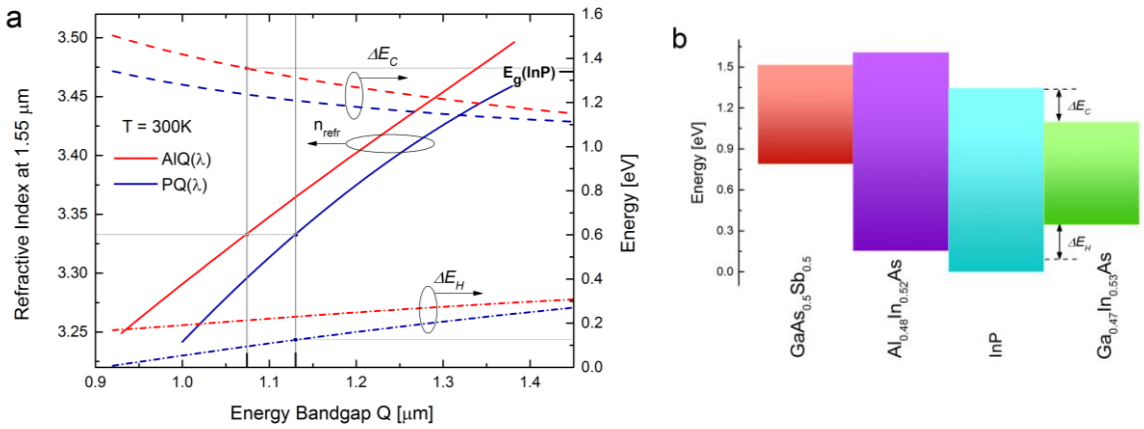

Figure 3.2: (a) Refractive index (solid lines) and band offsets (EH, valence band, dash-dot lines; EC, conduction band, dash lines) for InGaAsP (blue lines) and AlGaInAs (red lines) lattice matched to InP. The relative zero energy level is equal to the valence band edge of InP. (b) Band alignment of lattice matched to InP ternary alloys.

competing with carrier leakage [143]. Due to the high probability of oxygen and carbon incorporation into Al-contained alloys during crystal growth, an increased trap site and defect concentration may additionally affect laser performance [146]. The growth aspects concerning the suitability of Al-contained alloys for integration will be discussed in more detail in Chapter 4.1.

Alternatively, Sb-containing materials can be considered promising for the realization of MLLs. The staggered (type II) band lineup forming, for example, between AlGaInAs and AlGaAsSb (Figure 3.2 (b)) results in spatial separation of holes and electrons. Low carrier wavefunction overlap reduces spontaneous emission and increase saturation energy, which are of particular interest for passive MLLs with a long gain section for operation at low frequencies. At the same time, it gives a strong electro-optic response which is attractive for an EAM [147].

Increasing attention is paid to the possibility of extension of the emission band for cheaper GaAs-based devices towards the longer telecommunications wavelengths using dilute nitrides such as GaInNAs and GaInNAsSb [148] or narrow bandgap Sb-based alloys. However, nitrogen incorporation, even at low concentrations, deteriorates the crystalline quality. Formed defects reduce the carrier lifetime through the non-radiative recombination which can be advantageous for fast absorption recovery [149]. The room temperature emission from Sb-containing InAs/GaAs QDs has been shown reaching up to 1.6 um [150], however, graceful degradation of the optical properties has been observed. Similar results were reported in [151] by strain engineering of metamorphic InAs/InGaAs/GaAs QDs.

Due to the availability and taking advantage of relatively mature fabrication technology, the laser structures of MMLLs in the thesis are designed and fabricated using InGaAsP/InP and AlGaInAs/InP materials to deliver the best device performance.

3.2 Quantum Well Amplifier with Asymmetric Barrier Layers Structure

Epitaxial layer descriptions

The original QW SOA structure studied in the work, refractive index, optical losses and TE fundamental optical mode profiles are illustrated in Figure 3.3. The energy band diagram obtained using the CROSSLIGHT LASTIP commercial software is presented in Figure 3.4. The active region contains a narrow compressive-strained single InGaAs(P) QW sandwiched between 20 nm $Al_{0.48}In_{0.52}As$ layer from the p-side and 10 nm InP layer from the n-side forming an asymmetric barrier layer (ABL) structure. For convenience, this type of structure will be referred to as ABL QW SOA. The active layers are embedded in an asymmetric separate confinement heterostructure (SCH) consisting of nominally undoped PQ(1.13) and n-doped AlQ(1.07) layers as p- and n-waveguide (WG) layers, respectively. A 250 nm thick n-InP buffer layer and a 10 nm PQ(1.25) wet etch stop layer below the n-WG are included for the needs of integration with an EAM (see Section 4.2). The top cladding is composed of a 1.7 um thick InP layer with graded p-doping profile and heavily p-doped 100 nm PQ(1.25) and 175 nm InGaAs contact layers. For ridge etching, A 10 nm PQ(1.13) wet etch stop layer or a 20 nm AlInAs dry etch stop layer below the top cladding layers is used. Complete epitaxial layer descriptions of the ABL QW SOA structure and parameters used for modeling can be found in Appendix A.1. The top cladding layer description covering the detailed doping profile is given in Appendix A.8. The thicknesses of the waveguide layers and doping levels were varied during optimization as described below.

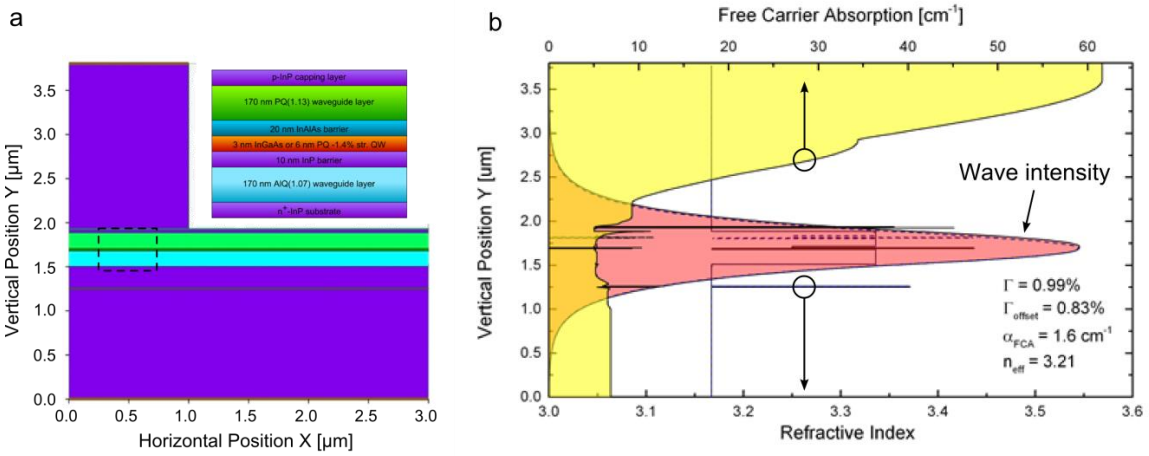

Figure 3.3: A schematic of the ABL QW SOA layer structure (left) and corresponding profiles of the optical mode, refractive index and FCA loss (right). The contact layers are not shown.

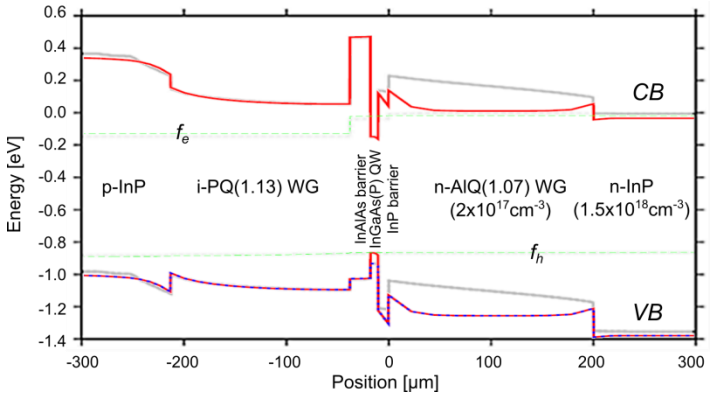

Figure 3.4: Energy band diagram of the ABL QW SOA at threshold for the case of a doped (in colour) and undoped (gray lines) n-side WG. The dashed green lines indicate the quasi-Fermi levels for holes f_h and electrons f_e; *CB* and *VB* are the conduction and valence bands, respectively. The red and blue dashed lines in the *VB* show heavy hole and light hole subbands.

Strained Quantum Well

Two kinds of QWs were examined as a gain medium in the ABL QW SOAs: an ultra narrow 3.2 nm compressive-strained (-1.47% str.) $In_{0.75}Ga_{0.25}As$ QW and a wider 6.2 nm (-1.34% str.) $In_{0.81}Ga_{0.19}As_{0.86}P_{0.14}$ QW. Such narrow and highly strained single QWs allow for achieving high population inversion and as expected, can provide smaller carrier fluctuation as outlined in Chapter 2 along with an improved internal quantum efficiency. In fact, high compressive strain in QWs causes heavy hole (*hh*) and light hole (*lh*) subband splitting and a reduced density of states in the valence band. This results in more symmetric population inversion between electrons and holes. In such a case, the reduced number of states to be filled by carriers increases the differential gain near transparency. Due to fast saturation and a flat gain curve, the differential gain decreases rapidly at higher carrier densities [79], [152]–[154]. Furthermore, a wide temperature range of MLL operation up to 100ºC was demonstrated in [155] for a strained and narrow InGaAs/GaAs QW which is beyond the limit of 60ºC obtained for InAs/GaAs QDs. At the same time, the band diagram modification and low threshold carrier density reduce intervalence band absorption (see Section 3.4) [156]–[158] and carrier losses via Auger recombination (AR).

Auger recombination in narrow QWs

The AR rate is related to the electron and hole densities (n and p) as:

$$R_{Auger} = (C_n n + C_p p)np, \tag{3.1}$$

where C_n and C_p are the Auger coefficients showing the probability of the recombination processes shown schematically in Figure 2.5 (c). The AR efficiency depends strongly on energy band gap, temperature, strain [152]–[154], [159], [160], and, in case of QWs, on barrier height, thickness and other parameters resulting in variation of the electron – hole wavefunction overlap [161]–[163]. Compared to bulk materials, AR in QW is enhanced in the presence of heteroboundaries with barriers, which relax restrictions on the momentum conservation. Thus, the theory predicts an increase of the AR probability with decreasing the QW width. However, for sufficiently narrow QWs, an AR reduction can be expected (Figure 3.6) due to the smaller overlap integral [162]. Therefore, both 3.2 nm and 6.2 nm QWs are assumed to have a similar AR carrier loss contribution. For the same reason, no large difference in the material gain is expected for these SOAs.

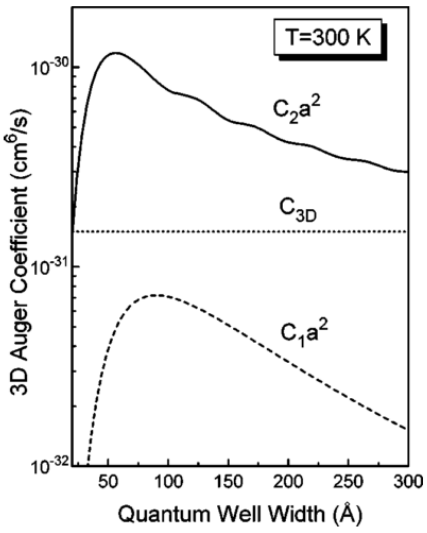

Figure 3.6: Auger coefficients vs. QW thickness calculated for a strained $In_{0.533}Ga_{0.467}As$/InP QW. C_{3D} corresponds to the bulk AR coefficient; C_1 and C_2 are the 2D AR coefficients associated with scattering from heteroboundaries and Coulomb interaction, respectively. Reprinted from [162].

Carrier leakage and asymmetric barrier layers

Another dominating non-radiative mechanism of carrier losses in long wavelength lasers is attributed to carrier leakage outside the active region promoted by thermionic emission [164]. The carrier overflow is escalated at elevated temperatures and high carrier densities. It affects not only the carrier injection efficiency, but also gives rise to parasitic spontaneous recombination and free-carrier absorption (FCA) in the adjacent cladding layers (see below).

The carrier leakage can be reduced using asymmetric unipolar high potential barriers (or carrier stopper layers). It was theoretically predicted and experimentally proven to increase the efficiency and temperature stability compared to conventional QW lasers [165]–[169]. This approach is used in the design of the described ABL QW SOAs structure. A wide-bandgap $Al_{0.48}In_{0.52}As$ barrier forms a high potential step > 400 meV for the electrons on the p-side, while it does not impede hole transport from

the p-contact[3]. The width of 20 nm is assumed sufficient to prevent carrier tunneling through the barrier. The simulation results presented in Figure 3.4 show a drop in electron quasi-Fermi function associated with InAlAs barriers. Similar function is assigned to 10 nm thin InP layer from the n-side of the QW. The height of the thermionic emission barrier for heavy holes is > 320 eV.

Quantum Well operation parameters

In order to estimate the ABL QW SOAs properties, namely density of states (*"DOS"*), static carrier distribution (*"Carriers"*), gain and absorption characteristics, MATLAB simulations were performed using a simplified model elaborated by K. Yvind [110]. The material parameters were taken from [140], [170]. For reference purposes, a conventional c-QW SOA structure was included this study. The active layers of c-QW SOA were composed of 6.5 nm $In_{0.75}Ga_{0.25}As_{0.86}P_{0.14}$ QW(s) (-1.02% str.) in $In_{0.49}Ga_{0.51}As_{0.86}P_{0.14}$ barriers (0.78% str.) embedded in a symmetric PQ(1.05) waveguide core (Appendix A.2).

Figure 3.7 shows the simulated band diagrams, carrier distribution and various numerical results for 3.2 nm ABL QW SOA (a) and 6.5 nm c-QW SOA (b) for a given injection level (a built-in electric field is not included). The carrier distribution was obtained by calculation of a gain coefficient required for amplification of a pulse of a fixed energy (*"Gaincoefficient"*) and a corresponding carrier density (*"ntot"*) using parabolic band approximation (input parameters are displayed in Figure 3.7). The modal gain was related to the population inversion factor $(f_e + f_h - 1)$ as

$$g = \Gamma g_{max}(f_e + f_h - 1), \tag{3.2}$$

where f_e and f_h ("*fermifunc*") are the Fermi occupation probability for electrons and holes, respectively. The gain broadening due to the scattering processes and bandgap shrinkage via Coulomb screening were included in the model phenomenologically. Figure 3.8 shows a plot of calculated modal gain and saturation energy as a function of carrier density for the described ABL and c-SOA structures.

The benchmarking study of the results summarized in Table 3.1 reveals a significant reduction of the threshold carrier density for the deep ABL QWs compared to the c-QW and more than a 3-fold increase in the carrier confinement potential. Another benefit of more balanced carrier distribution in a highly compressive strained narrower 3.2 nm QW is illustrated in Figure 3.8 showing fast growth of the saturation energy with carrier density.

However, the simulations suggest that for long 10 GHz MLLs the required gain can be achieved at relatively low carrier density. Thus, the population inversion is not sufficiently high resulting in moderate saturation energies for the ABL QWs (Figure 3.8, purple dashed lines). Higher saturation energies can be achieved for 40 GHz lasers (Figure 3.8, green dashed lines).

[3] The data on band-edge alignment for AlQ can vary significantly depending on model used for calculation. For comparison see e.g. [210].

Offset QW and QD SOA

In order to maximize the advantages of the ABL QWs, the optical confinement can be intentionally reduced e.g. by displacement the active layer position against the maximum optical field ("offset ABL QW" in Figure 3.8 and Table 3.1) [171]. The required currier density at threshold is higher which demands higher population inversion and increases the saturation energy (Eq. 2.3). Moreover, the reduction of the FCA losses can be expected. For the given ABL QW SOA design optimized for integration with the EAM, the confinement factor can be reduced by -0.16% when the QW is pushed to the p-side as shown in Figure 3.3 (b) (dashed lines). A detailed epitaxial structure is given in Appendix A.3. In the opposite case, when the QW is placed closer to the n-side cladding, lateral hole spreading in the thick p-WG layer will increase FCA losses. Moreover, higher electron mobility should be considered for efficient carrier injection [172]. However, it does not offer significant improvements for 10 GHz MLLs as seen from Figure 3.8 (red and green curves). Further development can be done towards modification of the optical field profile by changing the waveguide layers geometry or materials (similar to e.g. [171], [173]). However, this approach raises a tighter demand on low internal losses.

As noted in Chapter 2, QD active material compares favorably with QWs due to the reduced number of states. It offers lower threshold carrier density while allows for achieving a higher saturation energy. In this work, stacks of self-assembled InAs/InP QDs was utilized alternatively to the QW SOAs. Due to the technological aspects commonly arising in the growth of a QD material, a brief discussion of the design of a QD SOA epitaxial structure will be provided along with QD epitaxial growth in Section 4.2.

Table 3.1. Comparison between various characteristics calculated for ABL SQW and c-SQW SOAs.

SCH Struct.	d_{QW} and strain	Γ	Carrier escape barrier* (n/p claddings), meV		n_{tr}, 10^{12} cm^{-2}	f_{rep} = 10 GHz			40 GHz		
			elec.	h.holes		n_{th}, 10^{12} cm^{-2}	Inv.(n_{th}) at E_g, (f_e/f_h)	Esat (n_{th}), pJ	n_{th}, 10^{12} cm^{-2}	Inv. (n_{th}) at E_g	Esat (n_{th}), pJ
Conv.	6.5 nm -1.02%	0.91	45	95	0.62	1.93	0.60 (0.93/0.67)	1.30	3.88	0.83	5.88
ABL	3.2 nm -1.47%	0.82	401/151	220/373	0.31	0.74	0.59 (0.88/0.71)	0.40	1.23	0.85	1.40
ABL	6.2 nm -1.34%	0.99	473/224	167/320	0.41	0.94	0.53 (0.90/0.63)	0.42	1.43	0.73	1.27
ABL, offset	6.2 nm -1.34%	0.83	473/224	167/320	0.41	1.02	0.56 (0.91/0.65)	0.53	1.69	0.78	2.00

d_{QW} is the QW width, Γ is the confinement factor, n_{tr} is the transparency carrier sheet density, n_{th} is the total (threshold) carrier sheet density, Inv. is the population inversion factor calculated at energy band gap E_g.

*Carrier escape barrier between the GS and the reservoir (no transition through excited states assumed). For the ABL structures, the GS energy level was calculated by averaging the values obtained for QWs with corresponding symmetric potentials.

(a) 3.2 nm InGaAs ABL QW SOA with asymmetric barrier layers

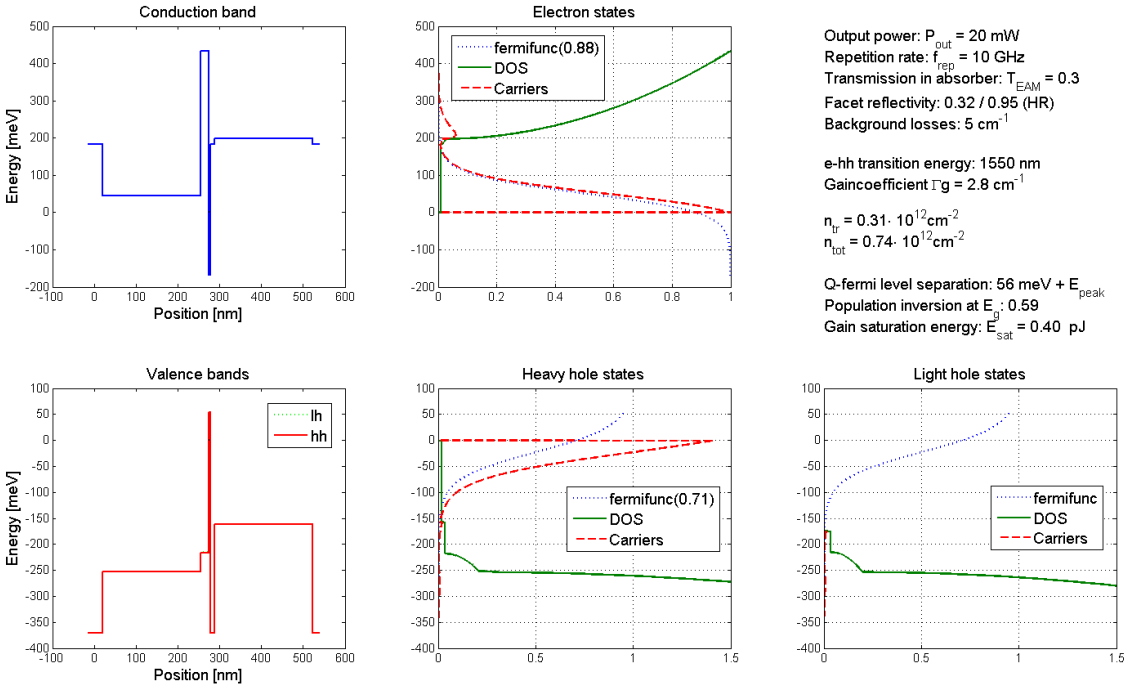

(b) 6.5 nm InGaAsP QW c-SOA

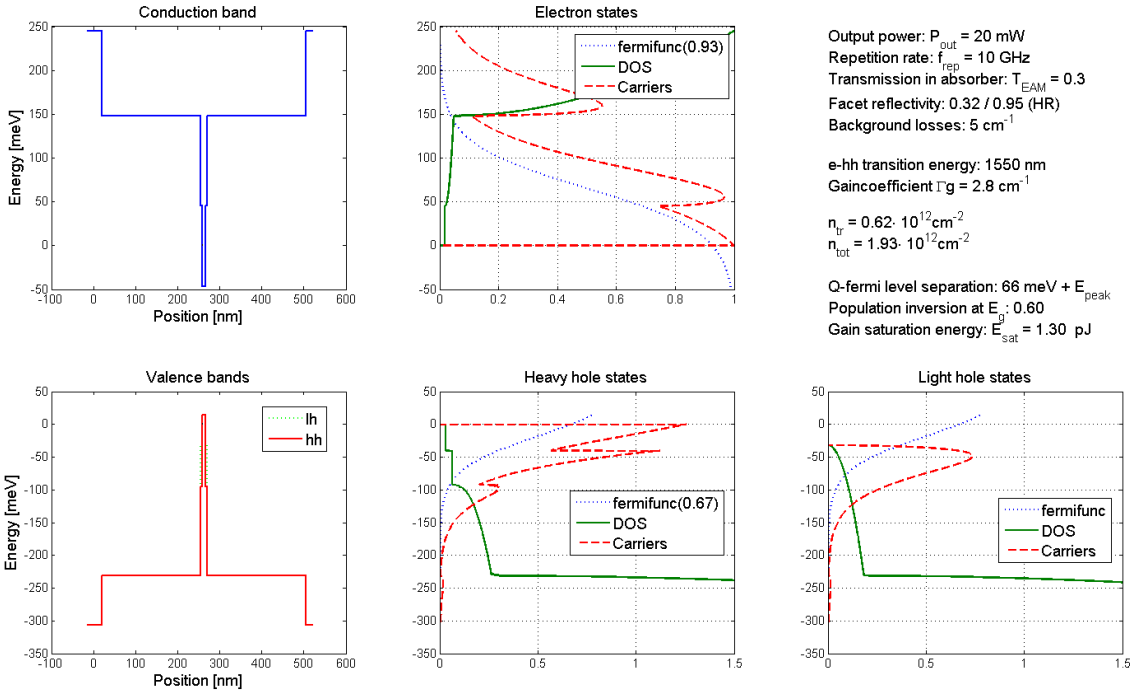

Figure 3.7: (a) ABL SQW SOA and (b) c-SQW SOA: calculated energy band diagram (left column) and density of states, quasi Fermi functions, carrier density for injected carrier density n_{tot} (center and right column) for conduction (top row) and valence band (bottom row). In the upper right corner the input data and resulting parameters are shown. See the text for details.

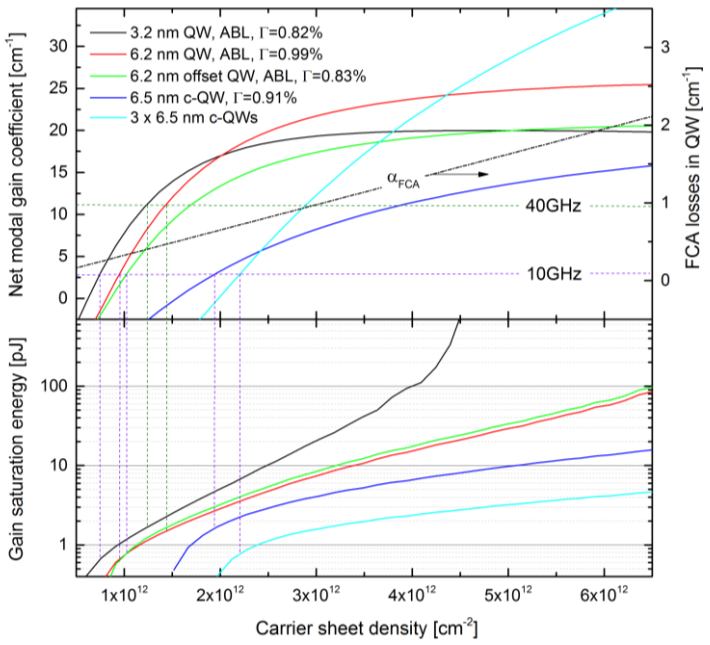

Figure 3.8: Net modal gain and saturation energy as a function of carrier concentration calculated for SOAs with c-QW and ABL QW of different width. The FCA losses show the carrier-concentration dependent absorption within the active layer. The dashed horizontal lines indicate the output mirror losses (without AR/HR coating) for 10 GHz and 40 GHz lasers.

Asymmetric Separate Confinement Heterostructure

While the asymmetric blocking barriers support carrier localization in the QW layer, the optical confinement was realized using high refractive index asymmetric SCH layers. InGaAsP and AlGaInAs materials were employed in the design in a way, that the carriers of corresponding polarity do not experience high potential barriers when travelling from the doped claddings to the active layer. Wider bandgap materials can provide larger light confinement and reduce AR if considering an exponential dependence of the AR probability on the energy bandgap [159]. As a compromise solution, AlQ(1.07) and PQ(1.13) with matched refractive indexes were used for n- and p- waveguide layers, respectively. The corresponding refractive indexes and band offsets are indicated by grey lines in Figure 3.2. Figure 3.3(b) shows the resulted TE mode profile and refractive index diagram for ABL QW SOA calculated using the beam propagation method available in the Selene OlympIOs software and the parameters listed in Appendix A. The ridge width of 2 µm were assumed to ensure operation on a single transverse mode, therewith more efficient coupling to the fiber [110].

3.3 Multi-Quantum Well Electro-Absorption Modulator

Epitaxial layer descriptions

The structure proposed for a saturable absorber consists of strain-compensated InGaAs MQWs separated by AlGaInAs (AlQ1.3) barriers. The SCH is composed of an InGaAsP waveguide core with a stepped energy bandgap profile as depicted in Figure 3.9. A detailed epitaxial layer description is presented in Appendix A.6. The emission wavelength for the MQW EAM was around 1.45 – 1.5 µm to take advantage of Quantum-Confined Stark Effect (QCSE) - based absorption modulation providing a faster absorption recovery at 1.55 µm under reverse biasing [89].

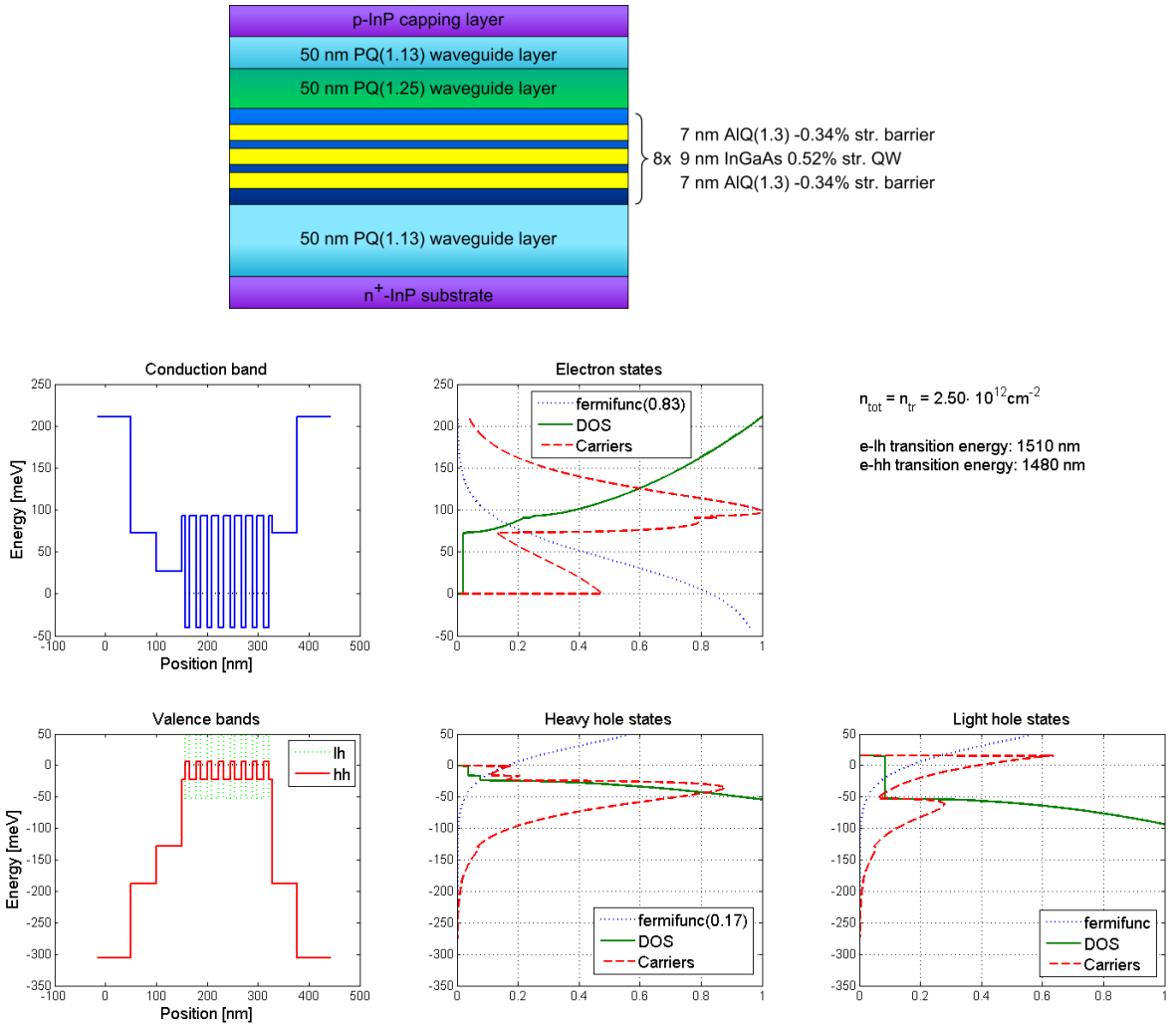

Figure 3.9: A sketch of the MQW EAM epitaxial structure proposed for a fast saturable absorber, its band diagram and carrier distribution at transparency current density.

The QW and barrier width and composition were chosen to promote efficient carrier escape of photo-generated carriers required for fast absorption recovery. Since it is more critical for holes as heavier carriers, the potential barrier in the valence band should be compatible with kT at best ("shallow" QWs), which was possible by realizing benefits of the AlGaInAs band discontinuity properties. Thus, the confinement of heavy holes in these QWs was about 29 meV. By the same token, the stepped SCH layers were employed from the p-side. Furthermore, the low carrier localization using relatively wide QWs (8.6 nm) in the EAM active medium are beneficial for wide-band absorption modulation. A comprehensive analysis of the influence of the EAM design on absorption dynamics can be found in [95].

The number of the QWs was varied to obtain optimal transmission:

$$T = \exp(-\Gamma\alpha(V)L_a), \tag{3.3}$$

where $\Gamma\alpha(V)$ is the net modal absorption dependent on applied reverse bias (the confinement factor for eight QW EAM was 12.5%). Since the QWs are 0.52% tensile-strained, the MQW EAM exhibits mainly TM-polarized absorption (electron - heavy hole transitions; electric field vector is oriented in

the growth direction), while contribution to the TE absorption is smaller (electron - light hole transitions; electric field vector parallel to the QW layers), comparing to compressive-strained QWs in the SOAs emitting solely in TE mode [79].

SOA – EAM mode coupling

A critical design aspect for integrated devices is low coupling losses. To accomplish this requirement, the thickness of the EAM SCH was obtained by tailoring the TE mode profile while the maximal mode coupling with the gain section being provided. The resulting coupling between the modes shown in Figure 3.10 is better than 99.7%. The effective index difference between the sections is found to be lower than 0.05. The simple evaluation predicts for an ideal alignment and vertical interface the coupling losses of 0.013 dB and a minimal reflection of 6×10^{-5}, which should be further reduced for practical applications as it will be discussed in Chapter 4.2. A common approach is based on the formation of the angled interface between section being integrated, however it implies a reduction in light transmission [173], [174].

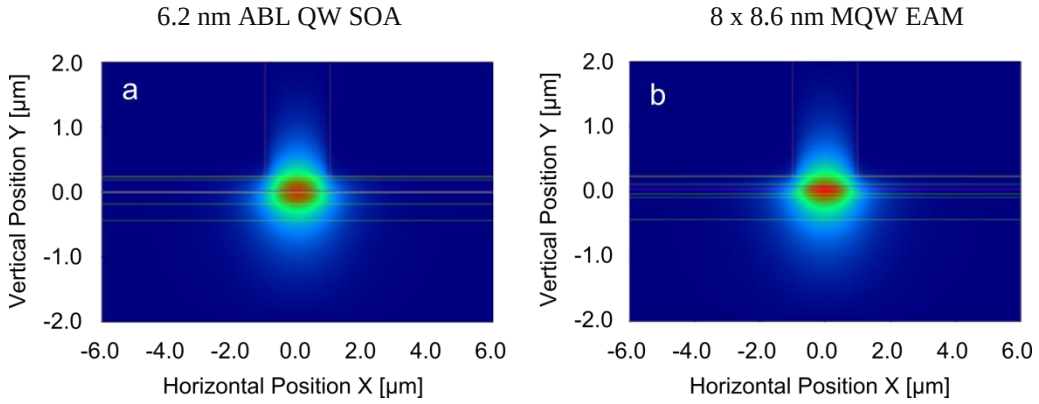

Figure 3.10: TE fundamental mode intensity profiles for 2 µm wide ridge ABL QW SOA (a) and MQW EAM (b) simulated with Selene. The resulting mode overlap is 99.72%.

Alternative structures for a saturable absorber

The proposed MQW EAM relies on band-edge absorption, and therefore, strong spectral dependence of the absorption (chirp) is expected [175]. Alternatively, a saturable absorber can be based on a bulk absorption modulator utilizing the Franz–Keldysh effect or a long-wavelength absorber with nearly constant absorption coefficient over the pulse spectrum. A larger modal absorption should be considered for both cases. The requirement imposed on the optimal transmission discussed in Section 2.2.4 of Chapter 2 can restrict the applicability of these absorbers when taking into account a minimal length of an integrated absorber section of 5 µm feasible for cleaved devices (can be estimated using Eq.(3.3)). The last type of absorbers consisting of a lower number of QWs was examined in this work. The active material in the basic MQW EAM structure was replaced by four $In_{0.53}Ga_{0.47}As$ (well)/AlQ(1.44) (barrier) QWs with the energy band gap around 1.6 µm (see an epitaxial structure description in Appendix A.7).

3.4 Doping and Optical Losses

Free carrier absorption

Design considerations on a doping profile of laser epitaxial structures are trade-off between the need of efficient carrier injection to the active layers (low resistance) and avoidance of excessive optical losses. In addition to light scattering on the waveguide imperfections and surface roughness, an increase in optical losses are commonly referred to FCA within one band (intraband) associated with phonons or interband, such as intervalence band absorption (IVBA) [157], [176]–[178]. In narrow-gap semiconductors, such as InP, the contribution of FCA has approximately linear dependence on the carrier density (for moderate doping levels) and can be estimated via the empirical free-electron and free-hole absorption cross-section (σ_n and σ_p) as follows:

$$\alpha_{FCA} \cong \sigma_n n + \sigma_p p, \tag{3.4}$$

where n and p are the electrons and hole concentrations, respectively. The FCA coefficients for InP and related alloys at 1.55 μm taken for calculation were σ_n = 2.3x10^{-18} cm^2 and σ_p = 2.3x10^{-17} cm^2 [177], [179]. The larger FCA cross-section for holes is explained by the dominance of the IVBA mechanism upon the proximity of the photon energy to the valence band separation. Therefore, it is important to minimize light interaction with p-doped material [173], [180] or optimize doping concentration.

Zinc diffusion

In practice, an optimization of the doping profile should be done with respect to the properties of specific dopant including the diffusivity, dopant incorporation behavior and activation energy. During the work on this PhD, it appeared that diffusion of zinc (Zn) atoms used for p-type doping into the active region and the p-side waveguide had significant influence on device performance as it will be demonstrated in Chapter 5. Therefore, to avoid unintentional doping, calculation of a nominal dopant profile for the epitaxial growth was performed with a correction for the strong atom diffusion at elevated growth temperatures. The dopant distribution with time t can be estimated using Fick's second law solution

$$N(x,t) = N_0 \mathrm{erfc}\left(\frac{x}{2\sqrt{Dt}}\right) \tag{3.5}$$

where N_0 is the nominal concentration, D is the temperature-dependent diffusion coefficient. The diffusivity alters strongly with the growth condition, and thus must be evaluated experimentally for each specific case. Commonly observed, that Zn diffusion in InP exhibits a pronounced threshold concentration dependence. For example, the diffusion coefficient of 0.1 - 2.5×10^{-13} cm^2/s for concentrations below 2×10^{17} cm^{-3}, and 2 - 6×10^{-13} cm^2/s for higher doping levels for InP deposited at 600°C using diethylzinc as Zn source were obtained in [181]. The difference of more than one magnitude between the diffusion coefficients is due to the substitutional-interstitial diffusion mechanism inherent to Zn atoms [182], [183].

For the optimization, Zn diffusion was included by assuming a standard deviations of 50 nm for doping levels below 1×10^{17} cm^{-3} and 200 nm for higher concentrations. The p-side waveguide and active layers were left undoped. Figure 3.3 shows the resulting vertical profile of the FCA loss coefficient for optimized doping concentration for the QW SOA. The corresponding background

losses of 1.6 cm^{-1} (reduced by factor of two compared to the initial design) were calculated by integration over the fundamental TE optical mode (without FCA in the active layer).

Oppositely, in the lack of the doping in the n-side waveguide, high resistance and a tremendous reduction of the efficiency due to heterobarrier leakage of hot carriers were observed in consistent with [184]. Moreover, as seen in the band diagram in Figure 3.4, the heterointerface between n-InP buffer and AlGaInAs waveguide layer creates a potential barrier, which may impede electron transport to the QW if the barrier is high. In order to reduce the resistivity, a moderate n-doping is applied for AlGaInAs WG layer. The reduced potential for electrons across the n-WG is demonstrated in Figure 3.4 doped (in colour) n-cladding compared to undoped (gray lines). This corresponds to a slightly reduced resistance at low current shown in Figure 3.11(inset). Directly at the heterointerface, δ-doping is considering to promote a sharper band discontinuity barrier which can be passed through by tunneling (not included in the simulations).

As already mentioned, efficient hole leakage to the n-side waveguide layer at high carrier flows results in rapid increasing of optical losses [176] as shown in Figure 3.11. The simulations of the ABL QW SOA structure with different doping levels of the AlGaInAs n-WG and n-InP buffer layers suggest that n-doping reduces parasitic FCA in the n-side waveguide layer at high current.

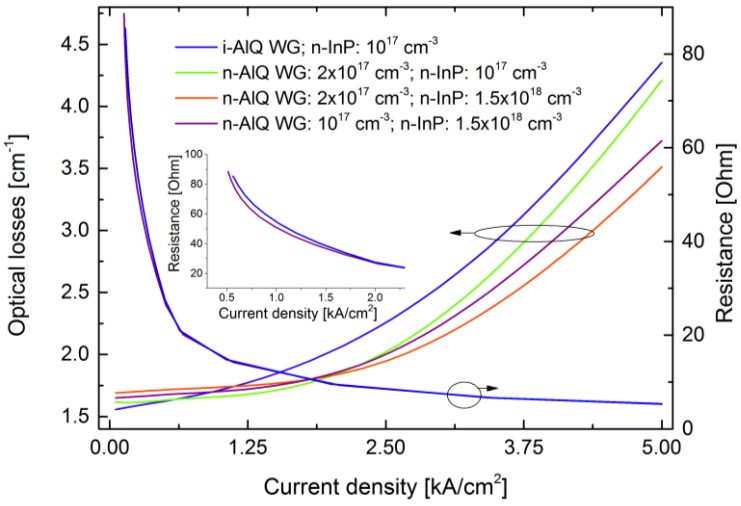

Figure 3.11: Internal optical losses and resistance as a function of the current density obtained for different doping profiles of AlQ(1.07) n-WG and adjacent n-InP buffer layers of the SOA structure shown in Figure 3.4.

3.5 Summary

This chapter described major factors that have been taken into consideration for designing the gain and saturable absorber sections of monolithically integrated MLLs. The bandgap, strain, thickness, doping of both active layers and SCH were optimized independently to achieve desirable SOA and EAM performance.

For the gain material operating at 1.55 μm, a single narrow InGaAs(P)/InAlAs/InP QW (or a stack of InAs/InP QD layers) within asymmetric barrier layers were proposed. Owing to the large band discontinuity, an improved internal efficiency and low threshold current were predicted compared to InGaAsP-based conventional c-QW SOA. The simulation study revealed a rather moderate population inversion (and saturation energy) for long 10 GHz MLLs due to the high gain coefficient. The

possibility to increase these parameters using an offset QW SOA design was discussed. An asymmetric waveguide structure based on AlInGaAs and InGaAsP materials was shown to have beneficial carrier transport properties while maintaining low losses, proper optical confinement and symmetric optical field.

The InGaAs/AlInGaAs shallow MQW QCSE-based EAM with reduced carrier confinement and stepped SCH energy bandgap profile was chosen to perform absorber functions with enhanced absorption recovery under reverse biasing.

The SCH structures of the SOA and EAM were optimized to achieve maximal mode overlap required for low internal reflection on the interface between the sections. The reflectivity was shown to be 6×10^{-5} for ideal vertical coupling, and further minimization using an angled interface is considered. In order to reduce optical losses, the optimization of the doping profile of the cladding layers was performed taking into account strong Zn diffusivity.

Chapter 4

Fabrication of Integrated Mode-Locked Lasers

In this chapter, the growth of the designed epitaxial structures as well as the fabrication of mode-locked lasers operating in the 1.55 um telecommunication range is discussed. The first section gives an overview on metal-organic vapour phase epitaxy (MOVPE). Particular emphasis is placed on the growth of QDs since the growth conditions have a strong influence on the morphology and composition of QDs, which in turn determine optical and electrical properties of the material.

The second section describes the butt-joint regrowth scheme applied for the realization of monolithically integrated SOA and EAM sections. Due to the strict demands on low intracavity reflection and coupling losses, the closest attention is paid to the quality of the coupling interface. A complete investigation of the structural, compositional and optical properties is presented.

At the end of the chapter, the process flow used for the fabrication the MLLs is outlined. A detailed description is addressed in Appendix B.

4.1 Epitaxial Layer Growth

4.1.1 MOVPE Growth Process

The realization of the designed MLL structures was performed using the MOVPE system available at DTU Danchip. The MOVPE technique allows for deposition on a single crystal substrate of thin semiconductor films of excellent crystalline quality and compositional uniformity with abrupt interfaces between layers, as required for QW growth, and controllable doping level. The growth process is based on a complex interaction between the heated substrate and vapors of volatile molecules containing constituent elements of the growing film, or precursors. The used precursors for the deposition of III-V semiconductors are typically the simplest metalorganic compounds (group III alkyls) and group V hydrides. Control over the growth process requires understanding of the main growth mechanisms coming into play in MOVPE. An introduction to the basic principles to the MOVPE technology can be found e.g. in [185]–[187]. Briefly, the MOVPE can be described as follows (see Figure 4.1):

- *Mass transport of precursors to the growing surface by a carrier gas;*

A gas mixture, composed primarily of the carrier gas (typically H_2 or N_2) and precursors, is injected into the MOVPE growth chamber and delivered to the substrate by a laminar gas flow. The laminarity is ensured by a proper design of the reactor configuration. Just above the hot growing

surface, the convective flow is negligible, and transport of the precursors toward the surface occurs by diffusion driven by the temperature and concentration gradient. The formation of this boundary (stagnant) layer is an essential condition for achieving uniform material distribution across the substrate.

- *Thermal decomposition (pyrolysis) of the delivered precursors into the elemental species within the stagnant layer and at the hot surface;*

Decomposition of group III alkyls is typically stagewise and can be completed at temperatures below the optimal growth range (550 - 700°C for InP), whereas the pyrolysis temperatures for group V hydrides are usually much higher (~ 850°C for PH_3). In this case, the surface acts catalytically and facilitates precursor decomposition [187]. In order to minimize other reactions, which can take place within the stagnant layer and negatively affect the material quality, the growth is typically carried out at a low pressure (10 - 100 mbar).

- *Surface reactions: adsorption, incorporation, desorption;*

The arriving to the substrate atoms or radicals can be adsorbed by establishing a weak physical bond with surface atoms, and then migrate until being incorporated into the lattice at the most energetically favorable position (kink and step sites) or by nucleation with another atom via strong chemical bonding. In another case, the atom desorbs back into the vapor. The preferential growth of a solid film over evaporation is governed by thermodynamics, while the growth rate is determined by kinetics of the incorporation process.

Depending on the growth temperature, deposition can be limited either by the diffusion of precursors through the boundary layer to the surface at moderate temperatures (the diffusion limited regime), or kinetically limited, e.g. at low temperatures, when the activation energy of bond formation is a determinal factor. At elevated temperatures, the enhanced desorption of the species from the surface deters growth (the desorption limited regime). Moreover, the probability of parasitic reactions in the gas phase increases with temperature. An operation in the diffusion limited regime is preferable due to the low temperature sensitivity, thereby allowing for careful compositional control.

- *Transportation of the desorbed from the surface radicals and remained gases away via the exhaust system.*

A desired layer composition can be obtained by mixing precursors of relevant III and V elements in a ratio accordant to the elemental concentration in solid phase. The control is carried out by setting predetermined fluxes of each precursor. The high quality epitaxy implies strict condition on the lattice

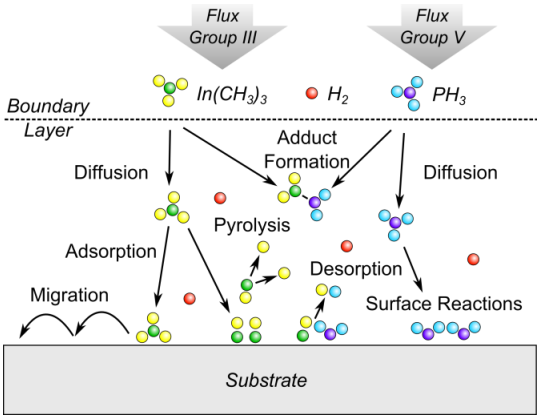

Figure 4.1: Schematic illustration of main processes occurring during MOVPE growth [186].

parameters of the grown alloys, which should match the lattice constant of the substrate. The growth of mismatched layers, or so-called pseudomorphic growth, can be performed if the thickness of the layer does not exceed the critical thickness given by a strain value (e.g. used in growth of strained QWs) [188]. Above the critical thickness, lattice relaxation yields the surface corrugation, bending, and the formation of dislocation. An independent variation of the lattice constant and energy bandgap in a wide range is feasible using quaternary compound semiconductors. However, the miscibility of grown compounds should be taken into account. Behind the miscibility range, thermodynamically unstable compounds can experience destructive phase segregation [136].

Doping of an epitaxial layer is attainable by introducing a dopant precursor to the gas mixture in an appropriate concentration. As exemplified in Section 3.4 for Zn doping, a free carrier concentration can differ from a dopant concentration, because of it depends not only on the decomposition and incorporation efficiency, but also on the dominant incorporation mechanism and dopant activation energy for defined growth conditions. Thus, the saturation of the electrically active dopant concentration occurs at sufficiently high dopant flows. Moreover, the free carrier concentration profile can be affected by detrimental processes such as dopant diffusion increasing with temperature, passivation by hydrogen leading to reducing of the level of activated dopants, interaction between dopants and adsorption from the hot surface.

4.1.2 Growth of QW SOA and MQW EAM Structures

The design epitaxial structures of the SOA and EAM were grown on epi-ready (100) S-doped InP substrates using a low-pressure (60 Torr) 3 x 2-inch vertical Turbodisc® MOVPE system (EMCORE D125). Epitaxial layers have been produced using trimethylindium $In(CH_3)_3$ (TMIn), trimethylgallium $Ga(CH_3)_3$ (TMGa) and trimethylaluminum $Al(CH_3)_3$ (TMAl) as group III precursors, and arsine AsH_3, phosphine PH_3, and tertiarybutylphosphine (TBP) as group V sources and hydrogen (H_2) as carrier gas. N-type and p-type doping up to 10^{19} cm^{-3} and 1.5×10^{18} cm^{-3} for InP, respectively, was realized using disilane Si_2H_6 and diethyl zinc $Zn(CH_3)_2$ (DEZn). The possibility of *in-situ* InP etching was available with tetrabromomethane CBr_4 [189].

The growth pressure, total gas flow and susceptor rotation speed were kept constant at 60 Torr, 9500 sccm and 1000 rpm, respectively, as the optimal conditions for the current reactor configuration. These parameters ensure laminar gas supply in the growth chamber and formation of a stagnant boundary layer. The growth pressure of 60 Torr is low enough to suppress parasitic reactions in the gas phase (in the used temperature range). As explained in the following, a lower pressure can be used to advantage in selective area growth (SAG) process for reducing mask overgrowth [190]. However, this effect could not be applied in the work due to the limited reactor capabilities.

The growth temperatures of 610°C for InGaAs(P) alloys and 650°C for AlIn(Ga)As compounds and a high group V to group III flow ratio ranged from 80 for InGaAs to 145 for InP were used in order to perform deposition in the diffusion limited regime. An elevated temperature for the growth of Al-containing compounds was chosen due to the high probability of oxygen and carbon incorporation, acting as non-radiative recombination centers [146], [191]–[193]. Generally, the presence of oxygen is attributed to TMIn source (solid) due to the difficulties in purifying compared to TMAl or TMGa source (liquid). Another reason is to enhance the diffusion of Al species. Because of TMAl exists partially as a dimer in contrast to TMIn and TMGa molecules, the decomposition process is more complicated resulting in a lower mobility of Al result and increased surface roughness. The possibility of low-temperature growth at 600°C was demonstrated in [194], where the low V/III ratio of 30 was used to encourage longer surface migration and achieve better layer uniformity. Another approach

was applied in [195] where the surface roughness is believed to be improved by the following growth of thin 5 Å GaAs layer.

An excess partial pressure of the group V precursors is used to compensate fast desorption of group V atoms from the surface back to the gas phase and, therefore, prevents decomposition of the grown film from the stoichiometric composition. In addition, the probability of unintentional p-doping related to carbon incorporation reduces at high V/III ratios. The growth rate is defined by incorporation of the group III atoms proportionally to the precursor molar flow (at high group V overpressure). For the given conditions, for InGaAsP alloys the rates were measured between 0.5 nm/s for InP and 1.0 nm/s for (Al)InGaAs depending on the composition.

Upon the listed parameters, the QW SOA and MQW EAM were grown. The favorable for the QDs growth conditions typically lie beyond the optimal ones [196], what will be discussed irrespectively of the above in Section 4.1.3. The details of the epitaxial structures: composition, growth temperature and doping level are presented in Appendix A. Prior the growth of an actual structure, the substrates were preheated at 650°C for 15 min under PH_3 atmosphere in the growth chamber for deoxidation followed by deposition of 0.8 μm thick n^+-InP buffer layer on blank InP substrates to achieve a smooth surface [197]. The layer compositions and uniformity were characterized by room temperature photoluminescence (RT PL) and X-ray diffraction (XRD) measurements. The in-plane strain for lattice-matched layers were assumed to be better than $\Delta a_{\perp}/a_{InP} < 2\times10^{-4}$ (corresponds to XRD peak separation between the layer and InP substrate < 50 arc sec).

Figure 4.2 shows typical PL spectra and peak wavelength map acquired on a wafer consisting on integrated MQW EAM (the dominant area coverage) and QW SOA (insets) materials obtained using

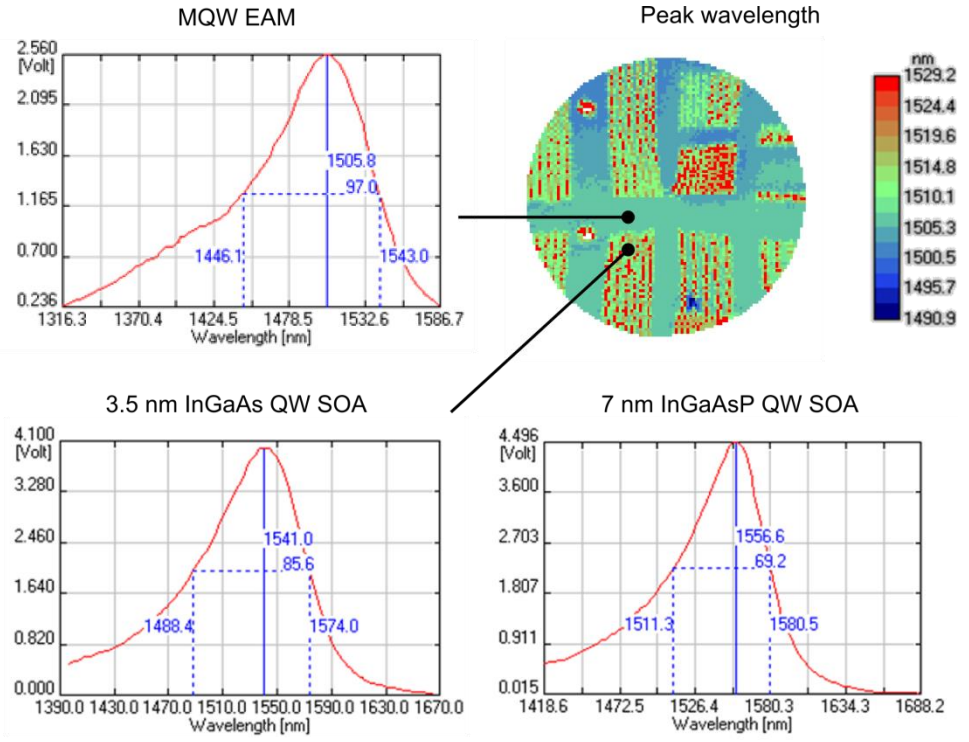

Figure 4.2: Example of RT PL peak wavelength map and corresponding PL spectra of integrated 3.5 nm InGaAs QW SOA and MQW EAM sample. For comparison, 7 nm InGaAsP QW SOA spectrum is presented.

980 nm CW laser as an excitation source with a resolution of 0.1 mm. The spectra of SOAs were obtained before the integration with a resolution of 1 mm.

The spectral broadening attributed to a narrower 3.5 nm InGaAs QW compared to wider 7 nm InGaAsP QW grown on top of the InP barrier is related to the memory effect between group V elements (As/P exchange) at high V/III ratio, and hence undulation of the heterostructure interface. The thickness and compositional variation shifts the quantization levels stronger in such a narrow QW [198], [199].

Additional uncertainty is due to the need of the fast temperature ramp from 650°C (AlGaInAs layer growth) down to 610°C (QW growth) as shown in Figure 4.3. To improve layer uniformity and reproducibility, the change of the temperature was performed during the growth interruption for 1 min under PH_3 for temperature stabilization and 1 s under AsH_3 atmosphere for switching of P to As at the heterointerface. Due to the more efficient substitution of As atoms by P observed in experiments [200], the growth of the InAlAs barrier after InGaAs QW on InP is beneficial for achievement an abrupt QW interface.

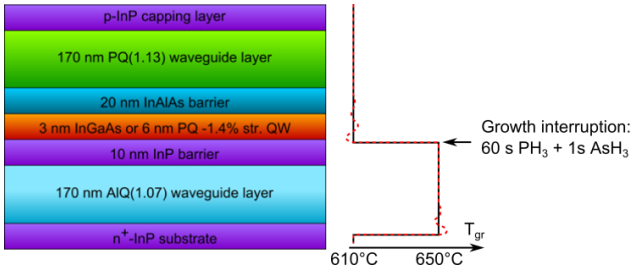

Figure 4.3: Schematic of the QW SOA structure and the growth temperature profile. The red dashed lines shows modulation during temperature ramp.

4.1.3 Quantum Dot Growth

The QD material studied in the work was grown in a self-assembled (Stranski-Krastanov (SK)) mode schematically presented in Figure 4.4. The principle is based on elastic strain relaxation occurring on the surface when a lattice-mismatched layer is being grown. Beyond a strain dependent critical layer thickness (typically around a few monolayers (ML[4]) for InAs/InP) reduction of the surface free energy starts to favor three-dimensional (3D) nucleation against 2D growth and the local growth rate enhancement [201]. Formed nanostructures embedding into a higher band gap material exhibit 3D carrier confinement and quantization of the energy states, which are attributed to QDs. Due to intrinsic self-defined nature of the process, a SK-grown QD ensemble typically has a significant size distribution and complex compositional profile, giving a strong inhomogeneous broadening of electronic and optical properties.

Figure 4.4: Schematic of the growth process of self-assembled QDs in the Stranski-Krastanov mode [19].

[4] ML - monolayer, equals to a half a lattice constant for crystals with a Zinc Blende structure

Recently, great advances have been achieved in growth of InAs/GaAs QDs covering 1 - 1.35 µm spectral range [202]. The growth of In(Ga)As/InP QDs which are of interest for applications at 1.55 µm has remained challenging. The problem originates from the lower lattice mismatch of 3% existing between InAs and InP comparing to 7% inherent to InAs/GaAs system and the group V exchange at the interface [203]. Therefore, SK growth of InAs on an InP substrate typically results in the formation of large, flattened QDs or elongated QDashes or QWires (e.g. [204]) with an inherently low carrier localization and small separation between energy levels. The wavelength of big QDs is often much beyond the 1.55 µm range. Thus, the development in the growth of InAs/InP QDs is focused on improvement of the spatial aspect ratio and size distribution, while small volume QDs are required for achieving laser emission at 1.55 µm.

The development and growth of the QD material used in this work were performed by Prof. Dr. E. S. Semenova using the MOCVD system and the sources specified in Section 4.1.2. The following sections present the current results on the QD material been achieved during this PhD project.

GaAs capped InAs QDs in the InGaAsP matrix

The first set of QD SOA was grown using the QD capping technique described in [205], [206]. The QD SOA structure consists of three layers of 1.65 ML QDs of InAs capped with a thin 1.7 ML GaAs layer reducing a residual strain and a subsequent 10 nm PQ(1.08) spacer layer. Growth of the layers was performed at 515°C with V/III ratio of 5. It was shown that the given growth condition favours the growth of smaller QDs with a larger density due to the reduced surface migration. The QD layers were separated by 60 nm of PQ(1.08) barrier layers and embedded between 190 nm thick undoped PQ(1.08) waveguide layers grown at 610°C.

A schematic of the structure is illustrated in Figure 4.5 (a). Cross-sectional and plane view scanning transmission electron microscopy (STEM) images are presented in Figure 4.6 (b) and (d), respectively. The brighter region corresponds to As atoms within QDs, which has the higher atomic number, compared to lighter P atoms composing the surrounding matrix. An overview of the application of the STEM technique to the morphological and compositional analysis of QW and QD nanostructures can be found in [10]. For comparison, Figure 4.6 (a) and (c) show the QDs grown without the GaAs capping layer.

The STEM investigation showed a lens shaped profile of GaAs-capped QD with the average height and base diameter of 2.0 ± 0.2 nm and 23.5 ± 1.8 nm, respectively, against 3.1 ± 0.2 nm 22.65 ± 2.0 nm obtained for QDs without GaAs capping. The reduction of QD size distribution in the growth direction occurs due to material redistribution during the growth [207]. By optimizing the

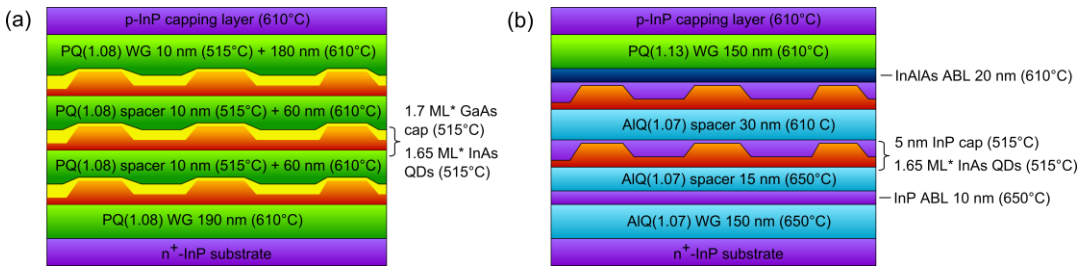

Figure 4.5: Schematics of the QD SOA structures with (a) GaAs capped InAs QDs in a PQ(1.08) matrix and (b) InAs QDs buried by AlQ(1.07) layers embedded in an asymmetric waveguide core. The growth temperature for each layer is shown in the brackets. Sequences with the sigh "+" within one layer should be read as a bilayer with different growth temperatures (from the left to the right). See the detailed epitaxial layer structures in Appendix A4 and A5, correspondingly.

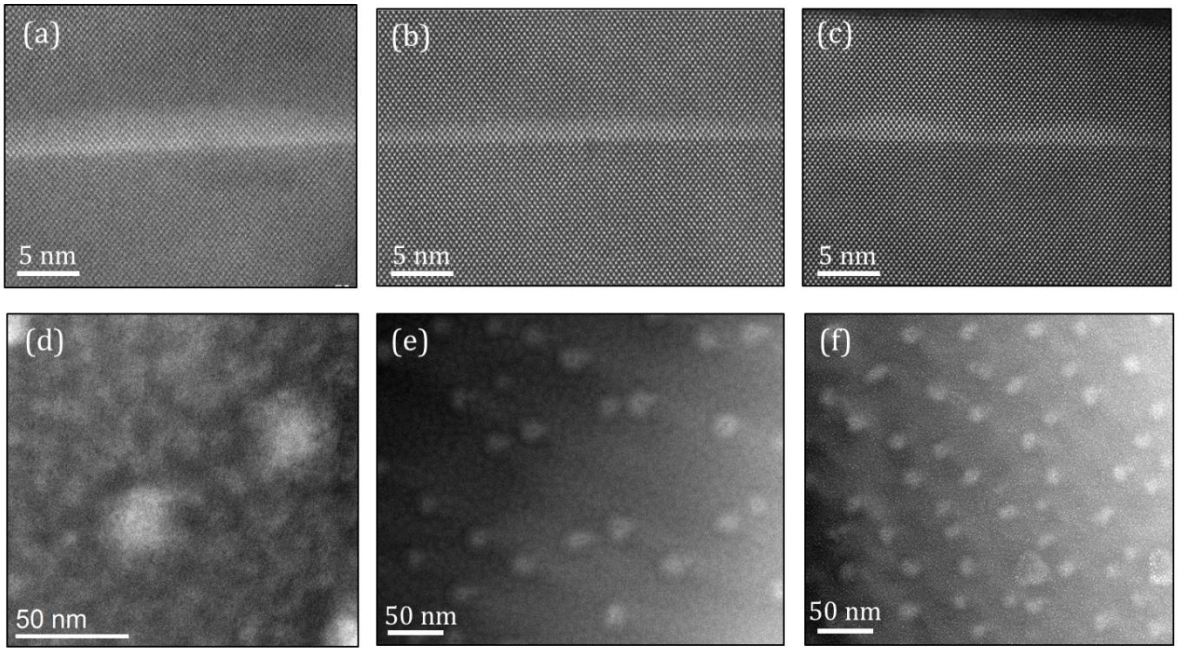

Figure 4.6: Cross-sectional and plane view STEM images of QDs formed from depositing 1.65 ML of InAs in an InGaAsP matrix and capped with: (a), (c) InGaAsP and (b), (d) 1.7 ML of GaAs followed by InGaAsP; (c) and (f) InAs/InP QDs deposited under tailored growth condition.

GaAs thickness, the emission wavelength was shifted from > 1.7 µm for QDs without GaAs to the target wavelength of 1.55 µm for 1.7 ML thin GaAs capping.

The STEM investigation showed a lens shaped profile of GaAs-capped QD with the average height and base diameter of 2.0 ± 0.2 nm and 23.5 ± 1.8 nm, respectively, against 3.1 ± 0.2 nm 22.65 ± 2.0 nm obtained for QDs without GaAs capping. The reduction of QD size distribution in the growth direction occurs due to material redistribution during the growth [207]. By optimizing the GaAs thickness, the emission wavelength was shifted from > 1.7 µm for QDs without GaAs to the target wavelength of 1.55 µm for 1.7 ML thin GaAs capping. The corresponding RT PL spectrum and peak wavelength map obtained using for excitation 532 nm CW laser is demonstrated in Figure 4.7. The PL emission is centered around 1550 nm. The FWHM is 170 nm (88 meV).

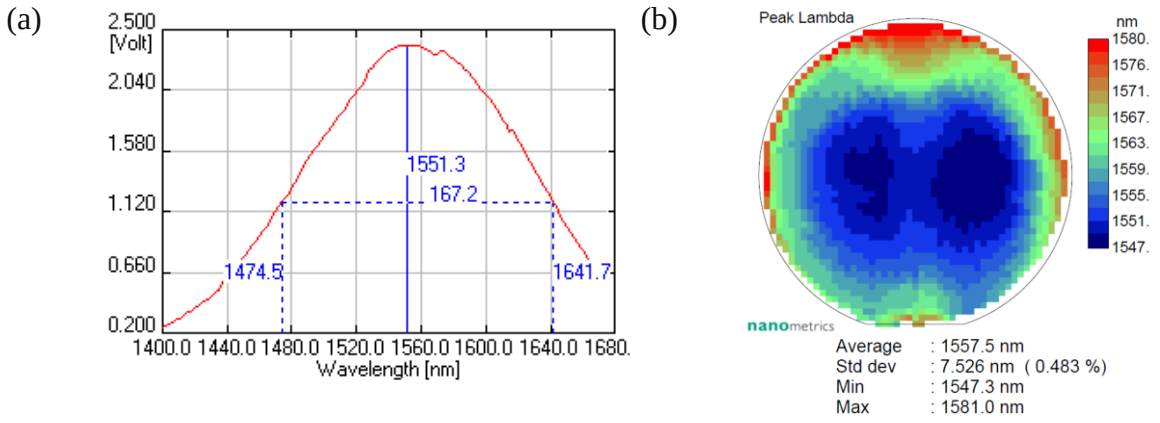

Figure 4.7: RT PL spectrum (a) and peak wavelength map (b) of InAs/InGaAsP/InP QDs capped with thin GaAs layer.

The low aspect ratio of these QDs results in a small separation between the energy levels and poor carrier confinement due to the affinity to a wetting layer ("shallow" QDs) as described in Section 2.4. Figure 4.8 shows the ground-state and excited-state transitions for a single QD calculated using a simplified model in terms of 8-band k*p theory [208]. The GaAs capped QDs exhibit 40 meV energy separation (red curve) and 50 meV for the QDs grown without GaAs (green curve). In combination with homogeneous broadening at room temperature and strong inhomogeneous broadening of an ensemble, it results in smearing of the spectrum over energy.

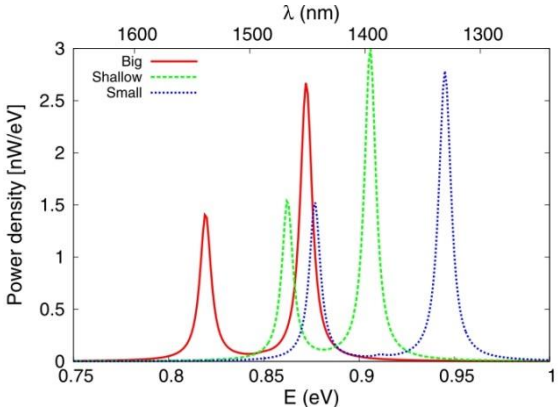

Figure 4.8: 8-band k*p theory calculation at 7 K of a ground state and excited state transitions for "large" InAs/InP QDs emitting above 1.6 µm wavelength (red solid curve), InAs/GaAs/InP QDs demonstrate shallow shape (green dashed curve) and "small" InAs/InP QDs grown under tailored growth regime, suppressing surface diffusion (blue dotted curve) [209].

InAs QDs in the InP and AlGaInAs matrix

Further development was aimed to refine the control on the QD aspect ratio and carrier confinement, while keeping the small QD volume for the designed operating wavelength. The poor electron confinement originates from the low conduction band offset attributed to the QD grown in the PQ(1.08) barriers. Inserting the InAs QD within a wider bandgap matrix, such as InP, increases potential barrier. These situations are presented in Figure 4.9 (a) and (b), respectively, which give qualitative evaluation of carrier confinement by a simplified calculation of the band diagrams. The QDs are represented by thin $In_{0.9}Ga_{0.1}As$ QW layers without taking into account the strain relaxation effects. The composition of the QWs was tailored to get the emission wavelength at 1.55 µm with knowledge of the QD average height from the STEM experiments for (a) and (b) cases.

Figure 4.9 (c) shows the most favorable situation, when QDs are buried in AlGaInAs layer with a high band offset for electrons on one side, and reduced barrier in the valence band favourable for hole injection on the other. The non-uniform carrier distribution reduces the gain, and increase carrier dependent losses [210]. For example, the InAs QDs in high InP barriers were shown to have higher the threshold current density compared to the InAs QDs in InGaAsP due to the inhibited vertical carrier transport [211]. Moreover, AlGaInAs compounds have a higher refractive index than InP and therefore, offers better optical confinement. The sketch of the proposed SOA with InAs/AlGaInAs QD active medium embedded in ABLs and asymmetric WLs is depicted in Figure 4.5 (b). From the fabrication point of view, deposition of InAs QDs onto an AlGaInAs layer has another advantage in eliminating the group V exchange. A high ground-to-first-excited-state energy separation of 65 meV and improved lasing characteristics were reported for InAs/AlGaInAs QDs grown by molecular-beam epitaxy in [212]–[215] .

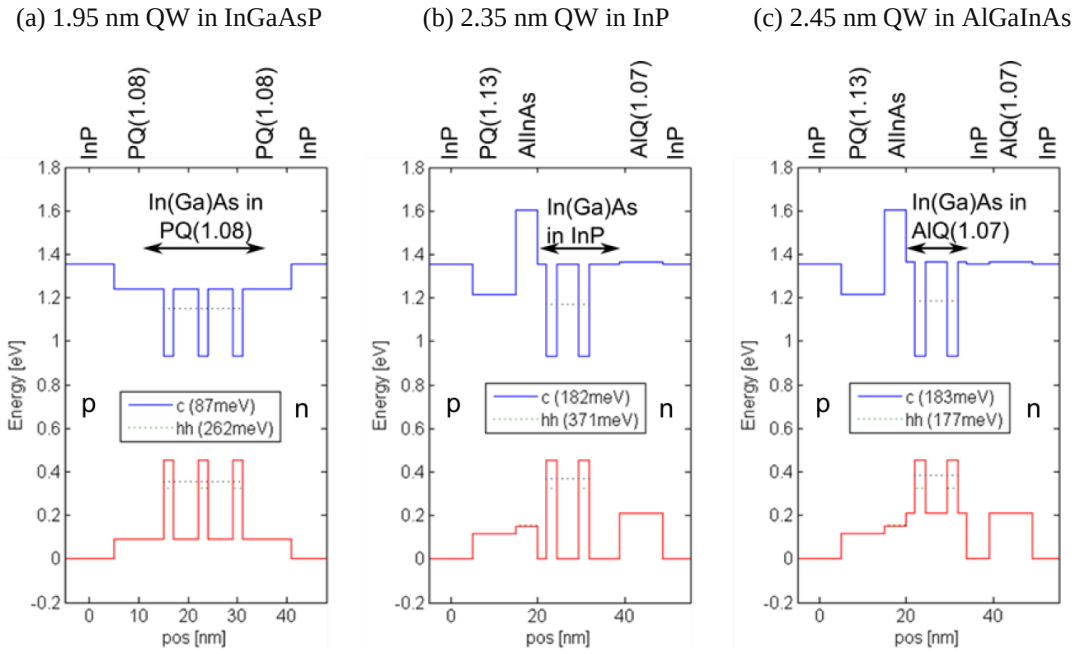

Figure 4.9: Calculated bandgap diagram of thin In0.9Ga0.1As QWs representing QDs buried in the (a) InGaAsP, (b) InP and (c) AlGaInAs matrix. QD layers in (b) and (c) are embedded in the ABLs and asymmetric WGs (see Section 3.2). Insets show the confinement of electrons (c) and heavy holes (hh) on the ground states.

In practice, the MOVPE growth of QDs on AlGaInAs layer is challenging due to the large difference in the preferable growth temperatures for AlGaInAs (650°C) and QDs (< 500°C) in MOVPE. The re-evaporation of the QD material during the long temperature ramp can be avoided by covering with thin InP layer at low temperature. If the layer is transparent for carrier tunneling, the time for the filling of QD will depend on the tunneling efficiency and, in this wise, can be potentially extended, which is beneficial for MLLs. Another important issue is related to surface roughness of AlGaInAs material upon a QD layer due to the difference in group III atom behavior, and, in particular, low surface migration of Al as discussed in Section 4.1.2.

The recent results on growth of the InAs QD in InP matrix showed a higher aspect ratio and smaller QD size in comparison with GaAs capped QDs, which clearly seen in Figure 4.6 (c) and (f). The InAs/InP QDs are 2.34 ± 0.16 nm in height and 13.6 ± 1.0 nm long in the [-110] direction and 18.7 ± 1.6 nm in the [-1-10] direction. The theoretical calculation predicts an increase in the ground and excited state separation up to 70 meV as shown in Figure 4.8 (blue curve). The improvements are resulted from the reduced growth temperature down to 485°C and suppressed QD segregation associated with GaAs capping. A detailed discussion can be found in [209].

The first results on growth of the QD SOA structure consisting of two layers of 5 nm InP capped InAs QDs in the AlGaInAs barriers (Figure 4.5 (b)) revealed an significant increase of the peak wavelength distribution across the wafer up to 1.7% (Figure 4.10) compared to 0.5% the GaAs capped QDs (Figure 4.7). The problem is presumably originated firstly, from the reduced mobility at lower temperature, and secondly, from the high surface roughness and low planarization capability of AlGaInAs compared to InP and InGaAsP alloys. The discrepancy between the two QD layers indicated as two equally broadened overlapping PL peaks of different intensity across the wafer was observed. Therefore, the latest advances in growth of InAs QD material in InP and AlGaInAs matrix showed their perspective for laser application. However, no device fabrication from the wafers consisting of these types of QDs was carried out during the work on this Ph.D. thesis.

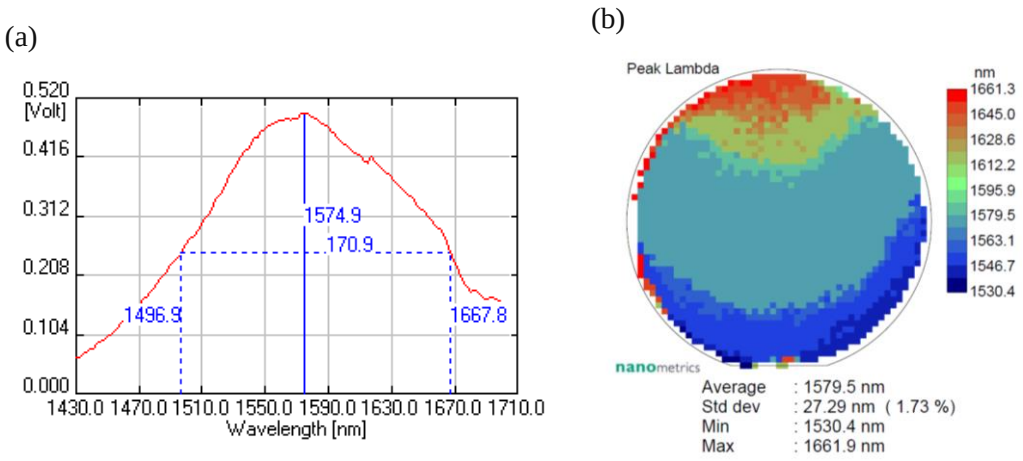

Figure 4.10: RT PL spectrum at the center point (a) and peak wavelength map (b) of the InAs QDs grown in the InAlGaAs matrix.

An alternative solution is MOVPE selective area etching and growth using e-beam or block copolymer lithography [216]. This method does not rely on the strain relaxation process, and thereby can be potentially employed for the design of QD shape and composition, and ultimately for control over its energy state configuration. The development of the block copolymer lithography was partially done at DTU Fotonik during this Ph.D. study, and the preliminary results on selective area growth of the QDs employing block copolymer lithography can be found in [209], while the MOVPE in-situ etching and growth processes were studied in [217].

4.2 Butt-Joint Integration

Monolithic integration of the SOA and EAM section was performed by MOVPE selective area growth (SAG) on a non-planar substrate, known as butt-joint regrowth (BJR). The BJR scheme involves three main steps: growth of one type of epitaxial material, its partial removal by patterning with a dielectric mask, and growth of an alternative material on the opened from the mask area. This approach offers the highest degree of flexibility in integration of diverse epitaxial structures on a single chip compared to the other integration schemes, such as planar SAG, quantum well intermixing, offset and dual QW growth. A good comparative overview of the different technique available for the realization of photonic integrated circuits and relevant examples can be found in [137], [218].

Integration of semiconductor optical components has been developing intensively from the early 80s and has been successfully implemented for fabrication of buried heterostructure lasers and photonic integrated circuits for telecommunications applications based on the conventional InP-based InGaAsP and AlGaInAs material systems [2], [137]. However, monolithic integration of AlGaInAs-based devices has been limited due to the strong tendency of Al-containing alloys to oxidize [192], [193], [219]. Improvements in the precursor purity, namely trimethylaluminum and trimethylindium, as well as in the quality of the equipment employed for MOVPE in the past decades have made possible the growth of high-quality Al containing layers [193]. In case of BJR, the process requires partial removal of an as-grown material, therefore, exposed to air mesa sidewalls composed of AlGaInAs material may result in AlO_x formation. Formed AlO_x on mesa block facets may act as micro-masking and induce structural defects at the BJR interface. These imperfections give rise to excessive optical and carrier losses, as well as intracavity reflection.

In particular, minimizing reflection back to the waveguide is of high importance for stable operation of integrated waveguide devices. Even a small internal reflectivity leads to lasing wavelength instability and frequency chirp in distributed-feedback lasers integrated with EAMs [220]–[222]. This is more crucial for monolithic MLLs, where such an optical feedback leads to detrimental multicavity effects, for instance the multipulsing regime reported in [134]. An acceptable level of reflectivity, e.g. for MLLs, has been estimated to be below 10^{-5} [223]. The low reflectivity between integrated active optical components of about 10^{-5} per interface was obtained by realizing an angled interface was reported in [174], while exhibiting high internal losses of 1.5 dB. In comparison, the reflectivity down to 0.5×10^{-5} and 0.46 dB losses were demonstrated for active – passive integration in [224]. Thus, achievement of low internal reflectivity along with high mode coupling is required for fabrication of the next-generation optical devices. Besides that, crystal defects contribute to the carrier losses as deep-level recombination centers reducing the quantum efficiency.

Another requirement concerns the surface flatness, which is difficult to achieve in the BJR due to the mask effect described below. First, a non-planar surface contributes to light scattering. Secondly, the surface quality is essential from the technological aspects for further device processing, which will be discussed in Section 4.3.

One more issue is of high importance for the realization of photonic integrated circuits. The increased demands on more functionality along with compactness requires the composition uniformity and associated invariability of optical properties within one section or device when all-active integration is performed.

In following sections, an overview of BJR process is given, and influence of the growth parameters on the growth morphology and compositional profile is discussed. Next, the integration process developed for this work is described. To validate the applicability of the used approach for the fabrication of MLLs with respect to the given requirements, complete investigation of martial properties, such as the crystalline perfection, morphology, composition uniformity and optical properties on the coupled interfaces, is presented.

4.2.1 Selective Area Growth and Growth Rate Enhancement

The selectivity of growth of semiconductors against dielectric material in MOVPE SAG is a well-known effect originates from the difference between the surface kinetic of semiconductor and dielectric materials. Because of the surface has a catalytic effect on precursor decomposition, the growth species cannot be fully cracked and incorporated upon the amorphous glass surface[5], leading to an excessive concentration in the adjacent to the mask area over the substrate. The resulting gradient forces the precursors and radicals to migrate towards the mask openings (Figure 4.11 (a)). The limited vapor phase diffusion (VPD) of the precursors enhances the growth rate in the adjusted to the mask. With respect to the growth conditions, the growth rate enhancement (GRE) vanishes in the range from a few tens to hundreds of microns away from the mask edge [225]. The magnitude of the GRE depends linearly on the mask area [226], [227]. At the closest vicinity, a significant material piling can be observed due to the shorter (up to a few microns [228]) migration of the adatoms over the surface (Figure 4.11 (b)).

[5] For standard growth conditions. In case of classical Molecular Beam Epitaxy, where elemental atoms are used for growth, the process results in the formation of a polycrystalline film on the dielectric surface.

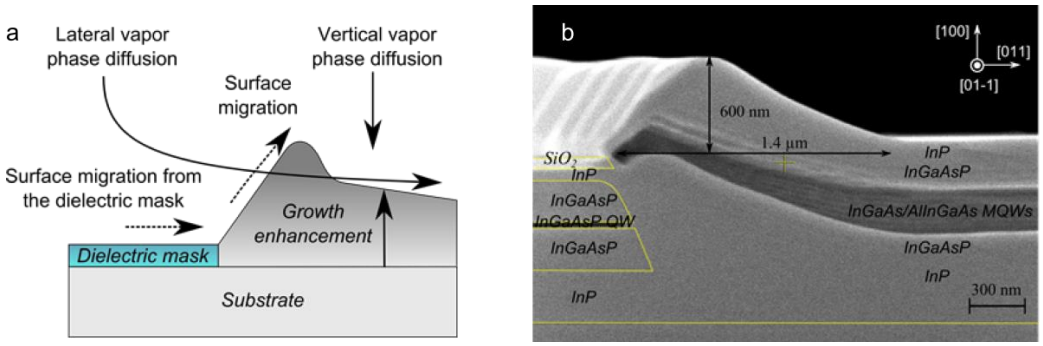

Figure 4.11: (a) Schematic of the diffusion and migration processes during SAG and (b) a cross-section SEM image of the first BJR integrated material.

The growth evolution is typically described in terms of the VPD model (see e.g. [229]–[231]) through the effective diffusion length D/k_s, as a characteristic parameter, where D is the diffusion coefficient in vapor phase, and k_s is the flux of source material ongoing a phase change from vapor to solid. This process depends on the probability of surface reaction, and, owing to the difference in the diffusion and sticking coefficient specific for each material. It results in a divergent composition near the mask compared to the nominal one. In combination with the thickness variation, it allows for bandgap engineering, e.g. of QWs based on ternary and quaternary compounds within a single growth step by varying mask geometry (planar SAG) [137], [232]. To evaluate the local growth enhancement and profile at the mask edge, the surface migration of the precursors from the dielectric mask must be considered along with VPD [233], [234], [228].

Beside these aspects, achievement of uniform layer deposition on the one hand, and a planar interface on the other have been considered one of the biggest challenges of both the BJR and narrow-stripe SAG processes. Two main approaches have been applied so far to circumvent material piling. The most straightforward solution for BJR is to compensate the excess material arriving from dielectric by etching a cavity below the mask. However, the migration length of the species can be not sufficiently long to be transported under the large mask overhang, and consequently, voids can be created [133], [235], [236]. Another way is suppression of the GRE near the mask edge by promotion of longer diffusion. It requires optimization of the MOVPE conditions affecting on surface migration and vapor phase diffusion.

- *Growth pressure and temperature*

The vapor phase diffusion is strongly dependent on the chamber pressure. The kinetic theory of gases predicts an increasing of the vapor diffusion *D* with reducing the growth pressure *p*:

$$D \propto \frac{(k_B T)^{3/2}}{p\sigma^2} \tag{4.1}$$

where *T* is the growth temperature, k_B is the Boltzmann's constant and σ is the collision cross section of the diffusing molecule. At high pressure, the probability of collision becomes higher and hence, the mean-free path is shorter. A planar BJR regrowth at low growth pressure of 20 mbar was demonstrated in [237]. In a minor way, diffusion increases with temperature.

The atomic sticking probability and the residence time to incorporation, which determine the surface migration, are defined by a characteristic activation energy, and thus, temperature dependent. Decreasing the growth temperature reduces surface migration. However, experimental observations in [238], [239] showed an increase in the coefficient k_s with temperature (smaller effective diffusion

length). In this case, the other growth parameters should be included in the discussion due to the complexity of the MOVPE processes.

- *Composition*

Because of group III precursor molecules are approximately similar in size (equal collision diameters σ in Eq. 4.1), the dependence of the composition on diffusion in the gas phase *D* is expected to be negligible [240]. However, much evidence points to the conclusion of spatial inhomogeneity of the group III composition. In particular, the results showed that the effective diffusion length D/k_s is larger for Ga than for Al and the shortest for In species [225], [241], [242]. Thus, a higher In concentration in the vicinity to the mask is typically observed. The sticking probability of In species is two - three times larger than Ga [243]. *However,* the difference in the sticking coefficient makes a minor contribution to the effect of compositional distribution. In fact, TMIn molecules are less stable than TMGa (lower decomposition temperature) and can be decomposed faster. Due to the higher diffusion coefficients of decomposed molecules, the excess In material can be consumed more efficiently at the mask edge, giving a rise to higher In content [244]. Studies also show the dependence on group V composition. In incorporation is found to be more efficient on P terminated surface than on As one in [239]. An increase of the Ga incorporation rate with increasing of As content in InGaAsP alloys was reported in [227]. The result is consistent with an assumption of the catalytic influence of the group V decomposed molecules on group III precursors.

- *Crystallographic orientation*

Besides the growth conditions, the sticking coefficient and growth rate diverge for different crystallographic planes. The anisotropy is a result of a specific electronic configuration and availability of bonding sites, which are defined the adsorption probability and incorporation (or the activation energy). For instance, the preferential growth behavior arises for the (100) plane against {111} planes. The (100) plane has two electrons established the binding to the crystal and two dangling bond participating in chemical reactions, while on {111} planes each atom is bound by three electrons and only one dangling bond is available. The reduced amount of the adsorption sites leads to a significant growth suppression on the {111} planes. Taking into account the compositional dependence of the decomposition and incorporation processes, the deposition of ternary and quarternary alloys, such as InGaAsP, is hampered comparing to InP, if the exposed surface is formed by {111} crystallographic plane [245].

In the absence of a symmetry center in zinc-blende crystals like InP, <111> directions have a polar nature, resulting in the nonequivalence of the etching and growth properties [246]. Specifically, the {111}A planes terminated by group III atoms are more stable to chemical reactions since three electrons of an In atom are bounded to the crystal. The {111}B planes are consisted of group V atoms and have two spare electrons on the dangling bond and, thus, typically more reactive in etching. However, these electrons create a high potential barrier impeding atom incorporation. Therefore, the growth is suppressed on {111}B, while moderate growth can occur on the {111}A planes [244]. For the growth conditions in [20], the surface migration length on an (100) InP surface was estimated of In and Ga species to be about 1 μm and 8 μm, respectively. On {111}B, the migration of In was larger, 1.4 μm.

The effect of the growth rate suppression on {111} planes is often utilized to reduce overgrowth at the mask edge. The developing of the {111} facet can be obtained in a self-limiting manner during preferential wet etching of a waveguide core [237]. However, to achieve complete planarization, low growth pressure (20 mbar) was required to enhance diffusion of spices from the masked area.

Another approach is to grow on initially misoriented substrates (toward the (111)B plane), which was shown to improve growth behavior, e.g. in case of chemical beam epitaxy in [247]. However, growth of active material on alternative to (100) substrates complicates further device processing.

- *V/III molar flow ratio and growth rate*

Higher growth rates or relatively low V/III ratios support fast incorporation, and, therefore, lower the surface migration length is expected on the (100) plane. However, the effect is dependent on the crystallographic orientation, growth temperature [248] and other surface conditions. Thus, the overgrowth suppression in the vicinity of the mask at lower growth rate was demonstrated in the SAG process in [190].

- *Surface conditions*

The migration behavior on a local scale can be affected by the other factors, such as strain, surface curvature and compositional inhomogeneity [249]. The lateral change of these parameters creates a potential gradient, which forces species to diffuse towards the area with lower potential. The enhanced growth rate upon the locally induced strain was applied for growth of QDs, known as the stressor approach [250], or utilizing the capillarity effect growth of *QWires and QDs* on V-grooved substrates [251].

In this work, the waveguide core of the QW SOA to be regrown is asymmetric and composed of AlGaInAs and InGaAsP material, which does not allow for formation of {111} planes directly by selective wet etching, and rather highly developed topology of the mesa sidewall is expected. The change of the growth parameters depends on the capabilities offered by an epitaxial growth system and may complicate control over the growth. Therefore, an optimization of the integration process and all growth steps were carried out under the optimal growth conditions listed in Section 4.1.2.

4.2.2 Butt-Joint Regrowth: Process Overview

The MLL laser structures with integrated the SOA and EAM sections designed in Chapter 3 have been realized a three-steps MOCVD growth sequence illustrated schematically in Figure 4.12. The detailed process description can be found in Appendix B.1.

First, the QW or QD SOA structure was grown and coated with a ~100 nm thick SiO2 layer using plasma enhanced chemical vapor phase deposition (PECVD) followed by the conventional ultraviolet (UV) photolithography and CHF3/O2 reactive ion etching (RIE) or, alternatively, wet etching in a buffered HF (BHF) solution, to pattern the surface with an SAG mask protecting selected SOA areas (Figure 4.12 (a)). The mask layout consisted of the 20 μm wide stripes oriented along the laser waveguide [011] direction. The edge of each stripe was 30° angled towards the [0-11] direction as depicted in Figure 4.13 to minimize back reflection from the interface. The width mask can be varied, considering that the amount of excess material is nearly proportional to the mask area on the one side [244], and a process tolerance on the other.

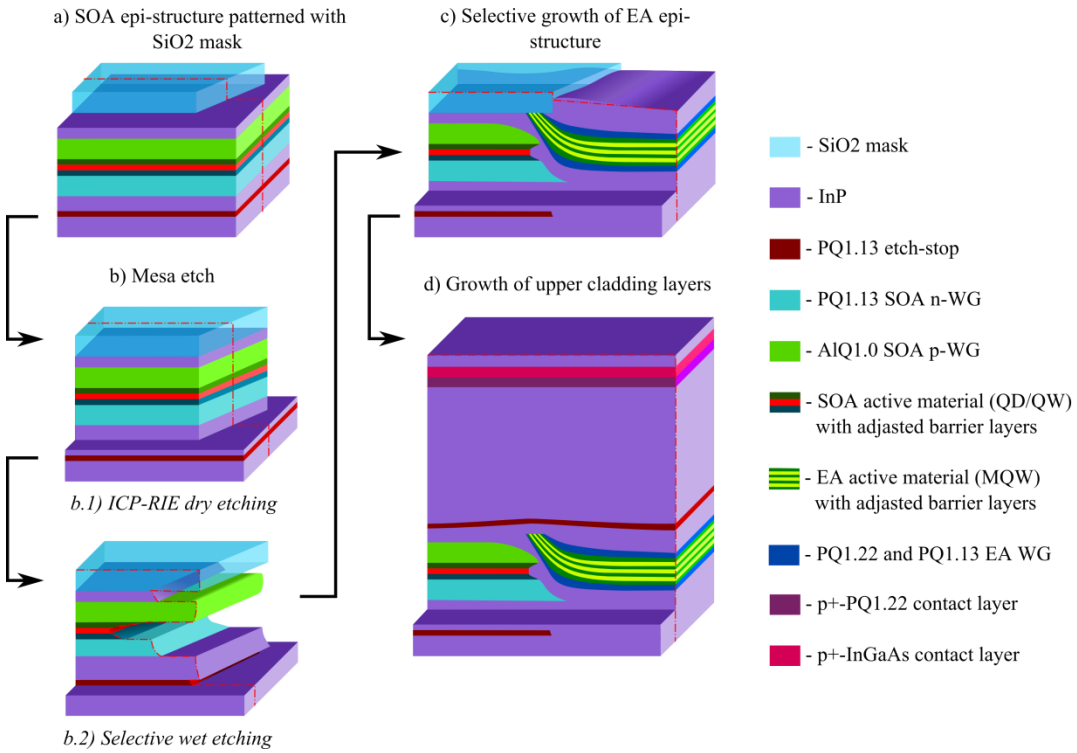

Figure 4.12: Schematic overview of the butt-joint regrowth process used for fabrication of the integrated MLLs with individually optimized SOA and EA sections.

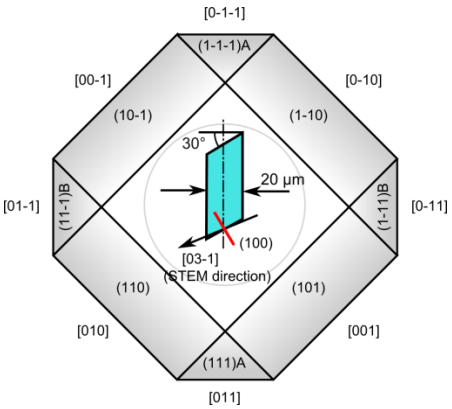

Figure 4.13: Mask orientation in a planar representation of cubic form (European-Japanese option).

Mesa etching

After pattering, the unprotected SOA material was etched by non-selective Cl2/CH4/Ar inductively coupled plasma RIE down to the InP buffer layer to form vertical mesa blocks (Figure 4.12 (b)). This was followed by isotropic wet etching in 1 HCl : 4 H3PO4 (by volume) of the buffer down to a sacrificial etch stop layer. Thus, a damage-free and smooth surface required for epitaxial growth was produced. The stop layer ensured precise vertical alignment with the regrown EAM structure. Moreover, etching revealed the {211} planes bounded to the base, which can be attributed to the waveguide crossing angle of 30°. The second wet etching with 1 H2SO4 : 8 H2O2 : 80 H2O was applied to remove AlGaInAs and InGaAsP compounds selectively, and, thereby, created a mask undercut in a controllable manner. The final mesa profile is presented in Figure 4.14 (a).

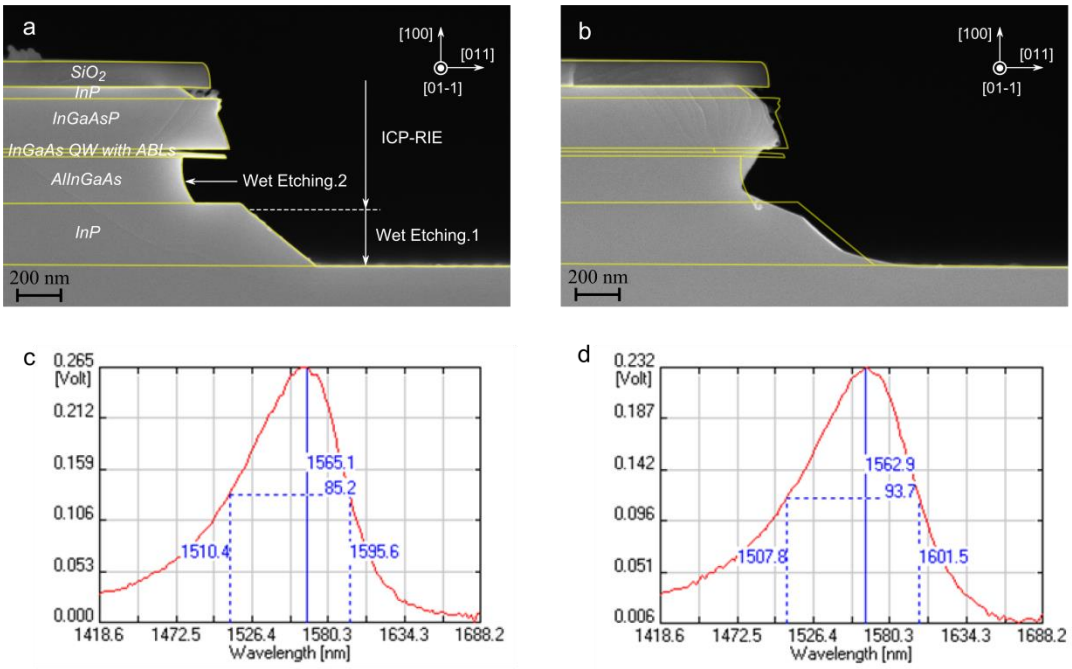

Figure 4.14: Cross-sectional SEM image of the QW SOA mesa edge etched for 25s with H2SO4:H2O2:H2O (1:8:80 VP) before (a) and after (b) in-situ annealing at 650°C for 15 min; (c) and (d) show corresponding µ-PL spectra.

An alternative approach based on CH_4/H_2 RIE was examined in case of ICP-RIE inaccessibility. This method does not rely on a stop layer for alignment and can be employed for a multi-regrowth process. First, RIE was applied to etch down to the AlQ waveguide layer, which terminates the etching process (Figure 4.15 (b.1)). The selectivity of CH_4/H_2 RIE to AlQ originates from the low reactivity to the etchant and progressive polymer contamination of the surface prohibiting ongoing etching [240], while an addition of oxygen, typically used to remove polymers, resulting in rapid Al oxidation. The moderate AlQ etching rates of a few nm/min without etching termination were demonstrated using CH_4/H_2/Ar RIE in [252]. After RIE, the AlQ layer was etched away by 1 H_2SO_4 : 8 H_2O_2 : 80 H_2O selectively to the InP buffer layer, and, simultaneously, an undercut was formed (Figure 4.15 (b.2)). However, uncompleted etching of the AlQ layer may lead to defect formation after regrowth as shown in Figure 4.16 (a) (see digital version). Therefore, overetching is highly recommended to achieve smooth regrowth surface (Figure 4.16 (b)). However, an introduction of a buffer layer, allowing for reduction of defects, can be limited by the design of epi-structures.

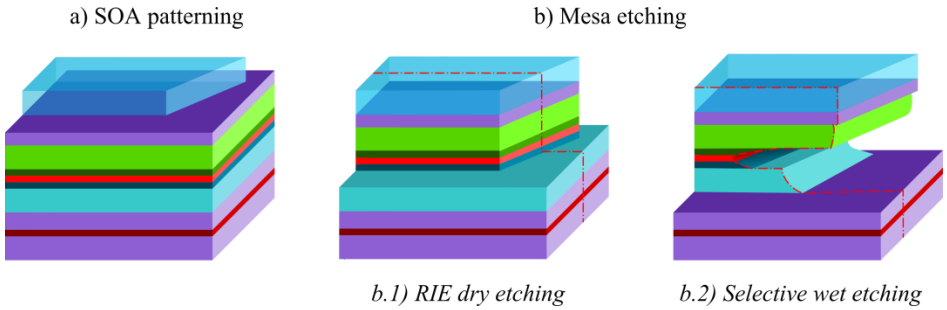

Figure 4.15: Alternative SAG mesa etching process.

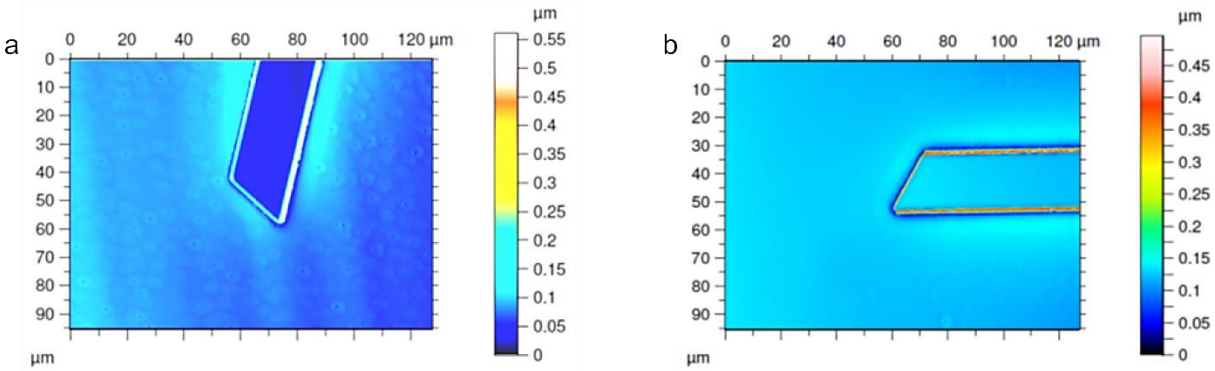

Figure 4.16: 3D optical interference profilometry[6] top view images of the samples after regrowth prepared by CH4/H2 RIE: (a) uncompleted wet etching resulting in defects (in high contrast) and (b) with 15 s overetching time (cross-section SEM image is presented in Figure 4.19 (b)).

Cleaning

Prior the second growth the wafer was cleaned in oxygen plasma and etched in H_2SO_4 (conc.) for 5 min to remove any organic contamination, surface damage, and a native oxide layer, and reduce carbon incorporation as suggested in [253]. The etch rate of InP was measured to be 5 - 7 nm/min. As shown in [253], etching in strong acid solutions reveals a hydrophilic surface with hydrogen passivated phosphoric bonds. During rinse in deionized water and N_2 drying, a thin oxide coating is produced. To minimize oxidation, the loading time between the etching and regrowth must be as short as possible. To promote the residual AlO_x deoxidation, the cleaning procedure was completed by a standard pre-growth heating at 650°C in the MOVPE chamber under PH_3 overpressure. The annealing time was shorten to 15 min compared to the 45 min recommended in [254], which was shown to be sufficiently effective by investigation of crystalline quality after regrowth (see Section 1.2.4). The changes in the mesa topology were observed after the heating as a result of material redistribution as demonstrated in Figure 4.14 (b). The corresponding RT PL spectra are shown in Figure 4.14 (c), (d). The inspection revealed insignificant blue-shift of the peak position of few nm and broadening around 10 nm in average[7] compare to the initial spectrum.

Regrowth

In the second growth step, the absorber structure with a MQWs active region was deposited (Figure 4.12 (c)). No parasitic nucleation on the glass mask was detected. The protective mask was removed by BHF wet etching, and the surface cleaning procedure was repeated. After that, the integrated SOA - EAM structure was overgrown with a 2 µm thick p-doped InP cladding and InGaAsP and InGaAs contact layers over the entire wafer.

[6] Due to the low lateral resolution (2.5 µm, max slope 21° at x20 magnification, PLu Neox 3D Optical Profiler Sensofar), the sharp features, such as a piling near the edge, were not defined correctly. For these measurements, standard stylus profilometry and SEM were used.

[7] The estimation is rough because of the PL resolution of 0.1 mm is larger than the mesa width of 20 µm (RT, 980 nm CW excitation)

4.2.3 Growth Morphology and Compositional Analysis

In order to predict the growth morphology and estimate the material distribution at the BJR interface for the given growth conditions and the developed mesa topology, the QW SOA was regrown with a test structure consisting of a 50 nm InP buffer layer and a stack of repeating 50 nm thick InP and lattice-matched InGaAs for a total thickness of 950 nm, which is significantly thicker than the etched depth plus mask. To examine microscopic changes in the vicinity to the mask, scanning electron microscopy (SEM) and STEM imaging were employed. The elemental analysis was performed using energy dispersive X-ray spectroscopy (EDS) available in the STEM system. Our STEM and EDS analyses were carried out on an approximately 100 nm thin lamella prepared in the direction perpendicular to the angled mask edge, as shown in Figure 4.13, using focused ion beam milling.

Figure 4.17 (a) shows the cross-sectional STEM image of the regrowth profile of the InGaAs/InP multilayer stack projected along the [013] crystallographic direction. At the first stage of the regrowth, below the mask level near the mesa edge (marker A), growth tends to occur with the formation of {311} or high index planes (indistinctly), such as {511}, {711}, etc., consisting of longer {100} terraces interleaved with {111}A steps, which is initiated by the exposed {211} facets at the bottom, and increased concentration of source molecules arriving from the dielectric mask. The growth of InGaAs is suppressed by a factor of 0.85 (on average), as seen from Figure 4.17 (b) for the markers A and B than on (100), which is consistent with [244]. This leads to the material pile-up

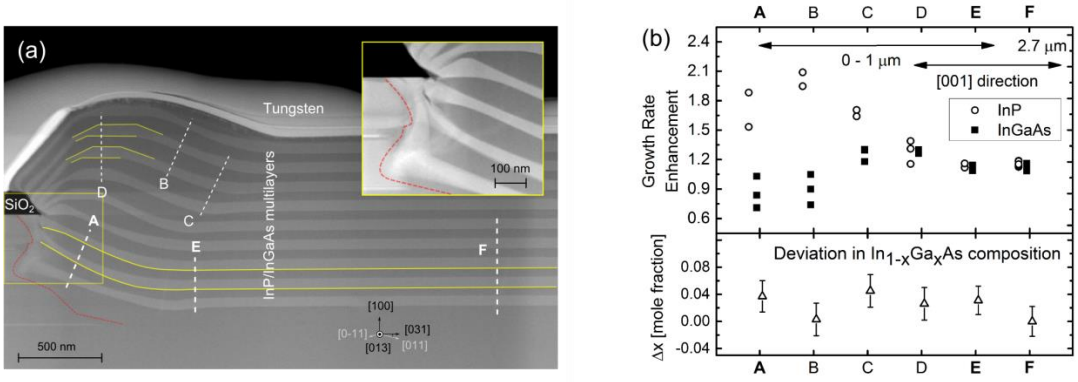

Figure 4.17: (a) Cross-sectional STEM image of the InP/InGaAs test structure integrated with the QW SOA (Inset: BJ interface). The red dashed line shows the SOA mesa profile before regrowth. (b) Growth rate and absolute group III composition deviation of Ga in In1-xGaxAs from the nominal one obtained from EDS analysis at different points marked in the STEM image in (a). The error bars show the EDS experimental deviations with the average uncertainty of 4.5 ± 0.3%.

observed within a 1 µm range from the mask. Above the mask level, the InGaAs layers form trapezoidal prisms terminated by the slowly developing {311} facets (marker D), while the InP growth displays a planarizing effect and, thus, a more smooth topology. This distinctive behavior was found to be in good agreement with the growth of InP and InGaAs on non-planar substrates reported in [229], where the tendency of InGaAs to restore low index planes during growth was also demonstrated.

The EDS compositional analysis showed an increase in Ga concentration by a few percent near the mask edge (Figure 4.17 (b), markers A – E), while In-rich material is generally observed due to the shorter surface migration length [228], [242], [244]. Indeed, the Ga incorporation rate can be enhanced compared to In one for the growth of alloys with a higher As fraction, as demonstrated in [227].

Moreover, non-planar growth is strongly dependent on the local differences in surface energy, e.g. attributed to the curvature in the undercut cavity, surface states, strain, etc. Minimization of the potential is the driving force for atom incorporation. Thus, the highest deviation of the InGaAs composition of 0.045 by mole fraction (equivalent to 0.34% in-plane strain) with respect to the nominal value was measured closest to the interface (marker A) and the bent areas (marker C), which is assumed to compensate the curvature effect. Comparing the A and B markers of the similar topology, strain reduction is clearly observed for overlying layers.

The most pronounced material perturbation occurs in the mask undercut and directly at the interface as displayed in the inset of Figure 4.17 (a). The red contour outlines the mesa profile of Figure 4.14 (b). During the growth of the first layers (~ 200 nm in this case), the filling of the mask underetch occurs following by forming a bent up profile. The smeared intensity profiles of the InP/InGaAs interfaces in STEM images and the compositional profiles in the EDS spectra can be attributed to the spatially shifted transient interface region within the lamella due to a misalignment of ~3.4º between the mask edge and the crystallographic direction chosen for STEM as shown in Figure 4.13, as well as providing evidence for interfacial material intermixing [255]. Promisingly, no dislocations caused by phase segregation or related to oxidation of the AlGaInAs layer could be observed.

The growth rate enhancement (GRE) of approximately 1.14% on the {100} planes for both InP and InGaAs layers near the interface (markers E, F), is associated with diffusion of the precursors in the vapor phase from the masked area inherent to the SAG process. This effect vanishes gradually within a few tens of microns as determined by 3D optical interference profiling.

SEM images of the mesa profiles and BJR interfaces along both the [110] and [1-10] directions are presented in Figure 4.18. The inspection revealed a higher growth enhancement in [1-10] of 1.4/1.2 (markers A/B) against 1.2/1.1 in [110] due to the larger mask covering per unit interface length than at the stripe edge considering that the vapor phase diffusion length is larger than a half of mask width [227].

The difference in mesa and growth profiles is consistent with crystallographic anisotropy discussed in Section 4.2.1. It is seen that the (211) facet formed by wet etching of the InP buffer layer (Figure 4.18 (a)) favors more uniform layer deposition at the interface comparing to the steep undercutting (110) plane adjacent to the mesa base (Figure 4.18 (c)).

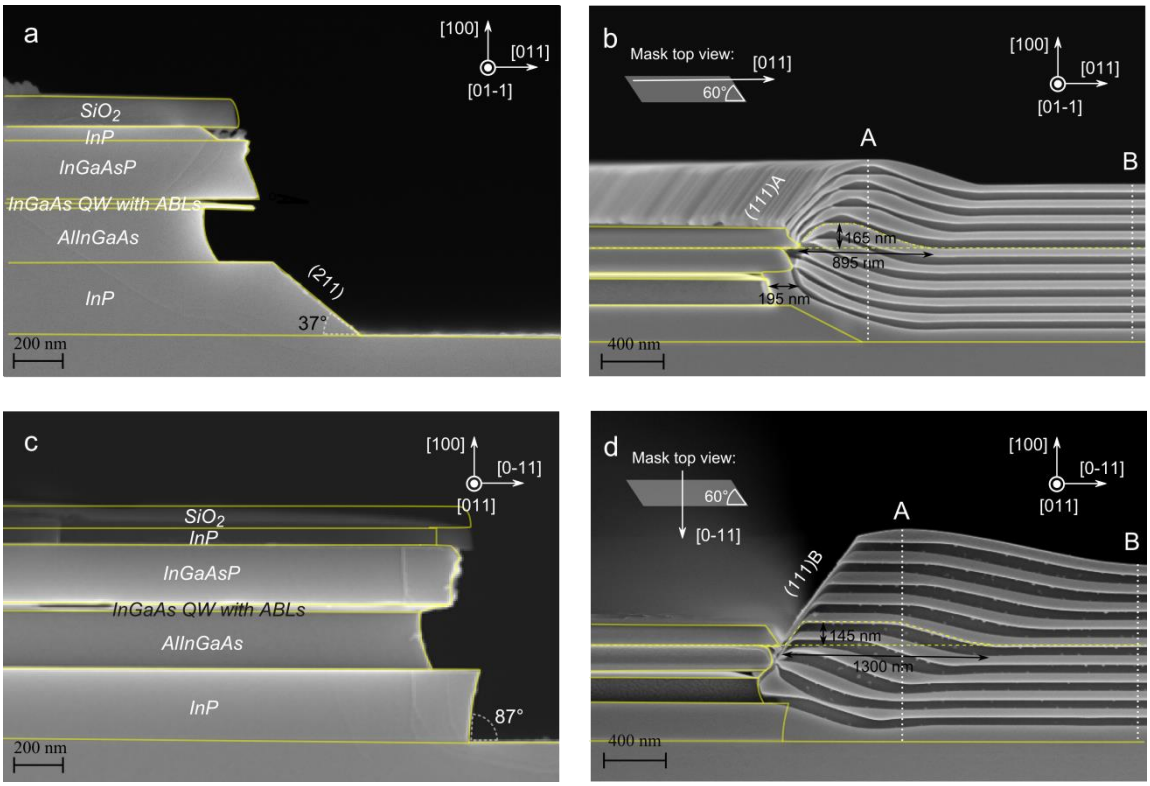

Figure 4.18: Cross-sectional SEM image of the BJR interface between QW SOA section BJ regrown with InP/InGaAs test structure in the [110] and [1-10] direction (after stain etching).

4.2.4 Regrowth Optimization

The discovered tendency of the compositional dependency of growth rate was used to suppress mask overgrowth by controlling the ratio between the deposited InP and quaternaries and by adjusting the undercut volume. To find an optimal underetch the etch time was varied and the growth morphology (profile) was investigated by SEM and the stylus profilometer Dektak.

Figure 4.19 and Figure 4.11 (b) present the examples of the BJR interface in the [011] direction for the situation of underetching (Figure 4.11 (b)) and overetching (Figure 4.19 (a)) resulting in material piling of 600 nm and – 350 nm, respectively. Figure 4.19 (b) shows the result of the BJR process carried out without etching of the InP buffer layer (see Figure 4.15).

Figure 4.19 (b) and (c) display the optimized butt-coupled interfaces between the QW SOA and QD SOA and MQW EAM in the [011] direction. To enhance the contract the samples were stain etched with 1 H_2SO_4 : 8 H_2O_2 : 80 H_2O. The surface non-planarity for both epi-structures was measured to be below 100 nm. No voids for large overhangs above 0.8 µm in depth (Figure 4.19 (d) Inset) were observed. Consistently with the InP/InGaAs test regrowth, the resulting EAM profile is bending up by ~ 500 nm at the interface with drastic reduction of the QWs and cladding layer thicknesses. It was also notices that this shallow piling can disappear after the third epitaxial growth thanks to the redistribution of excess material during the annealing step (for example see Figure 4.24).

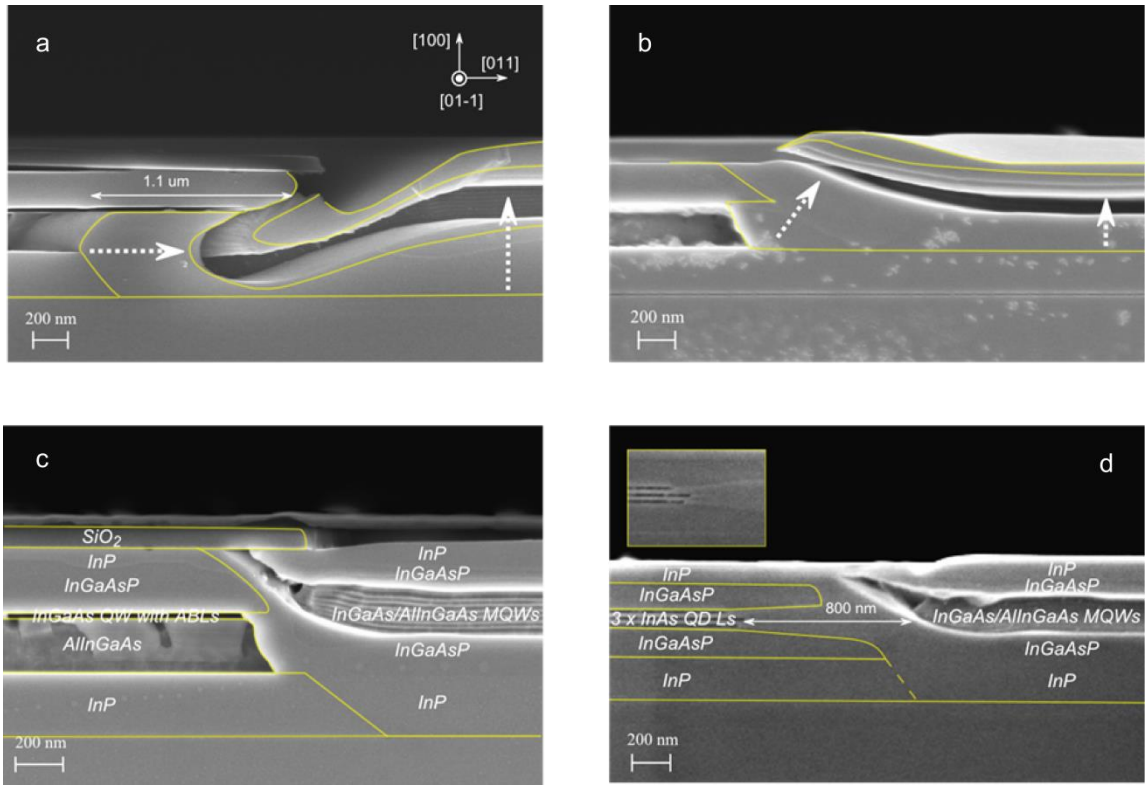

Figure 4.19: SEM images of cross-sections of a single QW SOA mesa block etched for regrowth (a) and BJR interfaces between the single QW SOA (b) and 3 layer QD SOA (c) with MQW EAM.

4.2.5 Optical Properties

The optical properties of the integrated material were evaluated for the QW SOA and MQW EAM structure at room temperature by confocal μ-PL spectroscopy with a ~ 1.5 μm detection spot size (×100 microscope objective lens with NA=0.9) using a 980 nm CW laser diode for excitation and cryogenically cooled InGaAs detector to collect the signal. The detailed setup description can be found in [256].

The μ-PL spectral map of the integrated QW SOA and EAM structure (see SEM image in Figure 4.19 (c)) is presented in Figure 4.20 (a). The spectra labeled SOA and EAM show the reference PL signal taken at points a few tens of microns away from the mask edge, where the mask proximity effects can be neglected. The emission from the as-grown SOA section exhibits abrupt intensity cutoff at the interface. The PL peaks centered at ~ 1475 nm are broadened towards shorter wavelengths due to the high carrier density within the 3.4 nm QW at high optical excitation (3 mW). For comparison, the left diagram (labeled "SOA Low PEx") shows the SOA spectrum at a lower excitation power (0.14 mW), resulting in a peak position at 1485 nm. The lasing wavelength from a 4 mm edge-emitting laser made from this material was measured as 1535 nm, which is due to fast band filling in such a narrow QW and low output losses. The MQW EAM PL peak intensity grows smoothly and reaches its half-maximum value at 1 μm away from the interface, as depicted in Figure 4.20 (b). In total, the peak wavelength blue-shifts by approximately 30 nm (17 meV) with respect to the reference level. The shift is induced by the complex change in the composition and width of QWs and barriers, schematically represented in Figure 4.21 for points labeled in Figure 4.20 (a). The magnitude of the changes was evaluated from the STEM results shown in Figure 4.17. However, due to modulations both laterally and in the QW stack, a rough quantitative estimation is provided.

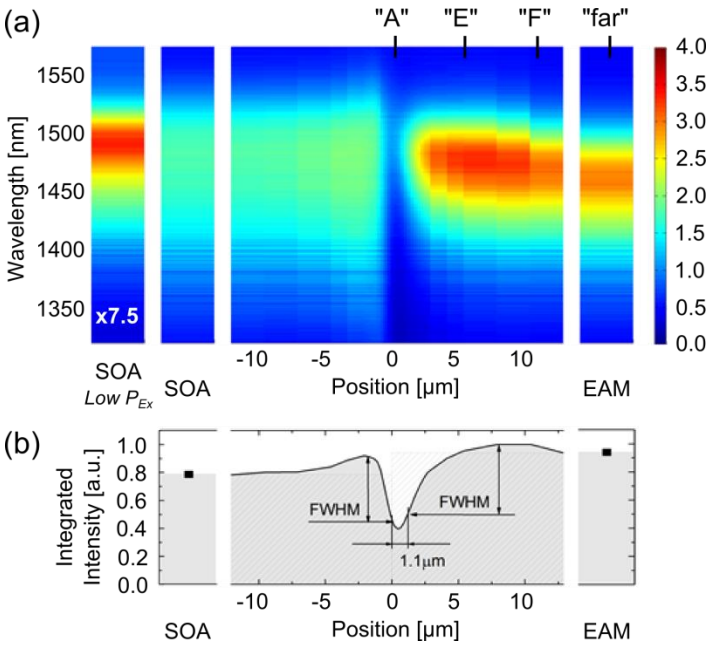

Figure 4.20: (a) Color map of RT μ-PL spectra of the QW SOA and EAM acquired along the [011] direction and (b) the corresponding profile of the PL intensity integrated over energy.

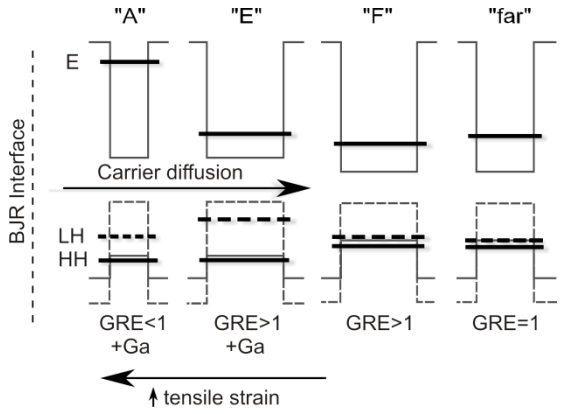

Figure 4.21: Schematic of a QW energy band structure illustrating BJR-induced changes expected in the MQW material. The solid and dashed lines represent the light hole (LH) and heavy hole (HH) ground state positions, respectively. The letters refer to those marked in Figure 4.17 and Figure 4.20.

The slow reduction of the PL peak wavelength by 15 nm (8.5 meV) over a few tens of microns (Figure 4.21 "F" – "far") is in agreement with a growth rate enhancement of about 1.15. The composition change, as determined by EDS, is negligibly small in this range. Approaching the mask, the PL peak wavelength increases faster accompanied by moderate broadening for longer wavelengths. At the same time, according to the EDS data, the Ga content increases, which will have the opposite effect on the bandgap shift. When the Ga fraction in the QW increases, the strain and, therefore, the separation between light and heavy holes (LH and HH) states become larger as schematically shown in Figure 4.21 ("E" – "F"). The contribution of the electron - light hole pair recombination becomes more pronounced, which can lead to the PL red-shift and broadening. Assuming the tensile strain of about 1% (+4% of Ga with respect to the nominal composition) in combination with the quantum confinement effect results in the energy separation of less than 25 meV which is in agreement with experimental data in [257].

In the range of approximately 500 nm from the interface (marker "A" in Figure 4.17, Figure 4.20 and Figure 4.21), growth of InGaAs is drastically reduced due to surface faceting, as mentioned before, and the QW energy level separation is higher. Driven by the bandgap variation, the carriers move toward the narrow-bandgap material thereby lowering their energy; the migration length of a few microns can be assumed. Thus, the PL intensity can be suppressed due to the carrier out-diffusion from the excitation area, while the integrated power in the region adjacent to the interface is higher, as shown in Figure 4.20 (b). The fraction of carriers lost estimated from the integrated intensity is around 30%.

Another important effect causing carrier losses at the interface is nonradiative recombination on the deep-level recombination centers due to crystal defects. An impact of the defect on the device performance was estimated by measuring of leakage current through the integrated devices. The results will be provided in Chapter 5.2 along with an evaluation of the induced internal reflection and coupling losses.

4.3 Device Fabrication

The MLL devices were fabricated on the grown wafers using the cleanroom facilities available at DTU DANCHIP. A standard for ridge waveguide lasers process sequence was used for the fabrication including extra steps to create an electrical isolation between multiple sections. The MLL mask layout and a top view 3D optical interference image of the fabricated device are shown in Figure 4.22. A schematic of the main process steps is presented in Figure 4.23.

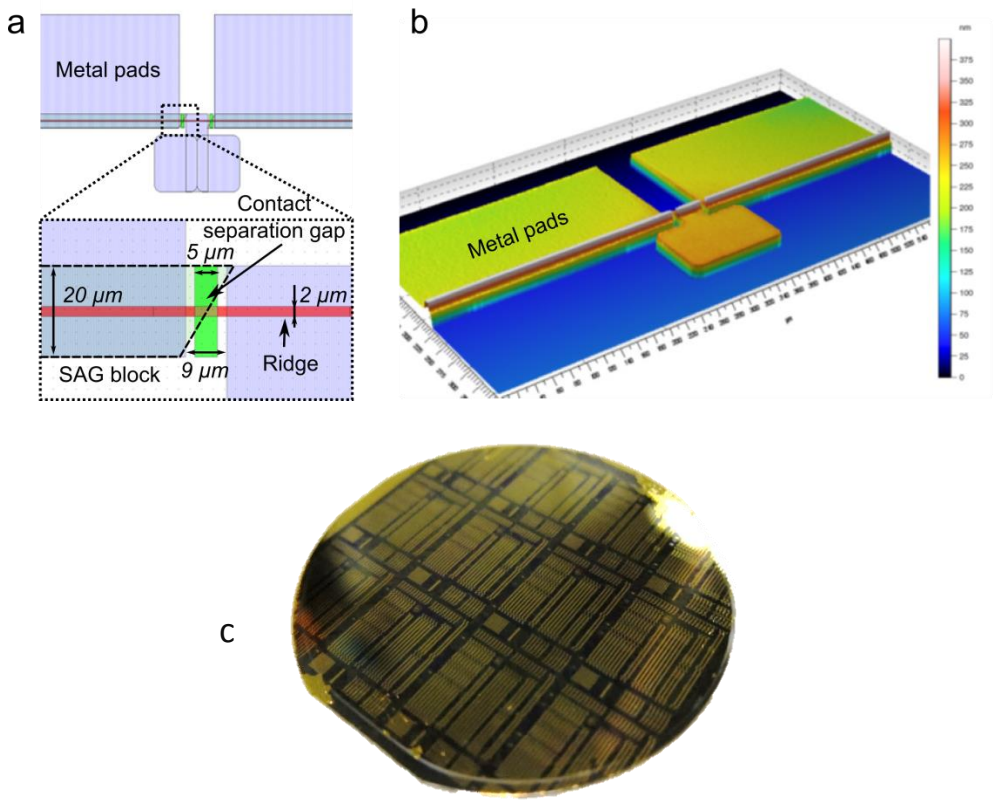

Figure 4.22: (a) MLL mask layout, (b) corresponding top-view 3D optical interference image of a final device and (c) processed 2 inch wafer before cleaving.

The process included four UV (365 nm) photolithography steps, which were employed for definition of SAG mesa blocks, ridge waveguides, contact separation gaps for electrical isolation between laser sections, and p-side contact pads (Figure 4.22). The mask layout was consisted of patterns for MLLs, Fabri-Perot lasers and various multi-contact devices devoted for characterization of material properties (will be shown together with measurement results). The patterns were transferred to SiO_2 layer by CHF_3/O_2 RIE that improves pattern definition.

Both wet and dry etching methods were considered for etching of a ridge waveguide. Low-loss devices were fabricated using wet etching because of the ridge sidewall and surface roughness are negligible in this case, compared to dry etched ridges (see Figure 4.24). This helps to escape light scattering and excessive propagation losses, which can be significant due to the proximity of the waveguide layers to the surface in the design. However, the dry etching method is more powerful in terms of realization of more advanced devices, where dimensional control is essential (e.g. distributed Bragg gratings or deeply etched waveguides with an improved optical confinement, etc.). Secondly, it allows for better electrical isolation between sections, which was performed by etching through the highly doped contact layers in 5 μm[8] wide separation gaps. The measured resistance was ~ 6 kOhm in case of wet etching (only the contact layers could be removed) and 10 - 20 kOhm for dry etching with respect to the etch depth of the InP top cladding. Benzocyclobutene (BCB) was utilized for planarization. Positive and negative tone resists were used in the lift-off process. Metallization was done through electron-beam evaporation. An alternative electroplating process was tested. The detailed description of each step can be found in Appendix B.2.

[8] Nominal value. In case of isotropic wet etching of the contact layers, the resulting gap was few times larger due to mask underetching.

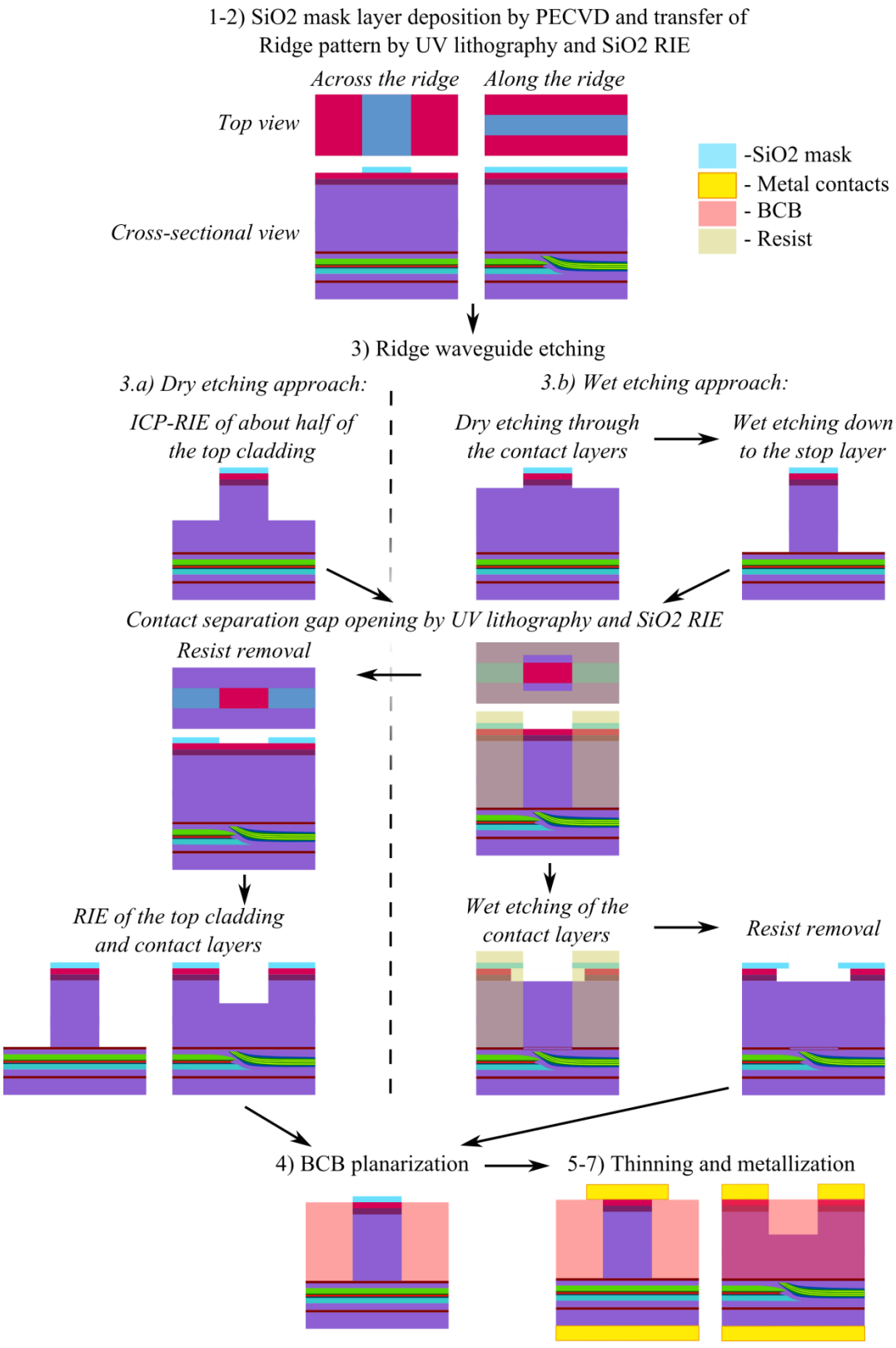

Figure 4.23: Schematic of MLLs processing. The colour scheme is the one defined in Figure 4.12. Step numbers are referring to the described in Appendix B.2.

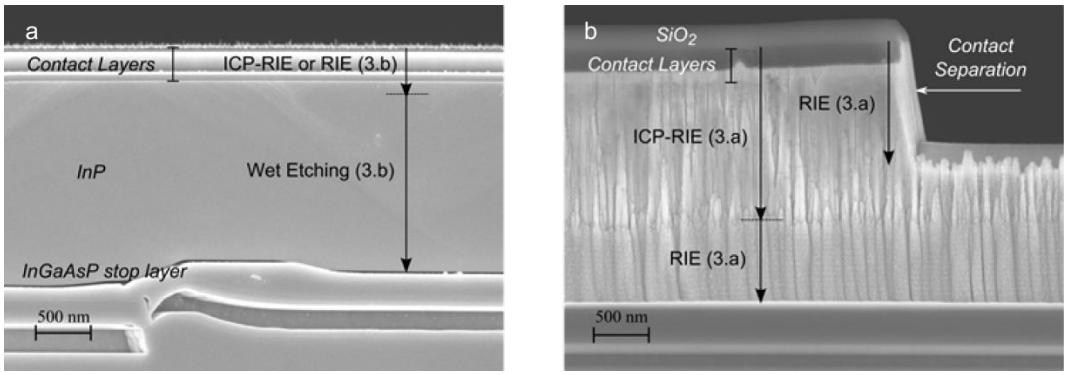

Figure 4.24: SEM images of sidewalls of wet-etched (a) and dry-etched (b) ridges oriented along the [011] direction.

When processing a wafer consisting of BJR structures, several issues concerning the surface flatness must be considering. First, contact UV lithography on a non-planar surface may cause deformation of the pattern been transferred and degradation of sidewall quality. The minimal feature size in the MLL processing was 1.9 μm on the ridge waveguide pattern (for the dry-etching case), which was defined on top of the cladding layers. Owing to the planarization properties of InP, the surface flatness can be improve, e.g. as seen in Figure 4.24 (a), for the BJR piling up to 250 nm when growing 2 μm thick InP cladding layer on top.

Another possible problem is related to sustainability of the etch stop layer on the BJR interface against dry etching. The growth rate of the stop layer (nominally 20 nm thin AlInAs) can be reduced on an arching BJR surface, and thus, can be unintentionally overetched during the second RIE step. This situation is shown in Figure 4.25, where local defects at the BJR interface were revealed by a cross-section SEM imaging. These defect at the interface increase optical losses and light scattering, and thus must be avoided. To prevent defect formation, the growth of top cladding layers can be performed after planarization by InP thick buffer layer followed by in-situ etching back in presence of CBr4, schematically presented in Figure 4.25. Thus, the depth of burial of the waveguide layers is kept at the designed level. Precise etch depth control is feasible using emissivity corrected pyrometry

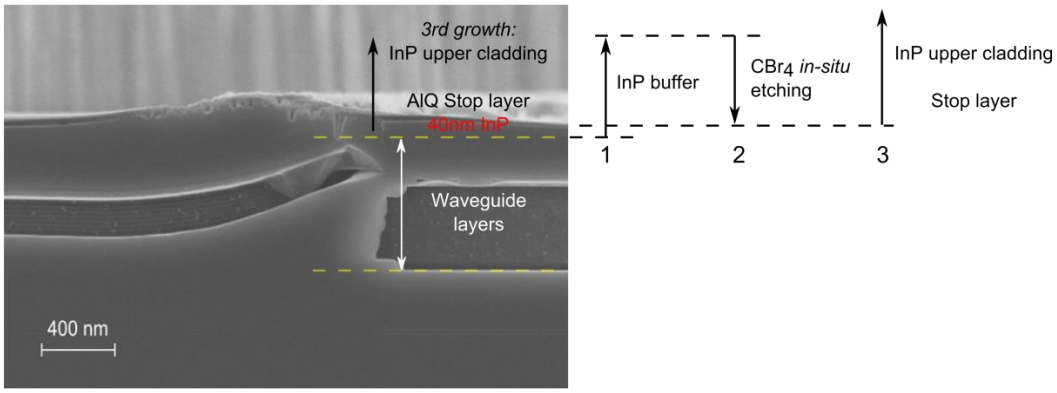

Figure 4.25: Cross-sectional SEM image of a BJR interface after dry etching of the ridge waveguide.

[258] and moderate etch rates[9]. In case of wet etching, this is not critical due to the larger selectivity of wet etching of InP over InGaAsP used as a stop layer.

In addition to the surface defects, the insertion losses can arise from sidewall roughness of the mesa etched for regrowth, and therefore material imperfections at the BJR interface. Figure 4.26 illustrates transferring of the roughness from the glass mask etched by RIE and its deterioration during chlorine-based ICP-RIE etching (see Appendix B.2.1). Following wet etching and annealing smooth the sidewalls, however, significant corrugation was observed. An improvement can be achieved by using wet etching for the mask definition and optimization of the ICP-RIE process.

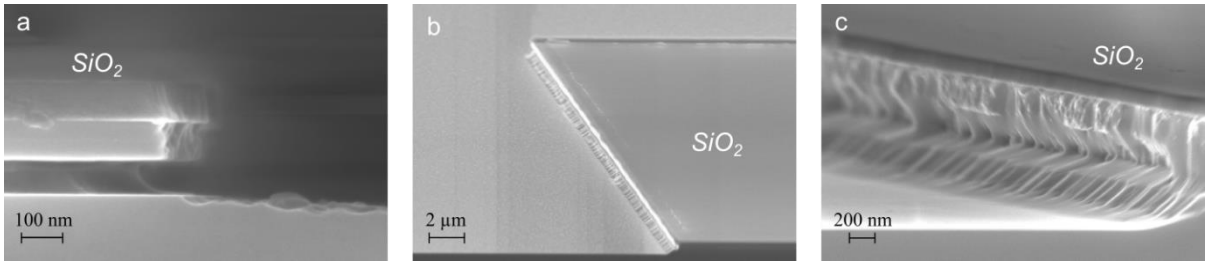

Figure 4.26: Mesa sidewall roughness after (a) ICP-RIE, (b) wet etching and (c) after in-situ cleaning.

4.4 Summary

In this chapter, MOVPE epitaxial growth, integration of the designed SOA and EAM structures based on InP/AlInGaAs/InGaAsP platform and fabrication of monolithic two-section MLLs are described. An overview of the MOVPE process is presented explaining the choice of the used growth parameters. It is shown, that the growth condition of self-assembled QD formation for emission at 1.55 µm are beyond the optimal ones. A small lattice mismatch inherent for InAs/InP material system of 3% comparing to 7% for InAs/GaAs system results in big volume QDs and a shift of the energy gap to the longer wavelengths above 1.6 µm. In order to reduce the sizes and achieved the desired wavelength range, GaAs capped InAs QDs in the InGaAsP matrix were grown. The investigation showed shallow lens-shaped QDs. As a result, the "shallow" QD behavior is expected for this material. The other possibilities of QD growth in InP and AlGaInAs matrix are proposed. The first results demonstrate an improved aspect ratio, and a higher energy level separation is theoretically predicted, which makes these QDs a promising candidate for low noise MLLs.

The MOVPE BJR technique is introduced for integration of the SOA and EAM sections. The major factors affecting the growth evolution on partially masked and non-planar substrates are summarized followed by the detailed description of the carried out BJR process optimization. The material piling at the mask edge was impaired using two effects: mask underetching to compensate the excess material, and growth rate suppression of quaternaries on high-index planes close to {111}. Planar BJR integration of the symmetric waveguide core QD SOA and asymmetric QW SOAs with the MQW EAM is demonstrated. The analysis of the influence of the growth morphology, thickness and compositional variation associated with BJR process on the optical quality of MQW EAM revealed an increase in the energy bandgap directly at the interface resulting from the combined effect of growth rate suppression and higher Ga concentration. This increase in bandgap energy makes the

[9] The measured rate was about 10 nm/min for InP at the growth pressure and temperature of 60 Torr and 610ºC; CBr4 flow: 116 sccm, PH3 flow: 200 sccm.

interface partially transparent (thus beneficial for unaffected light transmission) and forces carriers away from possible interfacial defects. The regrown MQW material exhibits a small bandgap blue-shift of less than 20 meV over tens of microns from the regrowth interface, which allows for the realization of a short efficient EAM section.

Finally, the device processing is outlined. The main issues, which were faced during the fabrication and affect the device performance are illustrated, such as ridge sidewall roughness, surface and interfacial defects and imperfections related to the BJR integration.

Chapter 5

Material Characterization and Laser Performance

This chapter is devoted to the static characterization of designed and fabricated QW and QD amplifier and absorber active materials for monolithic MLLs. First, the measurements of modal gain and absorption spectra are presented and discussed along with power-current-voltage and temperature performance of Fabry-Perot (FP) lasers based on the gain materials. The extracted data on the gain and absorption parameters are analyzed with respect to the MLL conditions described in Chapter 2 for the realization of 10 GHz and 40 GHz MLLs. Second, the properties of the integrated material, such as interfacial losses and reflectivity on the BJR interface are quantified to validate the applicability of the BJR technique for integrated MLLs. Next, examples of the performance of 10 GHz MLLs consisting of integrated ABL QW SOA and MQW EAM are presented.

All devices used for the test measurements, FP lasers and MLLs consisting of one type of integrated epitaxial material were processes on a single wafer according to Section 4.3, cleaved and soldered epi-side up onto AlN substrates using AuSn soldering for efficient heat dissipation. The output facet was AR(5%)/HR(95%) coated if specified.

5.1 Static Material Properties

5.1.1 Modal Gain and Absorption Measurements

Segmented Contact Method

Evaluation of the gain and loss coefficients was performed using the Segmented Contact Method (SCM), which is based on measuring single pass amplified spontaneous emission (ASE) spectra from a multi-segment device illustrated in Figure 5.1 [259], [260]. The ASE intensity is related to the light transmission length *x* as

$$I(\lambda, x) = \frac{I_{sp}(\lambda)}{G_{net}(\lambda)}\left(e^{xG_{net}(\lambda)} - 1\right), \tag{5.1}$$

where $I_S(\lambda)$ is the intensity of the spontaneous emission at given wavelength λ, G_{net} is the *net* modal gain. When a different number of sections is pumped at fixed driving conditions, the ratio of the measured ASE intensity is proportional to the *net* modal gain. In case of the basic three-section measurement scheme illustrated in Figure 5.1 (a), where each section of the device is *L* long, the

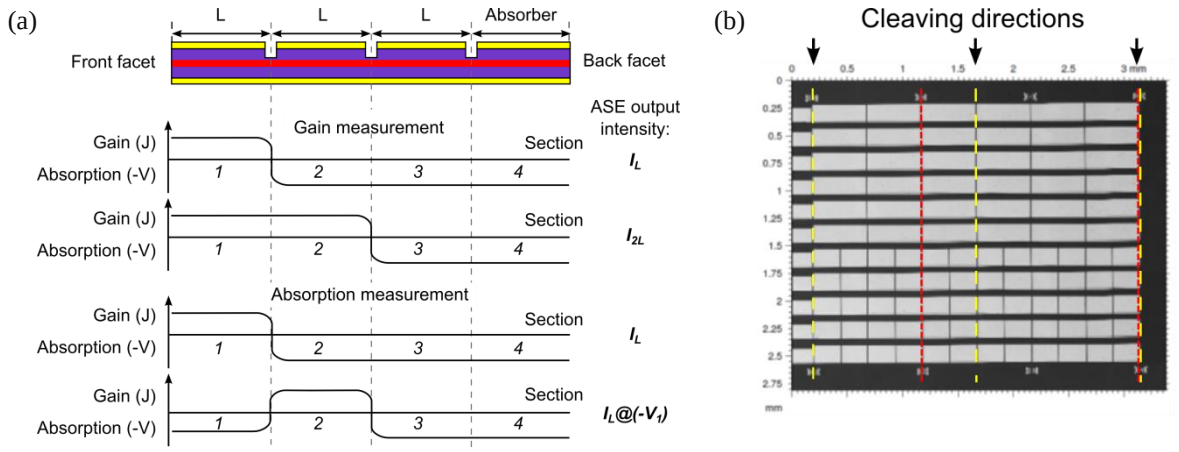

Figure 5.1: (a) A schematic of a multi-segmented contact device and scenarios of the gain and absorption measurements for the 3-section scheme. See the text for the experimental details. (b) a top-view photograph of the processed multi-segmented devices (the cleaving directions for 3-section (yellow lines) and 4 section (red lines) device bars are shown).

net modal gain G_{net} can be derived as following

$$G_{net} = \frac{1}{L}\left[\ln\left(\frac{I_{2L}}{I_L} - 1\right)\right] = \Gamma g + \alpha_i \tag{5.2}$$

where g is the material gain, I_L and I_{2L} are the ASE intensity acquired for one section (L) and two section ($2L$), respectively. The background optical losses α_i caused e.g. by light scattering on waveguide imperfections from lithography and etching, can be obtained from the long-wavelength range below the energy bandgap. To avoid multi-pass amplification, the reflection from an output facet has to be eliminated, which can be achieved by making the rear section(s) absorbing under reverse biasing. The high electrical isolation between adjusted sections is necessary to minimize current spreading and gain distribution along the device which can lead to disputable results [261].

In order to obtain the *net* modal absorption coefficient α_{net}, the second section is used as a source of ASE of the intensity $I_{L,2}$ equal to I_L, while the first (front) section was reverse biased (V_1) and absorbed the light resulting in the output intensity $I_{L,1}$ (see Figure 5.1 (a)). The relative ASE spectral attenuation gives the *net* modal absorption

$$\alpha_{net} = \frac{1}{L}\left[\ln\left(\frac{I_{L,2}@(-V_1)}{I_{L,1}}\right)\right] = \Gamma\alpha + \alpha_i \tag{5.3}$$

The more advanced four-section schemes with three independently controlled sections can be employed which allows to eliminate a background component associated with unguided spontaneous emission, and therefore improve the measurement accuracy as described in [262].

SCM devices and setup description

The multi-segmented devices used for measurements were fabricated as 2 µm wide ridge waveguide devices consisted of either SOA or EAM active region. Individual sections with a length 250 or 500 µm each were electrically separated by etching separation gaps through the contact layers. The resulting resistance between the sections was measured to be 10 - 20 kOhm in case of dry etching

and ~ 6 kOhm for wet etching approach. The fabricated structures were cleaved into bars with 3- and 4- segmented devices shown by yellow and red lines in Figure 5.1 (b). No facet coatings were deposited.

The experimental setup is presented in Figure 5.2. The devices were mounded onto copper heatsinks equipped with a Peltier element for temperature control (TC). Each section of the device was independently biased using a bipolar power supply (Hirex Engineering BE510) through the set of four sense-force probe pairs shown in Figure 5.2 (c). The ASE emitted from the device was collected through the integrated optical head shown in Figure 5.2 (b) consisting of collimating high NA objective followed by a polarizing beam-splitting cube (PBS) used for independent measurements of the TE and TM components simultaneously (an extinction ratio for the transmitted beam was > 30 dB and for the reflected 20 dB). The polarized beams were guided to two arms lens-coupled into fibers.

To filter undesirable leaking modes of opposite polarization and suppress parasitic reflection, an optical isolator and a linear polarizer were incorporated along the light path. The ASE spectra and power were recorded by an optical spectrum analyzer (OSA) (Ando AQ6317) and a power meter (HP 8153A) used for convenience of alignment. Since the OSA sensitivity is specified down to -90 dB in the range of 1.20 – 1.65 μm [263], the accuracy was limited already above 1.60 μm due to noisy low-intensity ASE spectra.

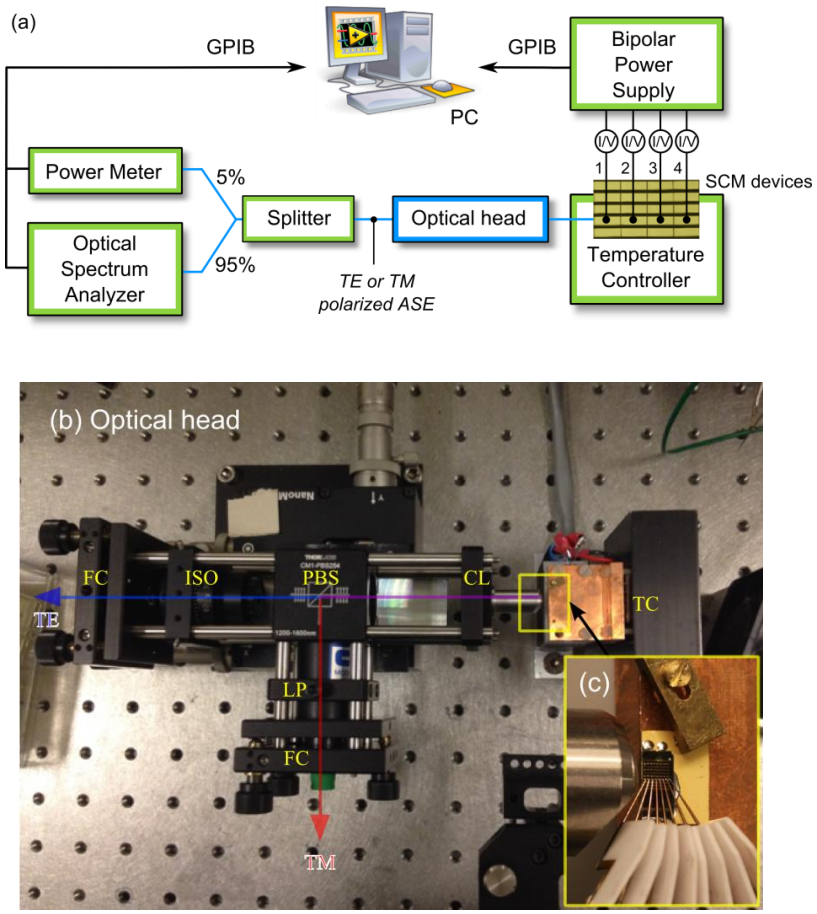

Figure 5.2: (a) Experimental setup for the SCM measurements independently for TE and TM polarizations. (b) Optical head with (c) devices mounted on a probe stage. PBS - polarizing beam splitter, CL - collimating lens, FC - fiber coupler, ISO – isolator, LP - linear polarizer, GPIB - general purpose interface bus.

Due to a high sensitivity of beam alignment in the lens-coupled optical system to a temperature drift occurring during the switching between amplified sections and the slow-response TC, the four section segmented method, in spite of the considered advantageous [262], showed stronger intensity deviation and therefore larger error compared to the three section SCM used thereafter. Additionally, the interruptions between each measurement were added to ensure that the device has achieved its thermal equilibrium. Furthermore, a pulsed current source can be utilized to minimize the influence of heating.

5.1.2 Quantum Well Amplifier

Gain and absorption spectra: c-QW and ABL QW SOAs

Figure 5.3 shows the net modal gain and absorption spectra for 6.5 nm wide InGaAsP-based c-QW (-1.02% str.) and 3 nm InGaAs ABL QW (-1.47% str.) SOAs extracted using the SCM method at room temperature (RT) under different biasing conditions. The corresponding energy band diagrams can be found in Chapter 3, Figure 3.7, and the detailed epitaxial structures in Appendix A1, A2. Due to the compressive strain, the emission was associated with electron – heavy hole (e-HH) transitions releasing in-plane TE polarized light. Thereby, the measurements were done for the dominant transverse electric (TE) polarization.

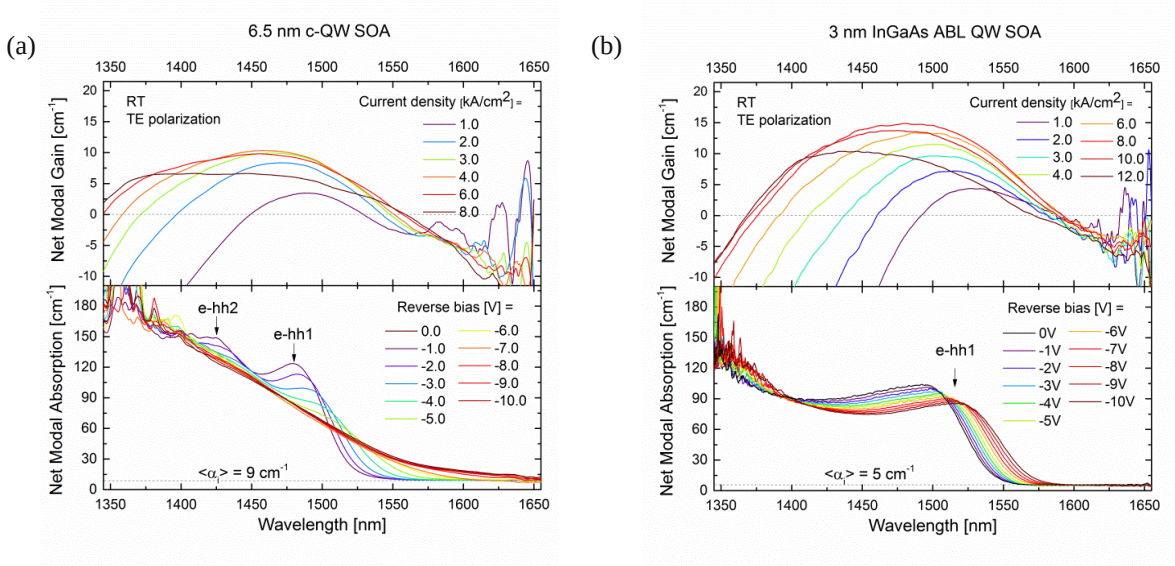

Figure 5.3: RT net modal gain (top) and absorption spectra (bottom) for (a) 6.5 nm wide InGaAsP-based c-QW SOA and (b) 3 nm InGaAs ABL SOAs obtained for different bias conditions using 3 section SCM measurements.

The maximum *net* modal gain for 6.5 nm c-QW and 3 nm ABL QW was measured to be 10.3 cm^{-1} at 4 kA/cm^2 and 14.7 cm^{-1} at 8 kA/cm^2, respectively. The peak gain shift with increasing current density of about ~ 50 nm towards the shorter wavelength and the spectral broadening were observed due to the band filling effect. The internal losses of -9 cm^{-1} and -5 cm^{-1} for c-QW and ABL QW were extracted from the absorption spectra. Due to the highly noisy gain spectra above 1.6 µm, it was difficult to resolve the exact internal losses, however the growth of the losses with carrier injection was revealed after data analysis. A rough estimate gives an increase from 5 to 6.5 cm^{-1} in the range from 1 to 12 kA/cm^2 for ABL QW which is attributed to carrier density dependent FCA (see also in Figure 5.8 for QD SOA). The high internal optical losses for these devices are related to light

scattering on the narrow ridge waveguide sidewalls and surface imperfections resulting from the non-optimized dry etching process used for the fabrication (see the ridge sidewall view in Figure 4.24 (b)). Another origin is high FCA in the adjacent to the QW layers due to the high p-doping level in the adjacent p-cladding layer. Using wet etching and an optimized doping level taking into account strong Zn diffusion as described in Section 3.3, the internal losses were reduced to 2 - 2.5 cm^{-1}.

Taking into account the internal losses, the modal gain was found to be higher for the wider c-QW at lower carrier densities (12.4 vs 9.4 cm^{-1} at 1 kA/cm^2) due to the larger confinement factor. However, a significant increase in injection current results in many-body and heating effects recognized as gain suppression at current densities > 6 kA/cm^2 and > 10 kA/cm^2 for the c-QW and ABL QW, respectively. The fast saturation for the gain coefficient of c-QW SOA gives evidence of poor electron confinement provided by the PQ barriers.

The absorption spectra shown in Figure 5.3 illustrate the difference in energy level structure between the two types of QWs in agreement with the simulation results provided in Chapter 3.2. The contribution of the multiple hole states is clearly seen as two exciton peaks in the c-QW absorption spectrum in Figure 5.3 (a, bottom), while the ABL QW shows a single peak and nearly constant absorption over the wide energy range. Both QWs exhibit QCSE identified by a blue-shift of the exciton peak and a reduction of the absorption coefficient at the band edge with increasing a reverse bias. The c-QW SOA showed a larger absorption shift per voltage in the range from 0 to -6 V which is inherent for wider QWs, and fast saturation at biasing above -6 V when the exciton states disappear. The latter can be explained by coupling of the electron state to the continuum due to the low potential barrier for electrons (< 100 meV for the GS).

ABL QW vs c-QW Fabry-Perot laser characteristics

Since the material properties directly affect device performance, the steady state investigation of ridge waveguide Fabry-Perot (FP) lasers was performed. The conventional temperature dependent light output – current – voltage (L-I-V-T) characteristics were measured to evaluate and compare the basic parameters of the designed SOA material by means of efficiency and temperature stability.

The measurements were carried out using a setup presented in Figure 5.4. The devices were mounted onto a TC copper stage (Temperature Controller Wavelength Electronics LFI-3751) and driven under CW current conditions by a bias source (MG 06 DLD 103). The TC and bias source allow to vary the temperature up to 70°C; the current was limited to 400 mA. The emitted optical power was measured using an integration sphere with an optical power meter (MG 13 PDC 001). To record an optical spectrum, the output light was lens-coupled into a single mode fiber (SMF) and delivered to an OSA (Ando AQ6317).

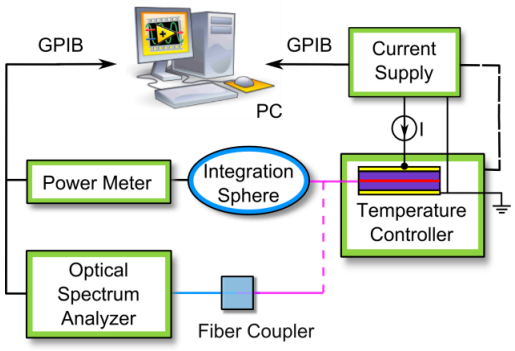

Figure 5.4: Experimental setup for characterization of Fabry-Perot lasers.

Figure 5.5 shows the L-I-V-T curves measured for 4 mm long uncoated 2 µm wide ridge FP lasers based on (a) c-QW SOA and (b), (c) ABL QW SOAs. The measured RT threshold current for c-QW and ABL QW FP laser was 57.8 mA (Figure 5.5 (a)) and 63.8 mA (Figure 5.5 (b)), correspondingly, due to the high internal losses. The laser in Figure 5.5 (c) had a reduced internal optical losses by factor of two as discussed above, which resulted in decreasing the threshold current down to 29.5 mA. A maximum optical power of 48.8 mW per facet was reached at RT for the ABL QW laser at 400 mA compared to 20.4 mW for c-QW SOA without achieving the thermal roll-over. This corresponds to the slope of approximately 0.31 W/A and 0.14 W/A, respectively. The series resistance above threshold was measured to be around 2.5 - 3 Ohm for both devices.

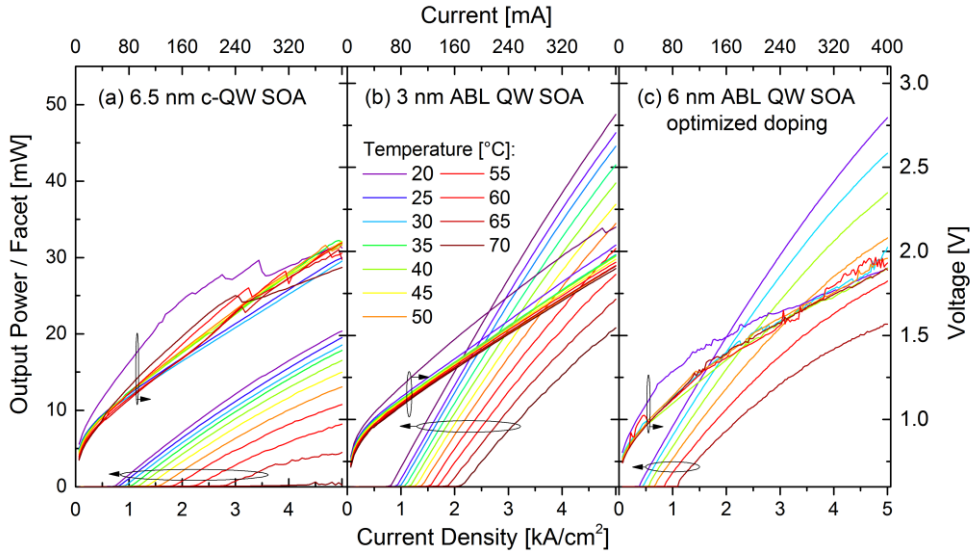

Figure 5.5: L-I-V-T characteristics of the 4 mm long uncoated FP QW lasers consisting of (a) conventional InGaAsP-based c-QW SOA and (b) InGaAs(P)/InAlAs/InP asymmetric barrier layers QW SOA with asymmetric InGaAsP/InAlGaAs waveguides before and (c) after p-doping optimization.

The effect of the ABL structure can be estimated through the laser internal quantum efficiency η_i, which accounts the injection efficiency η_{inj} affected by the vertical leakage, lateral current spreading η_s, and the differential radiative efficiency η_{rad}:

$$\eta_i = \eta_s \eta_{inj} \eta_{rad} \,. \tag{5.4}$$

The internal efficiency η_i can be extracted from L-I curves above threshold, where the output power P_{opt} is ideally linearly proportional to the injection current I:

$$P_{opt} = \eta_d \frac{h\nu}{e}(I - I_{th}), \qquad I > I_{th}, \tag{5.5}$$

where $\eta_d = \eta_{opt} \cdot \eta_i$ is the external differential quantum efficiency, and η_{opt} is the optical efficiency representing the fraction of the light which is not collected as a useful power due to the internal losses:

$$\eta_{opt} = \frac{a_{mir}}{a_i + a_{mir}} \,. \tag{5.6}$$

The external η_d and internal η_i differential efficiency was found to be approximately 38% and 92% for 3 nm ABL QW FP at RT and 25% and 60% at 70 ºC (at $I \sim 3 \times I_{th}$). For the c-QW the resulted values were much lower, ~ 17% and 46% at RT, respectively. The slightly reduced internal efficiency of 71% for a wider and less strained 6 nm ABL QW was obtained (Figure 5.5 (c)), which can be attributed to more efficient Auger recombination for the 6 nm QW compared to 3 nm QW. This leads to the conclusion that the Auger recombination rate does not increase for sufficiently narrow QWs, which was disputed in Chapter 3.2.

The overall significant improvements in the ABL QW SOA efficiency is attributed to the enhancement of the carrier confinement, and hence, the injection efficiency, since the carrier blocking layers prevent barrier overflow at high current densities as well as at high operation temperatures. The temperature stability is usually estimated through the temperature dependence of the threshold current density J_{th} expressed as

$$J_{th}(T) = J_{th,0} \exp\left(\frac{T}{T_0}\right), \tag{5.7}$$

where T_0 is the characteristic temperature. Figure 5.6 shows a comparison of the characteristic temperature for c-QW and ABL QW SOAs in the range from 20 to 70 °C calculated as [264]

$$T_0(T) = \frac{2\Delta T}{\ln J_{th}(T + \Delta T) - \ln J_{th}(T - \Delta T)}. \tag{5.8}$$

Larger T_0 values above 45 K at elevated temperatures up to 70°C for the ABL QW FP lasers compared to the c-QW counterparts (~ 22 K at 70°C) proves the concept of ABL structure providing better carrier confinement. The weak temperature dependence is also a sign of smaller parasitic (mainly Auger) recombination outside the active layers and in the ABL QW SOA. Moreover, a smaller increase in optical losses (i.e. threshold gain) with temperature associated with IVBA accompanied by carrier overflow can further improve the temperature stability [265] and results in a better differential efficiency as demonstrated above.

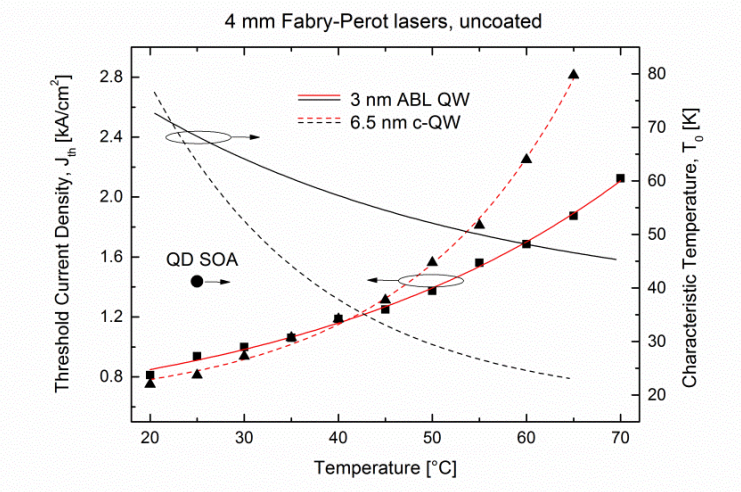

Figure 5.6: Temperature dependence of the threshold current density (black curves) and characteristic temperature (red curves) for 4 mm FP lasers based on ABL QW (solid lines) and c-QW (dashed lines) extracted from the data in Figure 5.5. The characteristic temperature of the QD SOA (dot) was estimated for 1 mm laser (see L-I-V-T curves in Figure 5.9 (a)).

Larger T_0 values above 45 K at elevated temperatures up to 70°C for the ABL QW FP lasers compared to the c-QW counterparts (~ 22 K at 70°C) proves the concept of ABL structure providing better carrier confinement. The weak temperature dependence is also a sign of smaller parasitic (mainly Auger) recombination outside the active layers and in the ABL QW SOA. Moreover, a smaller increase in optical losses (i.e. threshold gain) with temperature associated with IVBA accompanied by carrier overflow can further improve the temperature stability [265] and results in a better differential efficiency as demonstrated above.

Typical optical spectra under different biasing and temperature conditions are shown in Figure 5.7 obtained for the ABL QW SOA. This carrier-density dependent behavior follows the gain spectra broadening shown in Figure 5.3 (b). However, the central wavelength is nearly constant, which is related to the bandgap narrowing at high injection due to carrier-carrier interaction. A red-shift caused by the many-body effects compensates the blue-shift expected from the band filling. At low internal losses, the band-gap renormalization should be considered to have a larger influence on the spectral shift. With increasing the temperature, the spectrum shifts to the longer wavelength range with an ~ 0.67 nm/°C step, which is consistent with the temperature dependent energy bandgap $E_g(T)$ change [266].

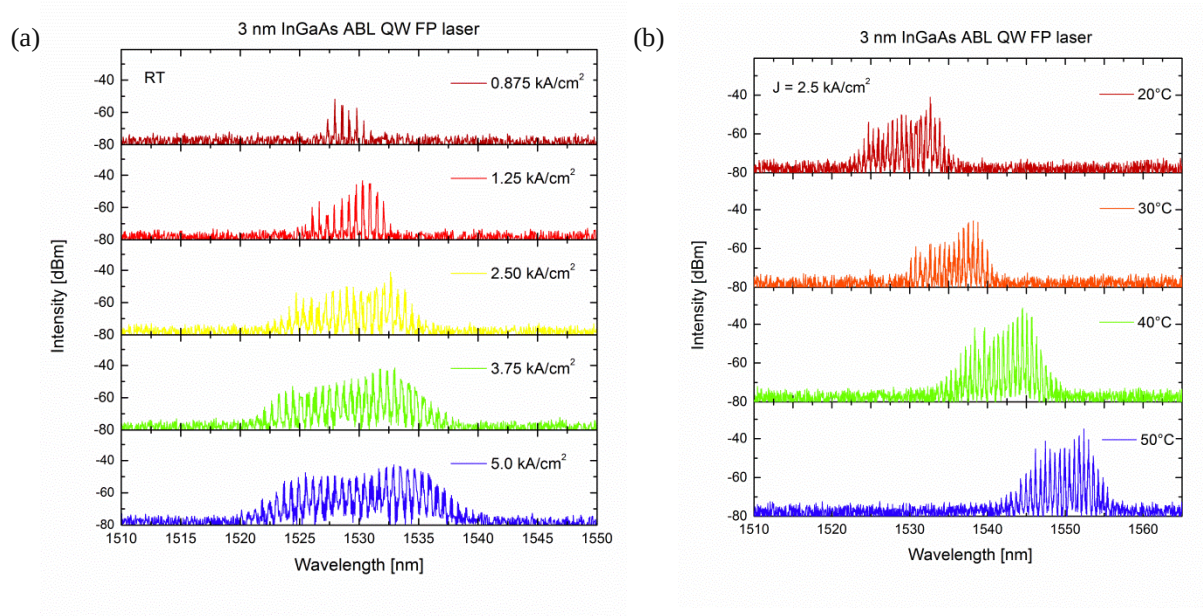

Figure 5.7: Lasing spectra of the 4 mm uncoated 3 nm ABL QW based FP laser corresponding to the L-I-V-T curves in Figure 5.5 (b): (a) at 20 °C as a function of injection current and (b) at J = 2.5 kA/cm² as a function of temperature. Note the spectral modulation here is the result of the chosen OSA resolution/sensitivity settings.

5.1.3 Quantum Dot Amplifier

Gain and Absorption spectra: GaAs capped InAs/InGaAsP/InP QD SOA

Figure 5.8 shows the gain and absorption spectra for the QD SOA consisting of three layers of InAs/InGaAsP/InP QD as described in Chapter 4.1.2 (Appendix A.4). The emission was dominantly TE polarized due to a strong compressive biaxial strain in this type of flat QDs [267].

The observed GS modal gain centered at 1560 nm was found to be in good agreement with the measured PL peak (see in Figure 4.7). The GS *net* modal gain saturates at ~2.5 cm^{-1}, which corresponds to the maximal GS modal gain of ~6 cm^{-1}, taking into account the waveguide losses

estimated to be around -3.5 cm^{-1} at low carrier density. The maximal *net* modal gain of ~10.5 cm^{-1} is supported by exited state (ES) transitions around 1450 nm. An observed significant blue-shift of the gain peak wavelength over 100 nm with increasing carrier density and weakly pronounced GS and ES gain is typically attributed to big and shallow asymmetric QDs (see Figure 2.10). According to [128], the overlap integral between the hole and electron states decreases with the QD base size, which lowers the GS gain. The small separation between GS and ES states in combination with the strong inhomogeneous broadening (PL FWHM ~170 nm (88 meV)) indicates quasi-continuum density of states in the QD ensemble [268]. This leads to smearing of the gain spectrum over energy. For comparison, the pronounced discrete GS and ES gain contribution is typically reported for small InAs/GaAs QDs when the GS – ES energy separation is high (~100 meV) (see e.g. in [60]).

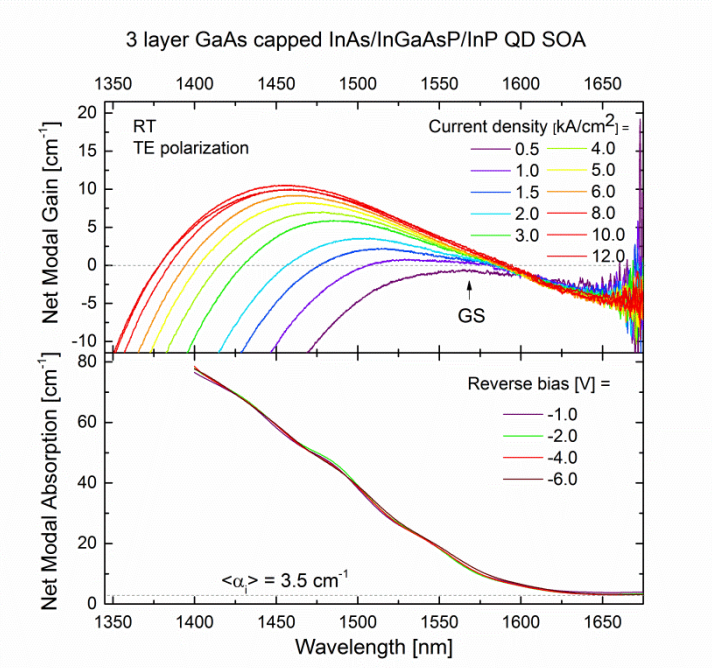

Figure 5.8: RT net modal gain and absorption spectra obtained for QD SOA consisting of three layers of GaAs capped InAs QDs in the InGaAsP matrix.

Similarly, a smooth increase in modal absorption was observed (Figure 5.8 (bottom)). The small height of the examined QDs results in weakly confined electron states (see Figure 4.6 (b)) and its decoupling with applying reverse bias, which eliminates the QCSE shift similar to the case of c-QW absorption at high voltages shown in Figure 5.3 (a, bottom).

QD Fabry-Perot laser characteristics

Due to the low carrier confinement and increasing with carrier density internal losses attributed to FCA, the threshold gain and electro-luminescence from the QD Fabry-Perot laser was achieved in the significantly shorter wavelength range around 1465 nm corresponding to ES emission. The threshold current was ~ 5 kA/cm^2 for a 1 mm device with HR-coated back facet, which is relatively high compare to other long-wavelength QD lasers due to the excessive optical losses (e.g. [131], [215], [269]). Figure 5.9 (b) shows the optical spectra at different applied currents exhibiting irregularities caused by scattering on imperfections (the internal losses was higher for this device ~ 6 cm^{-1}). Among the other, high inhomogeneous broadening can lead to the increased spontaneous emission and carrier losses via Auger recombination if the carrier density is not pinned of above the laser threshold due to non-uniform carrier distribution as claimed in [270]. One of the evidences of a high Auger

recombination rate is a low characteristic temperature of 41 K in the 20 - 30°C range compared to QW lasers as shown in Figure 5.6. Moreover, shallow QDs suffer from increased thermal escape of carriers, which further reduce the internal quantum efficiency evaluated to be below 10% at RT.

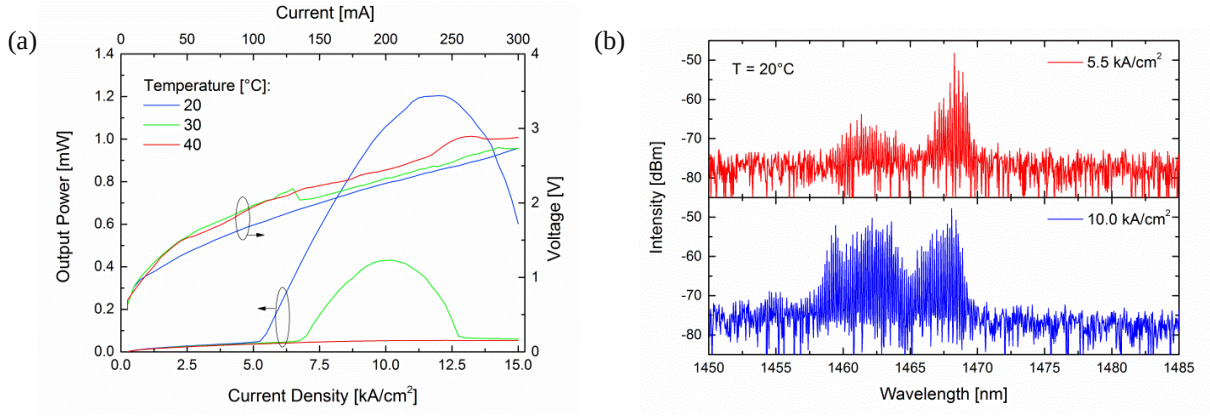

Figure 5.9: (a) L-I-V-T characteristics and (b) the continuous wave lasing spectra for 2 µm wide ridge QD laser (L=1 mm) at 20°C.

Concerning the application the QD SOA in MLLs, the quasi-continuum energy structure of these QDs reduces the maximal modal gain and saturation energy. Furthermore, it influences on the carrier dynamics as discussed in Chapter 2.4. Fast and efficient carrier-carrier recombination is expected to be dominant in the gain recovery process similar to the QW behavior. Moreover, shallow QDs exhibit a poor quantum efficiency, which increases threshold carrier density and as a consequence, spontaneous recombination noise. No mode-locking was achieved using this type of material.

As mentioned in Section 4.1.3, improvements can be done using InAs QD in higher potential barriers, e.g. based on InP or AlGaInAs alloys. Assuming better carrier localization and distance between energy levels, confirmed by theoretical calculations, lasing via the QD GS at the desired wavelength can be obtained with a lower current density and higher saturation energy (see below) leading to noise reduction. The development of this material is currently in progress.

MQW Saturable Absorbers

The absorption characteristics of the MQW EAM saturable absorber based on eight 8.6 nm InGaAs QWs (0.52 % str.) (Appendix A.6) and "long-wavelength" absorber consisting of four 10.6 nm InGaAs QWs active region (Appendix A.7) are presented in Figure 5.10. Since the QWs used in the EAM are tensile-strained, the absorption occurs for both TE and TM polarized light with dominant TM absorption. The SCM setup allows for measurement of TM and TE components independently (see Figure 5.2), however, due to incomplete light splitting offered by the beam splitter, the TE absorption spectra of interest may include a residual TM fraction.

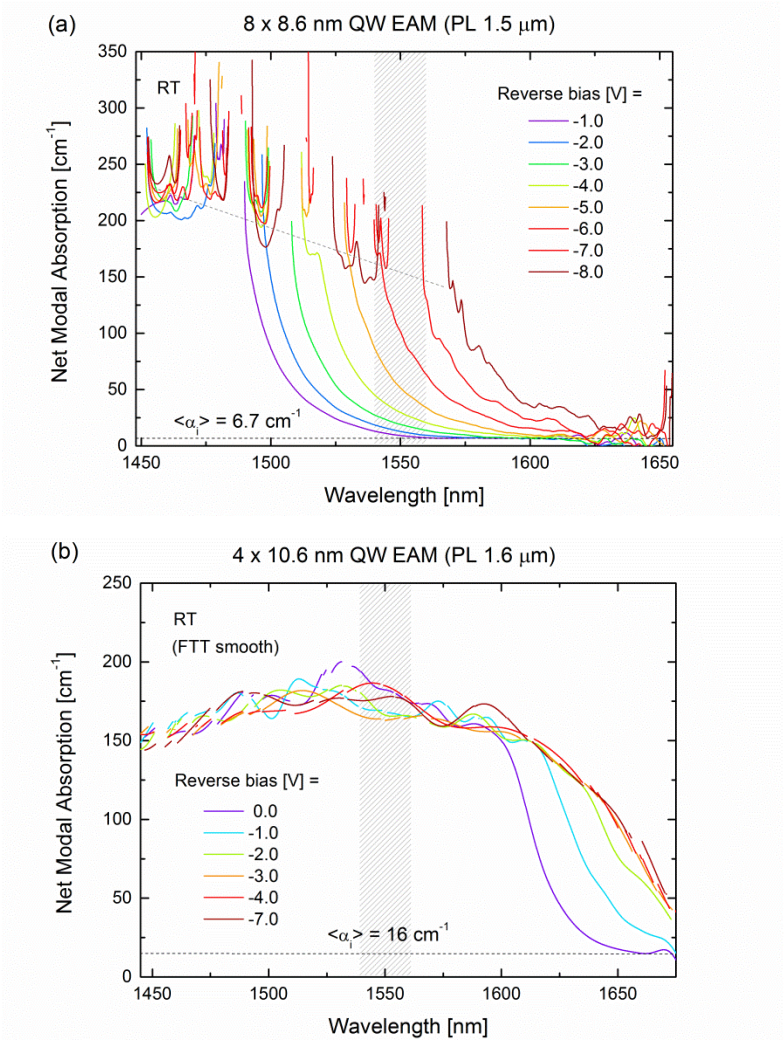

Figure 5.10: Net modal absorption spectra for shallow MQW Saturable Absorbers. (a) QCSE Electroabsorption Modulator based on 8 × InGaAs/AlGaInAs QWs, PL peak ~ 1.5 µm, (b) 4 x InGaAs/AlGaInAs QWs absorber, PL peak ~ 1.6 µm. The grey shaded region shows the designed operation wavelength range.

The absorption coefficient of the MQW EAM increases non-linearly with applied reverse bias in a wide spectral range near the band edge as demonstrated in Figure 5.11. Compared to the single QW and QD active material, which can be used as a saturable absorber in non-integrated monolithic MLLs, larger values of the absorption coefficient change, Shark shift and differential absorption demonstrated in Figure 5.11 offer wider design possibilities by means of laser geometry and operation conditions. More importantly, faster absorption recovery is expected in shallow MQW in the EAM as discussed in Chapter 2.2. On the other hand, due to the screening effect, the absorption edge would experience significant blue-shift. As an example, at 50 cm^{-1} absorption coefficient, the shift is ~ 13 nm/V (V > -3 V), while e.g. for the 3.5 nm QW (Figure 5.3 (b)) the value is 2.2 nm/V.

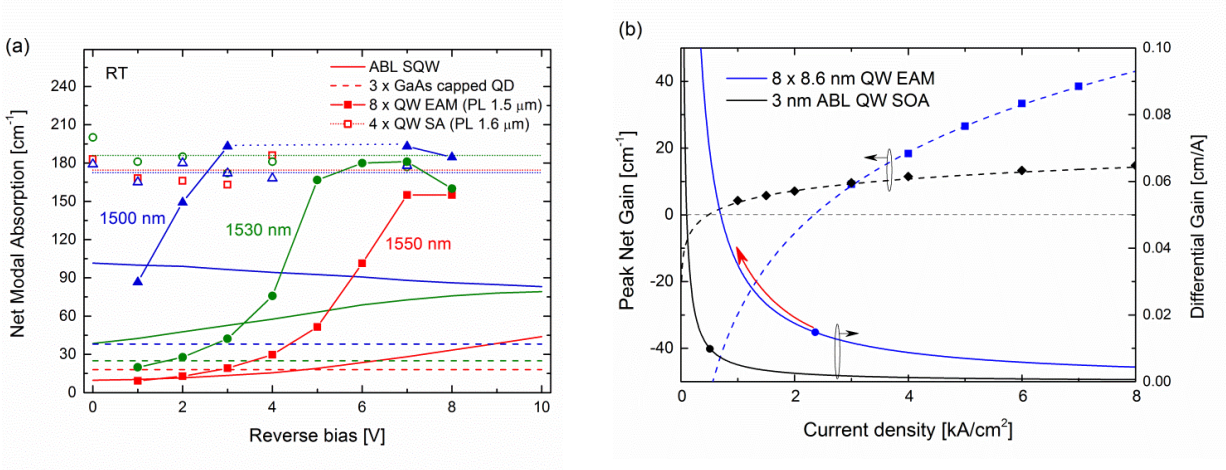

Figure 5.11: (a) Comparison of the absorption coefficients versus applied reverse bias at 1550 nm, 1530 nm, 1500 nm for single QW, QD, MQW based absorbers. (b) Net gain and differential gain for MQW EAM (black curves) in comparison with single QW SOA. The differential absorption at transparency shown by round symbols.

To avoid the distortion in the optical spectrum, the long-wavelength absorber was realized to operate above the band edge as shown in Figure 5.10 (b). The number of QWs were reduced from eight to four, however, the absorption coefficient of ~ 150 cm^{-1} introduced significant losses prohibited stable MLL operation even for long 4 mm QW lasers presumably due to the high internal losses in the SOA section.

5.1.4 QD vs QW SOA: Saturation Parameters

Figure 5.12 presents comparative plots of the peak gain wavelength, *net* modal gain and corresponding differential gain as a function of injection current density for ABL QW and QD SOAs extracted from the gain spectra in Figure 5.3 (b) and Figure 5.8 respectively. The *net* gain curves were obtained by fitting through the data points for the gain coefficient using the logarithmic function Eq. (2.6). The exponential fit (marked as "exp" fit) using Eq. (2.7) was applied for QD gain fitting, however, gave incorrect prediction at transparency. The shown *net* gain and differential gain curves correspond to a center emission wavelength λ_0 found at threshold for 10 GHz (4 mm) and 40 GHz (1 mm) lasers with one output facet HR coated (95%). The mirror losses shown by dashed lines marked with "α_{mir}" represents the threshold gain. A contribution of the absorption losses in the EAM section of a MLL was not included, but it obviously increases the required gain and threshold current density. The extracted parameters are summarized in Table 5.2.

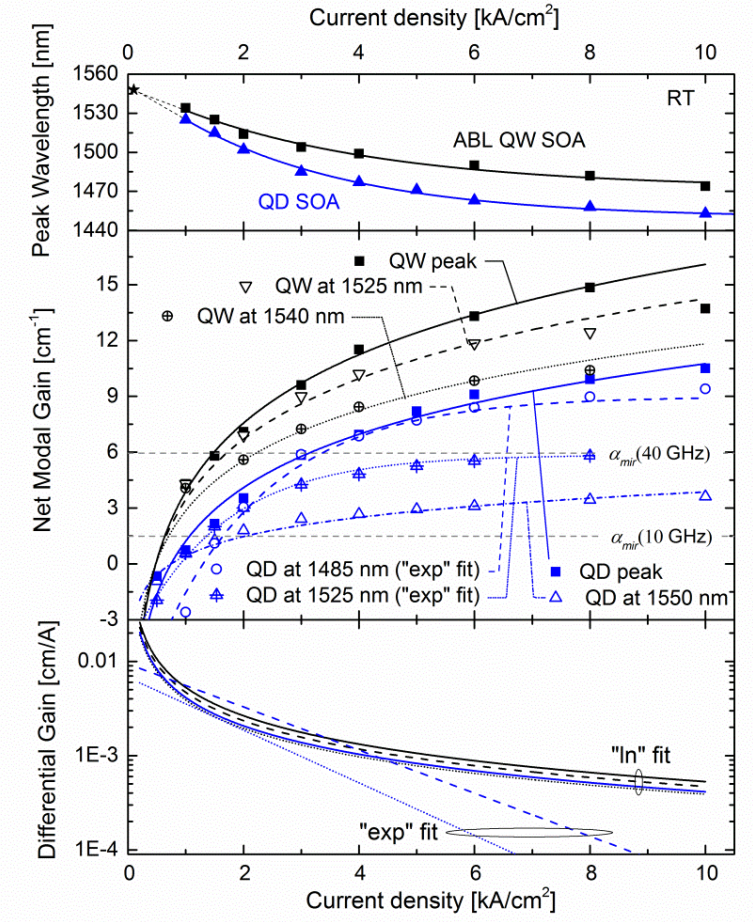

Figure 5.12: Peak gain wavelength (top), modal gain (middle), differential gain (bottom) as a function of injection current density for QW and ABL QW SOAs. The dashed horizontal line marked with α_{mir} indicate the output mirror losses for 10 GHz and 40 GHz lasers used as threshold values. See the text for details.

Table 5.2. Comparison of gain parameters for 3 nm ABL QW SOA, GaAs-capped InAs QD SOA and 3.5 nm offset ABL QW SOA acquired from Figure 5.12 and Figure 5.13.

Gain parameters		3 nm ABL QW	3 × InAs QD	3.5 nm offset ABL QW
J_{tr}, kA/cm2		0.48	0.74	0.90
$d\alpha/dJ \approx dg/dJ_{tr}$		10.9×10^{-3}	5.6×10^{-3}	6.5×10^{-3}
f_{rep}=10 GHz (α_{mir}=1.49 cm^{-1}, uncoat/HR)	J_{th}, kA/cm^2	0.63	1.1	1.2
	dg/dJ_{th}, cm/A	6.2×10^{-3}	3.4×10^{-3}	3.7×10^{-3}
	λ_0, nm	~ 1540	~ 1525	~ 1565
	dg/dJ_{th} / $d\alpha/dJ_{tr}$	**0.57**	**0.61**	**0.57**
	dg/dJ_{th} / $d\alpha/dJ_{tr}$ (MQW EAM)[10]	**0.41**	**0.23**	**0.25**
f_{rep}=40 GHz (α_{mir}=5.95 cm^{-1}, uncoat/HR)	J_{th}, kA/cm^2	1.47	3.14	-
	dg/dJ_{th}, cm/A	3.2×10^{-3}	1.8×10^{-3}	-
	λ_0, nm	~ 1525	~ 1485	-
	dg/dJ_{th} / $d\alpha/dJ$	**0.29**	**0.32**	-
	dg/dJ_{th} / $d\alpha/dJ$ (MQW EAM)	**0.21**	**0.12**	-

[10] The differential absorption coefficient dα/dJ for the MQW EAM is taken for quantitative evaluation at its transparency value of 15×10^{-3} as shown in Figure 5.11 (b), however, expected to be less under reverse biasing.

The ratio between the differential gain *dg/dJ* with respect to the differential absorption dα/dJ is important parameter which indicates the difference between the saturation energies in the gain and absorber critical for stable mode-locking as discussed in Section 2.2. The best conditions correspond to the lower differential gain *dg/dJ* and smaller $dg/dJ/d\alpha/dJ_{tr}$ values. The comparison shows that the lowest differential gain can be achieved with QDs using short gain section (1 mm for 40 GHz vs 4 mm for 10 GHz). However, taking into account larger gain broadening, the differential gain to absorption ratio is larger than for QW when considering one active media for monolithic MLLs. In case if the QDs are integrated with MQW EAM, the ratio (dg/dJ_{th} / $d\alpha/dJ_{tr}$ *(MQW EAM)*) is almost two times lower than for the integrated the QW – MQW EAM couple.

However, the demonstrated benefits of a higher differential gain of QDs is related to the low internal efficiency at high threshold current density rather than to GS saturation (indicated as a strong blue-shift of the emission wavelength). At the same time, the threshold conditions for the QW SOA can be achieved at relatively low carrier density which restricts the high population inversion, and therefore results in a higher differential gain (in agreement to the calculation results presented in Chapter 3.2).

Concerning the studied QD material, it is possible to achieve a higher saturation energy at low carrier density when operating at GS, which requires the internal losses to be reduced at least down to 1.5 cm^{-1} (for 10 GHz: J_{th} = 0.5 kA/cm^2, dg/dJ_{th} = 3.0 $x10^{-3}$ cm/A following the curve "QD at 1550 nm"). In order to significantly improve performance, the lower gain broadening and GS – ES state separation must be realized.

For QW SOA, one possible solution to extend the population inversion is to apply a low-reflection coating to the front-side facet which increases optical losses, or use extended cavity approach with a short gain section. Another possibility is a displacement of the QW from the optical field maximum to reduce confinement factor and further increase saturation energy and output power as suggested in Chapter 3.2.

5.1.5 Offset vs Centered QW SOA

The effect of the QW displacement was investigated on two ABL QW SOA structures consisting of 3.5 nm wide InGaAs QW active region. The first structure had QW in the peak of the optical mode (referred to as "centered" QW), and for the second ("offset") structure, the QW was displaced towards the top p-cladding by removing p-WG layer, and the n-WG layer below the QW was wider to support mode guiding equally to the "centered" case (a detailed layer description is given in Appendix A.3). The bandgap and optical mode profiles can be found in Figure 3.3 (b). Both structures had a slightly increased doping from the n- and p- sides compared to the ABL QW SOA studied above. The width of the QW was intentionally larger to shift the band gap to the longer wavelength (~ 1.6 μm) assuming the blue-shift occurring at higher carrier densities. Due to the difficulties in growth control of such narrow QWs mentioned in Chapter 4.1.2, the measured PL peak wavelengths were 1590 and 1615 nm for the offset and centered QWs, respectively, for the same growth parameters.

The measured *net* modal gain and absorption spectra, and calculated differential gain versus current density are presented in Figure 5.13. The values for a 10 GHz "offset" QW laser is put in Table 5.2 for comparison. The internal losses was found from the absorption spectra to be ~ 4 cm^{-1}. The offset QW exhibits larger slope at the absorption edge presumably due to the higher doping from the p-side cladding adjacent to the offset QW. A smaller depletion region leads to a larger induced

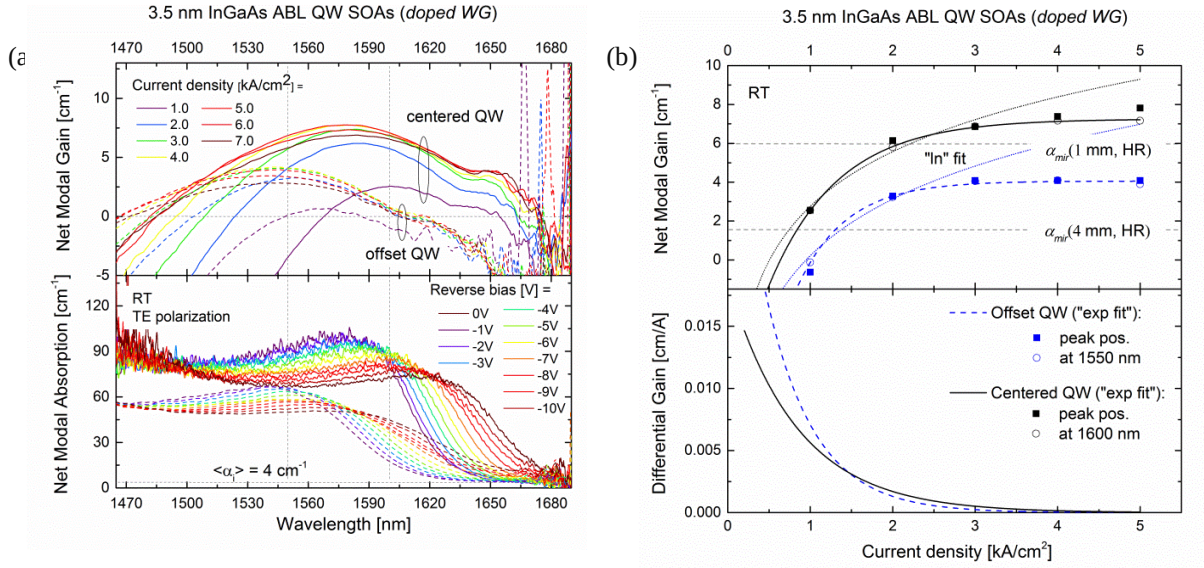

Figure 5.13: Net gain and absorption spectra of the "centered" and "offset" 3.5 nm QW SOAs with doped WG layers (left), and extracted gain and differential gain as a function of injection current density (right). Exponential fitting was used due to the higher accuracy for the gain curves with saturation.

electrostatic field, which deforms the band structure. The modal absorption coefficient at zero bias was decreased by factor of 1.4,which is slightly larger than expected from the confinement factor reduction of 1.2 for the offset QW calculated in Section 3.2 (see Table 3.1). The maximum gain is reduced by 1.9 which is presumably due to the larger optical losses induced by FCA in the QW and barriers in the presence of high hole densities. (At wavelength > 1650 nm, the accuracy of the data acquisition was limited by the OSA.).

The reduced optical confinement for the offset QW results in a smaller differential gain in correspondence with the discussion in Chapter 3.2, however, at relatively high carrier densities (above 1.4 kA/cm^2). This is related to the lower internal quantum efficiency (η_i = 46%) was observed for offset QW compared to the centered QW (90%). The degradation is attributed to the higher Auger recombination rates in the presence of higher hole concentration and unintentional p-doping of the active layer due to Zn diffusion from the adjacent p-cladding layer, which also affect the temperature stability (T_0 = 25 K vs 45 K at 60ºC). Another issue of the "offset" structure is carrier transport through the wide lightly-doped n-WG layer which increase self-heating and reduce laser efficiency. An increase in the serial resistance under forward biasing was found to be 0.2 – 0.3 V in the 1 – 5 kA/cm^2 injection current range.

A 4 mm MLL composed of the offset QW SOA integrated with 8 QW EAM (PL peak at 1510 nm) showed the emission with a typical for MLLs asymmetric spectrum presented in Figure 5.14 (see e.g. in Figure 5.24). However, the optical spectrum was beyond the EDFA bandwidth, which did not allow for further studying of the laser properties. (See more details on MLLs characterization in Section 5.4).

In order to utilize the benefits of the offset QW SOA approach, optical losses must be reduced by tuning the doping level and optimizing device processing. The confinement factor can be additionally lowered to obtain a higher saturation energy by designing the waveguide layers and ridge width to modify the optical field profile.

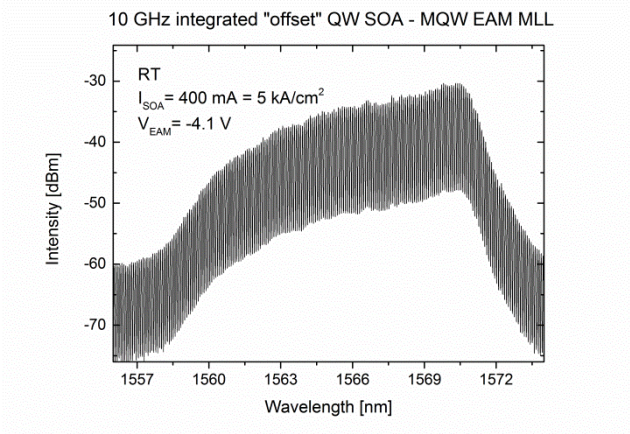

Figure 5.14: An example of an optical spectrum from integrated MLLs with the offset QW SOA as a gain section operating at 5 kA/cm^2 and 8 × QW EAM absorber section biased at - 4.1 V. An operation in the pulsed regime was not proven due to the setup limitation.

5.2 Characterization of Butt-Coupled Interface

5.2.1 Internal Reflectivity

Test devices

Intracavity reflection is a critical parameter for external-cavity and monolithically integrated MLLs resulting in pulse instabilities as discussed in Chapter 4.2. In order to quantify the reflection coefficients from the insertion facet between the integrated SOA and EAM section, Hakki-Paoli technique was used [271], [272]. This method involves measurement of ASE spectra with a high resolution and detection of its spectral modulation. The modulation depth M is related to the facet reflectivity R as [273]

$$M = \left[\frac{1+\sqrt{R_1R_2}G}{1-\sqrt{R_1R_2}G}\right]^2, \tag{5.9}$$

where G is the single-pass gain given by

$$G = \exp(g_m L). \tag{5.10}$$

A schematic of test devices are shown in Figure 5.15. The devices consisted of an electrically pumpled 2 mm long section based on either the SOA or EAM material as a source of amplified spontaneous emission of TE or primary TM polarization, respectively. The cavity length is a tradeoff between a maximum length resulting in spectral oscillation attainable to be resolved with the highest OSA resolution as exemplified in Figure 5.16 (a)), and a minimum length offering sufficient gain per round-trip G to resolve modulations at low reflectivity (Figure 5.16 (b)). To meet the requirements on spectral resolution, 2 mm long cavity was chosen, however, only relatively high reflectivity can be determined as demonstrated in Figure 5.16 (b) (e.g. R = 10^{-6} can be resolved at 40 cm^{-1} gain).

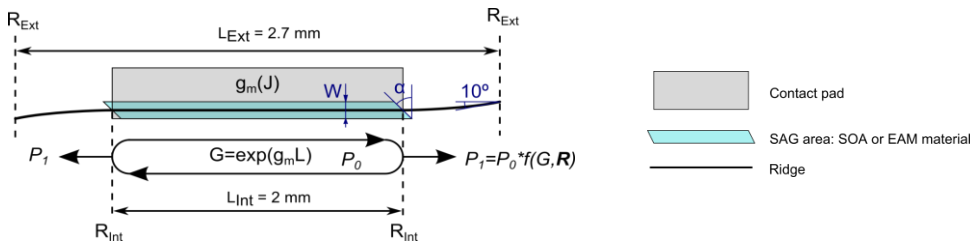

Figure 5.15: A schematic of the device used for internal reflection measurements. The pumped internal cavity (SAG area) was consisted either of SOA material or EAM material, while the output waveguides from the both sides have the opposite type of active material and do not have contact pads.

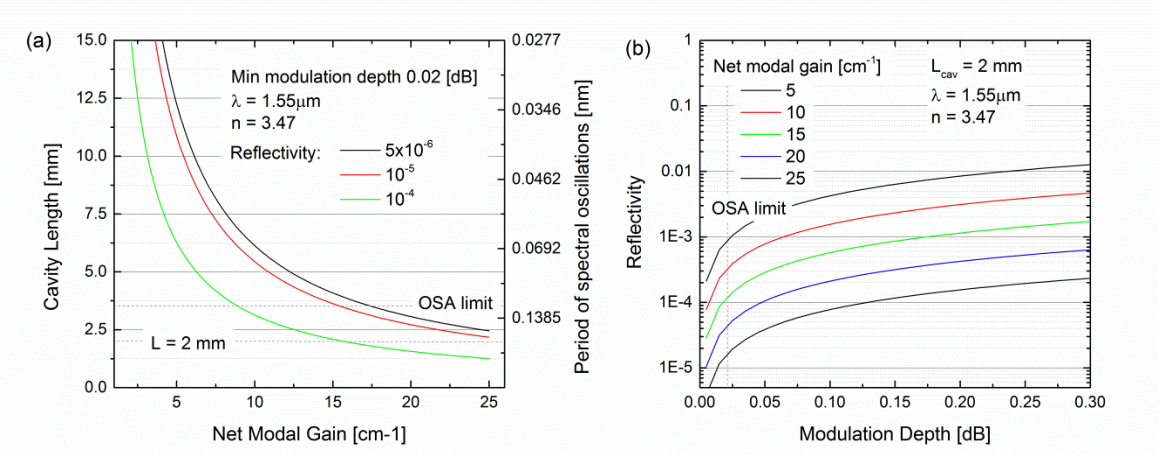

Figure 5.16: (a) Calculated cavity length required to determine the reflection coefficients of $5x10^{-6}$ (black), 10^{-5} (red) and 10^{-4} as a function of net gain. The right axis shows correspondence to the cavity length period of spectral modulation and the limit shows the highest OSA resolution. (b) Reflectivity as a function of spectral modulation depth for different net gain coefficients. The limit corresponds to the OSA sensitivity.

The amplifying section was integrated on each side with 350 μm long waveguide of the opposite type of active material (the total device length was 2.7 mm). In order to avoid reflection from the output facets, the output waveguides were 10° tilted to the cleaved facets by means of bending as shown in Figure 5.15. The length of the waveguides was chosen to tolerate the radiation losses out of the device which is defined by the bend curvature. Taking into account crystallographic-dependent wet etching behavior, an adiabatic ridge mask was designed to form 2 μm ridge width at the bottom. The sidewall angle φ is assumed to have a linear dependence on the waveguide angle γ toward the [011] direction as

$$\varphi = 87.8° - 1.4\gamma\,, \tag{5.11}$$

when anisotropic wet etching in 1 HCl : 4 H_3PO_4 is used for the ridge formation.

No electrical contacts were formed on the 350 μm output waveguide sections and they were consequently absorbing (recommended to). The spectral variation of the gain and absorption coefficient were assumed to be constant within the detected range of a few nanometers.

Experimental results

Figure 5.17 presents the FTT amplitude (left column) of the ASE spectra of a 5 nm span (examples shown in the right column) measured for both QW SOA (top row) and 3 × QW EAM material (bottom row) for different SAG mask width *W* and stripe edge angled α as specified in Figure 5.15. The recorded modulation depth for both types of devices corresponded to the "internal" cavity was below the accuracy of the amplitude measurements defined as 0.02 dB for our setup. The TE reflection was determined to be lower than 6.2×10^{-4} for the maximum achieved SOA gain coefficient of 3.1 cm^{-1} in the presence of the absorbing EAM arms. The TM amplification provided in the EAM section was about 22 cm^{-1}, and the reflectivity for the TM mode was estimated to be below 2.1×10^{-5}, which is assumed to be larger than the real TE reflection. The pronounced peak was observed at 2.7 mm corresponding to a residual modulation of 10^{-3} due to reflections on output facets ("external"). Applying AR coating, the "external" reflection was reduced down to 2×10^{-5}.

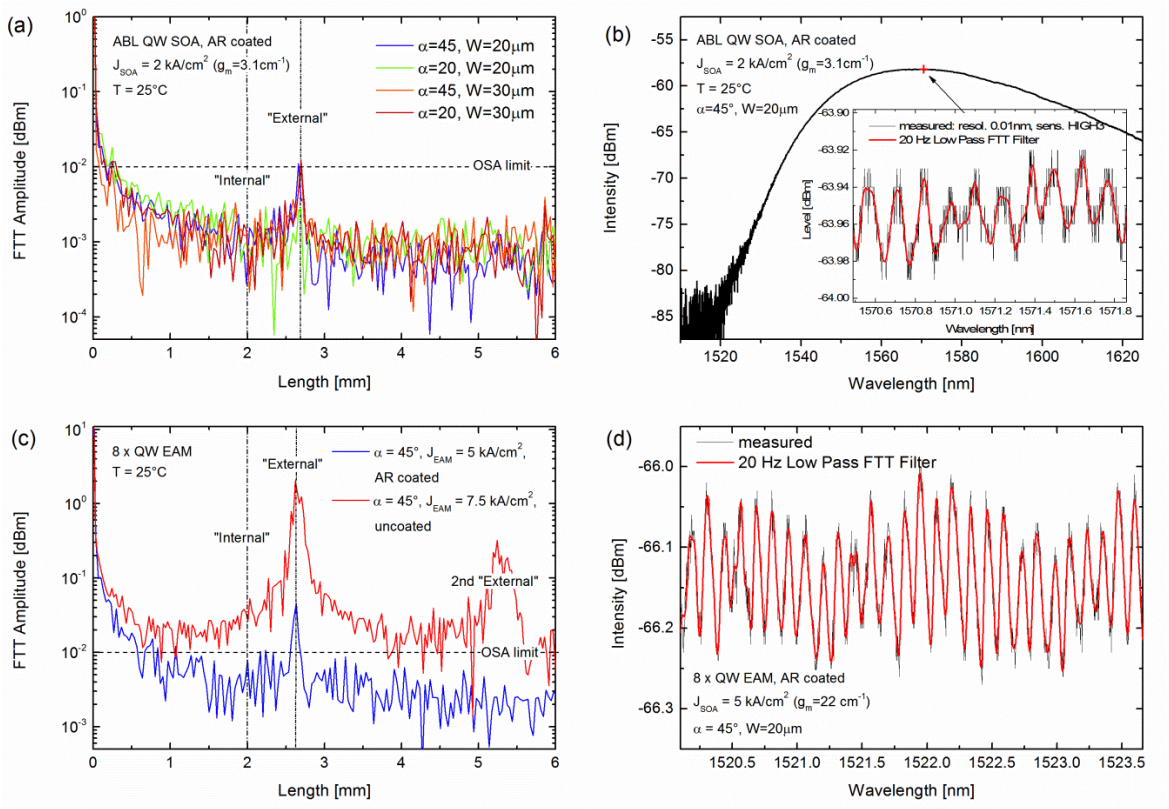

Figure 5.17: FFT analysis of spectral oscillation for (a) ABL QW SOA (TE gain) and (c) MQW EAM with dominant TM polarization. Corresponding optical spectra at the gain maximum are shown in (b) and (d). The resolution is 0.01 nm, high sensitivity.

5.2.2 Transmission

Excessive scattering of the light on the imperfections increases optical losses which is detrimental for low noise pulse generation. A contribution of the coupling losses at the interface losses were extracted for multiple butt-jointed linear cavity lasers divided by *n* gain and *n* absorber sections of the length L_{SOA} and L_{EAM}, respectively, as depicted in Figure 5.18. Increasing number of the BJ interfaces results in growth of the required gain at threshold as the additional losses term is multiplied [274].

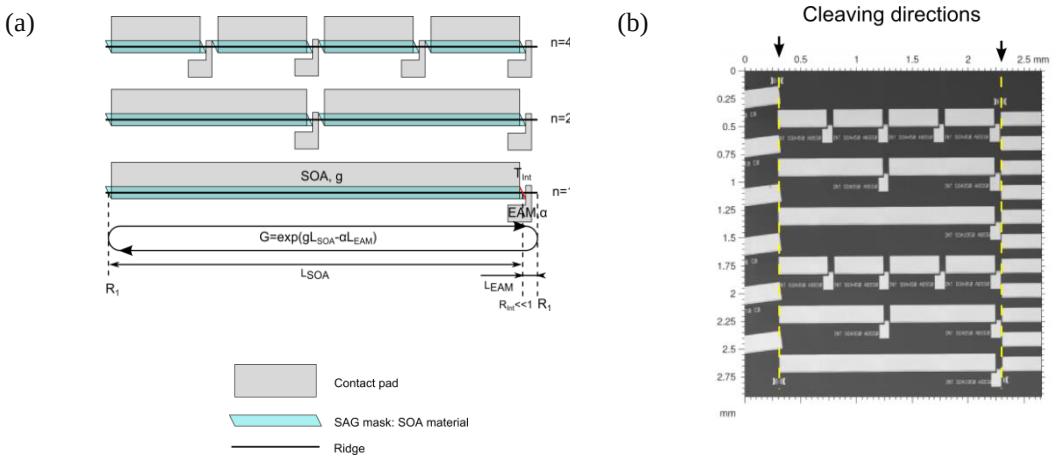

Figure 5.18: (a) A schematic of the device used for interface losses measurements and (b) a photograph of processed devices.

The round-trip ASE intensity *I* can written as

$$I = e^{2ng_0(J)L_{SOA}} \cdot e^{2n\alpha_0(V)L_{SOA}} \cdot T_{BJ}^{2(2n-1)} \cdot R_1R_2 \cdot I, \tag{5.12}$$

where R_1R_2 are the facet reflectivities, while the internal reflection R_{int} is assumed to be negligible small. The transmission T_{BJ} can be found as

$$T_{BJ}^{2(2n-1)} = (G^{2n}R_1R_2)^{-1}, \tag{5.13}$$

where the single pass net gain *G* equals to

$$G = e^{g_0(J)L_{SOA} - \alpha_0(V)L_{EAM}}. \tag{5.14}$$

The transmission was calculated for the multi-section devices consisting of QW SOA and MQW EAM of a total length of 2 mm (Figure 5.18 (b)) to be 0.774 ± 0.020 per interface. Net gain $g_0(J)$ and absorption $\alpha_0(V)$ spectra for different driving conditions were known from the SCM measurements on the devices from the same wafer. This corresponds to the coupling losses of 1.10±0.09 dB per interface, which is 0.4 dB better than that reported for an optimized SOA-EAM structure in [174]. Although, the losses are still high in comparison to the best results of 0.46 dB achieved for passive-active integration in passive light transmission measurements in [9].

One contribution to the excess optical losses can be related to the mode mismatch between the two undisturbed waveguide cores. Assuming perfectly optimal vertical alignment, the fundamental TE mode overlap of 99.72% calculated in Section 3.3 gives the negligible coupling losses of 0.013 dB.

Another reason is the fundamental interface regrowth behavior. Light scattering can occurs on imperfections, such as voids, material pilling and morphological non-uniformity, and its deflection away due to bending waveguide up. For illustrative purposes, Figure 5.19 shows the 2D finite-difference time-domain (FDTD) simulation for a similar "up-bent" morphology and resulting loss α and a reflectivity *R* taken from [174]. An additional lateral deflection for the fabricated BJR structure can be expected due to the angled SAG mesa and interface roughness owing to ICP-RIE mesa etching under non-optimized etching parameters.

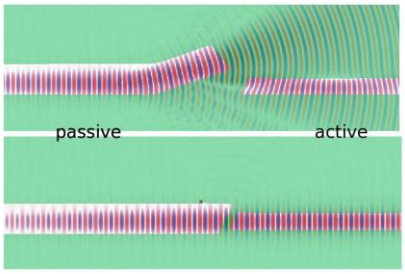

Figure 5.19: 2D FDTD simulation showing electrical field perturbation caused by the BJR interface up-bending modeled in [174].

5.2.3 Leakage Current

One of the main processes responsible for carrier losses is non-radiative recombination on deep-level recombination centers associated with crystal defects. To verify the quality of the crystal structure at the interface, the dark current through the multi-section devices including BJR interfaces (Figure 5.20 (Inset)) under reverse biasing was measured. With increasing defect density, the leakage current grows rapidly and may cause shortening of the p-n junction and device failure. For integrated and non-integrated sections, the current was below 10 nA at 0 - -3V reverse biasing and at a µA range at -7V. The absence of the break down at reverse biasing up to -9 V and low (few nA) dark current in the range of 0 - -3 V detected for both devices gave evidence of the good crystalline quality.

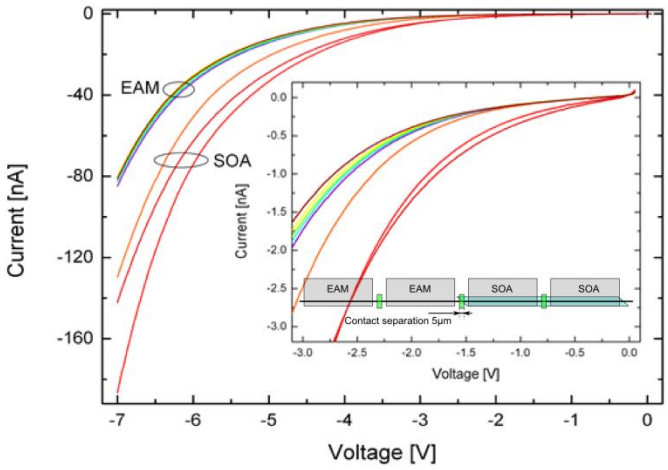

Figure 5.20: I-V characteristics of the integrated devices shown in Inset probed on the SOA and EAM sections with and without BJR junction.

5.3 Mode-Locked Laser Performance

In this section, the characterization of the fabricated monolithic MLLs is discussed. Investigation included the measurements of pulse characteristics such as pulsewidth, optical spectrum, and timing jitter. The experiments were performed on 10 GHz integrated ABL QW SOA – MQW EAM MLLs and on the MLLs consisting of a single ABL QW active material for both SOA and EAM sections ("non-integrated" MLLs) driven in the passive regime. The total MLL cavity length was around 4 mm, and the EAM length was varied from 20 to 300 µm. The back facet adjacent to the absorber section was HR coated to facilitate the self- CPM effect.

5.3.1 Experimental Setup

Experimental characterization of the MLLs was carried out using a setup schematically illustrated in Figure 5.21. A two-section integrated MLL under investigation was mounted onto a temperature controlled stage. The gain section was forward biased by a laser diode controller (SRS LDC 502). A reverse bias was applied to the absorber section using a DC source (Agilent 66312A). The output light was lens coupled to a SMF and distributed with an optical power meter (HP 8153A), OSA (Ando AQ6317), electrical spectrum analyzer (ESA) showing RF spectrum of a pulse train captured with a high-speed photodiode (22 GHz Lightwave section HP 70810B integrated in the Spectrum Analyzer System HP 70004A was used for 10 GHz MLLs). The RF spectra of a pulse train was used to estimate the jitter characteristics using D. von der Linde method described in [26] by measuring the single-sideband phase noise spectral density as depicted in Figure 1.6 (b). A part of the light was fed into a frequency-resolved optical gating (FROG) setup, which offers complete pulse characterization simultaneously in time and frequency domain [275]. Due to the low pulse intensity inherent for semiconductor MLLs (≤ 1 pJ), EDFA amplifiers were introduced along the routing.

A schematic diagram of the FROG setup is shown in Figure 5.22. The pulse sampling occurs using an autocorrelator (AC), which splits the signal into two replicas with a varying time delay between them. The replicas overlap in a second harmonic generating (SHG) crystal ($KTiOPO_4$ (KTP)), after

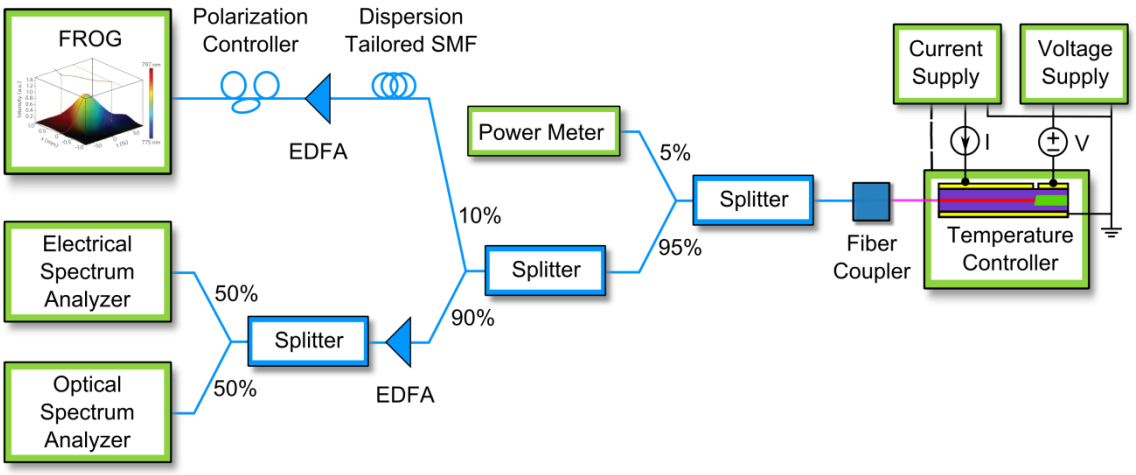

Figure 5.21: Experimental setup used for complex MLLs characterization. AC – autocorrelation, FROG – frequency-resolved optical gating.

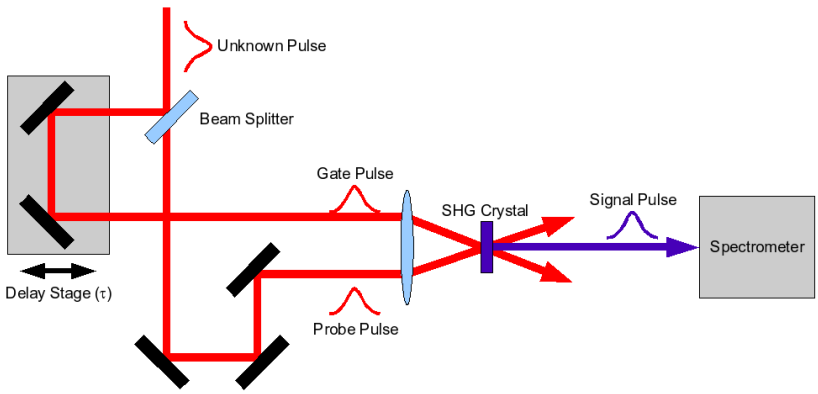

Figure 5.22: A schematic of a second-harmonic generation (SHG) based FROG setup.

which the SHG signal is detected using a high-resolution spectrometer (Ocean Optics HR2000) as a function of time delay. In such a manner, a time-dependent spectrally resolved electrical field of a pulse (a spectrogram) is collected. The measured FROG spectrogram can be converged using a phase retrieval algorithm to determine a pulse duration, optical spectrum, and spectral phase profile (pulse chirp). For comparison, commonly used intensity AC with a fast photodetector instead of a spectrometer results in symmetric pulse shape traces while losing phase information. Pulse asymmetry, typically seen for semiconductor MLLs, and highly structured pulses e.g. accompanied with trailing pulses cannot be adequately observed [123]. Therefore, AC provides unreliable pulse characteristics which raises a dispute on the credibility of 391 fs and 360 fs short pulse generation from QD MLLs reported in [58] and [60] as discussed in [123]. The FROG technique has more strict criteria for determining stable mode-locking. Thus, if pulses are strongly distorted and unstable, the resulting spectrogram is a complex combination of a multiple varied pulses, which leads to failure of the retrieval algorithm and incorrect pulse measurements.

In practice, it is important to obtain zero intensity at the spectrogram boundaries for pulse retrieval. The FROG spectrogram size and resolution are limited by an NxN matrix mesh, where N time delay points spaced by Δt and N wavelength points with a frequency spacing of $1/(N\Delta t)$, and by a bandwidth of an SHG crystal. In the performed experiments, a strong pulse broadening and high jitter were observed for both integrated and non-integrated QW passively MLLs, which, in most cases, resulted in the poor convergence of the measured FROG spectrograms with a high error (RMS deviation between measured and retrieved spectrograms > 0.02). This restricted accurate systematic study of the device performance. Thereby, only the best achieved results and general observations are described in this section.

5.3.2 Mode-Locked Laser Performance Characteristics

Pulse duration

The shortest pulse duration achieved for integrated MLLs was 890 fs (FWHM, assuming Gaussian pulse shape) at approximately ~10.8 GHz repetition rate (L_{tot} = 4.15 mm, L_{EAM} =20 µm). A gain current was 165 mA (I/I_{th} = 2.6) and an absorber reverse bias was -4 V. Due to the high internal losses for this device, the spectrum was centered around 1525 nm at RT (see FP spectrum in Figure 5.7). In order to utilize the EDFA bandwidth (1530-1560 nm), the measurements were performed at 34ºC by shifting the spectrum to longer wavelengths.

Figure 5.23 (top row) shows the measured and retrieved FROG spectrograms. The FROG error was 0.0098, which indicates sufficient agreement between the converged and measured pulse spectrum (retrieved optical spectrum shown in Figure 5.23 (middle row, right) has an asymmetric shape which was directly recorded by the OSA e.g. in Figure 5.24 (black)).

The corresponding temporal pulse trace depicted in Figure 5.23 (middle row, left) exhibits asymmetric shape. As described in Section 2.3, the fast absorber saturation makes the leading part steeper compared to the slow trailing edge due to the broadening in the gain section. The front is up-chirped in frequency and down-chirped in the tail in agreement to the arguments provided in Figure 2.6. Thus, the pulse width and the effective optical bandwidth were determined as 2.8 ps and 4.1 nm (0.51 THz), respectively, resulting in a TBP product of 1.43. The post-processing numerical pulse compression associated with a pass through ~ 40 m SMF results in 890 fs pulses with the TBP of 0.454. No high intensity trailing pulses or spectral modulation was detected, which proves the low

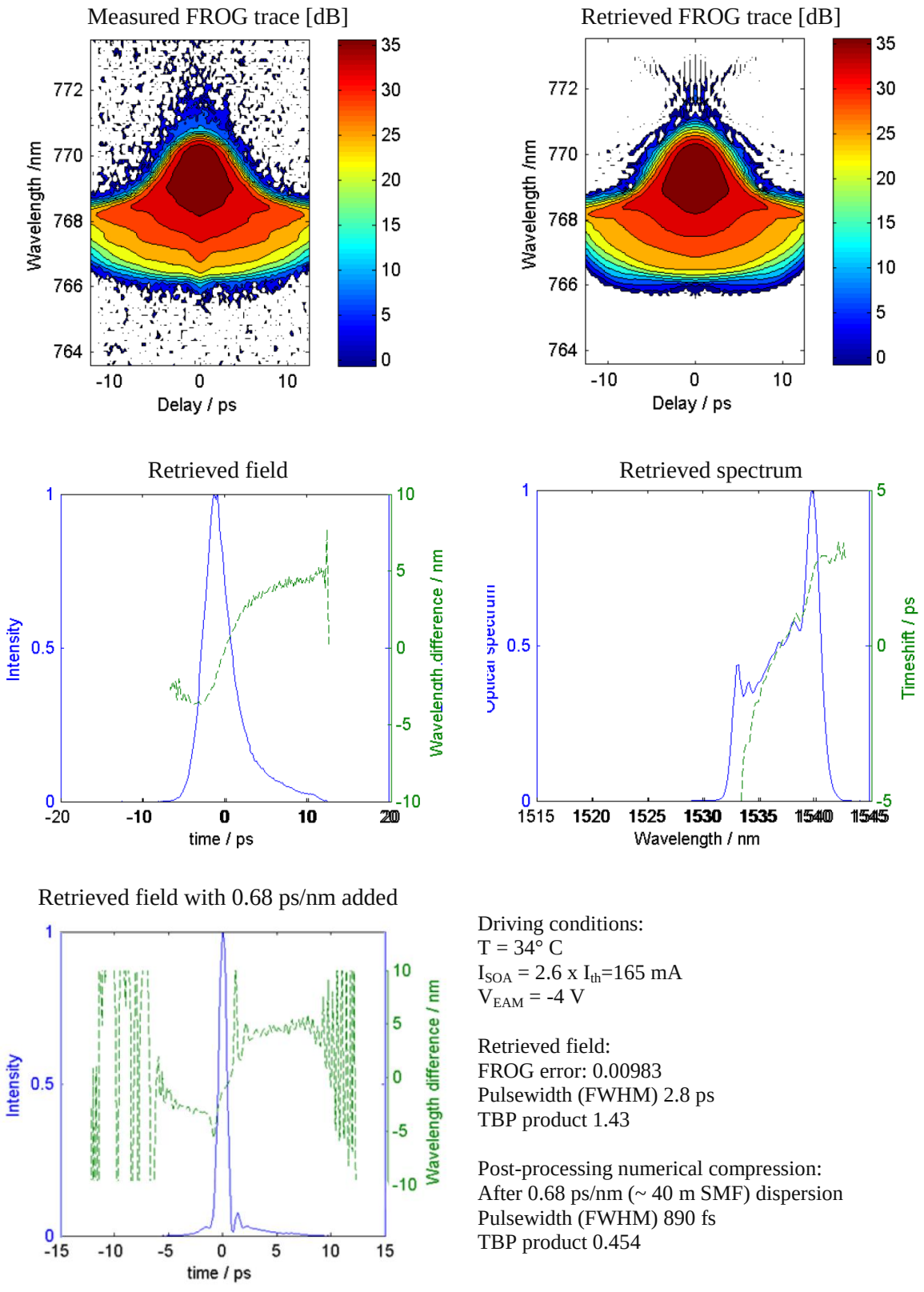

Driving conditions:
T = 34° C
I_{SOA} = 2.6 x I_{th}=165 mA
V_{EAM} = -4 V

Retrieved field:
FROG error: 0.00983
Pulsewidth (FWHM) 2.8 ps
TBP product 1.43

Post-processing numerical compression:
After 0.68 ps/nm (~ 40 m SMF) dispersion
Pulsewidth (FWHM) 890 fs
TBP product 0.454

Figure 5.23: FROG spectrograms (top row), retrieved electrical field in time and frequency domain (middle row) and pulse shape after dispersion compensation (bottom row) obtained for 10 GHz ABL QW SOA – MQW EAM integrated MLL with 20 µm long absorber section. EAM facet is HR coated.

internal reflection on the BJR interface (the small feature on the right side is a numeric artifact). For comparison, the smallest pulse duration for 10 GHz "non-integrated" ABL QW MLLs was 990 fs at 120 mA SOA current and - 2.4 V EAM bias (after numerical pulse compression. High FROG error of 0.0199). This result is among the best in term of pulse duration achieved for long (10 GHz) two-section all-active QW-based passively MLLs (see Figure 1.7 in Introduction), however, no significant improvements in terms of pulsewidth was achieved for the integrated MLLs due to the importance of ultrafast QW dynamics in the sub-ps range.

Optical spectrum

MLL operation in different lasing regimes is typically observed, such as stable mode-locking, incomplete mode-locking and self-pulsation or Q-switching, which can be detected by a complex change in pulse characteristics, optical and RF spectrum. Since passive mode-locking is the result of the dynamic interplay between the processes in the gain and absorber section as described in Chapter 2, MLL performance largely depends on the driving conditions. In order to explain the behavior, the gain saturation, absorber modulation depth and recovery times must be taken into account in combination with respect to the broadening effects and nonlinearities imposed by SPM and GDD.

Typical optical spectra acquired on the integrated MLL with 40 μm long absorber section under different reverse biasing are plotted in Figure 5.24. In particular in this plot, a small increasing of 0.4 V in the bias applied to the integrated EAM is shown to blue-shift the spectrum and modify its shape. One possible explanation is the transition between the mode-locking regime (black curve) to the Q-switching regime (red) associated with an increased band-edge absorption at higher voltages. However, no indicative degradation in optical spectral modulation or pulse RF spectra was observed in this case.

Another reason is the band-edge absorption detuning in the integrated MQW EAM with respect to the gain, which is anticipated to have a strong influence on the spectral behavior and establishing the pulse generation. If the absorption band-edge is near the gain peak and the losses at these wavelength are high (corresponding to a lower voltage), the emission is shifted to the longer wavelength. At larger reverse voltages, the maximum absorption (excitonic) peak is reduced due to QCSE and the emission wavelength is closer to the peak gain. At the same time, the absorption saturation in the long wavelength range is stronger at lower voltages that may lead to more efficient modulation, and thereby, more stable mode-locking and a smaller pulsewidth can be achieved as illustrated in Figure 5.23. However, the process is more complex, and the absorber reverse biasing affects also the

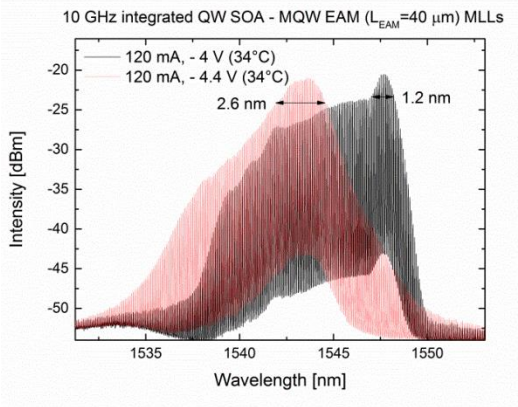

Figure 5.24: (a) Typical optical spectrum shaping observed for integrated MLLs at different driving conditions in dBm. T=34ºC. SA facet is HR coated. 3dB bandwidth is shown.

recovery time, may change SPM behavior. Additionally, many-body effects and heating should be taken into account as they shift absorption edge and strength, especially for sub-ps pulses. The screening of the external field at high carrier concentration blue-shifts the absorption band-edge and increase recovery time.

An increase in the current in the gain section commonly resulted in pulse broadening due to SFM, self-pulsation and CW component at current densities much above the threshold seen as additional peaks on the RF spectrogram. The nonlinear shift between the central emission wavelengths similar to Figure 5.24 was also observed.

Jitter

The best noise figure was achieved at low current densities and high reverse biasing of the absorber in case of integrated MLLs. Figure 5.25 (a) shows the RF spectra of integrated and non-

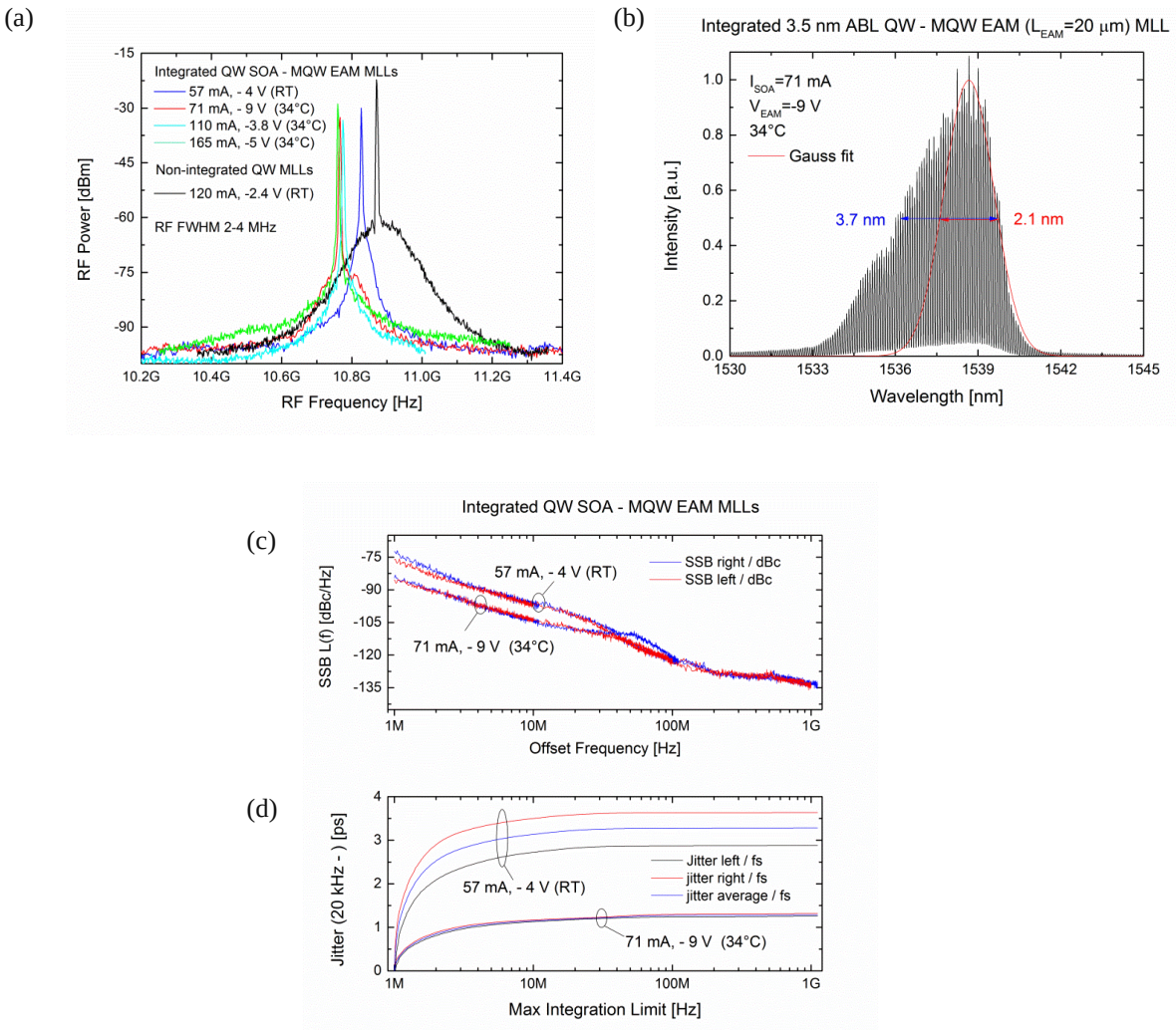

Figure 5.25: (a) RF spectra of non-integrated and integrated passive MLLs at various bias conditions. (b) Optical spectrum of the integrated 10 GHz device at 34°C with the lowest timing jitter of 1.3 ps (20 kHz – 320 MHz) measured for the investigated passively MLLs (Note the intensity is in arb. units), (c) corresponding single sideband phase noise spectra and (d) jitter integrated over the range from 20 kHz to the "Max Integration Limit".

integrated MLLs, where the reduction of the characteristic for QW pedestal associated with amplitude noise can be observed for in a wide range of operation conditions. The improvement is presumably due to larger non-saturable absorption provided by the MQW EAM compared to single QW absorber section in the "non-integrated" MLL and faster absorber recovery time when applying higher absorber voltage. This ensures more efficient modulation and reduces the CW component. Figure 5.25 (c, d) shows the single sideband phase (SSB) noise spectra and integrated jitter for the integrated MLLs corresponded to the RF spectra at I/Ith < 1.5. The jitter is reduced from 3 to 1 ps when applying higher absorber voltage (-4 V and -9 V, correspondingly).

5.4 Summary

In this section, intrinsic material properties of the QD and QW SOA and MQW absorber were investigated. Since the most of the devices were processed using dry etching for the ridge formation and had excessive p-doping in the top cladding, the high internal losses and consequently threshold currents were measured, which, in the prospective of MLLs, leads to high spontaneous recombination noise. The losses were reduced by factor of two using optimized doping in the p-cladding and wet etching, which is important to consider for the future work.

The QD gain and absorption spectra and QD-based FP lasers was found to consist of low GS gain and dominant ES gain components without pronounced GS and ES state separation, which is consistent with the analysis of the influence of the shape of these self-assembled QD on QD energy states structure provided in Section 4.1.3. Due to the dense energy spectrum, no significant increase in gain saturation energy was observed. Moreover, poor electron confinement and high inhomogeneous broadening resulted in reduced internal efficiency and high threshold carrier densities. Thereby, the application of this type of QDs in MLL amplifier was limited, and further development of QD material is needed.

The characterization of single QW amplifiers of different epitaxial layer design was performed. A twofold increase in efficiency and output power, and improved temperature stability was achieved in QW SOA with asymmetric unipolar barriers compared to the conventional symmetric QW structure owing to the reduced carrier leakage. It was shown that the high population inversion required for MLL noise reduction is difficult to realize in long (10 GHz) lasers due to the inherently high gain coefficient. The possibility to reduce the differential gain was demonstrated for the offset QW waveguide geometry with lowered confinement factor.

Since the quality of the BRJ interface can significantly affect the performance of the integrated MLLs, the internal reflectivity, losses and current leakage were measured to validate the applicability of the BJR technique for the realization MLLs. The resulting internal reflectivity below 2.1×10^{-5} was found sufficiently low to prevent intracavity feedback, which was further proven by the absence of spectral modulation and secondary pulse formation from integrated MLLs. The coupling optical losses were estimated to be 1.1 dB per interface due to the bent up growth profile and deflection of the light out of the waveguide.

The performance of 10 GHz passively MLLs consisting of integrated QW gain section with MQW EAM was demonstrated to allow for 900 fs pulse generation with reduced timing jitter compared to non-integrated QW MLLs owing to the fast EAM recovery. However, the detail study of the MLL behavior were restricted by the strong broadening in the long gain section.

Chapter 6

Conclusions and Outlook

6.1 Conclusions

This work has examined the material engineering for semiconductor monolithically integrated two-section mode-locked lasers for low-noise sub-picosecond pulse generation at wavelength of 1.55 μm using the InP/InGaAsP/AlGaInAs material platform. In order to overcome the ultrafast limitations, the design of the epitaxial material was performed independently for the amplifier and absorber sections with an emphasis on gain dynamics, which has shown to have a major influence on the pulse instabilities and broadening. The first option to improve pulse quality was to utilize quantum dots (QDs) for pulse amplification owing to the slow "ultrafast" gain recovery, and hence suppressed fast perturbation in carrier density. Due to technological constraints in the growth of 1.55 μm self-assembled QD material, a deep, narrow, and single quantum well (QW) was considered as a good alternative due to the reduced effects of carrier heating and spectral hole-burning on gain suppression under high population inversion. An advanced QW separate confinement heterostructure design was elaborated using the asymmetric barrier layer (ABL) approach and a tailored asymmetric waveguide core. In order to provide fast absorption recovery, and hence ensure efficient pulse reshaping, a QCSE electro-absorption modulator (EAM) consisting of shallow multiple quantum wells (MQWs) with a low carrier confinement and low saturation energy was chosen. Moreover, a high absorption coefficient can be obtained to realize the shortest possible absorber and thereby enhance self-colliding effect.

The development of a reliable in-plane integration process has been a critical part of the project since even low internal reflection at the insertion interface ($R > 10^{-5}$) has a destructive effect on pulse formation. Planar high-quality integration of QD and QW amplifiers consisting of either symmetric InGaAsP or complex InGaAsP/AlGaInAs waveguide core with MQW EAM has been successfully performed. The influence of growth morphology, thickness and compositional variation which are associated with the BJR process on the optical quality of the integrated material were experimentally analyzed. The results showed a small bandgap blue-shift of less than 20 meV over tens of microns when moving toward the regrowth interface which is favorable for avoiding uncontrollable absorption. The bent-up growth profile ensured a reflectivity lower than 2×10^{-5} which was sufficient to prevent intracavity feedback. The low internal reflection was further proven by the absence of spectral modulation and secondary pulse formation from integrated MLLs. The resulting deflection of the light out of the waveguide contributes to coupling optical losses estimated at 1.1 dB per interface. Therefore, the complete examination of the properties of the regrowth interface, which are critical for achieving high device performance, validated the applicability for the fabrication of MLLs and opened perspectives for the fabrication of more advanced compact all-active integrated devices including Al-containing materials.

The investigation of self-assembled InAs/InGaAsP/InP QDs grown by MOVPE showed the correlation between their structural and optical properties. Due to the small (3%) lattice mismatch inherent in InAs/InP material system, the resulting QDs demonstrated shallow lens shape with a low aspect ratio (the average height and base diameter were 2.0 ± 0.2 nm and 23.5 ± 1.8 nm), which leads to a small separation between the ground and excited energy states (50 meV at 7 K). In combination with strong inhomogeneous broadening of a QD ensemble (RT PL FWHM ~ 90 meV), the measured gain spectra was quasi-continuous with reduced GS gain (GS modal gain of 2 cm^{-1} versus peak (ES) modal gain of 5 cm^{-1} per QD layer) and enhances carrier-carrier interaction. This partially eliminates advantages of QD ultrafast dynamics. Moreover, low carrier confinement in the QDs with InGaAsP barriers accompanied by FCA reduces the internal efficiency (η_i ~ 10% at RT for 1 mm FP laser) and thereby would have implied high threshold current and spontaneous emission noise. Therefore, no mode-locking has been demonstrated using this material. Further development was suggested at aiming to refine the dimension control on the QDs and carrier confinement by using larger potential barriers based on InP or AlGaInAs. The first results on InAs/InP QDs showed improved aspect ratio (the average height and base diameter were 2.34 ± 0.16 nm and 13.6 ± 1.0 nm long in the [-110] direction and 18.7 ± 1.6 nm in the [-1-10] direction). An increase in the ground and excited state separation up to 70 meV (7 K) was predicted, which makes this material promising for laser application.

Superior laser properties were demonstrated for the designed 3 nm compressive-strained InGaAs(P)/InAlAs/InP ABL QW gain medium embedded in the asymmetric waveguide structure based on AlInGaAs and InGaAsP materials optimized for efficient carrier transport while maintaining proper optical confinement and symmetric optical field compared to the conventional InGaAsP/InP 6.5 nm c-QW SOA. The investigation of 4 mm long 2 µm wide ridge FP laser performance showed an increase in internal efficiency from 46% for the c-QW to 93% for the ABL QW and the characteristic temperature from 22 K to 45 K at 70°C owing to reduced carrier leakage. The output power from the ABL QW FP laser was > 45 mW per facet at 5 kA/cm^2 at RT without achieving thermal roll-over.

In correspondence with the simulation results, the threshold conditions for long (10 GHz) MLLs based on ABL QW material could be achieved at significantly low population inversion due to the high gain coefficient (peak modal gain ~ 20 cm^{-1}). The possibility to increase inversion, and thereby improve QW MLL performance, using an offset ABL QW SOA design (the confinement factor was reduced by factor of 1.2) was discussed and realized. However, the structure suffered from a higher series resistance on the wide lightly n-doped waveguide layer and increased Auger recombination (η_i ~ 46%) presumably due to the high hole concentration produced when the QW is placed above the p-doped top-cladding. Further improvement may be achieved by optimizing the separate heterostructure to lower the confinement factor and doping level to improve carrier transport and lower the losses.

Mode-locking operation was demonstrated for the centered and offset ABL QW 10 GHz passively MLLs integrated with MQW EAM and for the non-integrated ABL QW MLLs. The shortest pulse width of 890 fs and jitter of 1.3 ps (20 kHz – 320 MHz) were measured on integrated MLLs. Reduced noise compared to the non-integrated lasers (typically few ps) is due to the faster absorption recovery in shallow QWs used in the EAM. Pulse duration achieved (on the order of a few picoseconds) is comparable with previously reported results, which shows the importance of ultrafast carrier redistribution and gain dynamics in QW material in the sub-picosencond range. The systematic investigation of pulse properties was limited due to the strong broadening and high jitter, therefore not attainable by FROG technique.

6.2 Outlook

The design and investigation of the amplifier and saturable absorber properties have been done in this work based on the steady-state material parameters while the characterization of the dynamic properties has been beyond the scope of the work. More advanced analysis is required in order to estimate an interdependent effect of the gain and absorber dynamic changes, broadening, band-gap detuning. Extended modeling and application of time-resolved characterization tools, such as pulp-probe measurements of integrated devices, would provide more insight into the physics behind the dynamic regimes observed in integrated MLLs at different driving conditions and enable further optimization of these devices.

The properties of the QD material studied in this work is in accordance with the results on InAs/InP QDs that have been demonstrated over the last decade. These moderate improvements, when compared with achievements reported for 1.1 – 1.3 μm InAs/GaAs QDs, may suggest the physical limitations of the self-assembled mechanism for InAs/InP material system and significant influence of FCA. So far, MBE grown QDashes in AlGaInAs matrix has provided the best performance. An alternative solution is MOVPE selective area etching and growth using e-beam or block copolymer lithography. This method does not rely on the strain relaxation process, and thereby can be potentially employed for the design of QD shape and composition, and ultimately for control over its energy state configuration. The development of the block copolymer lithography was partially done at DTU Fotonik during this Ph.D. study, and the preliminary results on selective area growth of the QDs employing block copolymer lithography can be found in [209], while the MOVPE in-situ etching and growth processes were studied in [217].

Concerning the QW MLLs, an extended cavity configuration with a passive section made by quantum well intermixing or butt-joint regrowth, could be considered for achieving high population inversion and reduced pulse broadening during pulse propagation. Furthermore, improved performance can be achieved by implementing a DBR with tailored intracavity dispersion or e.g. external resonant filter cavities suitable for low frequency pulse generation.

Alternative materials such as Sb-containing alloys forming the staggered (type II) band alignment can be potentially used for MLLs since the reduced spontaneous emission and high saturation energy in the amplifier and a strong electro-optic response attractive for an EAM are expected.

Appendix A

Epitaxial Structure Description

The appendix includes detailed descriptions of the epitaxial layer structures of the single QW and QD SOAs and MQW EAM studied in this dissertation. The given material parameters used for the numerical calculation are determined by interpolation from binaries including bowing coefficients for ternaries taken from the review [276]. The refractive index of AlQ alloys are obtained from the empirical interpolation expression derived in [277]. The active layers are highlighted in pink.

A.3. Single QW SOA section with narrow (SOA_1) and wide (SOA_2) QW

Function	Material	E_g, uıStrain, %	d, nm	N_{dop}, cm-3	n_{refr}	T_{gr}, °C
Standoff	InP	0.92	40	n.i.d.	3.167	610
p-Waveguide	$In_{0.79}Ga_{0.22}As_{0.47}P_{0.53}$	1.13	235	n.i.d.	3.334	610
p-Barrier	$In_{0.52}Al_{0.48}As$	0.86	20	n.i.d.	3.26	610
QW *(SOA_1)*	$In_{0.81}Ga_{0.19}As_{0.86}P_{0.14}$	1.55 -1.34	6.2	n.i.d.	3.6	610
QW *(SOA_2)*	$In_{0.75}Ga_{0.25}As$	1.55 -1.47	3.2	n.i.d.	3.6	610
n-Barrier	InP	0.92	10	n.i.d./1e17	3.167	650-610
n-Waveguide	$In_{0.53}Al_{0.27}Ga_{0.20}As$	1.07	235	n.i.d./2e17 δ-dop. 2e18	3.334	650
Buffer	InP	0.92	250	2e18-1e17	3.167	610
Wet etch stop layer	$In_{0.70}Ga_{0.30}As_{0.65}P_{0.35}$	1.25	10	2e18	3.341	610
Buffer	InP	0.92	800	1.5e18	3.167	610
Substrate (µm)	InP	0.92	350		3.167	610

E_g is the energy bandgap for bulk materials or the ground state transition for QWs and QDs, d is the layer thickness, N_{dop} is the nominal doping concentration during growth, n_{refr} is the refractive index at 1.55 µm, T_{gr} is the growth temperature; n.i.d. - nonintentionally doped.

A.2. Reference single c-QW SOA section with a symmetric SCH structure

Function	Material	E_g, uıStrain, %	d, nm	N_{dop}, cm-3	n_{refr}	T_{gr}, °C
Standoff	InP	0.92	40	n.i.d.	3.167	610
p-Waveguide	$In_{0.85}Ga_{0.15}As_{0.32}P_{0.68}$	1.05	235	n.i.d.	3.279	610
p-Barrier	$In_{0.49}Ga_{0.51}As_{0.86}P_{0.14}$	1.32 0.78	4.6	n.i.d.	3.435	610
QW	$In_{0.75}Ga_{0.25}As_{0.86}P_{0.14}$	1.55 -1.02	6.5	n.i.d.	3.6	610
n-Barrier	$In_{0.49}Ga_{0.51}As_{0.86}P_{0.14}$	1.32 0.78	4.6	n.i.d.	3.435	610
n-Waveguide	$In_{0.85}Ga_{0.15}As_{0.32}P_{0.68}$	1.05	235	5e17	3.279	610
Buffer	InP	0.92	250	2e18-1e17	3.167	610
Wet etch stop layer	$In_{0.70}Ga_{0.30}As_{0.65}P_{0.35}$	1.25	10	2e18	3.341	610
Buffer	InP	0.92	800	1.5e18	3.167	610
Substrate (µm)	InP	0.92	350		3.167	610

A.3. "Offset" ABL QW SOA section

Function	Material	E_g, uıStrain, %	d, nm	N_{dop}, cm-3	n_{refr}	T_{gr}, °C
Standoff	InP	0.92	50	n.i.d.	3.167	610
p-Barrier	$In_{0.52}Al_{0.48}As$	0.86	20	n.i.d.	3.26	610
QW *(SOA_2)*	$In_{0.75}Ga_{0.25}As$	1.60 -1.47	3.6	n.i.d.	3.6	610
n-Barrier	InP	0.92	10	n.i.d.	3.167	650-610
n-Waveguide	$In_{0.53}Al_{0.27}Ga_{0.20}As$	1.07	470	1e17-2e18	3.334	650
Buffer	InP	0.92	250	1e17	3.167	610
Wet etch stop layer	$In_{0.70}Ga_{0.30}As_{0.65}P_{0.35}$	1.25	10	2e18	3.341	610
Buffer	InP	0.92	800	1.5e18	3.167	610
Substrate (µm)	InP	0.92	350		3.167	610

A.4. InAs/InGaAsP/InP QD SOA section

Function		Material	E_g, um	d, nm	N_{dop}, cm-3	n_{refr}	T_{gr}, °C
Standoff		InP	0.92	50	n.i.d.	3.167	610
p-Waveguide		$In_{0.83}Ga_{0.17}As_{0.38}P_{0.62}$	1.08	160	n.i.d.	3.300	610
x 3	**Barrier**	$In_{0.83}Ga_{0.17}As_{0.38}P_{0.62}$	1.08	30	n.i.d.	3.300	610
	Barrier	$In_{0.83}Ga_{0.17}As_{0.38}P_{0.62}$	1.08	10	n.i.d.	3.300	515
	Cap layer	GaAs		1.7 ML	n.i.d.		515
	QDs	InAs	1.55	1.65 ML	n.i.d.	3.6	515
Barrier		$In_{0.83}Ga_{0.17}As_{0.38}P_{0.62}$	1.08	30	n.i.d.	3.300	610
n-Waveguide		$In_{0.83}Ga_{0.17}As_{0.38}P_{0.62}$	1.08	160	n.i.d./2e17 δ-dop. 2e18	3.300	610
Buffer		InP	0.92	250	2e18-1e17	3.167	610
Wet etch stop layer		$In_{0.70}Ga_{0.30}As_{0.65}P_{0.35}$	1.25	10	2e18	3.341	610
Buffer		InP	0.92	800	1.5e18	3.167	610
Substrate (µm)		InP	0.92	350		3.167	610

A.5. InAs/AlGaInAs/InP QD SOA section

Function	Material	E_g, um	d, nm	N_{dop}, cm-3	n_{refr}	T_{gr}, °C
Standoff	InP	0.92	40	n.i.d.	3.167	610
p-Waveguide	$In_{0.79}Ga_{0.22}As_{0.47}P_{0.53}$	1.13	150	n.i.d.	3.334	610
p-Barrier	$In_{0.52}Al_{0.48}As$	0.86	20	n.i.d.	3.26	610
Barrier	InP	0.92	5	1e17	3.167	485
QDs	InAs	1.55	0.5	n.i.d.	3.6	485
Barrier	InP	0.92	5	n.i.d.	3.167	610
Spacer	$In_{0.53}Al_{0.27}Ga_{0.20}As$	1.07	20	n.i.d.	3.334	610
Barrier	InP	0.92	5	n.i.d.	3.167	485
QDs	InAs	1.55	0.5	n.i.d.	3.6	485
Barrier	InP	0.92	0.5	n.i.d.	3.167	650-610
n-Waveguide	$In_{0.53}Al_{0.27}Ga_{0.20}As$	1.07	150	n.i.d./2e17 δ-dop. 2e18	3.334	650
Buffer	InP	0.92	250	2e18-1e17	3.167	610
Wet etch stop layer	$In_{0.70}Ga_{0.30}As_{0.65}P_{0.35}$	1.25	10	2e18	3.341	610
Buffer	InP	0.92	800	1.5e18	3.167	610
Substrate (µm)	InP	0.92	350		3.167	610

A.6. MQW EAM section

Function	Material	E_g, uıStrain, %		d, nm	N_{dop}, cm-3	n_{refr}	T_{gr}, °C
p-Waveguide	InP	0.92		120	n.i.d.	3.167	610
p-Waveguide	$In_{0.85}Ga_{0.15}As_{0.32}P_{0.68}$	1.13		50	n.i.d.	3.334	610
p-Waveguide	$In_{0.70}Ga_{0.30}As_{0.65}P_{0.35}$	1.25		50	2e18	3.341	610
Barrier	$In_{0.59}Al_{0.16}Ga_{0.25}As$	1.3	-0.4	6.6	n.i.d.	3.47	650
***n* x QW**	$In_{0.46}Ga_{0.54}As$	1.5	0.52	8.6	n.i.d.	3.51	650
Barrier	$In_{0.59}Al_{0.16}Ga_{0.25}As$	1.3	-0.4	6.6	n.i.d.	3.47	650
n-Waveguide	$In_{0.85}Ga_{0.15}As_{0.32}P_{0.68}$	1.13		50	n.i.d.	3.334	610
Buffer	InP	0.92		350	2e18-1e17	3.167	610
Buffer	InP	0.92		800	1.5e18	3.167	610
Substrate (µm)	InP	0.92		350		3.167	610

n is the number of QWs which was varied to obtained the desired absorption strength. The WG layer thicknesses were adjusted for the optimal mode coupling (here the WGs were optimized for *n*=8).

A.7. Long-wavelength MQW absorber section

Function	Material	E_g, uıStrain, %	d, nm	N_{dop}, cm-3	n_{refr}	T_{gr}, °C
p-Waveguide	InP	0.92	120	n.i.d.	3.167	610
p-Waveguide	$In_{0.85}Ga_{0.15}As_{0.32}P_{0.68}$	1.13	50	n.i.d.	3.334	610
p-Waveguide	$In_{0.70}Ga_{0.30}As_{0.65}P_{0.35}$	1.25	50	2e18	3.341	610
Barrier	$In_{0.53}Al_{0.07}Ga_{0.40}As$	1.44	6	n.i.d.	3.50	650
***4* x QW**	$In_{0.53}Ga_{0.47}As$	1.60	10.6	n.i.d.		650
Barrier	$In_{0.53}Al_{0.07}Ga_{0.40}As$	1.44	6	n.i.d.	3.50	650
n-Waveguide	$In_{0.85}Ga_{0.15}As_{0.32}P_{0.68}$	1.13	50	n.i.d.	3.334	610
Buffer	InP	0.92	350	2e18-1e17	3.167	610
Buffer	InP	0.92	800	1.5e18	3.167	610
Substrate (µm)	InP	0.92	350		3.167	610

A.8. Laser upper cladding

Function	Material	E_g, um	d, nm	N_{dop}, cm-3	n_{refr}	T_{gr}, °C
Protective layer	InP	0.92	20	n.i.d.	3.167	610
Contact	$In_{0.53}Ga_{0.47}As$	1.65	175	>1e19	3.533	610
Contact	$In_{0.70}Ga_{0.30}As_{0.65}P_{0.35}$	1.25	100	5e18	3.341	610
Cladding	InP:Zn	0.92	25	2e18-5e18	3.167	610
Cladding	InP:Zn	0.92	550	2e18	3.167	610
Cladding	InP:Zn	0.92	*125*	1.5e18-2e18	3.167	610
Cladding	InP:Zn	0.92	*75*	0.75e18-1.5e18	3.167	610
Cladding	InP:Zn	0.92	400	0.25e18-0.75e18	3.167	610
Cladding	InP:Zn	0.92	500	0.1e18-0.25e18	3.167	610
Cladding	InP:Zn	0.92	*100*	8e17-1e17	3.167	610
Wet etch stop*	$In_{0.79}Ga_{0.22}As_{0.47}P_{0.53}$	1.13	10	1e17	3.334	610
Dry etch stop*	$In_{0.52}Al_{0.48}As$	0.86	20	9e17	3.26	610
Spacer	InP	0.92	10	1e17	3.167	610
Spacer	InP	0.92	10	Diffused from ↑	3.167	610

* depends if the wet or dry etching approach was used for the ridge waveguide etching (see Appendix B.2)

Appendix B

Process Flow

The appendix contains a step-by-step process flow used for the fabrication of integrated MLLs studying in the thesis. The MLL mask layout can be found in Figure 4.22 (a) and the schematic of MLLs processing was presented in Figure 4.23. All process steps were performed at the DANCHIP cleanroom using facilities available during the work on this Ph.D. project. The recipes need to be tested and adjusted in case of transferring to another machine.

B.1. Butt-joint Regrowth Process

1. Mask layer deposition

Cleaning	Acetone – 5 min; ethanol – 1 min; DI-water – 1 min; N2 blow dry
SiO2 deposition (100 nm)	PECVD SiH4/N2O/N2 12/392/1420 sccm, 550 mTorr, 100 W, 300 ^{o}C. Deposition rate: ~ 90 nm/min

2. SAG mask definition

Photoresist coating	HMDS – 15 min, air – 5 min; AZ5206E spinning 4000 rpm, 4000 rpm/s – 30 s (~ 600 nm); Softbake 90°C – 90 s	
UV exposure	Vacuum mode, 5 mW/cm2 – 3.5 s	
Development	AZ351B:DI-water (1:5 VP) – 45 s; DI-water – 1 min; N2 blow dry	
Postbake	90°C – 90 s	
Mask etching	Dry etching	Wet etching1
	RIE CHF3/O2 16/2 sccm; 100 mTorr; 60 W, RT. Etch rate (SiO2): ~ 29 nm/min	BHF – 60 s; DI-water – 1 min; N2 blow dry
Resist removal	Acetone – 5 min; ethanol – 1 min; DI-water – 1 min; N2 blow dry O2 plasma ashing 0.2 mbar, 100 W - 5 min	

3. Mesa block etching

Etching down to the InP buffer layer	ICP-RIE HBr/CH4/Ar 10/5/2 sccm, 1 mTorr, 600 W ICP, 50 W RF, 180°C. Etch rate (InP): ~ 200 nm/min; etch rate (SiO2): ~ 16 nm/min
Water rinse	DI-water – rinse; N2 blow dry
Wet etching of the InP buffer layer down to the stop layer	HCl:H3PO4 1:4 – 30 - 60 s, DI-water – 1 min; N2 blow dry, Etching rate (InP): 0.5 µm/min; etching rate (Q(1.1)): < 2 nm/min

Mask under-etching	H2SO4:H2O2:H2O 1:8:80 ~ 10-20 s for QW SOA and ~ 2.5 min for QD SOA (should be adjusted for each epi-structure)

4. Pre-growth cleaning

Ashing	O2 plasma ashing 0.2 mbar, 100 W - 5 min
Wet etching	H2SO4 – 5 min; DI-water – 1 min; DI-water – 3 min; N2 blow dry
In-situ deoxidation	Annealing at 650°C under PH3 atmosphere – 15 min

5. MOVPE growth of an EAM

SiO2 mask removal	BHF – 60 s; DI-water – 1 min; N2 blow dry

6. Pre-growth cleaning (see step 4)

7. MOVPE growth of a top cladding

[1]Improved edge roughness, but pattern definition suffers from underetching.

B.2. Device Fabrication

1. SiO2 mask layer deposition

Cleaning	Acetone – 5 min; ethanol – 1 min; DI-water – 1 min; N2 blow dry
InP Cap Layer Removal	HCl:H3PO4 (1:4 VP) – 1 min, DI-water – 1 min; N2 blow dry. Etch rate (InP) ~ 0.5 µm/min
SiO2 deposition (100 nm or 300 nm)	PECVD SiH4/N2O/N2 12/1420/392 sccm, 550 mTorr, 100 W, 300°C. Deposition rate: ~ 90 nm/min

2. Ridge mask definition

Photoresist coating with ~ 600 nm AZ5206E	HMDS – 15 min, air – 5 min; AZ5206E spinning 4000 rpm, 4000rpm/s – 30 s; Softbake 90°C – 90 s
UV exposure	Vacuum mode, 5 mW/cm2 – 3.5 s
Development	AZ351B:DI-water (1:5 VP) – 45 s; DI-water – 1 min; N2 blow dry
Postbake	90°C – 90 s
Descum	O2 plasma ashing 0.2 mbar, 40 W - 1 min
Mask etching	RIE CHF3/O2 16/2 sccm; 100 mTorr; 60 W, RT. Etch rate (SiO2): ~ 29 nm/min
Resist removal	Acetone – 5 min; ethanol – 1 min; DI-water – 1 min; N2 blow dry O2 plasma ashing 0.2 mbar, 100 W - 5 min

3. Ridge waveguide etching

3.a. Dry etching approach

Etching of ~ ½ top cladding	ICP-RIE Cl2/Ar/N2 20/10/40 sccm, 2 mTorr, 500W ICP, 100 W RF, 180°C – ~ 2 min. Etch rate (InP): ~ 500 nm/min; etch rate (SiO2): ~ 35 nm/min

Contact separation gap opening by UV lithography and SiO2 RIE etching:

Photoresist coating with ~ 2 µm AZ5214	Baking 150°C – 45 min
	HMDS – 15 min, air – 5 min;
	AZ5214 spinning 4000 rpm, 2000 rpm/s – 30 s;
	Softbake 90°C – 120 s
UV exposure	Vacuum mode, 5 mW/cm2 – 10 s
Development	AZ351B:DI-water (1:5 VP) – 60 s; DI-water – 1 min; N2 blow dry
Postbake	120°C – 120 s
Mask etching	RIE CHF3/O2 16/2 sccm; 100mTorr; 60 W, RT. Etch rate (SiO2): ~ 29 nm/min
Finishing etching of the top cladding down to stop layer and contact layers in the separation gaps	RIE CH4/H2 8.4/42 sccm, 80 mTorr, 60 W (with cyclic O2 injection to remove polymer). Etch rate (InP): ~ 29 nm/min, etch rate (InGaAs): ~ 9 nm/min

3.b. Wet etching approach

Etching through the contact layers	ICP-RIE Cl2/Ar/N2 20/10/40 sccm, 2 mTorr, 500W ICP, 100 W RF, 180°C – ~ 1 min. Etch rate (InP): ~ 500 nm/min; etch rate (SiO2): ~ 35 nm/min
Wet etching of InP upper cladding down to the stop layer	HCl:H3PO4 1:4 – 4 min, DI-water – 1 min; N2 blow dry, Etching rate (InP): 0.5 µm/min; etching rate(Q(1.1)): < 2 nm/min

Contact separation gap opening by UV lithography and SiO2 RIE etching (see step 3.a)

Wet etching of the contact layers in the separation gaps	H2SO4(10%) : H2O2 1:1 – 45 s, DI-water – 1 min; N2 blow dry
Resist removal	Acetone – 5 min; ethanol – 1 min; DI-water – 1 min; N2 blow dry
	O2 plasma ashing 0.2 mbar, 100 W - 5 min

4. BCB planarization

SiO2 deposition (~ 25 nm)	PECVD SiH4/N2O/N2 12/1420/392 sccm, 550 mTorr, 100 W, 300 oC. Deposition rate: ~ 90 nm/min
BCB coating	AP3000 spinning 1000 rpm, 1000 rpm/s – 60 s (open);
	Softbake 150°C – 1 min
	BCB (Cyclotene 3022-46) spinning 2000 rpm, 4000 rpm/s – 60 s (~ 3.5 µm);
	Softbake 170°C – 6 min
	Curing in an oven at 250°C – ~ 3 h
Etching back	RIE CHF3/O2 24/8 sccm; 30 mTorr; 30 W, RT. Etch rate (BCB): ~ 144 nm/min; etch rate (SiO2): ~ 29 nm/min

5. Top side (p-type) metallization

Photoresist coating2	Positive tone resist	Negative tone resist
	AP3000 spinning 1000 rpm, 1000 rpm/s – 60 s (open);	AP3000 spinning 1000 rpm, 1000 rpm/s – 60 s (open);
	Softbake 150°C – 1 min	Softbake 150°C – 1 min
	LOR5B spinning 4000 rpm, 4000	AZ2020 spinning 2000 rpm, 4000

	rpm/s – 45 s (~ 500 nm);	rpm/s – 60 s (~ 2 µm);
	Softbake 170°C – 5 min	Softbake 110°C – 60 s
	AZ5206 spinning 4000 rpm, 4000 rpm/s – 30 s (~ 600 nm);	
	Softbake 90°C – 90 s	
UV exposure	Vacuum mode, 5mW/cm2 – 7 s	Vacuum mode, 5mW/cm2 – 10 s
Post Exposure Bake	-	PEB 110°C – 60 s
Development	AZ351B:DI-water 1:5 – 120 s; DI-water – 1 min; N2 blow dry	AZ726 MIF – 120 s; DI-water – 1 min; N2 blow dry
SiO2 mask removal	BHF – 60 s; DI-water – 1 min; N2 blow dry	BHF – 60 s; DI-water – 1 min; N2 blow dry
Metal evaporation	Ti/Pt/Au 50/75/500 nm	Ti/Pt/Au 50/75/500 nm
Lift-off	Remover 1165 at 65°C – ~ 30 min; acetone – rinse; isopropanol – 1 min; N2 blow dry	Acetone – 15 min; ethanol – 1 min; N2 blow dry

6. Back side thinning

Wafer bonding	Bonding a wafer with wax to a glass carrier using a hot plate at 60-70°C
Thinning down to ~ 100 µm	Lapping down ~ 10 µm/min using 3 µm Al2O3 powder
Wafer release	Ecoclear at 65°C – ~ 30 min; ethanol – 1 min; N2 blow dry

7. Back side (n-type) metallization

Contact metal evaporation	Ni/Ge/Au 80/100/250 nm
Annealing	Rapid Thermal Annealing at 420°C - 5 s (n-side up)
Die-bonding metal evaporation	Ti/Pt/Au 50/75/500 nm

8. Cleaving into bars and die-bonding

Cleaving	Scribing with a precision of ~ 5 µm; manual cleaving
Die-bonding	Eutectic metal soldering at 335 °C (pulse heat) using Au/Sn 80/20 alloy (forming gas 10% H2 in N2) to AlN carriers with metallic coatings

9. High-reflection and anti-reflection coating

Cleaning	O2 plasma ashing 0.2 mbar, 100W - 2 min
Dielectric evaporation	AR coating: 1 pair of TiOx/SiO2 130/206.8 nm [110]
	HR coating: 4 pairs of SiO2/Si 266.7/121.9 nm [110]

[2] Negative tone AZ2020 resist showed better robustness for the lift-off process. Beware of the need to use AZ726 MIF developer containing TMAH, which is very toxic.

B.2.1. ICP-RIE Processes

For SAG mesa block etching by ICP-RIE, the critical requirements are surface smoothness and low etch rates allowing for good control over the etch depth. In spite of the following wet etching step, damaging ICP-RIE can lead to deterioration of the stop layer and process failure. For ridge waveguide etching it is important to achieve high anisotropy and smooth sidewalls. The process optimization was carried out within the FLASH project on SPTS ICP-RIE etcher (Inductively Coupled Plasma) equipped with a variety of process gases. The platen temperature is limited by 180°C, although better results on chlorine-based InP etching are typically reported at temperatures of 200°C and higher due to the low volatility of $InCl_3$ etch product. As a result, "grassy" surface morphology was often observed.

Process "J" – used for SAG etching:

- HBr/CH4/Ar 10/5/2 sccm, 1 mTorr, 600 W ICP, 50 W RF, 180°C
- Etch rate (InP): ~ 200 nm/min; etch rate (SiO2): ~ 16 nm/min
- Mirror-like surface
- An undercut profile and slight "grassy" sidewall roughness, pronounced under the mask, which could be due to continuing lateral etching during the process with the effect of micro-masking.

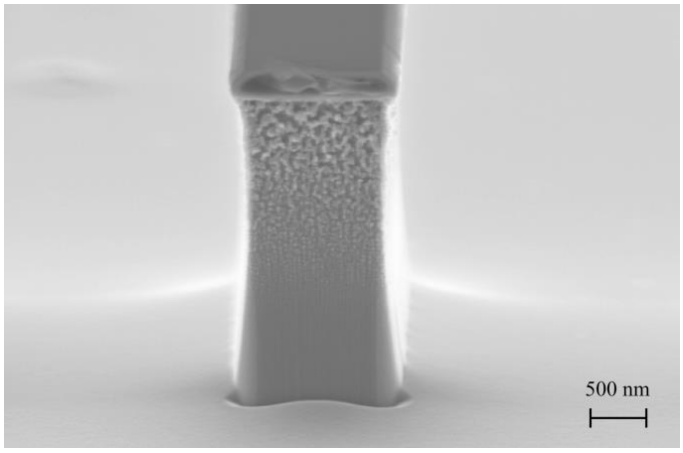

Figure B.1: SEM image of InP test structure etched with HBr/CH4/Ar gas mixture.

Process "D":

- Cl2/CH4/Ar 10/7/2 sccm, 1 mTorr, 600 W ICP, 50 W RF, 180°C
- Etch rate (InP): ~ 200 nm/min; etch rate (SiO2): ~ 40 nm/min
- Sidewall angle is close to 90°
- Strong micro-masking effect ("grassy" surface) as a result of the low volatility of InClx as a reaction product

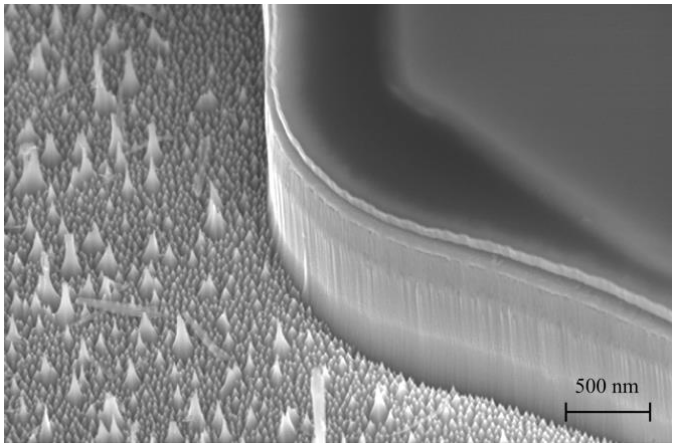

Figure B.2: SEM image of InP/AlGaInAsP test structure etched with Cl2/CH4/Ar gas mixture.

The sidewalls roughness was significantly improved compare to the result presented in Figure 4.24 (b), where the ***original SPTS chlorine-based etching*** process was used:

- ICP-RIE Cl2/Ar/N2 20/10/40 sccm, 2 mTorr, 500 W ICP, 100 W RF, 180°C
- Etch rate (InP): ~ 500 nm/min; etch rate (SiO2): ~ 35 nm/min
- Sidewall angle is 86 - 87°

B.2.2. Electroplating

If thick metal layers are required, e.g. to fabricate contact pads when BCB planarization is non-uniform for wide and narrow ridge waveguides, metal evaporation can be not feasible due to the limited holding capacity. In this case, an electroplating process can be considering. The results of the test process, described below, showed material spread-out within a separation gap only (Fig. 2) and contact interlocking. An improvement can be made in large part by optimizing the lithography step.

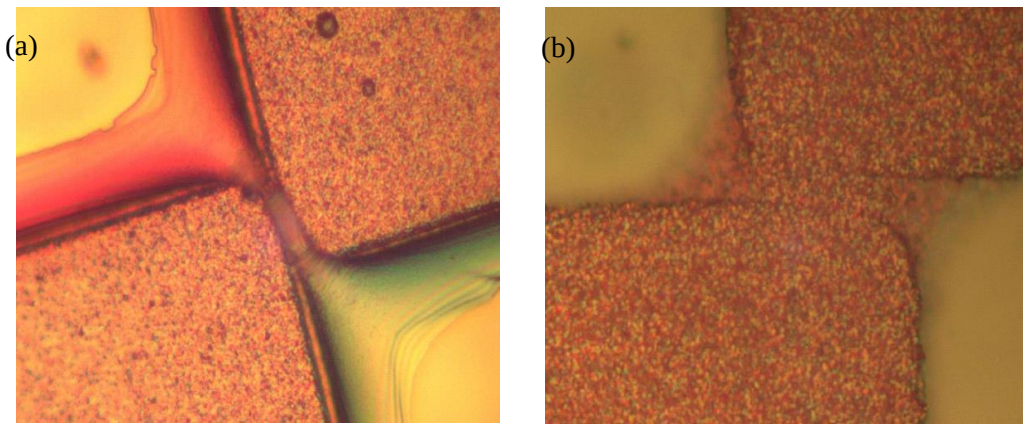

Figure B.3: Microphotographs of metal pads separated by 9 µm gap (a) after electroplating and (b) after lift-off and seed metal etching.

Electroplating of top side (p-type) metals

Seed metal evaporation	Ti/Pd/Au 50/50/50 nm
Photoresist coating	AZ4562 spinning 4000 rpm, 4000rpm/s – 30 s (~ 7.5);
	Softbake 100°C – 50 s; air – 10 min
UV exposure	Vacuum mode, 5 mW/cm2 – 120 s
Development	AZ351B:DI-water (1:5 VP) – 5 min; DI-water – 1 min; N2 blow dry
SiO2 deposition on the back side (~ 200 nm)	PECVD SiH4/N2O/N2 12/1420/392 sccm, 550 mTorr, 100 W, 300 ^{o}C. Deposition rate: ~ 90 nm/min
Resist descum	O2 plasma ashing 0.2 mbar, 40 W - 1 min
Electroplating	Au ~ 7.5 µm (done at IPU's technology development)
Lift-off	Remover 1165 at 65°C – ~ 30 min; acetone – rinse; isopropanol – 1 min; N2 blow dry
Seed metal etching	Pd/Au etching: 300g KI (solid):75g I2 (solid):1500mL H2O – 10 s; DI-water – 1 min; N2 blow dry
	Ti etching: BHF – 1 min; DI-water – 1 min; N2 blow dry (removes also SiO2 from the back side)

References

[1] E. B. Desurvire, “Capacity Demand and Technology Challenges for Lightwave Systems in the Next Two Decades,” *J. Light. Technol.*, vol. 24, no. 12, pp. 4697–4710, Dec. 2006.

[2] Http://www.ciscovni.com/forecast-widget/, *Cisco Visual Networking Index : Global Mobile Data Traffic Forecast Update, 2013 – 2018*. 2014.

[3] I. Kaminow, T. Li, and A. E. Willner, *Optical Fiber Telecommunications Volume VIA: Components and Subsystems*. Academic Press, 2013, p. 794.

[4] G. P. Agrawal, *Fiber-optic communication systems*. Wiley, 2010, p. 603.

[5] R. Ramaswami, K. Sivarajan, and G. Sasaki, *Optical Networks: A Practical Perspective*. Morgan Kaufmann, 2009, p. 982.

[6] R. S. . Tucker, G. . Eisenstein, and S. K. Korotky, “Optical Time-Division Multiplexing For Very High Bit-Rate Transmission,” *J. Light. Technol.*, vol. 6, no. 11, pp. 1737–1749, 1988.

[7] B. Kögel, J. S. Gustavsson, E. Haglund, R. Safaisini, A. Joel, P. Westbergh, M. Geen, R. Lawrence, and A. Larsson, “High-speed 850 nm VCSELs with 28 GHz modulation bandwidth operating error-free up to 44 Gbit/s,” *Electron. Lett.*, vol. 48, no. 18, pp. 1145–1147, Aug. 2012.

[8] D. M. Kuchta, C. L. Schow, A. V Rylyakov, J. E. Proesel, F. E. Doany, C. Baks, B. H. Hamel-Bissell, C. Kocot, L. Graham, R. Johnson, G. Landry, E. Shaw, A. MacInnes, and J. Tatum, “A 56.1Gb/s NRZ Modulated 850nm VCSEL-Based Optical Link,” in *Optical Fiber Communication Conference. Optical Society of America.*, 2013, p. OW1B–5.

[9] R. Safaisini, E. Haglund, A. Larsson, J. S. Gustavsson, E. P. Haglund, and P. Westbergh, “High-speed 850 nm VCSELs operating error free up to 57 Gbit/s,” *Electron. Lett.*, vol. 49, no. 16, pp. 1021–1023, Aug. 2013.

[10] W. Hofmann, “High-Speed Buried Tunnel Junction Vertical-Cavity Surface-Emitting Lasers,” *IEEE Photonics J.*, vol. 2, no. 5, pp. 802–815, Oct. 2010.

[11] W. Hofmann and D. Bimberg, “VCSEL-Based Light Sources—Scalability Challenges for VCSEL-Based Multi-100-Gb/s Systems,” *IEEE Photonics J.*, vol. 4, no. 5, pp. 1831–1843, Oct. 2012.

[12] J. Armstrong, “OFDM for Optical Communications,” *J. Light. Technol.*, vol. 27, no. 3, pp. 189–204, 2009.

[13] D. Hillerkuss, R. Schmogrow, T. Schellinger, M. Jordan, M. Winter, G. Huber, T. Vallaitis, R. Bonk, P. Kleinow, F. Frey, M. Roeger, S. Koenig, A. Ludwig, A. Marculescu, J. Li, M. Hoh, M. Dreschmann, J. Meyer, S. Ben Ezra, N. Narkiss, B. Nebendahl, F. Parmigiani, P. Petropoulos, B. Resan, A. Oehler, K. Weingarten, T. Ellermeyer, J. Lutz, M. Moeller, M. Huebner, J. Becker, C. Koos, W. Freude, and J. Leuthold, “26 Tbit s-1 line-rate super-channel transmission utilizing all-optical fast Fourier transform processing,” *Nat. Photonics*, vol. 5, no. May, pp. 364 – 371, 2011.

[14] H. C. H. Mulvad, L. K. Oxenløwe, M. Galili, A. T. Clausen, L. Gru, and P. Jeppesen, “1.28 Tbit/s single-polarisation serial OOK optical data generation and demultiplexing,” *Electron. Lett.*, vol. 45, no. 5, pp. 35–36, 2009.

[15] T. Richter, E. Palushani, M. Nölle, R. Ludwig, J. K. Fischer, and C. Schubert, "Single Wavelength Channel 10.2 Tb/s TDM-Data Capacity using 16-QAM and Coherent Detection," in *Optical Fiber Communication Conference. Optical Society of America.*, 2011, p. PDPA9.

[16] L. K. Oxenløwe, L. J. Christiansen, D. Larsson, K. Yvind, A. T. Clausen, J. Seoane, A. I. Siahlo, B. Sørensen, and P. Jeppesen, "Pre-scaled clock recovery with compact semiconductor devices for ultra high-speed OTDM systems," in *IEEE Eur. Conf. Optical Commun.(ECOC)*, 2004, pp. 2–3.

[17] M. Shirane, Y. Hashimoto, H. Kurita, H. Yamada, and H. Yokoyama, "Optical sampling measurement with all-optical clock recovery using mode-locked diode lasers," in *OSA/OFC*, 2001, no. Mlld 1, p. MG2.

[18] H. Kurita, Y. Hashimoto, I. Ogura, H. Yamada, and H. Yokoyama, "All-optical 3R regeneration based on optical clock recovery with mode-locked LDs," in *ECOC'99. 25th European Conference on Optical Communication*, 1999, pp. 195–200.

[19] H. Sanjoh, H. Yasaka, Y. Sakai, K. Sato, H. Ishii, and Y. Yoshikuni, "Multiwavelength light source with precise frequency spacing using a mode-locked semiconductor laser and an arrayed waveguide grating filter," *IEEE Photonics Technol. Lett.*, vol. 9, no. 6, pp. 818–820, Jun. 1997.

[20] S. Kawanishi, H. Takara, K. Uchiyama, I. Shake, and K. Mori, "3 Tbit/s (160 Gbit/s x 19 ch) OTDM/WDM Transmission Experiment," in *OSA/OFC*, 1999, no. d, p. PD1.

[21] A. A. Aboketaf, D. Adams, A. W. Elshaari, S. F. Preble, M. T. Crowley, L. F. Lester, and P. Ampadu, "Hybrid OTDM and WDM for multicore optical communication," *IEEE Int. Green Comput. Conf.*, pp. 1–5, Jun. 2012.

[22] R. G. Broeke, J. Cao, C. Ji, S. Seo, Y. Du, N. K. Fontaine, J.-H. Baek, J. Yan, F. M. Soares, F. Olsson, S. Lourdudoss, A. H. Pham, M. Shearn, A. Scherer, and S. J. Ben Yoo, "Optical-CDMA in InP," *IEEE J. Sel. Top. Quantum Electron.*, vol. 13, no. 5, pp. 1497–1507, 2007.

[23] P. R. Prucnal, *Optical code division multiple access : fundamentals and applications*. CRC Taylor & Francis, 2006, p. 377.

[24] H. Hu, F. Ye, A. K. Medhin, P. Guan, H. Takara, Y. Miyamoto, H. C. H. Mulvad, M. Galili, T. Morioka, and L. K. Oxenløwe, "Single Source 5-dimensional (Space-, Wavelength-, Time-, Polarization-, Quadrature-) 43 Tbit/s Data Transmission of 6 SDM × 6 WDM × 1.2 Tbit/s Nyquist-OTDM-PDM-QPSK," in *CLEO:2014*, 2014, p. JTh5B.

[25] Jens Ramskov, "DTU slår verdensrekord for datatransmission," *http://ing.dk/artikel/dtu-slaar-verdensrekord-datatransmission-169478*, 2014.

[26] M. Shirane, Y. Hashimoto, H. Yamada, and H. Yokoyama, "A compact optical sampling measurement system using mode-locked laser-diode modules," *IEEE Photonics Technol. Lett.*, vol. 12, no. 11, pp. 1537–1539, Nov. 2000.

[27] C. Schmidt-Langhorst and H.-G. Weber, "Optical sampling techniques," *J. Opt. Fiber Commun. Reports*, vol. 2, no. 1, pp. 86–114, Jun. 2005.

[28] C. Dorrer, "High-speed measurements for optical telecommunication systems," *IEEE J. Sel. Top. Quantum Electron.*, vol. 12, no. 4, pp. 843–858, Jul. 2006.

[29] G. C. Valley, "Photonic analog-to-digital converters," *Opt. Express*, vol. 15, no. 5, pp. 1955–1982, Mar. 2007.

[30] L. A. Jiang, E. P. Ippen, U. Feiste, S. Diez, E. Hilliger, C. Schmidt, and H. Weber, "Sampling Pulses with Semiconductor Optical Amplifiers," *IEEE J. Quantum Electron.*, vol. 37, no. 1, pp. 118–126, 2001.

[31] G. A. Keeler, B. E. Nelson, D. Agarwal, C. Debaes, N. C. Helman, A. Bhatnagar, and D. A. B. Miller, "The benefits of ultrashort optical pulses in optically interconnected systems," *IEEE J. Sel. Top. Quantum Electron.*, vol. 9, no. 2, pp. 477–485, Mar. 2003.

[32] S. Arahira, S. Oshiba, Y. Matsui, T. Kunii, and Y. Ogawa, "Terahertz-rate optical pulse generation from a passively mode-locked semiconductor laser diode," *Opt. Lett.*, vol. 19, no. 11, pp. 834–836, Jun. 1994.

[33] M. Wojtkowski, "High-speed optical coherence tomography: basics and applications," *Appl. Opt.*, vol. 49, no. 16, pp. D30–61, Jun. 2010.

[34] H. Guo, K. Sato, K. Takashima, and H. Yokoyama, "Two-photon Bio-imaging with a Mode-locked Semiconductor Laser," in *15th International Conference on Ultrafast Phenomena*, 2006, p. TuE8.

[35] S. Arahira, S. Oshiba, Y. Matsui, T. Kunii, and Y. Ogawa, "500 GHz optical short pulse generation from a monolithic passively mode-locked distributed Bragg reflector laser diode," *Appl. Phys. Lett.*, vol. 64, no. 15, p. 1917, 1994.

[36] J. E. Bowers, P. a. Morton, a. Mar, and S. W. Corzine, "Actively mode-locked semiconductor lasers," *IEEE J. Quantum Electron.*, vol. 25, no. 6, pp. 1426–1439, Jun. 1989.

[37] D. Auston, "Transverse mode locking," *IEEE J. Quantum Electron.*, vol. 4, no. 5, p. 372, 1968.

[38] H. A. Haus, "Mode-Locking of Lasers," *IEEE J. Sel. Top. Quantum Electron.*, vol. 6, no. 6, pp. 1173–1185, 2000.

[39] U. Keller, "Recent developments in compact ultrafast lasers," *Nature*, vol. 424, pp. 831–838, Aug. 2003.

[40] D. J. Derickson, P. A. Morton, and J. E. Bowers, "Comparison of timing jitter in external mode-locked semiconductor lasers and monolithic cavity," *Appl. Phys. Lett*, vol. 59, no. 26, pp. 3372–3374, 1991.

[41] R. Rosales, S. G. Murdoch, R. T. Watts, K. Merghem, A. Martinez, F. Lelarge, A. Accard, L. P. Barry, and A. Ramdane, "High performance mode locking characteristics of single section quantum dash lasers," *Opt. Express*, vol. 20, no. 8, pp. 8649–8657, 2012.

[42] Z. G. Lu, J. R. Liu, S. Raymond, P. J. Poole, P. J. Barrios, and D. Poitras, "312-fs pulse generation from a passive C-band InAs/InP quantum dot mode-locked laser," *Opt. Express*, vol. 16, no. 14, pp. 10835–10840, Jul. 2008.

[43] S. Joshi, C. Calò, N. Chimot, M. Radziunas, R. Arkhipov, S. Barbet, A. Accard, A. Ramdane, and F. Lelarge, "Quantum dash based single section mode locked lasers for photonic integrated circuits," *Opt. Express*, vol. 22, no. 9, p. 11254, May 2014.

[44] R. Kaiser, B. Hüttl, H. Heidrich, S. Fidorra, W. Rehbein, H. Stolpe, R. Stenzel, W. Ebert, and G. Sahin, "Tunable Monolithic Mode-Locked Lasers on InP With Low Timing Jitter," *IEEE Photonics Technol. Lett.*, vol. 15, no. 5, pp. 634–636, 2003.

[45] A. Clausen, H. N. Poulsen, L. K. Oxenløwe, A. Siahlo, J. Seoane, and P. Jeppesen, "Pulse source requirements for OTDM systems," in *LEOS*, 2003, no. 1, pp. 382–383.

[46] M. Jinno, “Effects of crosstalk and timing jitter on all-optical time-division demultiplexing using a nonlinear fiber Sagnac interferometer switch,” *IEEE J. Quantum Electron.*, vol. 30, no. 12, pp. 2842–2853, 1994.

[47] L. A. Jiang, E. P. Ippen, and H. Yokoyama, “Semiconductor mode-locked lasers as pulse sources for high bit rate data transmission,” *J. Opt. Fiber Commun. Reports*, vol. 2, no. 1, pp. 1–31, May 2005.

[48] P.-T. Ho, L. a. Glasser, E. P. Ippen, and H. a. Haus, “Picosecond pulse generation with a cw GaAlAs laser diode,” *Appl. Phys. Lett.*, vol. 33, no. 3, p. 241, 1978.

[49] K. A. Williams, M. G. Thompson, and I. H. White, “Long-wavelength monolithic mode-locked diode lasers,” *New J. Phys.*, vol. 6, pp. 179–179, Nov. 2004.

[50] D. Larsson, K. Yvind, and J. M. Hvam, “High-Power and Low-Noise 10-GHz All-Active Monolithic Mode-Locked Lasers with Surface Etched Bragg Grating,” in *Conference on Lasers and Electro-Optics (CLEO)*, 2007, p. CWA3.

[51] E. A. Avrutin, J. H. Marsh, and E. L. Portnoi, “Monolithic and multi-GigaHertz mode-locked semiconductor lasers: Constructions, experiments, models and applications,” *IEE Proceedings-Optoelectronics*, vol. 147, no. 4, pp. 251–278, 2000.

[52] K. Yvind, D. Larsson, L. J. Christiansen, L. K. Oxenlowe, J. Mork, J. M. Hvam, and J. Hanberg, “Design and evaluation of mode-locked semiconductor lasers for low noise and high stability,” in *Opto-Ireland 2005: Optoelectronics, Photonic Devices, and Optical Networks*, 2005, vol. 5825, pp. 37–48.

[53] K. Yvind, D. Larsson, L. J. Christiansen, C. Angelo, L. K. Oxenløwe, J. Mørk, D. Birkedal, J. M. Hvam, and J. Hanberg, “Low-Jitter and High-Power 40-GHz All-Active Mode-Locked Lasers,” *IEEE Photonics Technol. Lett.*, vol. 16, no. 4, pp. 975–977, 2004.

[54] K. Merghem, A. Akrout, A. Martinez, G. Moreau, J.-P. Tourrenc, F. Lelarge, F. Van Dijk, G.-H. Duan, G. Aubin, and A. Ramdane, “Short pulse generation using a passively mode locked single InGaAsP/InP quantum well laser,” *Opt. Express*, vol. 16, no. 14, pp. 10675–83, Jul. 2008.

[55] K. Sato, A. Hirano, and H. Ishii, “Lasers Integrated with Electroabsorption Modulators and Chirped Gratings,” *IEEE J. Sel. Top. Quantum Electron.*, vol. 5, no. 3, pp. 590–595, 1999.

[56] R. Scollo, H. J. Lohe, J. F. Holzman, F. Robin, H. Jäckel, D. Erni, W. Vogt, and E. Gini, “Mode-locked laser diode with an ultrafast integrated uni-traveling carrier saturable absorber,” *Opt. Lett.*, vol. 30, no. 20, pp. 2808–2810, Oct. 2005.

[57] J. J. Coleman, J. D. Young, and A. Garg, “Semiconductor Quantum Dot Lasers: A Tutorial,” *J. Light. Technol.*, vol. 29, no. 4, pp. 499–510, 2011.

[58] E. U. Rafailov, M. A. Cataluna, and W. Sibbett, “Mode-locked quantum-dot lasers,” *Nat. Photonics*, vol. 1, no. 7, pp. 395–401, Jul. 2007.

[59] M. A. Cataluna, E. U. Rafailov, A. D. McRobbie, W. Sibbett, D. A. Livshits, and A. R. Kovsh, “Stable Mode-Locked Operation up to 80 C From an InGaAs Quantum-Dot Laser,” *IEEE Photonics Technol. Lett.*, vol. 18, no. 14, pp. 1500–1502, 2006.

[60] M. G. Thompson, A. R. Rae, R. V. Penty, and I. H. White, “InGaAs Quantum-Dot Mode-Locked Laser Diodes,” *IEEE J. Sel. Top. Quantum Electron.*, vol. 15, no. 3, pp. 661–672, 2009.

[61] M. G. Thompson, D. Larson, a. R. Rae, K. Yvind, R. V. Penty, I. H. White, J. Hvam, a. R. Kovsh, S. S. Mikhrin, D. a. Livshits, and I. L. Krestnikov, “Monolithic Hybrid and Passive Mode-Locked 40GHz

Quantum Dot Laser Diodes," in *2006 European Conference on Optical Communications*, 2006, no. 1, pp. 1–2.

[62] K. Yvind, D. Larsson, J. Mørk, J. M. Hvam, M. Thompson, R. Penty, and I. White, "Low-noise monolithic mode-locked semiconductor lasers through low-dimensional structures," in *Proceedings of SPIE Novel In-Plane Semiconductor Lasers VII*, 2008, vol. 6909, p. 69090A.

[63] R. Schwertberger, D. Gold, J. P. Reithmaier, and A. Forchel, "Long-Wavelength InP-Based Quantum-Dash Lasers," *IEEE Photonics Technol. Lett.*, vol. 14, no. 6, pp. 735–737, Jun. 2002.

[64] P. Caroff, C. Paranthoen, C. Platz, O. Dehaese, H. Folliot, N. Bertru, C. Labbé, R. Piron, E. Homeyer, a. Le Corre, and S. Loualiche, "High-gain and low-threshold InAs quantum-dot lasers on InP," *Appl. Phys. Lett.*, vol. 87, no. 24, p. 243107, 2005.

[65] H. Y. Liu, D. T. Childs, T. J. Badcock, K. M. Groom, I. R. Sellers, M. Hopkinson, R. A. Hogg, D. J. Robbins, D. J. Mowbray, and M. S. Skolnick, "InAs – GaAs Quantum-Dot Lasers With Very Low Continuous-Wave Room-Temperature Threshold Currents," *IEEE Photonics Technol. Lett.*, vol. 17, no. 6, pp. 3–6, 2005.

[66] G. T. Liu, A. Stintz, H. Li, K. J. Malloy, and L. F. Lester, "Extremely low room-temperature threshold current density diode lasers using lnAs dots in In0.5Ga0.85As quantum well," *Electron. Lett.*, vol. 35, no. 14, pp. 1163–1165, 1999.

[67] R. L. Sellin, C. Ribbat, M. Grundmann, N. N. Ledentsov, and D. Bimberg, "Close-to-ideal device characteristics of high-power InGaAs/GaAs quantum dot lasers," *Appl. Phys. Lett.*, vol. 78, no. 9, p. 1207, 2001.

[68] M. Dontabactouny, R. Piron, K. Klaime, N. Chevalier, K. Tavernier, S. Loualiche, a. Le Corre, D. Larsson, C. Rosenberg, E. Semenova, and K. Yvind, "41 GHz and 10.6 GHz low threshold and low noise InAs/InP quantum dash two-section mode-locked lasers in L band," *J. Appl. Phys.*, vol. 111, no. 2, p. 023102, 2012.

[69] R. Rosales, K. Merghem, A. Martinez, A. Akrout, J. Tourrenc, A. Accard, F. Lelarge, and A. Ramdane, "InAs/InP Quantum-Dot Passively Mode-Locked," *IEEE J. Sel. Top. Quantum Electron.*, vol. 17, no. 5, pp. 1292–1301, 2011.

[70] G. Duan, A. Shen, A. Akrout, F. Van, F. Lelarge, F. Pommereau, O. Legouezigou, J. Provost, H. Gariah, F. Blache, and F. Mallecot, "High Performance InP-Based Quantum Dash Semiconductor Mode-Locked Lasers for Optical Communications," *Bell Labs Tech. J.*, vol. 14, no. 3, pp. 63–84, 2009.

[71] D. Gready, G. Eisenstein, C. Gilfert, V. Ivanov, and J. P. Reithmaier, "High-Speed Low-Noise InAs/InAlGaAs/InP 1.55-μm Quantum-Dot Lasers," *IEEE PHOTONICS Technol. Lett.*, vol. 24, no. 10, pp. 809–811, 2012.

[72] P. W. Smith, "Mode-Locking of Lasers," *Proc. IEEE*, vol. 58, no. 9, pp. 1342–1357, 1970.

[73] H. A. Haus, "Theory of mode locking with a slow saturable absorber," *IEEE J. Quantum Electron.*, vol. 11, no. 9, pp. 736–746, 1975.

[74] H. A. Haus, "Modelocking of Semiconductor Laser Diodes," *Jpn. J. Appl. Phys.*, vol. 20, no. 6, pp. 1007–1020, 1981.

[75] A. E. Siegman, *Lasers*. University Science Books, 1986, p. 1283.

[76] R. Paschotta and U. Keller, "Passive mode locking with slow saturable absorbers," *Appl. Phys. B Lasers Opt.*, vol. 73, no. 7, pp. 653–662, Nov. 2001.

[77] G. P. Agrawal and A. N. Olsson, "Self-phase modulation and spectral broadening of optical pulses in semiconductor laser amplifiers," *IEEE J. Quantum Electron.*, vol. 25, no. 11, pp. 2297–2306, 1989.

[78] R. Scollo, "Mode-locked InP based Laser Diode with a Monolithic Integrated UTC-Absorber for sub-ps Pulse Generation," *PhD thesis*, p. SWISS FEDERAL INSTITUTE OF TECHNOLOGY ZURICH, 2009.

[79] L. A. Coldren, S. W. Corzine, and M. L. Masanovic, *Diode Lasers and Photonic Integrated Circuits*. Wiley-Blackwell, 2012, p. 709.

[80] M. T. Crowley, D. Murrell, N. Patel, M. Breivik, C. Lin, Y. Li, B. Fimland, and L. F. Lester, "Analytical Modeling of the Temperature Performance of Monolithic Passively Mode-Locked Quantum Dot Lasers," *IEEE J. Quantum Electron.*, vol. 47, no. 8, pp. 1059–1068, 2011.

[81] C.-Y. Lin, Y.-C. Xin, Y. Li, F. L. Chiragh, and L. F. Lester, "Cavity design and characteristics of monolithic long-wavelength InAs/InP quantum dash passively mode-locked lasers," *Opt. Express*, vol. 17, no. 22, pp. 19739–48, Oct. 2009.

[82] J. K. Mee, R. Raghunathan, J. B. Wright, and L. F. Lester, "Device geometry considerations for ridge waveguide quantum dot mode-locked lasers," *J. Phys. D. Appl. Phys.*, vol. 47, no. 23, p. 233001, Jun. 2014.

[83] Y. Xin, Y. Li, V. Kovanis, A. L. Gray, L. Zhang, and L. F. Lester, "Reconfigurable quantum dot monolithic multi- section passive mode-locked lasers," *Opt. Express*, vol. 15, no. 12, pp. 7623–7633, 2007.

[84] D. J. Derickson, R. J. Helkey, A. Mar, J. R. Karin, J. G. Wasserbauer, and J. E. Bowers, "Short Pulse Generation Using Multisegment Mode-Locked Semconductor Lasers," *IEEE J. Quantum Electron.*, vol. 28, no. 10, pp. 2186–2202, 1992.

[85] R. G. M. P. Koumans and R. Van Roijen, "Theory for Passive Mode-Locking in Laser Structures Including the Effects of Self-Phase Modulation, Dispersion, and Pulse Collisions," *IEEE J. Quantum Electron.*, vol. 32, no. 3, pp. 478–492, 1996.

[86] S. Bischoff, J. Mørk, T. Franck, S. D. Brorson, M. Hofmann, K. Fröjdh, L. Prip, and M. P. Sørensen, "Monolithic colliding pulse mode-locked semiconductor lasers," *Quantum Semiclassical Opt. J. Eur. Opt. Soc. Part B*, vol. 9, no. 5, pp. 655–674, Oct. 1997.

[87] M. C. Wu, "Monolithic colliding-pulse mode-locked quantum-well lasers," *IEEE J. Quantum Electron.*, vol. 28, no. 10, pp. 2176–2185, 1992.

[88] D. J. Jones, L. M. Zhang, J. E. Carroll, and D. D. Marcenac, "Dynamics of Monolithic Passively Mode-Locked Semiconductor Lasers," *J. Quantum Electron.*, vol. 31, no. 6, pp. 1051–1058, 1995.

[89] J. R. Karin, R. J. Helkey, D. J. Derickson, R. Nagarajan, D. S. Allin, J. E. Bowers, and R. L. Thornton, "Ultrafast dynamics in field-enhanced saturable absorbers," *Appl. Phys. Lett.*, vol. 64, no. 6, pp. 676–678, 1994.

[90] E. L. Portnoi and A. V. Chelnokov, "Generation of High Repetition Frequency Subpicosecond Pulses at 1.535 vm by Passive Mode-Locking of InGaAsPAnP Laser Diode with Saturable Absorber Regions Created by Ion Implantation," in *12th IEEE International Semiconductor Laser Conference*, 1991, pp. 107–108.

[91] J. T. Gopinath, E. R. Thoen, E. M. Koontz, M. E. Grein, L. a. Kolodziejski, E. P. Ippen, and J. P. Donnelly, "Recovery dynamics in proton-bombarded semiconductor saturable absorber mirrors," *Appl. Phys. Lett.*, vol. 78, no. 22, pp. 3409–3411, 2001.

[92] P. Finch, P. Blood, P. M. Smowton, A. Sobiesierski, and R. M. Gwilliam, "Femtosecond pulse generation in passively mode locked InAs quantum dot lasers," *Appl. Phys. Lett*, vol. 131109, no. 103, pp. 3–6, 2013.

[93] M. Dulk, E. Dobeli, and H. Melchior, "Fabrication of saturable absorbers in InGaAsP-InP bulk semiconductor laser diodes by heavy ion implantation," *IEEE J. Sel. Top. Quantum Electron.*, vol. 7, no. 2, pp. 124–134, 2001.

[94] E. Lugagne Delpon, J. L. Oudar, N. Bouché, R. Raj, A. Shen, N. Stelmakh, and J. M. Lourtioz, "Ultrafast excitonic saturable absorption in ion-implanted InGaAs/InAlAs multiple quantum wells," *Appl. Phys. Lett.*, vol. 72, no. 7, pp. 759–761, 1998.

[95] F. Romstad, "Absorption and refractive index dynamics in waveguide semiconductor electroabsorbers," *PhD thesis*, p. Technical University of Denmark, 2002.

[96] R. P. Green, M. Haji, L. Hou, G. Mezosi, R. Dylewicz, and A. E. Kelly, "Fast saturable absorption and 10 GHz wavelength conversion in Al-quaternary multiple quantum wells," *Opt. Express*, vol. 19, no. 10, pp. 9737–9743, May 2011.

[97] J. Mark and J. Moerk, "Subpicosecond and theory gain dynamics in InGaAsP optical amplifiers: Experiment and Theory," *Appl. Phys. Lett.*, vol. 61, no. 19, pp. 2281–2283, 1992.

[98] S. Bischoff, M. P. Sørensen, J. Mørk, S. D. Brorson, T. Franck, J. M. Nielsen, and A. Møller-Larsen, "Pulse-shaping mechanism in colliding-pulse mode-locked laser diodes," *Appl. Phys. Lett.*, vol. 67, no. 26, pp. 3877–3879, 1995.

[99] C. Xing and E. A. Avrutin, "Multimode spectra and active mode locking potential of quantum dot lasers," *J. Appl. Phys.*, vol. 97, no. 10, p. 104301, 2005.

[100] G. P. Agrawal, "Effect of gain dispersion on ultrashort pulse amplification in semiconductor laser amplifiers," *IEEE J. Quantum Electron.*, vol. 27, no. 6, pp. 1843–1849, 1991.

[101] F. X. Kärtner and U. Keller, "Stabilization of solitonlike pulses with a slow saturable absorber," *Opt. Lett.*, vol. 20, no. 1, pp. 16–8, Jan. 1995.

[102] R. Paschotta, "Dispersion Compensation," *Encyclopedia of Laser Physics and Technology*. Wiley-VCH, p. 856, 2008.

[103] M. J. Strain and M. Sorel, "Design and Fabrication of Integrated Chirped Bragg Gratings for On-Chip Dispersion Control," *IEEE J. Quantum Electron.*, vol. 46, no. 5, pp. 774–782, May 2010.

[104] H. A. Haus and A. Mecozzi, "Noise of Mode-Locked Lasers," *IEEE J. Quantum Electron.*, vol. 29, no. 3, pp. 983–996, 1993.

[105] R. Paschotta, "Noise of mode-locked lasers (Part II): timing jitter and other fluctuations," *Appl. Phys. B*, vol. 79, no. 2, pp. 163–173, May 2004.

[106] D. Eliyahu, R. a. Salvatore, and A. Yariv, "Effect of noise on the power spectrum of passively mode-locked lasers," *J. Opt. Soc. Am. B*, vol. 14, no. 1, pp. 167–174, Jan. 1997.

[107] D. Von der Linde, "Characterization of the noise in continuously operating mode-locked lasers," *Appl. Phys. B Photophysics Laser Chem.*, vol. 39, no. 4, pp. 201–217, Apr. 1986.

[108] M. J. R. Heck, E. J. Salumbides, A. Renault, E. a J. M. Bente, Y.-S. Oei, M. K. Smit, R. van Veldhoven, R. Nötzel, K. S. E. Eikema, and W. Ubachs, "Analysis of hybrid mode-locking of two-section quantum dot lasers operating at 1.5 um," *Opt. Express*, vol. 17, no. 20, pp. 18063–75, Sep. 2009.

[109] L. Drzewietzki, S. Breuer, and W. Elsäßer, "Timing jitter reduction of passively mode-locked semiconductor lasers by self- and external-injection: Numerical description and experiments," *Opt. Express*, vol. 21, no. 13, p. 16142, Jun. 2013.

[110] K. Yvind, "Semiconductor Mode-Locked Lasers for Optical Communication Systems," *PhD thesis*, p. Technical University of Denmark, 2003.

[111] F. Camacho, E. a. Avrutin, P. Cusumano, a. Saher Helmy, a. C. Bryce, and J. H. Marsh, "Improvements in mode-locked semiconductor diode lasers using monolithically integrated passive waveguides made by quantum-well intermixing," *IEEE Photonics Technol. Lett.*, vol. 9, no. 9, pp. 1208–1210, Sep. 1997.

[112] D. Bimberg and U. W. Pohl, "Quantum dots: promises and accomplishments," *Mater. Today*, vol. 14, no. 9, pp. 388–397, 2011.

[113] J. Gomis-Bresco, S. Dommers-Völkel, O. Schöps, Y. Kaptan, O. Dyatlova, D. Bimberg, and U. Woggon, "Time-resolved amplified spontaneous emission in quantum dots," *Appl. Phys. Lett.*, vol. 97, p. 251106, 2010.

[114] T. W. Berg and J. Mørk, "Quantum dot amplifiers with high output power and low noise," *Appl. Phys. Lett.*, vol. 82, no. 18, pp. 3083–3085, 2003.

[115] B. S. Ooi, H. S. Djie, Y. Wang, C. Tan, J. C. M. Hwang, X. Fang, J. M. Fastenau, A. W. K. Liu, G. T. Dang, and W. H. Chang, "Quantum Dashes on InP Substrate for Broadband Emitter Applications," *IEEE J. Sel. Top. Quantum Electron.*, vol. 14, no. 4, pp. 1230–1238, 2008.

[116] E. U. Rafailov, P. Loza-Alvarez, W. Sibbett, G. S. Sokolovskii, D. a. Livshits, a. E. Zhukov, and V. M. Ustinov, "Amplification of femtosecond pulses over by 18 dB in a quantum-dot semiconductor optical amplifier," *IEEE Photonics Technol. Lett.*, vol. 15, no. 8, pp. 1023–1025, Aug. 2003.

[117] T. W. Berg, S. Bischoff, I. Magnusdottir, and J. Mørk, "Ultrafast Gain Recovery and Modulation Limitations in Self-Assembled Quantum-Dot Devices," *IEEE Photonics Technol. Lett.*, vol. 13, no. 6, pp. 541–543, 2001.

[118] J. Urayama, T. Norris, J. Singh, and P. Bhattacharya, "Observation of Phonon Bottleneck in Quantum Dot Electronic Relaxation," *Phys. Rev. Lett.*, vol. 86, no. 21, pp. 4930–4933, May 2001.

[119] M. Sugawara, K. Mukai, and H. Shoji, "Effect of phonon bottleneck on quantum-dot laser performance," *Appl. Phys. Lett.*, vol. 71, no. 19, p. 2791, 1997.

[120] R. Heitz, H. Born, F. Guffarth, O. Stier, A. Schliwa, A. Hoffmann, and D. Bimberg, "Existence of a phonon bottleneck for excitons in quantum dots," *Phys. Rev. B*, vol. 64, no. 24, p. 241305, Nov. 2001.

[121] K. Ikeda, H. Sekiguchi, F. Minami, J. Yoshino, Y. Mitsumori, H. Amanai, S. Nagao, and S. Sakaki, "Phonon bottleneck effects in InAs/GaInP quantum dots," *J. Lumin.*, vol. 108, no. 1–4, pp. 273–276, Jun. 2004.

[122] L. F. Lester, D. J. Kane, N. G. Usechak, C.-Y. Lin, Y. Li, Y.-C. Xin, and V. Kovanis, "Pulse characteristics of passively mode-locked quantum dot lasers," *Proc. SPIE Nov. In-pl. Semicond. Lasers IX*, vol. 7616, p. 761607, Feb. 2010.

[123] Y. Li, L. F. Lester, D. Chang, C. Langrock, M. M. Fejer, and D. J. Kane, "Characteristics and instabilities of mode-locked quantum-dot diode lasers.," *Opt. Express*, vol. 21, no. 7, pp. 8007–17, May 2013.

[124] A. Markus, J. X. Chen, C. Paranthoën, A. Fiore, C. Platz, and O. Gauthier-Lafaye, "Simultaneous two-state lasing in quantum-dot lasers," *Appl. Phys. Lett.*, vol. 82, no. 12, pp. 1818–1820, 2003.

[125] B. Johann, P. Reithmaier, G. Eisenstein, and A. Forchel, "InAs/InP Quantum-Dash Lasers and Amplifiers," *Proc. IEEE*, vol. 95, no. 9, pp. 1779–1790, 2007.

[126] N. Majer, "Nonlinear Gain Dynamics of Quantum Dot Semiconductor Optical Amplifier," *PhD thesis*, p. Technischen Universität Berlin, 2012.

[127] G. Gélinas, A. Lanacer, R. Leonelli, R. a. Masut, and P. J. Poole, "Carrier thermal escape in families of InAs/InP self-assembled quantum dots," *Phys. Rev. B*, vol. 81, no. 23, p. 235426, Jun. 2010.

[128] L. V Asryan, M. Grundmann, N. N. Ledentsov, O. Stier, R. A. Suris, and D. Bimberg, "Effect of Excited-State Transitions on the Threshold Characteristics of a Quantum Dot Laser," *IEEE J. Quantum Electron.*, vol. 37, no. 3, pp. 418–425, 2001.

[129] M. van der Poel, E. Gehrig, O. Hess, D. Birkedal, and J. M. Hvam, "Ultrafast gain dynamics in quantum-dot amplifiers: theoretical analysis and experimental investigations," *IEEE J. Quantum Electron.*, vol. 41, no. 9, pp. 1115–1123, Sep. 2005.

[130] I. Magnusdottir, S. Bischoff, a. Uskov, and J. Mørk, "Geometry dependence of Auger carrier capture rates into cone-shaped self-assembled quantum dots," *Phys. Rev. B*, vol. 67, no. 20, p. 205326, May 2003.

[131] S. G. Li, Q. Gong, C. F. Cao, X. Z. Wang, J. Y. Yan, Y. Wang, and H. L. Wang, "The developments of InP-based quantum dot lasers," *Infrared Phys. Technol.*, vol. 60, pp. 216–224, Sep. 2013.

[132] D. Kunimatsu, S. Arahira, Y. Kato, and Y. Ogawa, "Passively mode-locked laser diodes with bandgap-wavelength detuned saturable absorbers," *IEEE Photonics Technol. Lett.*, vol. 11, no. 11, pp. 1363–1365, Nov. 1999.

[133] Lohe H.-J., "Monolithic integration of mode locked laser diodes with fast absorber in MOVPE based local InGaAsP / InP technology using growth," 2007.

[134] R. Scollo, H. Lohe, F. Robin, D. Erni, E. Gini, and H. Jäckel, "Mode-Locked InP-Based Laser Diode With a Monolithic Integrated UTC Absorber for Subpicosecond Pulse Generation," *IEEE J. Quantum Electron.*, vol. 45, no. 4, pp. 322–335, 2009.

[135] O. Wada, *Optoelectronic integration: Physics, technology and applications*. Kluwer, 1994, p. 458.

[136] T. F. Kuech, L. J. Mawst, and A. S. Brown, "Mixed semiconductor alloys for optical devices," *Annu. Rev. Chem. Biomol. Eng.*, vol. 4, pp. 187–209, Jan. 2013.

[137] J. W. Raring, M. N. Sysak, A. Tauke-Pedretti, M. Dummer, E. J. Skogen, J. S. Barton, S. P. DenBaars, and L. A. Coldren, "Advanced Integration Schemes for High-Functionality/High- Performance Photonic Integrated Circuits," in *Proc. of SPIE Nanophotonic Packaging*, 2006, vol. 6126, p. 61260H.

[138] Y. Omigawa, Y. Kinoshita, N. Yamamoto, A. Kanno, K. Akahane, T. Kawanishi, and H. Sotobayashi, "Photonic crystal fiber based ultra-broadband transmission system for waveband division multiplexing," in *Proc. of SPIE*, 2011, vol. 8073, p. 80732T–80732T–1.

[139] M. Allovon and M. Quillec, "Interest in AlGalnAs on InP for optoelectronic applications," *IEE Proceedings-J*, vol. 139, no. 2, pp. 148–152, 1992.

[140] I. Vurgaftman, J. R. Meyer, and L. R. Ram-Mohan, "Band parameters for III–V compound semiconductors and their alloys," *J. Appl. Phys.*, vol. 89, no. 11, p. 5815, 2001.

[141] H. Temkin, K. Alavi, W. R. Wagner, T. P. Pearsall, and A. Y. Cho, "1.5–1.6-μm Ga0.47In0.53As/Al0.48In0.52As multiquantum well lasers grown by molecular beam epitaxy," *Appl. Phys. Lett.*, vol. 42, no. 10, pp. 845–847, 1983.

[142] C. E. Zah, R. Bhat, F. J. Favire, M. Koza, T. P. Lee, D. Darby, D. C. Flanders, and J. J. Hsieh, "Low threshold 1.3 um strained-layer AIxGayIn1-x-yAs quantum well lasers," *Electron. Lett.*, vol. 28, no. 25, p. 2323, 1992.

[143] A. Tandon, D. P. Bour, Y. L. Chang, C. K. Lin, S. W. Corzine, and M. R. Tan, "Low threshold, high To and high efficiency 1300nm and 1500nm lasers with AlInGaAs active region grown by MOCVD," in *Physics and Simulation of Optoelectronic Devices XII*, 2004, vol. 5349, no. 100, pp. 206–217.

[144] A. Grabmaier, A. Hangleiter, G. Fuchs, J. E. A. Whiteaway, and R. W. Glew, "Low nonlinear gain in InGaAs/InGaAlAs separate confinement multiquantum well lasers," *Appl. Phys. Lett.*, vol. 59, no. 23, pp. 3024–3026, 1991.

[145] T. Higashi, S. J. Sweeney, A. F. Phillips, A. R. Adams, E. P. O'Reilly, T. Uchida, and T. Fujii, "Observation of Reduced Nonradiative Current in 1.3-um AlGaInAs – InP Strained MQW Lasers," *IEEE Photonics J.*, vol. 11, no. 4, pp. 409–411, 1999.

[146] D. Biswas, A. Chin, J. Pamulapati, and P. Bhattacharya, "Traps in molecular beam epitaxial In0.53(GaxAl1−x)0.47As/InP," *J. Appl. Phys.*, vol. 67, no. 5, pp. 2450–2453, 1990.

[147] V. A. Shchukin, N. N. Ledentsov, L. Y. Karachinsky, S. A. Blokhin, I. I. Novikov, N. A. Bogoslovskiy, and A. V. Savelyev, "Efficient electro-optic semiconductor medium based on type-II heterostructures," *Semiconductors*, vol. 47, no. 11, pp. 1528–1538, Nov. 2013.

[148] M. Kondow, T. Kitatani, S. Nakatsuka, M. C. Larson, K. Nakahara, Y. Yazawa, M. Okai, and K. Uomi, "GaInNAs: a novel material for long-wavelength semiconductor lasers," *IEEE J. Sel. Top. Quantum Electron.*, vol. 3, no. 3, pp. 719–730, Jun. 1997.

[149] M. Le Du, J.-C. Harmand, O. Mauguin, L. Largeau, L. Travers, and J.-L. Oudar, "Quantum-well saturable absorber at 1.55 μm on GaAs substrate with a fast recombination rate," *Appl. Phys. Lett.*, vol. 88, p. 201110, 2006.

[150] J. M. Ripalda, D. Granados, Y. González, a. M. Sánchez, S. I. Molina, and J. M. García, "Room temperature emission at 1.6μm from InGaAs quantum dots capped with GaAsSb," *Appl. Phys. Lett.*, vol. 87, no. 20, p. 202108, 2005.

[151] L. Seravalli, P. Frigeri, G. Trevisi, and S. Franchi, "1.59 μm room temperature emission from metamorphic InAs⁄InGaAs quantum dots grown on GaAs substrates," *Appl. Phys. Lett.*, vol. 92, no. 21, p. 213104, 2008.

[152] A. R. Adams, "Band-structure engineering for low-threshold high-efficiency semiconductor," *Electron. Lett.*, vol. 22, no. 5, pp. 249–250, 1986.

[153] E. Yablonovitch and E. O. Kane, “Band structure engineering of semiconductor lasers for optical communications,” *J. Light. Technol.*, vol. 6, no. 8, pp. 1292 – 1299, 1988.

[154] P. J. A. Thijs, L. F. Tiemeijer, J. J. M. Binsma, and T. Van Dongen, “Progress in Long-Wavelength Strained-Layer InGaAs(P) Quantum- Well Semiconductor Lasers and Amplifiers,” *IEEE J. Quantum Electron.*, vol. 30, no. 2, pp. 477–499, 1994.

[155] M. T. Crowley, N. Patel, D. Murrell, Y.-C. Xin, A. Stintz, and L. F. Lester, “Comparison Of Monolithic Passively Mode-Locked Lasers Using In(Ga)As Quantum Dot or Quantum Well Materials Grown on GaAs Substrates,” *Int. J. High Speed Electron. Syst.*, vol. 20, no. 03, pp. 713–725, Sep. 2011.

[156] M. Asada, A. R. Adams, K. E. Stubkjaer, Y. Suematsu, Y. Itaya, and S. Arai, “The Temperature Dependence of the Threshold Current of GaInAsP/InP DH Lasers,” *J. Quantum Electron.*, vol. QE-17, no. 5, pp. 611–619, 1981.

[157] M. Asada, a. Kameyama, and Y. Suematsu, “Gain and intervalence band absorption in quantum-well lasers,” *IEEE J. Quantum Electron.*, vol. 20, no. 7, pp. 745–753, Jul. 1984.

[158] A. R. Adams, K. C. Heasman, and J. Hilton, “A reassessment of intervalence band absorption in 1.6 μm (GaIn)(AsP)/InP,” *Semicond. Sci. Technol.*, vol. 2, no. 12, pp. 761–764, 1987.

[159] A. Haug, “Auger recombination in direct-gap semiconductors: band-structure effects,” *J. Phys. C Solid State Phys.*, vol. 16, pp. 4159–4172, 1983.

[160] N. K. Dutta and R. J. Nelson, “The case for Auger recombination in In1−xGaxAsyP1−y,” *J. Appl. Phys.*, vol. 53, no. 1, pp. 74–92, 1982.

[161] N. A. Gun’ko, A. S. Polkovnikov, and G. G. Zegrya, “A numerical calculation of auger recombination coefficients for InGaAsP/InP quantum well heterostructures,” *Semiconductors*, vol. 34, no. 4, pp. 448–452, Apr. 2000.

[162] A. S. Polkovnikov and G. G. Zegrya, “Auger recombination in semiconductor quantum wells,” *Phys. Rev. B*, vol. 58, no. 7, pp. 4039–4056, Aug. 1998.

[163] R. I. Taylor, R. A. Abram, M. G. Burt, and C. Smith, “A detailed study of Auger recombination in 1.3μm InGaAsP/InP quantum wells and quantum well wires,” *Semicond. Sci. Technol.*, vol. 5, no. 1, pp. 90–104, 1990.

[164] J. Piprek, J. K. White, and A. J. SpringThorpe, “What Limits the Maximum Output Power of Long-Wavelength AlGaInAs/InP Laser Diodes?,” *IEEE J. Quantum Electron.*, vol. 38, no. 9, pp. 1253–1259, 2002.

[165] R.F. Kazarinov e G.L. Belenky, “Novel design of AlGaInAs-Inp lasers operating at 1.3 um,” *IEEE J. Quantum Electron.*, vol. 31, no. 3, pp. 423–426, 1995.

[166] H. Murai, Y. Matsui, Y. Ogawa, and T. Kunii, “Lasing characteristics under high temperature operation of 1.55pm strained InGaAsP/lnGaAIAs,” *Electron. Lett.*, vol. 3, no. 24, pp. 2105–2107, 1995.

[167] A. E. Zhukov, N. V. Kryzhanovskaya, F. I. Zubov, Y. M. Shernyakov, M. V. Maximov, E. S. Semenova, K. Yvind, and L. V. Asryan, “Improvement of temperature-stability in a quantum well laser with asymmetric barrier layers,” *Appl. Phys. Lett.*, vol. 100, no. 2, p. 021107, 2012.

[168] P. Abraham, J. Piprek, S. P. Denbaars, and J. E. Bowers, “Study of temperature effects on loss mechanisms in 1.55 μm laser diodes layer with In0.81Ga0.19P electron stopper layer,” *Semicond. Sci. Technol.*, vol. 14, pp. 419–424, 1999.

[169] L. V Asryan, N. V Kryzhanovskaya, M. V Maximov, A. Y. Egorov, and A. E. Zhukov, "Bandedge-engineered quantum well laser," *Semicond. Sci. Technol.*, vol. 26, no. 5, p. 055025, May 2011.

[170] D. Olego, "Compositional dependence of band-gap energy and conduction-band effective mass of In1−x−yGaxAlyAs lattice matched to InP," *Appl. Phys. Lett.*, vol. 41, no. 5, p. 476, 1982.

[171] E. A. Avrutin, B. S. Ryvkin, J. Kostamovaara, and E. L. Portnoi, "Analysis of Symmetric and Asymmetric Broadened-Mode Laser Structures for Short and Ultrashort Optical Pulse Generation," in *IEEE 12th International Conference on Transparent Optical Networks (ICTON)*, 2010, pp. 1–4.

[172] M. Lysevych, H. H. Tan, F. Karouta, and C. Jagadish, "Effect of active region position in Fabry-Perot single transverse mode broad-waveguide InGaAsP/InP lasers," *Opt. Express*, vol. 22, no. 7, pp. 8156–8164, 2014.

[173] Y. Zhang, "Design of ultra-high power multisection tunable lasers," *IEEE J. Sel. Top. Quantum Electron.*, vol. 12, no. 4, pp. 760–766, Jul. 2006.

[174] R. Scollo, W. Vogt, E. Gini, F. Robin, D. Erni, R. Harbers, and J. Heinz, "A Multiple Regrowth Process for Monolithically-Integrated InP-Based Mode-Locked Laser Diodes with Uni-Travelling Carrier Absorber," *Proc. SPIE Integr. Opt. Silicon Photonics, Photonic Integr. Circuits*, vol. 6183, p. 61831K–1, 2006.

[175] G. B. Morrison, J. W. Raring, C. S. Wang, E. J. Skogen, Y.-C. Chang, M. Sysak, and L. a. Coldren, "Electroabsorption modulator performance predicted from band-edge absorption spectra of bulk, quantum-well, and quantum-well-intermixed InGaAsP structures," *Solid. State. Electron.*, vol. 51, no. 1, pp. 38–47, Jan. 2007.

[176] L. V. Asryan and S. Luryi, "Effect of internal optical loss on threshold characteristics of semiconductor lasers with a quantum-confined active region," *IEEE J. Quantum Electron.*, vol. 40, no. 7, pp. 833–843, Jul. 2004.

[177] C. H. Henry, R. A. Logan, R. F. Merritt, and J. P. Luongo, "The Effect of Intervalence Band Absorption on the Thermal Behavior of InGaAsP Lasers," *IEEE J. Quantum Electron.*, vol. QE-19, no. 6, pp. 947–952, 1983.

[178] J. Taylor and V. Tolstikhin, "Intervalence band absorption in InP and related materials for optoelectronic device modeling," *J. Appl. Phys.*, vol. 87, no. 3, pp. 1054–1059, 2000.

[179] F. Fiedler and A. Schlachetzki, "Optical parameters of InP-based waveguides," *Solid. State. Electron.*, vol. 30, no. 1, pp. 73–83, 1987.

[180] Y. S. Yong, H. Y. Wong, and H. K. Yow, "Novel Separate Confinement Heterostructure Design for Long-Wavelength Lasers," *IEEE Electron Device Lett.*, vol. 32, no. 7, pp. 925–927, 2011.

[181] R. Jakomin, "MOVPE growth of InP-based III-V compounds doped with transition metals (Fe, Mn)," *PhD thesis*, p. Universita' degli studi di Parma, 2008.

[182] G. J. van Gurp, P. R. Boudewijn, M. N. C. Kempeners, and D. L. a. Tjaden, "Zinc diffusion in n-type indium phosphide," *J. Appl. Phys.*, vol. 61, no. 5, p. 1846, 1987.

[183] G. J. van Gurp, D. L. a. Tjaden, G. M. Fontijn, and P. R. Boudewijn, "Zinc diffusion in InGaAsP," *J. Appl. Phys.*, vol. 64, no. 7, p. 3468, 1988.

[184] M. S. Hybertsen, M. A. Adam, G. A. Baraff, R. K. Smith, G. L. Belenky, D. V. Donetsky, G. E. Shtengel, C. L. Reynolds, and R. F. Kazarinov, "Role of doping profile on semiconductor laser

performance: simulation and experiment," in *Lasers and Electro-Optics, CLEO'99*, 1999, vol. 347, no. 1980, pp. 309–310.

[185] U. W. Pohl, *Epitaxy of semiconductors : introduction to physical principles*. Springer, 2013, p. 326.

[186] G. B. Stringfellow, *Organometallic vapor-phase epitaxy : Theory and practice*. Academic Press, 1999, p. 572.

[187] J. J. Coleman, "Metalorganic chemical vapor deposition for optoelectronic devices," *Proc. IEEE*, vol. 85, no. 11, pp. 1715–1729, 1997.

[188] Matthews J.W. and Blakeslee A.E., "Defects in epitaxial multilayers. I. Misfit dislocations," *J. Cryst. Growth*, vol. 27, no. 1, pp. 118 – 125, 1974.

[189] S. Arakawa, M. Itoh, and A. Kasukawa, "In-Situ Etching of Semiconductor with CBr4 in Metalorganic Chemical Vapor Deposition (MOCVD) Reactor," *Jpn. J. Appl. Phys.*, vol. 41, no. Part 1, No. 2B, pp. 1076–1079, Feb. 2002.

[190] N. Dupuis, J. Décobert, P.-Y. Lagrée, N. Lagay, D. Carpentier, and F. Alexandre, "Demonstration of planar thick InP layers by selective MOVPE," *J. Cryst. Growth*, vol. 310, no. 23, pp. 4795–4798, Nov. 2008.

[191] R. Bhat, M. a. Koza, K. Kash, S. J. Allen, W. P. Hong, S. a. Schwarz, G. K. Chang, and P. Lin, "Growth of high quality AlInAs by low pressure organometallic chemical vapor deposition for high speed and optoelectronic device applications," *J. Cryst. Growth*, vol. 108, pp. 441–448, Feb. 1991.

[192] J. S. Roberts, J. P. R. David, L. Smith, and P. L. Tihanyi, "The influence of trimethylindium impurities on the performance of InAlGaAs single quantum well lasers," *J. Cryst. Growth*, vol. 195, no. 1–4, pp. 668–675, Dec. 1998.

[193] S. A. Rushworth, L. M. Smith, M. S. Ravetz, K. M. Coward, R. Odedra, R. Kanjolia, S. W. Bland, F. Dimroth, and A. W. Bett, "Correlation of reduced oxygen content in precursors with improved MOVPE layer quality," *J. Cryst. Growth*, vol. 248, pp. 86–90, Feb. 2003.

[194] M. Borgstrom, M. P. Pires, T. Bryllert, S. Landi, W. Seifert, and P. L. Souza, "InAs quantum dots grown on InAlGaAs lattice matched to InP," *J. Cryst. Growth*, vol. 252, no. 4, pp. 481–485, May 2003.

[195] P. B. Sishir Bhowmick, Md Zunaid Baten, Thomas Frost, Boon S. Ooi, "High Performance InAs/In0.53Ga0.23Al0.24As/InP Quantum Dot 1.55 μm Tunnel Injection Laser," *IEEE J. Quantum Electron.*, vol. 50, no. 1, pp. 7–14, 2014.

[196] T. D. Germann, "MOVPE Processes," in *Design and Realization of Novel GaAs Based Laser Concepts*, Berlin, Heidelberg: Springer Berlin Heidelberg, 2012, pp. 27–53.

[197] R. Beanland, D. Dunstan, and GoodhewPJ, "Plastic relaxation and relaxed buffer layers for semiconductor epitaxy," *Adv. Phys.*, vol. 45, no. 2, pp. 87 – 146, 1996.

[198] X. S. Jiang, A. R. Clawson, and P. K. L. Yu, "Study of interrupted MOVPE growth of InGaAs/InP superlattice," *J. Cryst. Growth*, vol. 124, pp. 547–552, Nov. 1992.

[199] F. E. G. Guimarães, B. Elsner, R. Westphalen, B. Spangenberg, H. J. Geelen, P. Balk, and K. Heime, "LP-MOVPE growth and optical characterization of GaInP/GaAs heterostructures: interfaces, quantum wells and quantum wires," *J. Cryst. Growth*, vol. 124, no. 1–4, pp. 199–206, Nov. 1992.

[200] J. Decobert and G. Patriarche, "Transmission electron microscopy study of the InP/InGaAs and InGaAs/InP heterointerfaces grown by metalorganic vapor-phase epitaxy," *J. Appl. Phys.*, vol. 92, no. 10, p. 5749, 2002.

[201] D. Leonard, K. Pond, and P. M. Petroff, "Critical layer thickness for self-assembled InAs islands on GaAs," *Phys. Rev. B*, vol. 50, no. 16, 1994.

[202] D. Bimberg, M. Grundmann, F. Heinrichsdorff, N. N. Ledentsov, V. M. Ustinov, a. E. Zhukov, a. R. Kovsh, M. V. Maximov, Y. M. Shernyakov, B. V. Volovik, a. F. Tsatsul'nikov, P. S. Kop'ev, and Z. I. Alferov, "Quantum dot lasers: breakthrough in optoelectronics," *Thin Solid Films*, vol. 367, no. 1–2, pp. 235–249, May 2000.

[203] S. Yoon, Y. Moon, T.-W. Lee, E. Yoon, and Y. D. Kim, "Effects of As/P exchange reaction on the formation of InAs/InP quantum dots," *Appl. Phys. Lett.*, vol. 74, no. 14, p. 2029, 1999.

[204] F. Lelarge, B. Dagens, J. Renaudier, R. Brenot, A. Accard, Frederic van Dijk, D. Make, O. Le Gouezigou, J. Provost, F. Poingt, J. Landreau, O. Drisse, E. Derouin, B. Rousseau, F. Pommereau, and G.-H. Duan, "Recent Advances on InAs/InP Quantum Dash Based Semiconductor Lasers and Optical Amplifiers," *IEEE J. Sel. Top. Quantum Electron.*, vol. 13, no. 1, pp. 111–124, 2007.

[205] E. S. Semenova, I. V. Kulkova, S. Kadkhodazadeh, M. Schubert, and K. Yvind, "Metal organic vapor-phase epitaxy of InAs/InGaAsP quantum dots for laser applications at 1.5 μm," *Appl. Phys. Lett.*, vol. 99, no. 10, p. 101106, 2011.

[206] C. Paranthoen, N. Bertru, O. Dehaese, a. Le Corre, S. Loualiche, B. Lambert, and G. Patriarche, "Height dispersion control of InAs/InP quantum dots emitting at 1.55 μm," *Appl. Phys. Lett.*, vol. 78, no. 12, p. 1751, 2001.

[207] C. Paranthoen, C. Platz, G. Moreau, N. Bertru, O. Dehaese, A. Le Corre, P. Miska, J. Even, H. Folliot, C. Labbe, G. Patriarche, J. C. Simon, and S. Loualiche, "Growth and optical characterizations of InAs quantum dots on InP substrate: towards a 1.55μm quantum dot laser," *J. Cryst. Growth*, vol. 251, no. 1–4, pp. 230–235, Apr. 2003.

[208] L. C. Lew Yan Voon and M. Willatzen, *The k-p method: Electronic Properties of Semiconductors*. Springer, 2010, p. 445.

[209] E. S. Semenova, I. V. Kulkova, S. Kadkhodazadeh, D. Barettin, O. Kopylov, A. Cagliani, K. Almdal, M. Willatzen, and K. Yvind, "Epitaxial growth of quantum dots on InP for device applications operating at the 1.55 μm wavelength range," in *Proc. of SPIE Quantum Dots and Nanostructures: Synthesis, Characterization, and Modeling XI*, 2014, vol. 8996, p. 899606.

[210] M. N. Akram, O. Kjebon, S. Marcinkevicius, R. Schatz, J. Berggren, F. Olsson, and S. Lourdudoss, "The Effect of Barrier Composition on the Vertical Carrier Transport and Lasing Properties of Multiple Quantum-Well Structures," *IEEE J. Quantum Electron.*, vol. 42, no. 7, pp. 713–724, 2006.

[211] V. Dijk, D. Make, O. Le Gouezigou, J. Provost, F. Poingt, J. Landreau, O. Drisse, E. Derouin, and B. Rousseau, "Recent Advances on InAs / InP Quantum Dash Based Semiconductor Lasers and Optical Amplifiers," vol. 13, no. 1, pp. 111–124, 2007.

[212] J. S. Kim, J. H. Lee, S. U. Hong, H.-S. Kwack, B. S. Choi, and D. K. Oh, "Well-defined excited states of self-assembled InAs⁄InAlGaAs quantum dots on InP (001)," *Appl. Phys. Lett.*, vol. 87, no. 5, p. 053102, 2005.

[213] J. S. Kim, C.-R. Lee, B. S. Choi, H.-S. Kwack, C. W. Lee, E. D. Sim, and D. K. Oh, "Vertical stacks of shape-engineered InAs⁄InAlGaAs quantum dot and its influences on the lasing characteristics," *Appl. Phys. Lett.*, vol. 90, no. 15, p. 153111, 2007.

[214] B. Jo, Y. Yang, J. Kim, M. Ko, K. J. Lee, C.-R. Lee, J. S. Kim, B. S. Choi, D. K. Oh, J.-Y. Leem, and J. S. Kim, "Enhancement in the gain of quantum dot laser by increasing overlap integral between electron and hole wave-functions," *Thin Solid Films*, vol. 517, no. 14, pp. 3983–3986, May 2009.

[215] V. Sichkovskyi, V. Ivanov, and J. P. Reithmaier, "High modal gain 1.5 μm InP based quantum dot lasers: dependence of static properties on the active layer design," *Proc. SPIE Nov. In-pl. Semicond. Lasers XII*, vol. 8640, p. 864004, Mar. 2013.

[216] T. F. Kuech and L. J. Mawst, "Nanofabrication of III–V semiconductors employing diblock copolymer lithography," *J. Phys. D. Appl. Phys.*, vol. 43, p. 183001 (18pp), May 2010.

[217] N. Kuznetsova, I. V. Kulkova, E. S. Semenova, S. Kadhodazadeh, N. V. Kryzhanovskaya, A. E. Zhukov, and K. Yvind, "Crystallographic dependent in-situ CBr4 selective nano-area etching and local regrowth of InP/InGaAs by MOVPE," *J. Cryst. Growth*, 2014.

[218] J. J. G. M. van der Tol, Y. S. Oei, U. Khalique, R. Nötzel, and M. K. Smit, "InP-based photonic circuits: Comparison of monolithic integration techniques," *Prog. Quantum Electron.*, vol. 34, no. 4, pp. 135–172, Jul. 2010.

[219] L. Lu, S. Feng, J. Xu, H. Yang, Z. Wang, J. Wang, Y. Wang, and W. Ge, "Deep centers in A1GaAs/GaAs GRIN-SCH SQW laser structures grown by MBE and MOCVD," *J. Cryst. Growth*, vol. 169, pp. 643–648, 1996.

[220] R. W. Tkach and A. R. Chraplyvy, "Regimes of feedback effects in 1.5 um distributed feedback lasers," *J. Light. Technol.*, vol. 4, no. 11, pp. 1655–1661, 1986.

[221] Y. Kawamura, K. Wakita, and H. Asahi, "Monolithic Integration of a DFB Laser and an MQW Optical Modulator in the 1.5 um Wavelength Range," *IEEE J. Quantum Electron.*, vol. QE-23, no. 6, pp. 915–918, 1987.

[222] A. Lestra and P. Brosson, "Design Rules for a Low-Chirp Integrated DFR Laser with an Electroabsorption Modulator," *IEEE Photonics Technol. Lett.*, vol. 8, no. 8, pp. 998–1000, 1996.

[223] M. Schell, A. G. Weber, E. Scholl, and D. Bimberg, "Fundamental Limits of Sub-ps Pulse Generation by Active Mode Locking of Semiconductor Lasers : The Spectral Gain Width and the Facet Reflectivities," *IEEE J. Quantum Electron.*, vol. 27, no. 6, pp. 1661–1667, 1991.

[224] T. Brenner, R. Dall'Ara, C. Holtmann, P. A. Besse, and H. Melchior, "High gain low reflectivity travelling wave semiconductor optical amplifiers integrated with passive waveguides operating at 1.3 μm wavelength," in *IEEE (5th) International Conference on Indium Phosphide and Related Materials*, 1992, pp. 88–90.

[225] T. Fujii and M. Ekawa, "Origin of compositional modulation of InGaAs in selective area metalorganic vapor phase epitaxy," *J. Appl. Phys.*, vol. 78, no. 9, p. 5373, 1995.

[226] O. Kayser, R. Westphalen, B. Opitz, and P. Balk, "Control of selective area growth of InP," *J. Cryst. Growth*, vol. 112, pp. 111–122, May 1991.

[227] J. E. Greenspan, "Alloy composition dependence in selective area epitaxy on InP substrates," *J. Cryst. Growth*, vol. 236, no. 1–3, pp. 273–280, Mar. 2002.

[228] T. Shioda, M. Sugiyama, Y. Shimogaki, and Y. Nakano, "Vapor phase diffusion and surface diffusion combined model for InGaAsP selective area metal–organic vapor phase epitaxy," *J. Cryst. Growth*, vol. 298, pp. 37–40, Jan. 2007.

[229] B. Garrett and E. J. Thrush, "Temporally resolved growth habit studies of InP/(InGa)As heterostructures grown by MOCVD on contoured InP substrates," *J. Cryst. Growth*, vol. 97, pp. 273–284, 1989.

[230] D. G. Coronell and K. F. Jensen, "Analysis of MOCVD of GaAs on patterned substrates," *J. Cryst. Growth*, vol. 114, pp. 581–592, 1991.

[231] R. Bhat, "Current status of selective area epitaxy by OMCVD," *J. Cryst. Growth*, vol. 120, no. 1–4, pp. 362–368, May 1992.

[232] A. K. Dutta, *WDM technologies*. Academic Press, 2003, p. 513.

[233] J.-S. Kim, J.-B. Yoo, D.-H. Jang, D.-K. Oh, and Y.-T. Lee, "Effects of pressure and temperature on epitaxial growth of InP on non-planar substrates using OMVPE," *J. Electron. Mater.*, vol. 21, no. 3, pp. 251–256, Mar. 1992.

[234] N. Waki, T. Nakano, M. Sugiyma, Y. Nakano, and Y. Shimogaki, "Role of surface diffusion during selective area MOVPE growth of InP," *Thin Solid Films*, vol. 498, no. 1–2, pp. 163–166, Mar. 2006.

[235] J. Wallin, G. Landgren, K. Streubel, S. Nilsson, and M. Oberg, "Selective area regrowth of butt-joint coupled waveguides in multi-section DBR lasers," *J. Cryst. Growth*, vol. 124, pp. 741–746, 1992.

[236] C. Blaauw, A. Szaplonczay, K. Fox, and B. Emmerstorfer, "MOCVD of InP and mass transport on structured InP substrates," *J. Cryst. Growth*, vol. 77, pp. 326–333, 1986.

[237] T. Brenner, E. Gini, and H. Melchior, "Low coupling losses between InP/InGaAsP Optical amplifiers and monolithically integrated waveguides," *IEEE Photonics Technol. Lett.*, vol. 5, no. 2, pp. 212–214, 1993.

[238] N. Dupuis, J. Décobert, P.-Y. Lagrée, N. Lagay, D. Carpentier, and F. Alexandre, "Demonstration of planar thick InP layers by selective MOVPE," *J. Cryst. Growth*, vol. 310, no. 23, pp. 4795–4798, Nov. 2008.

[239] Y. Wang, H. Song, M. Sugiyama, Y. Nakano, and Y. Shimogaki, "Surface Reaction Kinetics of InP and InAs Metalorganic Vapor Phase Epitaxy Analyzed by Selective Area Growth Technique," *Jpn. J. Appl. Phys.*, vol. 47, no. 10, pp. 7788–7792, Oct. 2008.

[240] H. E. G. Arnot, R. W. Glew, G. Schiavini, L. J. Rigby, and a. Piccirillo, "Selective etching of InP and InGaAsP over AlInAs using CH4/H2 reactive ion etching," *Appl. Phys. Lett.*, vol. 62, no. 24, p. 3189, 1993.

[241] J. Décobert, N. Dupuis, P. Y. Lagrée, N. Lagay, a. Ramdane, a. Ougazzaden, F. Poingt, C. Cuisin, and C. Kazmierski, "Modeling and characterization of AlGaInAs and related materials using selective area growth by metal-organic vapor-phase epitaxy," *J. Cryst. Growth*, vol. 298, pp. 28–31, Jan. 2007.

[242] N. Dupuis, J. Decobert, P. Y. Lagree, N. Lagay, C. Cuisin, F. Poingt, A. Ramdane, and C. Kazmierski, "AlGaInAs selective area growth by LP-MOVPE : experimental characterisation and predictive modelling," *IEEE Proc.-Optoelectron*, vol. 153, no. 6, pp. 276–279, 2006.

[243] Y. Wang, H. Song, M. Sugiyama, Y. Nakano, and Y. Shimogaki, "Surface Reaction Kinetics of InP and InAs Metalorganic Vapor Phase Epitaxy Analyzed by Selective Area Growth Technique," *Jpn. J. Appl. Phys.*, vol. 47, no. 10, pp. 7788–7792, Oct. 2008.

[244] M. Gibbon, J. P. Stags, C. G. Cureton, E. J. Thrush, C. J. Jones, R. E. Mallard, R. E. Pritchard, N. Collis, and A. Chew, "Selective-area low-pressure MOCVD of GalnAsP and related materials on planar InP substrates," *Semicond. Sci. Technoi*, pp. 998–1010, 1993.

[245] Y. D. Galeuchet, H. Rothuizen, and P. Roentgen, "In situ buried GaInAs / InP quantum dot arrays by selective area metalorganic vapor phase epitaxy," *Appl. Phys. Lett.*, vol. 58, no. 21, pp. 2423–2425, 1991.

[246] S. Adachi and H. Kawaguchi, "Chemical Etching Characteristics of (001) InP," *J. Electrochem. Soc.*, vol. 128, no. 6, pp. 1342–1349, 1981.

[247] C. . Verschuren, P. . Harmsma, Y. . Oei, M. . Leys, H. Vonk, and J. . Wolter, "Butt-coupling loss of 0.1dB/interface in InP/InGaAs MQW waveguide-waveguide structures grown by selective area chemical beam epitaxy," *J. Cryst. Growth*, vol. 188, no. 1–4, pp. 288–294, Jun. 1998.

[248] C. Rigo, R. Vincenzoni, A. Stano, and R. De Franceschi, "Chemical beam epitaxy on patterned substrates of InGaAs/InP heterostructures for optoelectronics and nanostructures applications," *J. Cryst. Growth*, vol. 164, pp. 327–333, 1996.

[249] G. Biasiol and E. Kapon, "Mechanism of self-limiting epitaxial growth on nonplanar substrates," *J. Cryst. Growth*, vol. 201–202, pp. 62–66, May 1999.

[250] A. Strittmatter, A. Holzbecher, A. Schliwa, J.-H. Schulze, D. Quandt, T. D. Germann, A. Dreismann, O. Hitzemann, E. Stock, I. A. Ostapenko, S. Rodt, W. Unrau, U. W. Pohl, A. Hoffmann, D. Bimberg, and V. Haisler, "Site-controlled quantum dot growth on buried oxide stressor layers," *Phys. Status Solidi*, vol. 209, no. 12, pp. 2411–2420, Dec. 2012.

[251] E. Kapon, "Quantum wires and quantum dots for optoelectronics: Recent advances with epitaxial growth on nonplanar substrates," in *NATO Advanced Research Workshop on Frontiers of Nano-Optoelectronic Systems*, 2000, vol. 6, pp. 41 – 64.

[252] S. Kollakowski, C. Lemm, A. Strittmatter, E. H. Bottcher, and D. Bimberg, "Buried InAlGaAs – InP Waveguides: Etching, Overgrowth, and Characterization," *IEEE Photonics Technol. Lett.*, vol. 10, no. 1, pp. 114–116, 1998.

[253] Y. Sun, Z. Liu, F. Machuca, P. Pianetta, and W. E. Spicer, "Optimized cleaning method for producing device quality InP(100) surfaces," *J. Appl. Phys.*, vol. 97, no. 12, p. 124902, 2005.

[254] Y. Takino, M. Shirao, N. Sato, T. Sato, T. Amemiya, N. Nishiyama, and S. Arai, "Improved Regrowth Interface of AlGaInAs/InP-Buried-Heterostructure Lasers by In-Situ Thermal Cleaning," *J. Quantum Electron.*, vol. 48, no. 8, pp. 971–979, 2012.

[255] S. Kadkhodazadeh, "High resolution STEM of quantum dots and quantum wires.," *Micron*, vol. 44, pp. 75–92, Jan. 2013.

[256] M. Schubert, "Coupled Photonic Crystal Cavity Array Laser," *PhD thesis*, p. Technical University of Denmark, 2010.

[257] J. Jin, J. Shi, and D. Tian, "Optimization of InGaAsP–InP tensile strained multiple quantum-well structures emitting at 1.34 μm," *Semicond. Sci. Technol.*, vol. 19, no. 6, pp. 742–746, Jun. 2004.

[258] M. J. Fordham, R. F. Gansman, and F. Y. Sorrell, "Emissivity correcting pyrometer for temperature measurement in low pressure chemical vapor deposition," in *Proceedings of the Tenth Biennial University/Government/Industry Microelectronics Symposium*, 1993, pp. 223–228.

[259] A. Oster, G. Erbert, and H. Wenzel, “Gain spectra measurements by a variable stripe length method with current injection,” *Electron. Lett.*, vol. 33, no. 10, pp. 864–866, 1997.

[260] P. Blood, G. M. Lewis, P. M. Smowton, H. Summers, J. Thomson, and J. Lutti, “Characterization of semiconductor laser gain media by the segmented contact method,” *IEEE J. Sel. Top. Quantum Electron.*, vol. 9, no. 5, pp. 1275–1282, Sep. 2003.

[261] S. Suchalkin, D. Westerfeld, G. Belenky, J. D. Bruno, J. Pham, F. Towner, and R. L. Tober, “Measurement of Semiconductor Laser Gain by the Segmented Contact Method Under Strong Current Spreading Conditions,” *IEEE J. Quantum Electron.*, vol. 44, no. 6, pp. 561–566, Jun. 2008.

[262] Y. Xin, Y. Li, A. Martinez, T. J. Rotter, H. Su, L. Zhang, A. L. Gray, S. Luong, K. Sun, Z. Zou, J. Zilko, P. M. Varangis, and L. F. Lester, “Optical Gain and Absorption of Quantum Dots Measured Using an Alternative Segmented Contact Method,” *IEEE J. Quantum Electron.*, vol. 42, no. 7, pp. 725–732, 2006.

[263] *LTD ANDO ELECTRIC CO. AQ6317 Optical Spectrum Analyzer Instruction Manual*. 1999.

[264] A. E. Zhukov, N. V. Kryzhanovskaya, F. I. Zubov, Y. M. Shernyakov, M. V. Maximov, E. S. Semenova, K. Yvind, and L. V. Asryan, “Improvement of temperature-stability in a quantum well laser with asymmetric barrier layers,” *Appl. Phys. Lett.*, vol. 100, no. 2, p. 021107, 2012.

[265] A. F. Phillips, S. J. Sweeney, A. R. Adams, and P. J. A. Thijs, “Compressively Strained InGaAs(P) MQW Semiconductor Lasers,” *IEEE J. Sel. Top. Quantum Electron.*, vol. 5, no. 3, pp. 401–412, 1999.

[266] Y. P. Varshni, “Temperature dependence of the energy gap in semiconductors,” *Physica*, vol. 34, no. 1, pp. 149–154, Jan. 1967.

[267] M. Usman, V. Tasco, M. T. Todaro, M. De Giorgi, E. P. O’Reilly, G. Klimeck, and A. Passaseo, “The polarization response in InAs quantum dots: theoretical correlation between composition and electronic properties,” *Nanotechnology*, vol. 23, no. 16, p. 165202, Apr. 2012.

[268] A. J. Zilkie, J. Meier, M. Mojahedi, P. J. Poole, P. Barrios, D. Poitras, T. J. Rotter, C. Yang, A. Stintz, K. J. Malloy, P. W. E. Smith, and J. S. Aitchison, “Carrier Dynamics of Quantum-Dot, Quantum-Dash, and Quantum-Well Semiconductor Optical Amplifiers Operating at 1.55 um,” *IEEE J. Quantum Electron.*, vol. 43, no. 11, pp. 982–991, 2007.

[269] S. Anantathanasarn, R. Nötzel, P. J. van Veldhoven, F. W. M. van Otten, Y. Barbarin, G. Servanton, T. de Vries, E. Smalbrugge, E. J. Geluk, T. J. Eijkemans, E. a. J. M. Bente, Y. S. Oei, M. K. Smit, and J. H. Wolter, “Lasing of wavelength-tunable (1.55 μm region) InAs⁄InGaAsP⁄InP (100) quantum dots grown by metal organic vapor-phase epitaxy,” *Appl. Phys. Lett.*, vol. 89, no. 7, p. 073115, 2006.

[270] A. R. Adams, I. P. Marko, N. F. Mass, and S. J. Sweeney, “Effect of non-pinned carrier density above threshold in InAs quantum dot and quantum dash lasers,” *IET Optoelectron.*, vol. 8, no. 2, pp. 88–93, Apr. 2014.

[271] B. W. Hakki and T. L. Paoli, “Gain spectra in GaAs double−heterostructure injection lasers,” *J. Appl. Phys.*, vol. 46, no. 3, p. 1299, 1975.

[272] Y. Barbarin, E. a. J. M. Bente, C. Marquet, E. J. S. Leclere, J. J. M. Binsma, and M. K. Smit, “Measurement of reflectivity of butt-joint active-passive interfaces in integrated extended cavity lasers,” *IEEE Photonics Technol. Lett.*, vol. 17, no. 11, pp. 2265–2267, Nov. 2005.

[273] T. Saitoh, T. Mukai, and O. Mikami, “Theoretical analysis and fabrication of antireflection coatings on laser-diode facets,” *J. Light. Technol.*, vol. 3, no. 2, pp. 288–293, 1985.

[274] T. Kitatani, K. Shinoda, T. Tsuchiya, H. Sato, K. Ouchi, H. Uchiyama, S. Tsuji, and M. Aoki, "Evaluation of the optical-coupling efficiency of InGaAlAs-InGaAsP butt joint using a novel multiple butt-jointed laser," *IEEE Photonics Technol. Lett.*, vol. 17, no. 6, pp. 1148–1150, Jun. 2005.

[275] D. J. Kane and R. Trebino, "Characterization of arbitrary femtosecond pulses using frequency-resolved optical gating," *IEEE J. Quantum Electron.*, vol. 29, pp. 571–579, 1993.

[276] M. Guden and J. Piprek, "Material parameters of quaternary III – V semiconductors for multilayer mirrors at 1.55 μm wavelength," *Model. Simul. Mater. Sci. Eng.*, vol. 4, pp. 349–357, 1996.

[277] C. Grasse, G. Boehm, M. Mueller, T. Gruendl, R. Meyer, and M.-C. Amann, "Empirical modeling of the refractive index for (AlGaIn)As lattice matched to InP," *Semicond. Sci. Technol.*, vol. 25, no. 4, p. 045018, Apr. 2010.

List of Abbreviations

ABL	Asymmetric Barrier Layer
AC	Autocorrelation
AlQ(λ)	Algainas Lattice-Matched to InP with a Bandgap of (λ) μm
AR	Auger Recombination
AR coating	Anti-Reflection coating
ASE	Amplified Stimulated Emission
BCB	Benzocyclobutene
BER	Bit Error Rate
BHF	Buffered HF
BJR	Butt-Joint Regrowth
CC scattering	Carrier-Carrier scattering
CH	Carrier Heating
CPM	Colliding Pulse Mode-Locking
c-QW	Conventional QW
CR	Clock Recovery
CW	Continuous Wave
DBR	Distributed Bragg Reflector
DCF	Dispersion Compensating Fiber
DOS	Density of State
EAM	Electro-Absorption Modulator
EDFA	Erbium Doped Fiber Amplifier
EDS	Energy Dispersive X-Ray Spectroscopy
ES	Excited State
ESA	Electrical Spectrum Analyzer
FCA	Free-Carrier Absorption
FFT	Fast Fourier Transform
FP laser	Fabry-Perot Laser
FROG	Frequency Resolved Optical Gating
FWHM	Full Width At Half Maximum
GDD	Group Delay Dispersion
GRE	Growth Rate Enhancement
GS	Ground State
HH	Heavy Holes
HR coating	High-Reflection coating
ICP-RIE	Inductively Coupled Plasma Reactive Ion Etching
IVBA	Intervalence Band Absorption
LH	Light Holes
L-I-V-T	Light (Power) vs. Current vs. Voltage vs. Temperature Characteristics
ML	Monolayer
MLL	Mode-Locked Laser
MORIE	Metal-Organic Reactive Ion Etching
MOVPE	Metal-Organic Vapor Phase Epitaxy
MQW	Multiple Quantum Wells
OCDMA	Optical Code Division Multiple Access
OFDM	Orthogonal Frequency Division Multiplexing

OSA	Optical Spectrum Analyzer
OTDM	Optical Time Division Multiplexing
PECVD	Chemical Vapor Phase Deposition
PL	Photoluminescence
PQ(λ)	Ingaasp Lattice-Matched to InP With a Bandgap of (λ) μm
PTER	Pulse Tail Extinction Ratio
QCSE	Quantum-Confined Stark Effect
QDs	Quantum Dots
QDashs	Quantum Dashs
QPSK	Quadrature Phase Shift Keying
QW	Quantum Well
RF	Radio Frequency
RIE	Reactive Ion Etching
RIN	Relative Intensity Noise
RMS	Root Mean Square
RT	Room Temperature
SA	Saturable Absorber
SAG	Selective Area Growth
SCH	Separate Confinement Heterostructure
SCM	Segmented Contact Method
SEM	Scanning Electron Microscopy
SHB	Spectral Hole Burning
SHG	Second Harmonic Generation
SK	Stranski-Krastanov
SMF	Single Mode Fiber
SOA	Semiconductor Optical Amplifier
SPM	Self-Phase Modulation
SQW	Single Quantum Well
SSB	Single Side Band
STEM	Scanning Transmission Electron Microscopy
TBP	Time-Bandwidth Product
TC	Temperature Controller
TE/TM	Transverse Electric/Magnetic (Field)
TPA	Two-Photon Absorption
UTC absorber	Uni-Traveling Carrier absorber
UV	Ultraviolet
VCSEL	Vertical Cavity Surface-Emitting Laser
VPD	Vapor Phase Diffusion
WDM	Wavelength Division Multiplexing
WG	Waveguide
WL	Wetting Layer
XRD	X-Ray Diffraction